MID-INFRARED PROPERTIES OF LOCAL ACTIVE GALACTIC NUCLEI

Dissertation

zur Erlangung des Doktorgrades
der Mathematisch-Naturwissenschaftlichen Fakultät
der Christian-Albrechts-Universität zu Kiel

vorgelegt von

Daniel Asmus

Kiel, 2012

Referent: Prof. Dr. Wolfgang J. Duschl

Koreferent: Prof. Dr. Holger Kersten

Tag der mündlichen Prüfung: 24.04.2012

Zum Druck genehmigt:

gez. Prof. Dr. Lutz Kipp, Dekan

Mittinfrarot-Eigenschaften von lokalen aktiven galaktischen Kernen

Die lokale Population von aktiven Galaxienkernen (AGN) erlaubt uns das detaillierte Studium der Strukturen und Strahlunsprozesse in der direkten Umgebung um die massereichen Schwarzen Löcher in Galaxienzentren und ermöglicht so das generelle Verständnis vom AGN-Phänomen weiter zu entwickeln. Zu diesem Zwecke steht nun durch *Swift*/BAT-Beobachtungen im harten Rntgenregime das erste unverfälschte Sample von 104 lokalen AGN zur Verfügung. Wir haben Mitinfrarot-photometrische (MIR) Beobachtungen mit hohen Winkelauflösungen (HR) von diesen AGN mit VLT/VISIR und Gemini/Michelle durchgeführt, um die Staubtori in jenen Objekten zu studieren – eine Schlsselkomponente in AGN-Modellen. Zur gleichen Zeit haben wir vergleichbare Daten fr ein komplementäres Sample von AGN im lichtschwachen Regime aufgenommen. In dieser Arbeit prsentiere ich die Resultate von beiden Programmen und zeige, dass in den AGN aus beiden Samples unaufgelöste MIR-Emission ($< 0.4''$) vorhanden ist. Andererseits zeigt ein Vergleich mit Daten von niedrigerer Auflösung ($\sim 30''$), dass die Wirtsgalaxien im MIR um ein Vielfaches heller sind als leuchtschwache und moderat-helle AGN. Dies demonstriert, wie wichtig ein hohes räumliches Auflösungsvermögen für die Isolierung und Untersuchung der MIR-Eigenschaften von AGN. Deshalb sind viele *Spitzer*/IRS-Spektren von nicht-nukleare MIR-Emission beeinträchtigt. Trotzdem kann ich die Emissionsstrke des polyzyklischen aromatischen Hydro-Karbonat-Features, welches in diesen Spektren gemessen wurde, benutzen um den maximalen Beitrag durch Sternentstehung zu der HR nuklearen Emission abzuschätzen, und zeige, dass er minimal ist. Anstatt dessen ist die beobachtete unaufgelöste MIR-Emission konsistent mit thermischer Strahlung von Staub in der direkten Umgebung des AGN. Insbesondere die gemittelten MIR spektralen Energieverteilungen zeigen das Silikat-Feature in Emission für Typ 1 AGN und in Absorption für Typ 2 AGN. Außerdem ist die MIR-Emission mit der Absorptions-korrigierten 2-10 keV Röntgenemission ber den gesamten Bereich von Leuchtkräften (10^{40} bis 10^{45} erg/s) stark korreliert, was ber einen großen Bereich ($L_{\mathrm{bol}}/L_{\mathrm{Edd}} \sim 10^{-3.8}$ bis 1) unabhängig von der Akkretionsrate ist. Andererseits besitzen Objekte mit $L_{\mathrm{bol}}/L_{\mathrm{Edd}} \lesssim 10^{-3.8}$ ein besonders hohes Verhltnis der MIR- zu Rntgenleuchtkr¨fte, welches auf den Beitrag einer weiteren Emissionsquelle hindeutet. Eine ähnliche Korrelation (fr̈ die MIR) mit der beobachteten 14-195 keV Strahlung wird festgestellt. Beide Korrelationen sind am stärksten fr Typ 1 AGN, während ihre Steigung und Normalisierung keine Abhängigkeit zur Obskuration des Kerns oder den Eigenschaften der Wirtsgalaxien zeigen. Dem gegenüber treten extrem obskurierte Objekte häufiger in auf der Seite liegenden (edge-on) Galaxien auf als unabsorbierte AGN. Dies deutet darauf hin, dass in einigen Fällen die Obskuration des AGN von nicht-nuklearen Strukturen innerhalb der Wirtsgalaxie stattfindet. Trotzdem deutet die Gleichförmigkeit des MIR-Rntgen-Verhltnisses darauf hin, dass die MIR-Strahlung von einer nuklearen Staubstruktur kommt, welche von der Akkretionsscheibe direkt geheizt wird. Zusammen mit der erfolgreichen Erklärung der Befunde von vorausgehende HR-MIR-Daten von AGN mit Modellen von klumpigen Staubtori impliziert dies, dass eine solche Struktur in allen AGN des gesamten untersuchten Leuchtkraftbereiches vorhanden ist. Deshalb könnte das Standard-Vereinheitlichungsmodell weiterhin für all Typen von AGN ohne größere Modifikationen gültig sein.

Mid-infrared properties of local active galactic nuclei

The local active galactic nuclei (AGN) population enables us to study in detail the structures and radiation processes in the direct environment of the supermassive black holes in galaxy centers and to develop an understanding of the general AGN phenomenon. For this purpose, the first unbiased sample of 104 local AGN has now become available thanks to *Swift*/BAT observations in the hard X-ray regime. We performed high-angular resolution (HR) mid-infrared (MIR) imaging observations of most of these AGN with VLT/VISIR and Gemini/Michelle in order to study the dusty tori in these objects – a key component in AGN models. At the same time, we obtained similar data of a complementary sample of AGN in the low-luminosity regime. In this thesis, I present the results of both programmes and show that unresolved ($< 0.4''$) MIR emission is present in the AGN of both samples. A comparison with large aperture ($\sim 30''$) data shows that the host galaxy outshines low-luminosity and moderate AGN in the MIR, which emphasizes the necessity of HR to isolate and investigate the MIR properties of AGN. Hence, many *Spitzer*/IRS spectra are affected by non-nuclear MIR emission. Nevertheless, I can use the polycyclic aromatic hydrocarbon emission feature strength determined from these spectra to constrain the maximum star formation contribution to the HR nuclear emission to be minor. Instead, the observed unresolved MIR nuclei are consistent with thermal emission from dust in the direct vicinity of the AGN. In particular, the average MIR spectral energy distributions show the silicate feature in emission for type 1 AGN and in absorption for type 2 AGN. Furthermore, the MIR emission is strongly correlated with the absorption-corrected 2-10 keV X-ray emission over the whole range of luminosities (10^{40} to 10^{45} erg/s) which is independent of the accretion rates over a large range ($L_{\mathrm{bol}}/L_{\mathrm{Edd}} \sim 10^{-3.8}$ to 1). On the other hand, objects with $L_{\mathrm{bol}}/L_{\mathrm{Edd}} \lesssim 10^{-3.8}$ exhibit high MIR–X-ray luminosity ratios indicating contribution of an additional component. However, they still follow well the correlation of the other AGN. A similar correlation (of the MIR) with the observed 14-195 keV emission is found. Both correlations are strongest for type 1 AGN while their slope and normalization do not show any dependence on the nuclear obscuration or host properties. On the contrary, highly obscured objects occur more often in edge-on galaxies than unobscured AGN. This indicates that in some cases the obscuration of the AGN is caused by non-nuclear structures in the host galaxy. Nevertheless, the fact that MIR–X-ray ratio is very uniform for all AGN types and host galaxies indicates that the MIR emission is coming from a dusty nuclear structure that is directly heated by the accretion disk. Together with the successful explanation of the findings from previous HR MIR data of AGN with models of dusty clumpy tori, this indicates that such a structure is present in all of the AGN from the whole probed luminosity range. Therefore, the standard unification model may be valid for all types of AGN without major modifications.

Centaurus A over Paranal

This composed image shows the radio galaxy Cen A (in approximately scaled and positioned) in the night sky over the Cerro Paranal observatory, Chile. The original photo of Paranal has been taken by Dr. Y. Beletsky and has been modified in order to create this composite. The image of Cen A itself is a composite of optical (white), radio (orange) and Gamma-rays (purple). The actual galaxy is only the whitish little dot in the center of the structure, while gigantic radio lobes extend to a distance more than 1.4 million light years away from the galaxy to an apparent size, which is almost twenty times larger than the one of the moon. These lobes are produced and fed by a highly-collimated, extremely fast outflow that originates in the very center of the galaxy. Its powerhouse is a super-massive black hole. Such nearby active galactic nuclei are the subject of this thesis.

Reproduced from ESO (`http://www.eso.org/public/images/potw1119a/`) and NASA (`http://www.nasa.gov/mission_pages/GLAST/news/smokestack-plumes_prt.htm`). Credit: aESO/Y. Beletsky; and NASA/DOE/Fermi LAT Collaboration, Capella Observatory, and I. Feain, T. Cornwell, and R. Ekers (CSIRO/ATNF), R. Morganti (ASTRON), and N. Junkes (MPIfR).

Contents

1. Introduction

Today it is commonly believed that every galaxy harbors a supermassive black hole (SMBH) of several tens of thousands up to tens of billions of solar masses ($10^5 M_\odot \lesssim M_\mathrm{BH} \lesssim 10^{10} M_\odot$) in its gravitational center. By definition, a black hole is not directly emitting radiation at any wavelength making its detection challenging. However, a black hole can be detected by its gravitational influence on surrounding matter, and indeed the most direct evidence for the existence of SMBHs comes from kinematic studies of nearby galactic centers. In particular in our own galaxy, the Milky Way, it has been possible for several years to study the motion of stars in the central parsec ($1\,\mathrm{pc} = 3.085 \cdot 10^{16}\mathrm{m} = 3.262$ light years) in the near-infrared. The observed orbits are only explainable with a very compact mass of $\sim 4 \cdot 10^6 M_\odot$ at the position of the radio point source Sgr A*, which can only be a black hole, or, according to the theory of gravitation, such an object would collapse to a black hole on short timescales. This result was found independently and in perfect agreement by two groups (e.g. Ghez et al. 2003; Schödel et al. 2003) and Fig. 1.1 shows the stellar orbits of the closest stars to Sgr A*. For most other galactic centers, it is not possible to resolve individual stars with current technology. However, studies of integrated stellar or gas kinematics reveal Keplerian rotation curves around extremely compact supermassive objects. One of the best examples is M 106 (NGC 4258), a nearby galaxy ($D \approx 7.4\,\mathrm{Mpc}$), in which water maser emission could be observed at radio wavelengths with very long baseline interferometry (Miyoshi et al. 1995). By this technique it is possible to achieve angular resolutions on the order of milli-arcsec, sufficient to resolve the gravitational black hole sphere of influence (Fig. 1.2). With these methods, it is not only possible to demonstrate the existence of SMBH but also to estimate their masses.

Interestingly, Gebhardt et al. (2000) and Ferrarese and Merritt (2000) then used these mass measurements from several SMBH in galactic centers to discover a fundamental correlation with the central stellar velocity dispersion, σ_*, of the host galaxies. The latter is measured in the central bulges of galaxies on scales much larger than the sphere of influence of the black hole. This discovery was surprising and far-reaching, because it implies a fundamental connection between the growth of the SMBH and the evolution of the galaxy itself. Explaining this relationship is one of the largest challenges in current astrophysics, and one of its important requirements is a comprehensive understanding of the growth of black holes.

1.1. Active galactic nuclei

A black hole can grow (in mass) by two processes: by merging with other stellar objects or black holes, or by accreting surrounding diffuse material like gas. Collisions of SMBH with

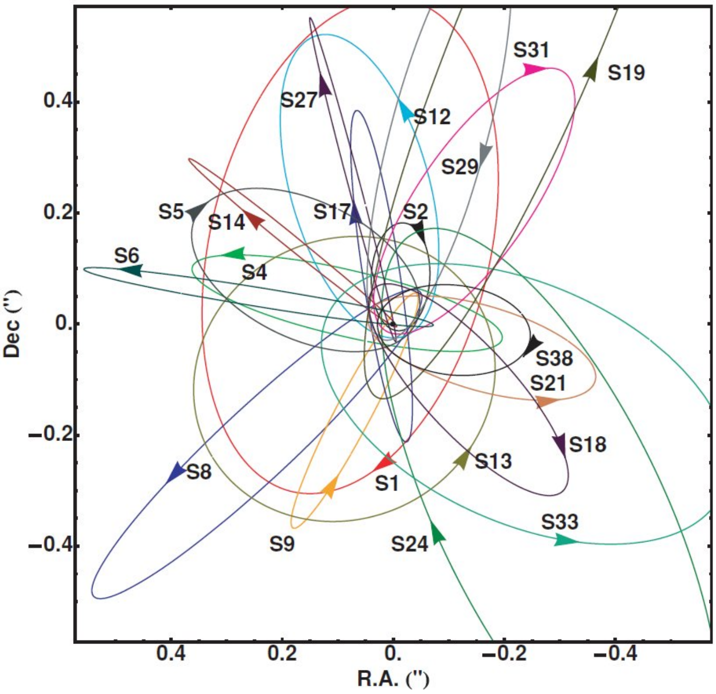

Figure 1.1: Position and orientation of the stellar orbits with respect to Sgr A*. Reproduced from Gillessen et al. (2009).

individual stars happen quite rarely (as demonstrated by Sgr A* because the friction of star with their surroundings is too low and they are not able to effectively lose angular momentum necessary to fall into the SMBH. A direct hit from a star incoming from a large distance away is also quite unlikely. On the other hand, current galaxy evolution theories predict the growth of galaxies by many mergers happening over cosmic time scales. Under the assumption that each merging galaxy hosts a SMBH, both of them would migrate into the new galactic center of mass quickly and form a binary black hole (Begelman et al. 1980). According to theory, the black holes should merge rapidly (on 1-Myr timescale) due to effective loss of energy by emitting gravitational waves (Milosavljević and Merritt 2001).

While SMBH mergers could be one of the major channels of black hole growth that explain the SMBH–galaxy relation, the other possibility (growth by accreting diffuse matter) might also enable sufficient growth rates to explain the observed SMBH masses at different cosmological epochs (Duschl and Strittmatter 2011). Indeed, contrary to SMBH mergers, actively accreting black holes are observed in large numbers. In fact, all SMBH seem to accrete even if with very low rates as, e.g., Sgr A*. Because of angular momentum conservation gas cannot directly fall into the SMBH either; instead a disk-like structure is formed, the accretion disk. Accretion disks are a universal astrophysical structure that form simply due to angular momentum conservation, and can be observed on size scales differing by orders of magnitude. For example, stars originate in a collapsing gas cloud that becomes an accretion disk, creating and then feeding the nascent stellar embryo. In the very same disk, the planets are formed as well. However, in order for the central object to accrete, the surrounding material

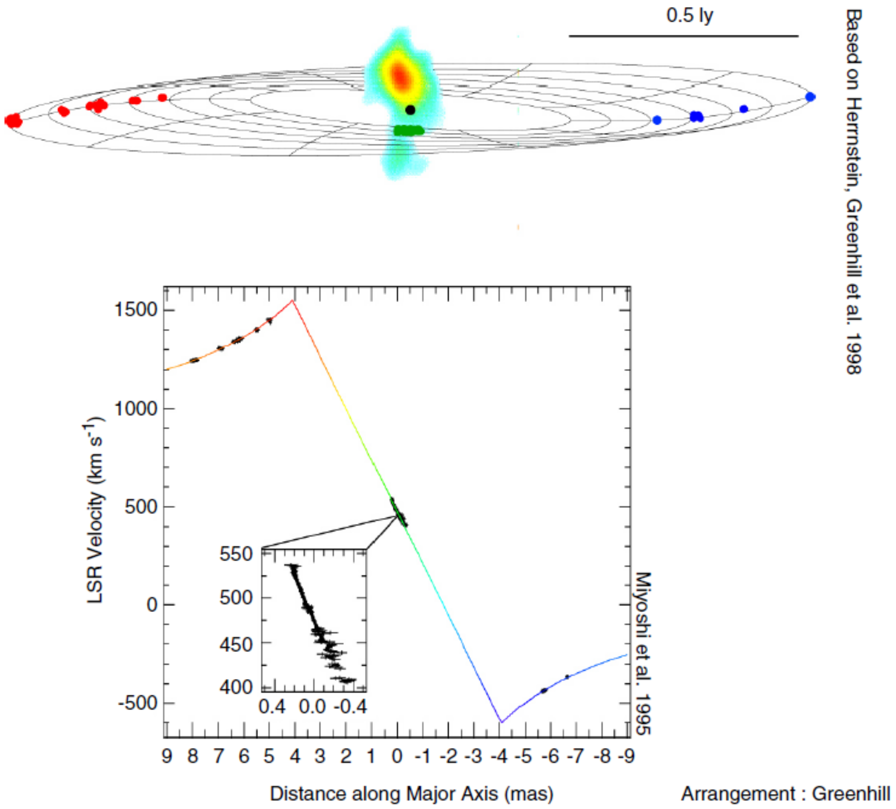

Figure 1.2: Upper panel: the red, blue and green spots show the relative locations of maser-emitting clouds in the gas disk at the center of M 106, as determined with radio interferometry. The black dot is the calculated position of the central supermassive BH. Emanating from the BH are the beginnings of twin jets. The dashed lines trace out a model of the disk. Lower panel: the dots show the line-of-sight velocities of the maser spots as a function of distance from the BH along the major axis of the disk. Note how perfectly the velocities follow the Keplerian profile traced by the line. By fitting the velocities, the mass of the BH is inferred to be $3.5 \pm \cdot 0.110^7 M_\odot$ (reproduced from Narayan (2005); see also Greenhill et al. (1995) and Herrnstein et al. (1998)).

must lose again angular momentum and the known processes of, e.g., molecular friction are not sufficient: the exact nature of the needed viscosity remains unknown at present. Shakura and Sunyaev (1973) circumvented this problem by parameterizing the viscosity and concentrating the unknown process into a variable (α). By these means it became possible to build an analytic model of geometrically thin and optically thick accretion disks (hereafter standard disk) that could explain well many of the observed accretion disks. These are usually relatively bright throughout the electromagnetic spectrum, because during the process of slowly approaching the black hole and drifting deeper into the gravitational trough, large amounts of energy are released that heat the gas and lead to various radiation processes. In fact, accretion onto a black hole is the most efficient energy release channel in the universe.

Hence actively accreting SMBH can become extremely bright at various wavelengths, enabling their observation even of cosmic distances. They are called active galactic nuclei (AGN)

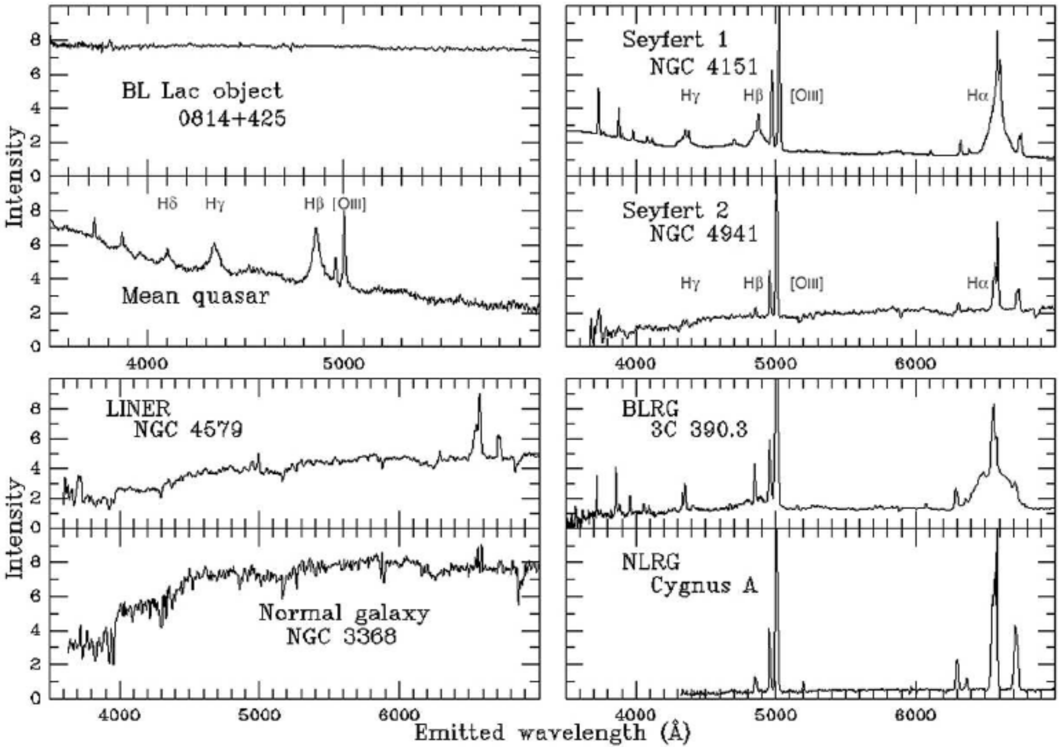

Figure 1.3: Optical spectra of various individual galactic nuclei that represent different the different classes of observed AGN and normal galaxies. Note the extremely broad Hα emission line at 6562.8Å in the Seyfert 1 galaxy NGC 4151 (top-right). See text for further explanation. Reproduced from `http://www.astr.ua.edu/keel/agn/spectra.html`. Credit: W. C. Keel.

and are the subject of this work. Further details on the AGN phenomenon are presented in Chapter 2.

1.2. AGN in the mid-infrared

AGN might be the most powerful non-transient objects in the universe, giving ample evidence for black hole growth over cosmic timescales. They appear in many different flavors, exhibiting a variety of emission characteristics at various wavelengths (see Fig. 1.3 for an overview of various optical spectra). One of the most noticeable characteristics of their spectra are the strong optical emission lines (like Hα and Hβ) that can show an extremely broad component (line width of several 1000 km/s) indicating a high velocity dispersion of the emitting gas. This gas must be in a region relatively close to the SMBH, which is called the broad line emitting region (BLR). The objects where this broad component is observed are called Seyfert 1 galaxies, or, more general, type 1 AGN. In other objects, this broad component is not observed but a much narrower, yet relatively broad and strong, component is seen instead (line width of several 100 km/s). This narrow-line emitting region (NLR) must be further away from the black hole, and AGN for which only this component is visible are called Seyfert 2 (Sy 2), or, more generally, type 2 AGN. Depending on other properties such as radio emission, AGN can be further distinguished into several other classes.

However, there is strong evidence that all phenomenologically different nuclei of objects can be explained by one unified physical model (Antonucci 1993). Its main constituent is the SMBH, surrounded by the accretion disk (see Fig.2.2). They are embedded in the BLR, which itself is surrounded by a dusty, molecular torus-like structure (hereafter simply torus). Thus, depending on the torus orientation with respect to the line of sight, optical broad emission lines can be observed (Sy 1) or are obscured (Sy 2). This torus absorbs the optical and ultraviolet (UV) radiation from the accretion disk and re-emits it in the infrared. However, the nature of the torus is still largely unknown, although some lines of evidence, including interferometric measurements, suggest it consists of many dusty clumps with a parsec-scale extent (e.g. Hönig et al. 2006). Such a structure can be best observed at mid-infrared (MIR) wavelengths (~ 4 to $\sim 30\,\mu$m) where the thermal emission from the dust is strongest. Probing this MIR emission of AGN is the major goal of this thesis.

1.3. Current challenges in AGN research

While the unification model can explain most observations to first order, it is not a complete physical model; i.e., the exact origin, properties and interaction of its components is not physically described. The major problem here is that for most AGN, structures such as the accretion disk or the torus cannot be resolved with current instruments. Even for the closest sources, only very complex instruments like large interferometers (e.g., VLTI/MIDI) can marginally resolve the torus. Thus, all key components of the unification model appear as one point source in the sky. Even worse, AGN are, by definition, in the centers of galaxies, where the density of stars is highest and isolation of the AGN emission can be very challenging, especially in the optical and ultraviolet, where most stars are brightest. In addition, large amounts of gas and dust can surround the nucleus or fall coincidently in the line of sight between the AGN and the observer. This leads to the extinction of significant amounts of emission from the near-infrared to the X-ray. Therefore, the AGN is best examined at wavelengths where other sources are faint, and the extinction is low, e.g., in the radio, MIR and hard X-rays (> 2 keV). Spectroscopy has proven to be a powerful tool, enabling the study of high-excitation emission lines that are believed to only be excited in the hard radiation fields of AGN. By these means, it is possible to extract information about the physical conditions (e.g., temperature, densities) in the vicinity of AGN. Another possibility is to try to isolate the AGN emission with high-angular resolution (HR) photometry in different suitable wavelength regions and to build a spectral energy distribution (SED) that can in turn be compared with predictions from physical models of the individual AGN components. This work represents the first step in this type of investigation, by probing the AGN with HR photometry in the MIR.

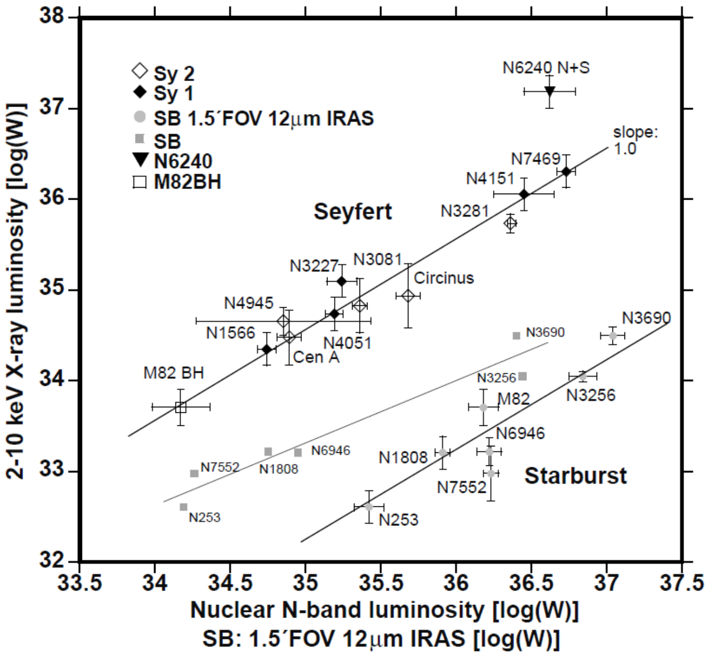

Figure 1.4: MIR–X-ray luminosity correlation for nearby Seyfert galaxies (black symbols). For comparison, also a selection of starburst galaxies is shown (in grey). Reproduced from Krabbe et al. (2001).

1.4. The MIR–X-ray correlation

As mentioned above, the MIR and hard X-ray regimes are optimally suited for investigation of AGN because of the relatively high brightness of AGN in these bands (in particular in X-rays) and the relatively low obscuration (at least in the MIR). Krabbe et al. (2001) were the first to combine measurements of local Seyfert nuclei in both bands, specifically the 12 μm and the 2-10 keV emission. They found a strong correlation between the luminosities measured in both bands ($L_{\mathrm{MIR}} \propto L_{\mathrm{X}}^{b}$; $b \approx 1$) valid for all observed Seyferts (Fig. 1.4). For this purpose it is important to correct the hard X-rays for absorption, because the later can have a major impact on the observed X-ray emission. Because the amount of absorption is usually unknown, the correction has to be determined by modeling the observed X-ray emission (more details in Chapter. 5). The MIR–X-ray correlation was later verified by Lutz et al. (2004), albeit with larger scatter, for a larger sample of AGN using the 6 μm emission. It implies a fundamental physical connection between the AGN emission in these wavelength regions that can be understood by the following considerations: the hard X-ray emission originates presumably in a hot corona above the accretion disk very close to the black hole (at a few Schwarzschild radii). It is reasonable that the X-ray emission scales roughly with the UV emission produced by the accretion disk itself, and the latter is mainly absorbed by the dust in the obscuring torus structure. The heated dust then thermally radiates in the mid-infrared, leading to the observed correlation between X-ray and MIR. Of course, the amount of radiated MIR emission will depend on the geometry and properties of the obscuring material, but it should roughly scale with the total amount of emitted UV. The fact that the correlation is comparable for Sy 1 and Sy 2 supports the unification scheme that predicts only orientation effects and no intrinsic differences between both types.

One reason for the significant scatter in the correlation found by Lutz et al. (2004) can be the low angular resolution ($\theta_0 = 24''$) used for the MIR measurements with the Infrared Space Observatory (*ISO*). High-angular resolution is important for MIR observations of AGN because thermal emission from dust can be caused not only by AGN but also by star forming regions. Star formation (SF) in galaxies also frequently occurs close to the nucleus and can become bright at infrared wavelengths (in particular in the far-infrared). Lutz et al. (2004) tried to correct for this possible contamination by subtracting SF templates from their *ISO* spectra. However, there are several uncertainties in this method that can easily lead to the observed scatter.

For this reason, Horst et al. (2006, 2008) used the mid-infrared instrument VISIR mounted on the VLT to reexamine the MIR–X-ray correlation at HR. Thanks to the 8-meter mirror, VLT/VISIR provides an subarcsec angular resolution which enables sufficient isolation the AGN emission in most nearby galaxies. They verified the MIR–X-ray correlation with low scatter and no evidence for any object-type dependency. Recently, Gandhi et al. (2009) (hereafter G09) and Levenson et al. (2009) extended these HR measurements with similar results (Fig. 1.5). Apart from local Seyfert galaxies, the sample from G09 also includes three low-ionization nuclear emission line regions (LINERs), a different faint subclass of AGN (bottom left in Fig. 1.3). The nature of LINERs is debated in the literature, because the power necessary to provide the observed emission line properties could, in principle, also be explained by stellar processes rather than accretion onto a SMBH. On the other hand, in many LINERs, point-like radio and X-ray emission is detected, which indicates the presence of an actively accreting SMBH.

For all classes of AGN, the MIR–X-ray correlation can provide a potentially powerful tool to test the unification scheme and especially torus models, as discussed below. However, some issues remain open that must be resolved to completely verify this correlation.

1.5. Motivation for this work

A first open issue of the MIR–X-ray correlation regards the low-luminosity regime of AGN ($L_X \lesssim 10^{42}$ erg/s). None of the previous works had sufficient coverage in this luminosity range, which is particularly interesting because several structural changes are predicted to occur at low powers, notably the disappearance of the dusty torus (e.g., Hönig and Beckert 2007; see Sect. 2.3 for more details). If the torus indeed “collapses” or “evaporates,” the MIR emission should also be dramatically reduced and such low-luminosity AGN (LLAGN) should deviate significantly from the MIR–X-ray correlation. However, the lowest-luminosity AGN in the G09 sample instead exhibit an excess of MIR emission (Fig. 1.5). Depending on whether this excess, proves to be true, it could indicate that an additional AGN component contributes to the MIR emission of LLAGN. The best candidate would be the jet, a collimated outflow

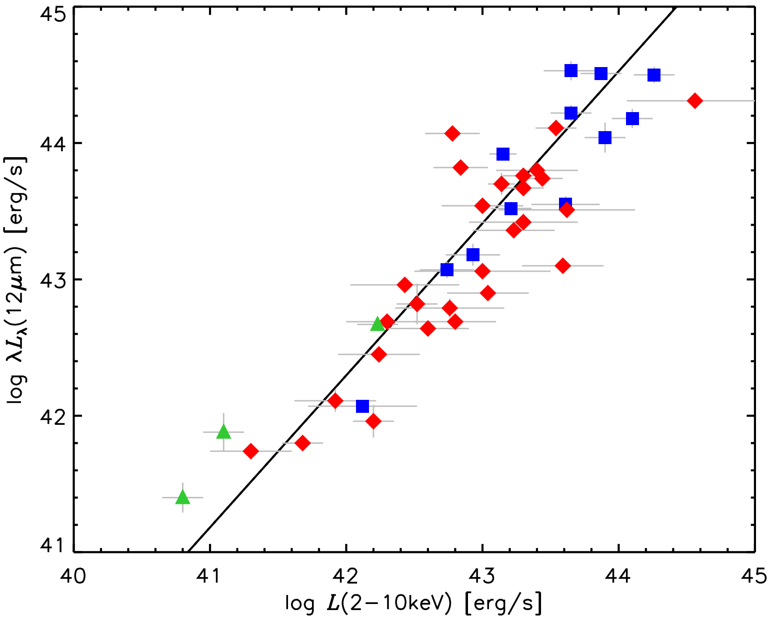

Figure 1.5: MIR–X-ray luminosity correlation for nearby AGN from G09. Blue squares are Sy 1, red diamond Sy 2, and green triangles LINERs. The solid black line represents a linear fit to all data points. Note that the X-ray luminosity is chosen for the abscissa because by originating from the central accretion processes it resembles more the independent variable with respect to the MIR emission. After data from G09.

perpendicular from the accretion disk of highly energetic particles. This jet is expected to emit copious amounts of synchrotron emission that can also contribute significantly to the MIR (e.g., Hardcastle et al. 2009). Indeed, it is known from, mainly, radio observations that many of the LLAGN host strong jets and emit strongly at these wavelengths. Therefore, it is important to determine the MIR dominating component in LLAGN and to find out whether they follow the same MIR–X-ray correlation as the brighter Seyferts do.

Another weakness of the current MIR–X-ray correlation studies is that the chosen samples are not complete in any sense and might not represent well the whole (local) AGN population. Indeed there are many indications that a large group of heavily obscuring AGN is missing so far (see Chapter. 5). A complete HR MIR survey of a uniform and unbiased AGN sample is necessary in order to verify the validity of the correlation for the whole AGN population and to accurately determine its properties. This is obviously also important for the determination of any significant deviation occurring for particular sub-classes such as the LLAGN. Finally, such a complete study will set indispensable constraints on the torus models and enable important tests on the unification scheme of AGN.

Exploration of the low-luminosity regime and extension of the MIR–X-ray correlation to a complete sample of AGN are the two main goals of this work.

Hence. the structure of this manuscript is split in several major parts: first I discuss the current understanding of the AGN phenomenon with emphasis on LLAGN in Chapter 2 and review their theoretical mid-infrared properties. Then, in Chapter 3, the methods employed, instruments and technical aspects of this investigation are presented, and in Chapter 4, the observations and resulting MIR properties of the LLAGN are presented. HR MIR observations and results of a uniform AGN sample follow in Chapter 5, and Chapter 6 presents the analysis of the MIR–X-ray relations for both samples. A discussion of these results, and in particular the origin of the MIR emission in AGN, is provided in Chapter 7, and finally Chapter 8 concludes and summarizes this work, additionally presenting in addition some perspectives for future work.

Finally, the extensive Appendix provides reference material and additional tables belonging to this thesis. However, their consultation is not necessary in order to follow the discussion in the main text.

Note that throughout this thesis the cgs system of units is used, as is common in astrophysics. A list of acronyms and physical symbols can be found in the Appendix. For better readability, I abridge the longest object identifiers by skipping the declination designator, e.g., 2MASX J03502377-5018354 becomes 2MASX J03502377.

2. Physics of active galactic nuclei

Carl Seyfert was the first (1943) to systematically study a peculiar class of galaxies showing extremely bright nuclei with strong emission lines. The emission lines came from a point-like region, but showed a broad velocity width, and hence could not have been excited by stellar processes. If the emitting gas were gravitationally bound, then its velocity would typically be $v^2 = GM/r$ with r being the radial distance from the gravitational center and M the enclosed (central) mass. Now, if one interprets the line width as Doppler broadening, $\Delta\lambda/\lambda = \Delta v/c$, the resulting gas velocity would be $v \sim 1000\,\mathrm{km/s}$. In addition, from the fact that the emitting region is unresolved it follows that $r \leq 100\,\mathrm{pc}$. This in turn implies an enclosed mass, $M \geq 10^{10}(r/100\,\mathrm{pc})M_\odot$, which would be an enormous amount of mass in the center of these galaxies, unless the emitting region is much smaller than 100 pc. On the other hand, a small r ($\lesssim 1$ pc) implies an enormous concentration of energy in the nucleus. These simple considerations already demonstrated that in the nuclei of these Seyfert galaxies very energetic, non-stellar processes happen. Later, they were shown to be actively accreting SMBHs (Salpeter 1964; Lynden-Bell 1969).

Roughly at the same time, the first systematic sky surveys at radio wavelengths led to the discovery of radio sources that did not coincide with known galaxies. Instead, they appeared point-like in the optical and thus were called quasi-stellar radio sources (quasar). Schmidt (1963) was the first to determine the redshift of one of these sources (3C 273) to be $z = 0.158$, which implied that it is ~ 100 times more luminous than any normal galaxy. Eventually, it turned out that the quasars and Seyferts galaxies have the same physical origin, as we will see below.

However, this chapter is not intended to be a complete discussion of the AGN phenomena and all its aspects, which can be found in Krolik (1999). Instead, I concentrate on those aspects that are most relevant for this work.

2.1. AGN classification

Historically, AGN are classified by their optical emission line properties. In order to separate AGN from star forming galaxies, the most common method used consists of a set of empirical diagnostic diagrams (hereafter BPT diagram; Baldwin et al. 1981; Fig. 2.1). For example, the narrow emission line ratios [OIII]λ5007 to H_β versus [NII]λ6584 to H_α can be used for this purpose because SF (HII) nuclei and AGN form two well-defined wings in such a diagram (e.g., Kewley et al. 2006). This separation is caused by the upper limit on the intensities of the collisionally excited lines that can be powered by the massive stars in SF nuclei with respect to

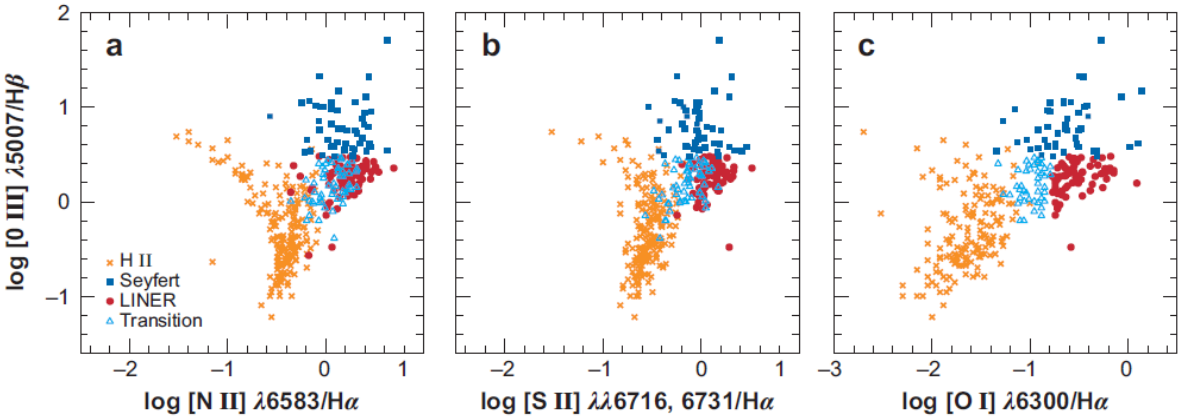

Figure 2.1: Galaxy nuclei classification with the BPT diagnostic diagrams of optical emission line ratios. H II nuclei are SF powered. Seyferts are SMBH powered, while for LINERs and transition objects, it is presumably a combination of both. Reproduced from Ho (2008). Credit: Ho et al. (1997).

the recombination lines (such as H_α or H_β). In contrast, AGN are far more powerful, leading to more intense collisionally excited lines (Trouille and Barger 2010). However, the transitions between different populations are continuous and, in particular, LINERs are located in the same wing as Seyferts, just with a lower [OIII]λ5007 to H_β ratio. For some border line objects, it can even happen that different diagrams yield different classifications (see Sect. 4.2.1).

At the same time, AGN can also be identified at other wavelengths: in particular, in the radio and X-rays, a nuclear point source of a certain power is a good indicator (e.g., Ho 2008). Interestingly, among others, Trouille and Barger (2010) find that ~ 50% of the X-ray identified AGN are misclassified as SF nuclei in the BPT diagrams. Furthermore, a significant number of AGN are completely obscured in the optical and thus remain unidentified as active, if not several other indicators are combined (e.g. Goulding and Alexander 2009).

In addition to the distinction between SF nuclei and AGN through the BPT diagrams, the AGN themselves are divided into several sub-classes, depending on the properties of the Balmer lines. The first systematic study of the emission line properties of Seyfert galaxies revealed that an extremely broad component ($\geq$ 1000 km/s, i.e. the BLR) was only visible in some objects, while all Seyferts showed at least a strong narrow component (~ 100 km/s), i.e. the NLR (Khachikian and Weedman 1974). Hence, an observational classification scheme was introduced (Osterbrock 1977, 1981) and later extended: all objects with broad Balmer lines (~ 1000 km/s) and a high [OIII]λ5007 to H_β ratio (where the narrow component of H_β is used) are called Sy 1.0; then, Sy 1.2, Sy 1.5 and Sy 1.8 simply have decreasing [OIII]λ5007 to H_β ratios with Sy 1.8 exhibiting the lowest ratio but still having the broad line components; Sy 1.9, on the other hand, have only broad H_α; and finally in Sy 2.0, neither broad H_α nor H_β are visible. Historically, additional classifications like the quasars and quasi-stellar objects (QSO) were introduced, although it has turned out in the meanwhile that QSO 1 are just more luminous Sy 1 while all other properties are similar. Hence, nowadays only type 1 (Sy 1.0-1.5 and QSO 1) and type 2 AGN (Sy 1.8 - 2.0 and QSO 2) are commonly distinguished. Finally,

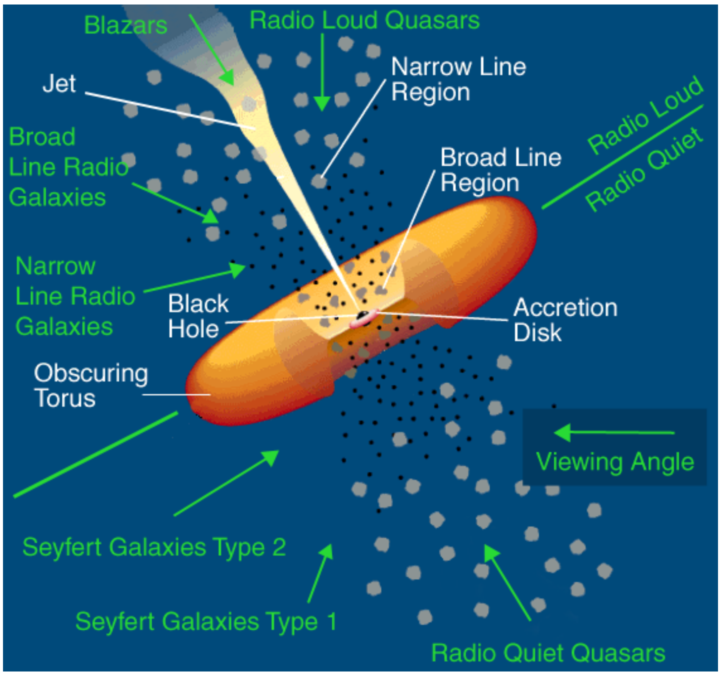

Figure 2.2: Schematic of the unification model of AGN. The scale is roughly logarithmic. Note that the torus is simply represented by a smooth donut-like structure. According to new observations and simulations this structure will most likely be much more complex consisting on many distinct clumps. Credit: NASA, after Urry and Padovani (1995).

the LINERs (Heckman 1980) are usually kept distinct because it is not settled yet whether their main powering source is indeed accretion onto SMBHs. An overview of all the different optical AGN classes can be found in Véron-Cetty and Véron (2010).

While a lot of AGN types have been discovered throughout the last decades, all can presumably be unified with one scheme that is now further explained.

2.2. The unification scheme

The discovery of the broad component in polarized light of type 2 AGN yielded solid evidence that type 1 and 2 AGN are intrinsically similar (e.g., Antonucci and Miller 1985; Tran et al. 1992). This implied that the BLR is also present in type 2 AGN, but hidden from the observer by an obscuring structure. However, light from the BLR can escape that structure in a different direction and, further out, is scattered towards the observer, leading to the polarization. It follows that the obscuring structure has to have some opening angle, and depending on its orientation, the BLR is directly visible or hidden. The simplest such structure is a dusty torus, which is the key component of the unification scheme of AGN (Antonucci 1993; Urry and Padovani 1995; Barthel 1989). As illustrated in Fig. 2.2, the unification scheme in the first place assumes that a SMBH, surrounded by an accretion disk, is located in the center of each AGN. The existence of both components is strongly supported by, e.g., the observed Fe

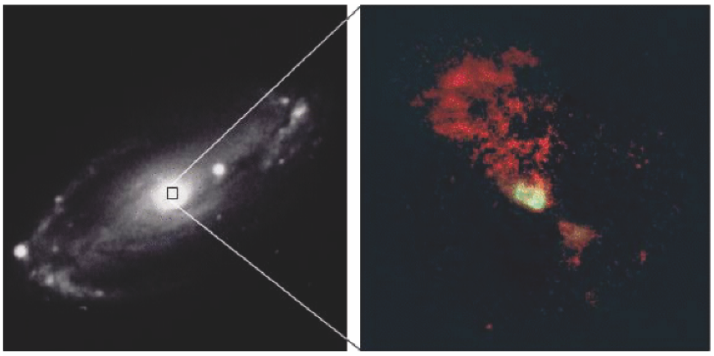

Figure 2.3: Image of the Seyfert galaxy NGC 5728. Left: large scale optical image; right: HST narrow-band filter image centered on the [OIII]λ5007 emission line. Reproduced from Schneider (2006). Credit: A. Sandage.

Kα emission line profile in X-rays of iron in the accretion disk, which shows certain highly relativistic effects, possible only in the very strong gravitational fields of SMBH (Fabian et al. 2000).

Furthermore, the BLR must be located close to the SMBH, at distances of the order of $\sim 1000\, r_{\mathrm{S}}$ with $r_{\mathrm{S}} = 2GM_{\mathrm{BH}}/c^2 \approx 3 \cdot 10^5 M_{\mathrm{BH}}/M_{\odot}$ cm being the Schwarzschild radius. Hence, the gas is excited by the direct accretion disk emission. The size of the BLR is constrained from reverberation measurements that determine the time lag between variations in the disk emission and the response in the BLR emission (e.g., Peterson et al. 2004). The SMBH gravitational field causes the high-speed motion of the gas and the corresponding broadening of the lines, while it is still unknown if the material is rotating, outflowing or inflowing. However, the emission line properties allow for a determination the gas temperature and density of the electrons: $T \sim 20000$ K and $n_{\mathrm{e}} \sim 3 \cdot 10^9\,\mathrm{cm}^{-3}$. The gas in the BLR is presumably located in small optically thick clouds with a total filling factor of the order of 0.1.

As mentioned above, these inner components are surrounded by an obscuring dusty structure, the torus, which is further discussed in Sect. 2.2.3.

Unlike the BLR, the NLR extends further out (~ 100 pc) with a roughly conical shape, along the opening of the torus. Because of its relatively large extent, it could successfully be resolved in some nearby objects with single dish telescopes, foremost the Hubble Space Telescope (HST), as demonstrated in Fig. 2.3. One of the strongest narrow lines is [OIII] λ5007Å, whose properties suggest temperatures of $T \sim 16000$ K and densities of $n_{\mathrm{e}} \sim 10^3\mathrm{cm}^{-3}$. Also the NLR seems to be organized in clumps and clouds with a very small filling factor (1%).

Finally, depending on the accretion structure, a collimated outflow perpendicular to the accretion disk exists: the jet (see Sect. 2.2.2). Although the inner components of the unification scheme could not be spatially resolved so far, observations of the outer components, e.g., NLR and jet, at least match the unified scenario. One of the best examples is NGC 4261, which possesses a large scale bipolar jet and a dusty obscuring disc on smaller scale perpendicular to the jet axis (Fig. 2.4). Note however, that NGC 4261 is optically classified as a LINER and therefore the applicability of the unification scheme is uncertain for this object.

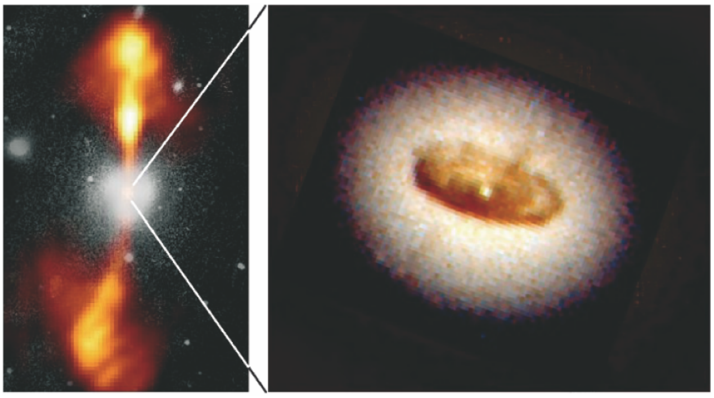

Figure 2.4: Image of the LINER galaxy NGC 4261. Left: large scale optical (white) and radio (orange) composite image (horizontal scale 380″, 27 kpc) ; right: HST optical image of the central region. the diameter of the dusty disc (brown) is ∼ 1.7″, or ∼ 120 pc. Reproduced from Schneider (2006). Credit: W. Jaffe.

2.2.1. The accretion disk

The accretion disk releases most of the observable energy in AGN and it also affects the structure and properties of all other AGN components. Therefore, I review very briefly some of the accretion disk aspects without detailed derivation (mainly following Schneider 2006). Detailed information on accretion disks can be found in Frank et al. (2002) and Kato et al. (2008).

Energy release through gravitation is one of the most efficient processes in the universe. According to the virial theorem, half of the gravitational potential energy of matter with a mass m being accreted from the radius r is transformed in kinetic energy (rotation of the disk), while the remaining energy can be dissipated: $E_{\mathrm{rad}} = 1/2 \cdot G M_{\mathrm{BH}} m/r$. The resulting luminosity is

$$L = \frac{\mathrm{d}E_{\mathrm{rad}}}{\mathrm{d}t} = \frac{1}{2}\frac{G M_{\mathrm{BH}} \dot{M}}{r} = \eta \dot{M} c^2 \tag{2.1}$$

with $\dot{M}$ the accretion rate and η the efficiency, which lies in the range of $0.06 < \eta < 0.42$ depending on the spin of the SMBH. Hence, for the observed luminosities in typical Seyfert galaxies, an accretion rate of $\sim 0.5 M_{\odot}\mathrm{yr}^{-1}$ is needed. However, matter can only be accreted as long as the inward gravitational force is stronger than the outward force caused by the radiation pressure. This leads to a maximum accretion rate that can be achieved by a SMBH, given by the Eddington limit: $\dot{M}_{\mathrm{Edd}} = L_{\mathrm{Edd}}/\eta/c^2$ and the corresponding Eddington luminosity

$$L_{\mathrm{Edd}} := \frac{4\pi G c m_{\mathrm{p}}}{\sigma_{\mathrm{T}}} M_{\mathrm{BH}} \approx 1.26 \cdot 10^{38} \frac{M_{\mathrm{BH}}}{M_{\odot}} \mathrm{erg\,s^{-1}}. \tag{2.2}$$

with m_{p} the proton mass and $\sigma_{\mathrm{T}} = 6.65 \cdot 10^{-25}\mathrm{cm}^{-2}$ being the Thomson cross-section, which applies for the scattering of high-energy photons with electrons (Compton-scattering). Therefore, the Eddington limit depends on the black hole mass only. Note that here the assumption of isotropic emission is made and thus, in reality, it is possible to exceed the Eddington limit if the radiation is not isotropic (although not by large factors).

For an optically thick accretion disk ($\tau \gg 1$), each ring in the disk emits like a blackbody, which leads to a disk temperature of

$$T(r) = \left(\frac{3c^6}{64\pi\sigma_{\mathrm{SB}}G^2}\right)\dot{M}^{1/4}M_{\mathrm{BH}}^{-1/2}\left(\frac{r}{r_{\mathrm{S}}}\right)^{-3/4} \approx 6.3\cdot 10^5\mathrm{K}\left(\frac{\dot{M}}{\dot{M}_{\mathrm{Edd}}}\right)^{1/4}\left(\frac{M_{\mathrm{BH}}}{10^8 M_{\odot}}\right)^{-1/4}\left(\frac{r}{r_{\mathrm{S}}}\right)^{-3/4} \tag{2.3}$$

as a function of radius, with σ_{SB} being the Stefan-Boltzmann constant. Interestingly, $T(r)$ decreases with increasing M_{BH} and is independent of the dissipation mechanism because Eq. 2.3 is independent of the viscosity description. This is fortunate because the exact viscosity mechanism in accretion disks is still not well understood (probably related to magnetic instabilities Balbus and Hawley 1991). However, this description of an optically thick and geometrically thin accretion disk (hereafter standard disk) introduced by Shakura and Sunyaev (1973) allows for predictions of the expected emission, independent of the exact viscosity mechanism. Here, the emitted spectrum is approximately that of a superposition of blackbodies from each ring of the accretion disk, leading to a broad energy distribution that can be described as a power-law $F_\nu \approx \lambda^{-1/3}$ over most of its width. The characteristic SMBH accretion disk temperatures of $T \sim 10^5$K lead to an emission peak in the UV for AGN accretion disks. Indeed, the predicted spectrum is in good agreement with observations, which show an emission maximum in the UV, the so-called big blue bump (e.g. in QSO spectra, Elvis et al. 1994).

2.2.2. The jet

Under certain (poorly understood) conditions a jet is launched from the base of the accretion disk. It mainly consists of plasma, that moves at supersonic, sometimes highly relativistic, speeds away from the SMBH and creates lobes extending over large (galactic) scales. These outflows are often highly collimated over these scales. Formation, acceleration and collimation of jets are poorly understood processes in AGN (see, e.g., Belloni 2010 for an overview). However, one important constituent for these phenomena are certainly magnetic fields, and they also cause the fundamental emission process observed in jets: synchrotron emission. Relativistic electrons move helically around the magnetic field lines accelerated by the Lorentz force, which causes the electrons to radiate. An electron energy of $E = \gamma m_e c^2$ leads to a characteristic frequency for the synchrotron emission of:

$$\nu_c = \frac{3\gamma^2 eB}{4\pi m_e c} \sim 4.2\cdot 10^6\gamma^2\frac{B}{1\mathrm{G}}\mathrm{Hz} \tag{2.4}$$

with B the magnetic field strength and $\gamma = 1/\sqrt{1-(v/c)^2}$ the Lorentz factor. For $\nu < \nu_c$ the spectrum of a single electron is $\propto \nu^{1/3}$ and exponentially declines for frequencies higher thanν_c.

Jets were first discovered at radio wavelengths, where they often extend to galactic-scale structures (e.g., Fig. 2.4). In order to create emission at radio wavelengths, the electrons have to

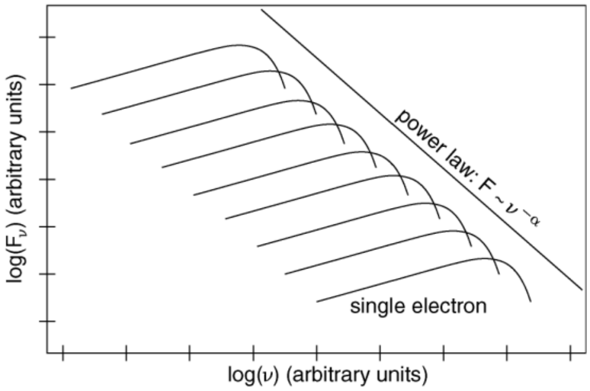

Figure 2.5: Electrons at a given energy emit a synchrotron spectrum which is indicated by the individual curves. Their superposition results in a power law if the energy distribution of the electrons follows a power law. Reproduced from Schneider (2006).

be highly relativistic ($\gamma \sim 10^5$). Therefore, efficient acceleration on all scales is necessary and presumably happens in shock fronts. When the energy distribution of the relativistic electrons is a power-law, $N(E)\mathrm{d}E \propto E^{-s}\mathrm{d}E$, the observed emission is also described by a power-law $F_\nu \propto \nu^{-\alpha}$ with the index $\alpha = (s-1)/2$, as illustrated in Fig. 2.5. Jets can also be visible at shorter wavelengths, e.g., in the optical and even in X-rays, due to inverse Compton-scattering of low energy photons by the relativistic electrons. This is well demonstrated by the jet in the elliptical galaxy M 87 with a LINER nucleus: its large scale structure is visible at all wavelengths (Fig. 7.10).

2.2.3. The torus

The obscuring torus-like structure is the cornerstone of the unification scheme. It is thought to consist of material roughly similar in composition to the interstellar medium (ISM), containing $\sim$ 99% gas and $\sim$ 1% dust in terms of mass. The latter dominates the optical thickness at optical and UV wavelengths as required by the unification scheme. The main ingredients of astrophysical dust are carbon, e.g., amorphous structure or crystalline graphite, and silicate grains, e.g., olivine, pyroxene and silicon-carbide (Draine 2003). These grains are heated by absorbing the accretion disk emission, and they will be destroyed when the local temperature exceeds the sublimation limit, T_sub, which depends again on the grain composition. The result is an inner edge of the dust distribution that is in fact determined by the graphite grains, which have the highest $T_\mathrm{sub} \approx 1500\,\mathrm{K}$, (Draine and Lee 1984). With the assumption of an radiative equilibrium, the corresponding sublimation radius, r_sub becomes

$$r_\mathrm{sub} = 0.46 \left(\frac{L_\mathrm{bol}}{10^{45}\mathrm{erg\,s^{-1}}}\right)^{1/2} \left(\frac{T_\mathrm{sub}}{1500\,\mathrm{K}}\right)^{14/5} \left(\frac{r_\mathrm{dust}}{0.04\,\mu\mathrm{m}}\right)^{1/2} \mathrm{pc} \tag{2.5}$$

with L_bol the bolometric luminosity and $r_\mathrm{dust} \sim 0.04\,\mu$m being the average grain size (Barvainis 1987). Thus, the inner edge of the dusty torus is of the order of parsecs for typical

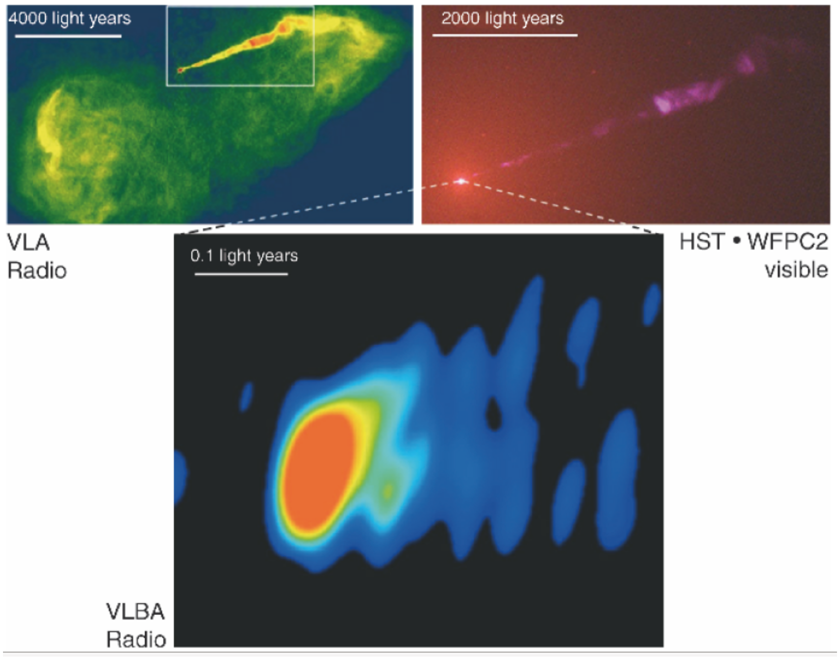

Figure 2.6: Top-left: large-scale radio map of the LINER galaxy M 87. Top-right: HST optical image. Bottom: small-scale radio map showing that the jet is formed within ~ 0.03 pc. Reproduced from Schneider (2006). Credit: J. Biretta.

AGN. Infrared reverberation measurements (Kishimoto et al. 2007) and interferometric MIR data (Tristram and Schartmann 2011) could confirm this characteristic size and the luminosity dependence of the sublimation radius $r_{\mathrm{sub}} \propto L_{\mathrm{bol}}^{0.5}$. On the other hand, the outer radius of the torus is far less certain and might smoothly connect to the host galaxy structures (Beckert and Duschl 2004).

However, the vertical extent of the torus is statistically constrained by the ratio of the observed type 1 to type 2 AGN, which is $\sim 1/3$ (e.g., Osterbrock and Martel 1993; Maiolino and Rieke 1995), implying an opening angle of $\sim 45°$, and thus, a radius-to-height ratio of ~ 1 for the torus. Nevertheless, the physical mechanism maintaining this geometrical thickness and preventing the gravitational collapse into a thin disk is still unknown. Vertical pressure support might arise from SF including supernovae located inside the torus (Schartmann et al. 2005), or in case of clumpiness, by cloud collisions (see below).

In addition to the physical dimensions of the torus, its internal structure is also important in order to understand the observational results. The simplest assumption is that the material is smoothly distributed (Pier and Krolik 1992). However, the predictions of such a distribution do not agree with observational results (e.g., Efstathiou and Rowan-Robinson 1995; Thompson et al. 2009). Also from the theoretical point of view, a clumpy structure of the torus is preferred, as argued by (Krolik and Begelman 1988): the velocity dispersion in the vertical direction has to be of the order of the rotational velocity ($\gtrsim 100$ km/s) in order to maintain the geometrical thickness. This motion cannot be of thermal nature because the implied temperatures ($\sim 10^6$ K) would immediately destroy any dust. On the other hand, for cool gas, the velocities are highly super-sonic and, hence, dissipation of the velocity differences can only be prevented when the material is distributed in clouds with low collision rates. These clouds might be confined by self-gravity and in fact resemble the outermost part of the accretion disk as material reservoir for feeding of the accretion. Such a physical model was developed by Vollmer et al. (2004) and Beckert and Duschl (2004). Here, the largest clouds would have sizes close to the tidal shear limit due to the gravitational field of the SMBH and the central star cluster. These would dominate the dynamics and obscuration properties of the torus. Angular momentum is efficiently transfered by cloud collisions allowing accretion of material from distances of more than $100 r_{\mathrm{sub}}$. This model predicts that the cloud optical thickness, being $\tau_{\mathrm{cl}} \gg 1$, decreases with increasing distance ($\tau_{\mathrm{cl}} \propto 1/r$), while the clouds become larger at the same time. Eventually, they smoothly connect to the ISM of the host galaxy. At the same time, the masses of clouds close to r_{sub} are predicted to be of the order of 1 to 5 $M_{\odot}$ with radii of 0.01 to 0.05 pc, which is only weakly dependent on the SMBH properties. Furthermore, only a small number of clouds (6-10) would be in the line of sight of a typical type 2 AGN, which will cause significant fluctuations in the column density, as it is observed in many AGN in the X-ray emission (e.g., Risaliti et al. 2005). Some of these predictions could be verified by Hönig et al. (2010) for typical Seyferts by comparison with models: the number of clouds along the equatorial line of sight is 5-8 and their density is distributed following a power law $\sim r^{-1}$.

Another consequence of the clumpy torus model is that the amount of obscuration should decrease at high luminosities (close to the Eddington limit) because an increasing number of clouds is blown away by the radiation pressure caused by the accretion disk (Hönig and Beckert 2007). Consequently, the type 1 to type 2 AGN ratio should increase toward higher luminosities. Note that the same prediction is also made by the conceptual model of the receding torus, which contains a luminosity dependence for the opening angle of the torus (Lawrence 1991; Simpson 2005).

In general, simulations of the radiative transfer in clumpy tori have successfully been performed in a growing number of works (e.g., Nenkova et al. 2002; Dullemond and van Bemmel 2005; Hönig et al. 2006; Schartmann et al. 2008; Nenkova et al. 2008a, b; Hönig and Kishimoto 2010). An example of such a model and the predicted MIR image is shown in Fig. 2.7. It can satisfactorily reproduce observational results of nearby AGN and also verifies the dust composition in tori to be comparable with the ordinary ISM.

However, direct imaging of the torus structure is not possible because 1 pc at a typical object distance of 20 Mpc corresponds to 10 milli-arcsec on the sky, while single dish telescopes provide only angular resolutions of the $\gtrsim$ 100 milli-arcsec. On the other hand, it is possible to reach the required resolutions with infrared interferometric observations and at least marginally resolve the dust structure in nearby AGN. First results show that the dusty structure is indeed only a few parsecs in size (e.g. Jaffe et al. 2004; Raban et al. 2009; Tristram et al. 2009; Burtscher et al. 2009). Furthermore, a large number of interferometric observations of individual objects with different base lines and orientations will enable reconstruction of the structure in more detail. Corresponding results are expected to become available soon and will allow major progress in the understanding of the torus (e.g., Hönig et al., 2012, in prep.).

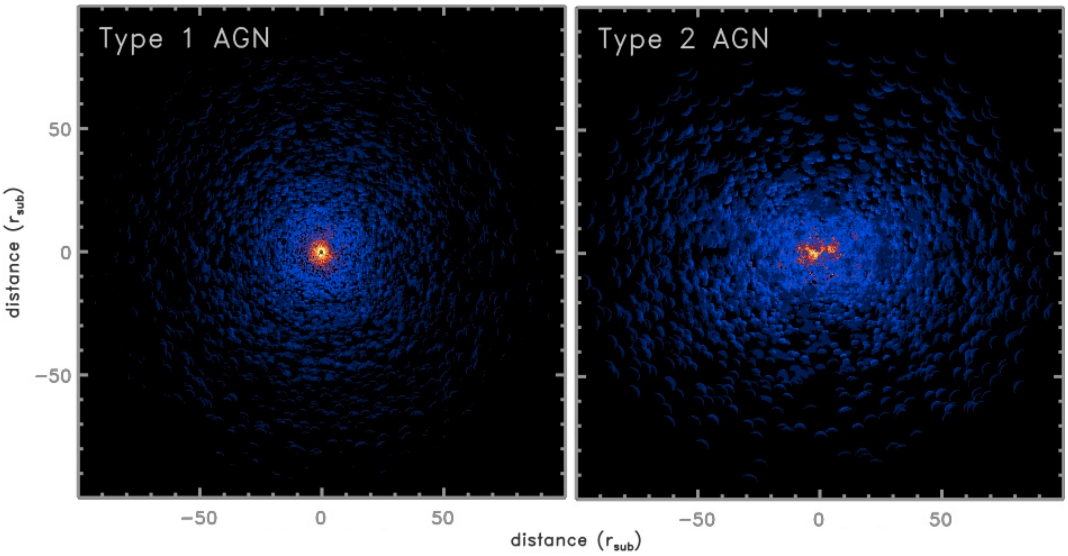

Figure 2.7: Simulated 13 μm images of clumpy tori for type 1 and 2 AGN using radiative transfer modeling. The difference is only the inclination angle (face-on in type 1 and edge-on in type 2). White corresponds to regions with high emission and blue to low emissivity. Reproduced from Hönig and Kishimoto (2010).

Finally, I would like to point out that consistent hydrodynamical simulations of the clumpy torus are still lacking, and that a number of other models, e.g., large warps in the accretion disk (Pringle 1996; Schinnerer et al. 2000) or dusty winds from the accretion disk (e.g., Elvis 2000; Elitzur and Shlosman 2006), have also been proposed in order to explain the observed nuclear obscuration. Therefore, the question of the physical nature of this AGN component is far from being settled.

2.3. Low-luminosity AGN

The unification scheme of AGN has proven very successful in explaining the majority of AGN related phenomena. On the other hand, it does not apply to our own galactic center, where no obscuring torus is present, nor a bright accretion disk or a powerful jet. Still, temporary signs of activity, in the form of flares, are observed at various wavelengths, giving evidence that accretion is still ongoing in Sgr A*, even if at low rates (e.g., Baganoff et al. 2001; Genzel et al. 2003). This raises the question at which accretion rates and physical conditions the transition, i.e. the change in the accretion structure (from AGN to "normal" nucleus), occurs, and if there are any intermediate states. As we can conclude from Sgr A*, the key components of the unification scheme, such as the accretion disk and the dusty obscuring torus, seem to vanish during non-active phases and are built up again when new material reaches the galactic nucleus presumably through any kind of larger-scale disturbance. However, the connection between the processes of formation and evolution of torus and accretion disk is unknown. Therefore, it is important to look for transitional objects that have lower luminosities than "normal" AGN.

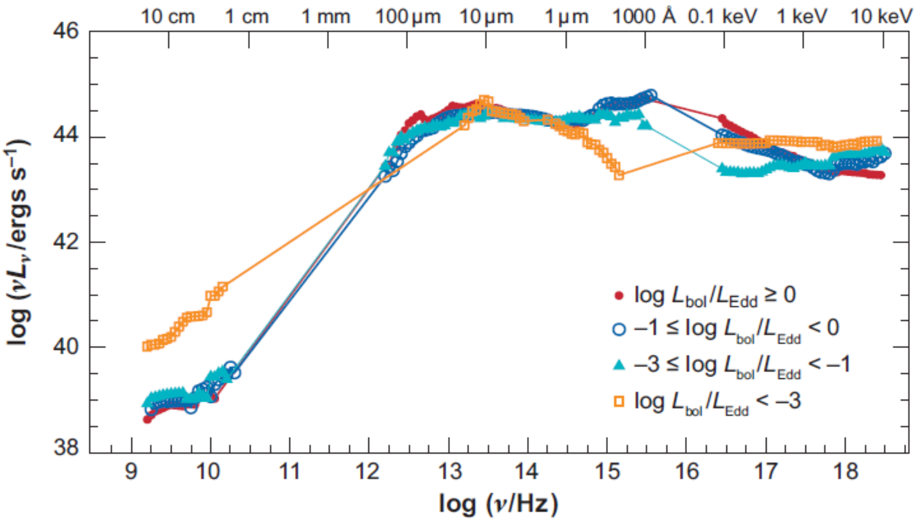

Figure 2.8: Comparison of SEDs for the Palomar AGN sample. The AGN have been binned by their accretion rate (approximated with the Eddington ratio). Reproduced from Ho (2008).

In fact, many intrinsically faint AGN, e.g., LINERs, have indeed been found, in particular, in nearby galaxies. These low-luminosity AGN are presumably even the most common of all AGN (for a review see Ho 2008). Note that the class of LLAGN is not uniformly defined in the literature, although most commonly the somewhat arbitrary criterion of $L_{\rm X} \lesssim 10^{42}$ erg/s is used to separate LLAGN from AGN. Thus it is also adopted throughout this work. LLAGN seem to represent these sought-after AGN in the transitional stages at the beginning or end of the AGN's active phases and, thus, are of great interest.

Conclusive observational evidence has been found for structural changes in LLAGN. For example, Fig. 2.8 shows the average SEDs of AGN from the Palomar optical spectroscopic survey of nearby galaxies (Ho et al. 1997) binned for different accretion rates. Because the accretion rate cannot be measured directly, the Eddington ratio, $\eta_{\rm Edd} = L_{\rm bol}/L_{\rm Edd}$, is used as a proxy. While objects accreting at high rates show the characteristic big blue bump in the UV, which is the fingerprint of an optically thick and geometrically thin accretion disk (Sect. 2.2.1), it disappears for the lowest accretion rate objects. This implies that the structure of the accretion disk is different for objects with $\log L_{\rm bol}/L_{\rm Edd} \lesssim -3$. Such a change has indeed been predicted by theory: the standard disk transforms into a geometrically thick, optically thin accretion disk in the inner part. This new disk structure is called radiatively inefficient accretion flow (RIAF) or advection-dominated accretion flow (ADAF) mode (Narayan and Yi 1994). The density of the gas in such an accretion disk decreases so much that the gas becomes optically thin and cannot efficiently cool anymore by thermal radiation. Hence, an increasing amount of the energy will be consumed by the SMBH, because the material crosses the Schwarzschild radius before it can radiate half of its potential energy. Instead of thermal emission, the RIAF emission is dominated by synchrotron and Comptonization processes, which lead to a very different SED throughout the whole electromagnetic spectrum. The ADAF and RIAF models are very successful in explaining the observed SEDs of individual objects (e.g., Yuan 2007).

Therefore, they are favored for LLAGN.

At the same time, the LLAGN emit significantly more radio emission: they become "radio-loud" (Fig. 2.8). This radio-loudness is attributed to a strong jet, that might even dominate the whole SED in some cases (Falcke and Markoff 2000).

In contrast to the case of the accretion disk, there is far less evidence for the disappearance of the obscuring torus, although the absence of hot dust has been demonstrated in some radio galaxies, often harboring LLAGN (e.g., Donato et al. 2004; Balmaverde and Capetti 2006). Apart from the fact that the mechanism that maintains the geometrical thickness of the torus is unknown, there are various theoretical studies predicting its disappearance below certain bolometric luminosities or accretion rates. E.g., Hönig and Beckert (2007) argue in the framework of the clumpy (accreting) torus model presented above that without sufficient energy supply the torus will collapse to a thin disk;this happens at roughly $L_{\text{bol}} \approx 5 \cdot 10^{42}$ erg/s. Also in the wind model, where the clumpy torus is formed by clouds blown away from the accretion disk, for low accretion rates, the wind becomes too weak to release clouds and maintain the geometrical thickness of the outflow (Elitzur and Shlosman 2006). Interestingly, the threshold for the torus collapse is very similar in these two models, and it is comparable to the luminosity used to define LLAGN.

Finally, the BLR is also predicted to disappear in LLAGN (e.g., Nicastro et al. 2003), but is not be further discussed here.

After presenting the individual AGN components and their basic properties, the next two sections give brief overviews of the expected X-ray and MIR continuum emission, which is the subject of this work.

2.4. X-ray continuum emission of AGN

The thermal spectrum of the standard accretion disk peaks in the UV and contributes only marginally above ~ 0.5 keV (Shakura and Sunyaev 1973). Therefore, the observed 2-10 keV X-ray emission must originate from an additional non-thermal component. The observed fast variability (on ~minute timescales) in X-rays restricts the size of the emission region to $\sim 100 r_{\text{S}}$. This structure is presumably a hot corona of electrons above (and below) the accretion disk, which are ejected from the disk by the strong UV radiation and then further heated by the magnetic fields (comparable to the solar corona). The lower-energy photons emitted from the accretion disk are then transferred to higher energies (i.e. X-rays) through inverse Compton-scattering by the hot electrons. Multiple scattering processes lead to a power-law for the energy distribution $N(E)\mathrm{d}E \propto E^{-1.9}\mathrm{d}E$ of the electrons (Nandra and Pounds 1994) and the characteristic X-ray emission power-law spectrum $F_\nu \propto \nu^{-\alpha}$ with $\alpha \sim 0.9$. This power-law eventually cuts-off at a few hundred keV (approaching the rest-mass energy of electrons, 512 keV), because at these energies, the photons lose energy in Compton scattering, rather than gaining any more. In addition, excess emission is often present above 10 keV peaking at ~ 30 keV, the reflection hump. It is caused by X-ray emission from the corona that is reflected by the colder material in the accretion disk (and also by the inner rim of the torus).

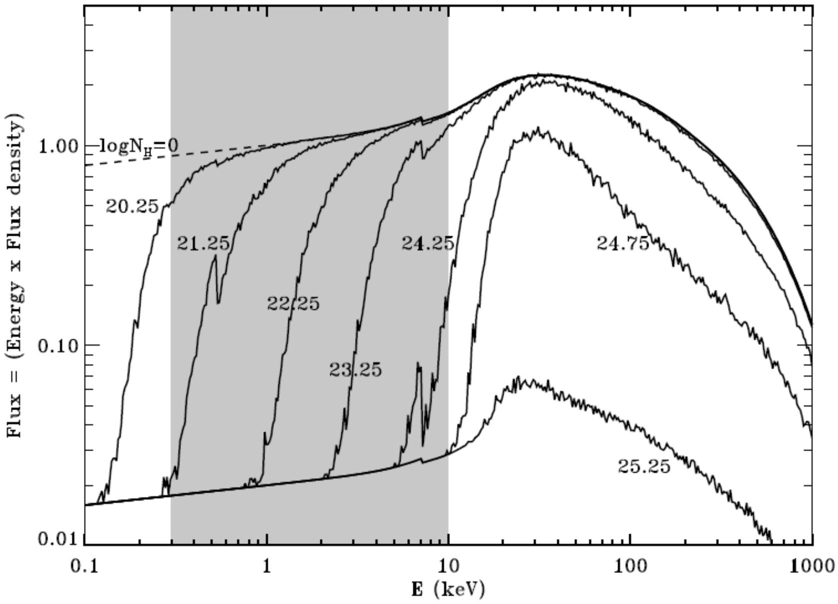

Figure 2.9: Simulated AGN rest-frame SED for different nuclear obscuration in N_H. The gray area marks the 2-10 keV range that is mostly used throughout this work. The dashed line indicates the intrinsic AGN power-law with a photon-index of $\Gamma = 1.9$. At energies between 10 and 100 keV the reflection hump caused by cold material (the accretion disk) is visible. Finally the minimum flux below 10 keV is given by a 2% fraction of primary radiation that is scattered by, e.g., hot plasma in the NLR into the line of sight. Reproduced from Gandhi (2005).

Furthermore, below 10 keV, the X-rays can suffer from obscuration by gas (located in the torus) through photoelectric absorption. At X-ray wavelengths the amount of obscuration is quantified by the column density of hydrogen atoms along the line of sight, N_H. Note however, that in reality, this obscuration is not only caused by hydrogen, but also other atoms are present and contribute significantly. In fact, most of the obscuration is caused by oxygen atoms, and the conversion to hydrogen column density usually assumes a solar abundance (Morrison and McCammon 1983). The effect of increasing N_H on a typical AGN X-ray SED is demonstrated in Fig. 2.9.

In cases where $N_H > 1.5 \cdot 10^{24}\,\mathrm{cm}^{-2}$, the obscuration becomes Compton-thick (CT), which means that the optical depth for photons crossing the medium becomes one: $\tau = N_H \cdot \sigma_T$. In the Compton-thick case only minor radiation might escape from the obscured nucleus at any optical to X-ray wavelength. In those cases, often the observed X-ray radiation is not primary emission from the corona but solely scattered emission (of the order of $\sim 2\%$) from colder components (as the accretion disk, torus, and NLR).

Interestingly, these spectral features of the AGN X-ray emission are not only unchanged over cosmic timescales (e.g., Vignali et al. 2005), but they also explain well the observed 30 keV peak in the cosmic X-ray background (e.g., Gandhi and Fabian 2003; Gilli et al. 2007).

For LLAGN, the situation changes: the obscuration through a torus might disappear, and with the transition of the standard disk to a RIAF or ADAF, the hot corona becomes indistinguish-

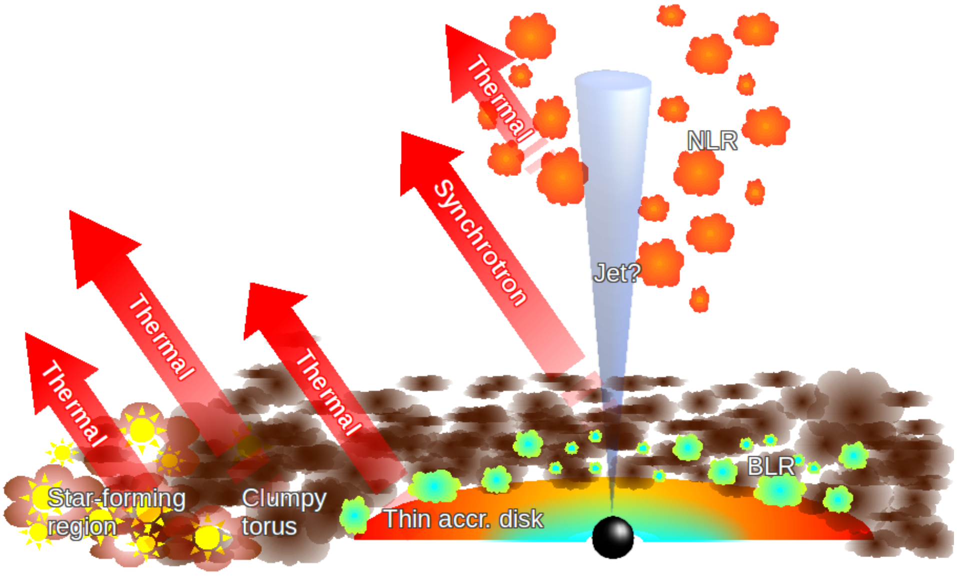

Figure 2.10: Schematic view of the AGN components and their respective possible contribution to the total MIR emission of the AGN, indicated by red arrows. Note that the jet might not be present or very weak in particular in Seyfert nuclei.

able from the geometrical thick accretion flow itself, whose emission is dominated by the same non-thermal processes. In addition, bremsstrahlung processes also occur. Finally, a jet component will presumably exist and contribute significantly also by X-ray emission from the synchrotron process and inverse Compton-scattering as described above, resulting overall in complex X-ray SEDs for LLAGN.

More information on X-ray emission of AGN can be found in e.g., Gandhi (2005).

2.5. MIR continuum emission of AGN

The possible contributions to the total MIR emission in moderate and luminous AGN are illustrated in Fig. 2.10. First of all, the torus with temperatures between 200 K and 1500 K will mostly emits in the infrared as a superposition of blackbodies. In particular the peak of its continuum emission is located in the MIR regime. Also, the outer parts of the standard accretion disk are cool enough to emit thermally in the infrared. However, this contribution to the total MIR emission is expected to be small. Whenever a jet is present, its non-thermal emission will also be visible – and can be significant – in the MIR. Furthermore, the NLR can also contain large amounts of dust, that have to be distributed rather smoothly because otherwise it would provide significant obscuration, in contradiction the unification model. For example, in the prototypical type 2 AGN, NGC 1068, Mason et al. (2006) have found significant extended MIR emission from dust in the ionization cones. On the contrary, Groves et al. (2006) and Mor et al. (2009) argue that in general a major contribution of the NLR to the total MIR emission is unlikely.

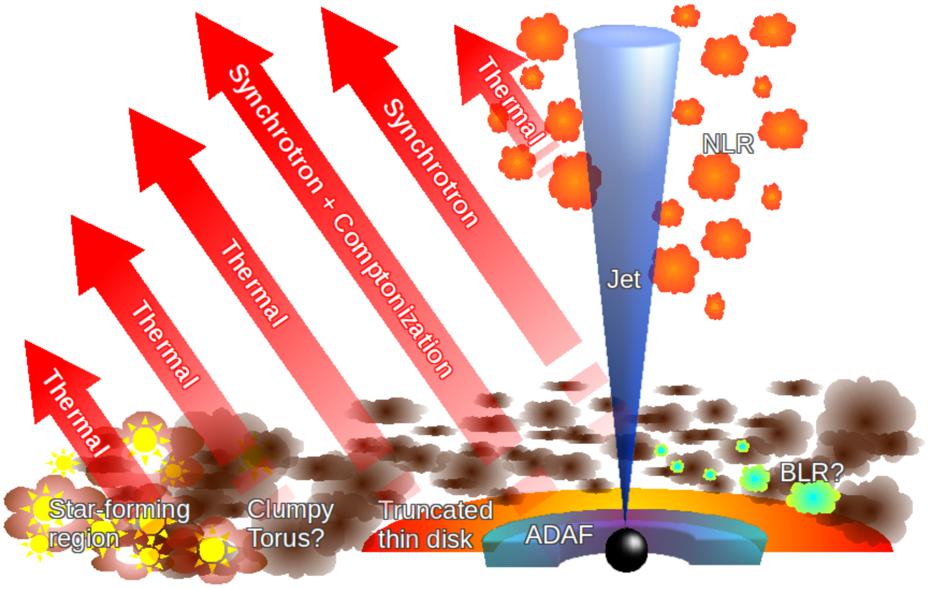

Figure 2.11: Schematic view of the LLAGN components and their respective possible contribution to the total MIR emission of the AGN, indicated by red arrows. Note the slight changes to Fig. 2.10. The torus and BLR component are uncertain to exist in most LLAGN while the jet component is usually strong.

The situation becomes even more complicated for the LLAGN (Fig. 2.11): the change in the accretion structure creates a RIAF or ADAF, whose non-thermal emission due to the processes described in the previous section will also be significant in the MIR. In addition to the ADAF, the thin accretion disk may still exist in the outer parts as a truncated standard disk, emitting thermally. A strong jet seems to exist in many LLAGN and, together with the thermal emission from the putative torus, its synchrotron emission certainly dominates the AGN MIR SED (e.g., Whysong and Antonucci 2004). Therefore, the long term goal (although beyond the scope of this work) will be to characterize the MIR emission of LLAGN in detail and disentangle the emission of all the different AGN components.

Finally, the large amounts of material in the galaxy centers presumably also trigger SF, which in turn heats significantly the surrounding dust, leading to MIR emission, that is spatially close to the AGN albeit unrelated to the accretion processes. At least the luminous AGN easily outshine any nearby stellar emission sources. However, in particular for the intrinsically faint LLAGN, the total AGN emission becomes comparable to (or even weaker than) SF-related emission. Therefore, for all AGN MIR studies, it is of uttermost importance to isolate the AGN related emission from the circum-nuclear stellar phenomena. Apart from the HR, spectral features in the MIR regime also help to disentangle the emission sources, as we will see in the next chapter.

3. Observing in the MIR

The mid-infrared (MIR) wavelength domain ($\sim$ 3 to $\sim$ 30 μm) is located between the near-infrared ($\sim$ 1 to $\sim$ 3 μm) and far infrared ($\sim$ 30 to $\sim$ 1000 μm) regions of the electromagnetic spectrum. Its borders are somewhat arbitrary and not standardized in the literature, but are motivated by (i) the threshold when the background emission (due to thermal emission from instrument, atmosphere, etc.) starts to dominate over the astrophysical source emission, (ii) the sensitivity ranges of astrophysical detectors, and (iii) the atmospheric transmission windows. Four bands are defined by these transmission windows to belong to the MIR regime: L (2.8 to 4.2 μm), M (4.5 to 5.5 μm), N (7.5 to 13.5 μm), and Q (16 to 25 μm; see Fig. 3.1 for the N- and Q-band transmission windows). However, only the N-band is used in this work and hereafter will be referred to as MIR.

3.1. Spectral features in the MIR

The MIR regime gives access to some important spectral features of astrophysical objects like molecular emission and absorption features, and many recombination and fine-structure lines. In particular, dusty phenomena like star formation and AGN tori can be probed in an unique way because extinction is usually very low in the MIR, allowing to pierce into/through the obscuring clouds and observe the physical conditions in the cores of these structures. Especially, spectral lines contain information on densities and temperatures in the emitting regions. Fig. 3.2 shows examples of AGN N-band spectra taken with the infrared spectrograph IRS (Houck et al. 2004) on the Spitzer Space Telescope (Werner et al. 2004) with commonly observed spectral features. One of these features is the characteristic emission of the silicate in the astrophysical dust due to molecular vibrations. These transitions lead to the silicate features at $\sim$ 9.7 μm (Si-O stretching) and $\sim$ 18.5 μm (O-Si-O bending). The exact shape of these very wide features depends on the state of the solid phase (crystalline or amorphous) and excitation of the individual modes and their coupling (e.g., Draine 2003). Overall, silicate features are a very important indicator to characterize dusty astrophysical structures.

Other important molecular features originate from polycyclic aromatic hydrocarbons (PAH) at, e.g., 7.62, 8.6, 11.3, (12.0) and 12.7 μm presumably due to C-C and C-H stretching and bending vibrations. These molecules are suspected to be located either in very small ($\sim$ 0.05 μm) amorphous carbon dust grains or large carbon-rich ring molecules ($>$ 50 atoms) which are excited by UV photons (Puget and Leger 1989; Draine and Lee 1984). These emission features can become very bright, in particular in star forming regions, because of the hot young stars emitting mainly in the UV, and around 10% of the total infrared emission of

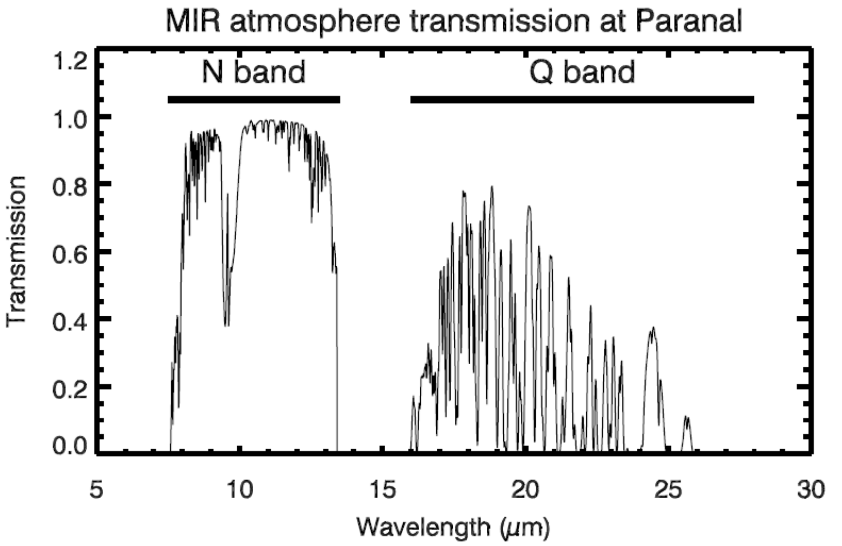

Figure 3.1: Atmospheric transmission in the MIR. Computed with HITRAN for an altitude of 2600 m and 1.5 mm of precipitable water vapor at zenith. Reproduced from Smette and Vanzi (2007).

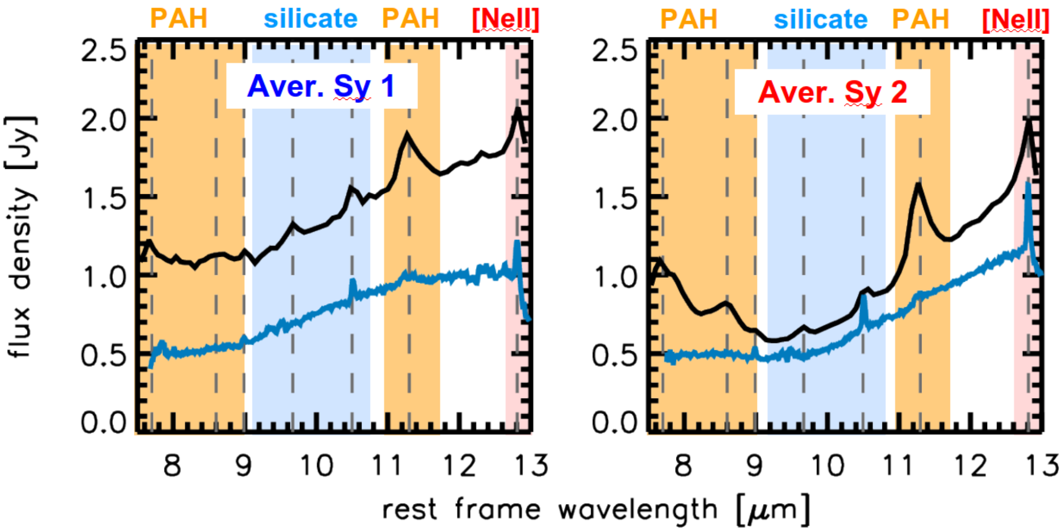

Figure 3.2: Comparison of average Sy 1 and Sy 2 N-band spectra in *Spitzer*/IRS (black line; Hernán-Caballero and Hatziminaoglou 2011) and VLT/VISIR (blue line; Hönig et al. 2010). The grey dashed lines mark positions of commonly occurring lines (from left to right): PAH (7.62 and 8.6 μm), [ArIII] (8.99 μm), H_2 (9.67 μm), [SIV] (10.5 μm), PAH (11.3 μm) and [NeII] (12.81 μm). The colorized areas mark the spectral regions which are affected by PAH, the silicate feature and the [NeII] line.

galaxies can be released through these lines (Smith et al. 2007). Therefore, PAH emission is commonly used as a star formation tracer (e.g., Calzetti et al. 2007). On the other hand, PAH should be destroyed in the strong radiation fields in the vicinity of AGN. Indeed, while in Fig. 3.2 the PAH features are still visible in the lower spatial resolution *Spitzer*/IRS AGN spectra, they disappear in the VLT/VISIR spectra almost completely.

3.2. Instruments

The brightness of the Earth's atmosphere in the MIR poses a big challenge for ground-based astronomy. It radiates approximately as a blackbody at the ambient temperature ($\sim 290\,$K), so a comparable temperature as the observed astrophysical objects. In addition, the telescope itself emits thermally at $\sim 283\,$K, while the instruments have to be cooled, especially the detectors (down to $\sim 5\,$K). Taking all effects into account, the background radiation amounts to approximately 3700 Jy/arcsec^2 in N-band (Smette and Vanzi 2007), which is orders of magnitude brighter than any astrophysical object. Consequently, the large amount of photons reaching the detector every second ($\sim 10^8$) makes it necessary to read out the detector on milli-second timescales.

In addition, the molecules in the atmosphere (H_2O, CH_4, CO_2, CO, O_2, O_3) absorb a large number of MIR photons from the astrophysical sources and leave only several separate transmission windows for astronomical observations as already mentioned above. In particular the amount of water vapor in the atmosphere strongly affects the transmission and thus achievable sensitivity.

An obvious way to circumvent these problems is to use satellite-based telescopes in space. Several of those have been built and successfully operated over the last decades, e.g., the InfraRed Astronomical Satellite (IRAS), the Infrared Space Observatory (ISO), the Spitzer Space Telescope, the Wide-Field Infrared Survey Explorer (WISE) and Akari. However, all of these platforms feature mirrors smaller than 1 meter, severely restricting the angular resolution, θ_0. The angular resolution is particularly critical in AGN research, as demonstrated already in Sect. 1.4, and also in Fig. 3.2 by the absence of the PAH and the significantly lower continuum emission in the VLT/VISIR spectra compared to the *Spitzer* spectra.

Contrary to space missions, ground-based telescopes with large mirrors are available that provide high-angular resolution (HR). This is illustrated in Fig. 3.3 where the diffraction-limited angular resolution (diameter of the first Airy ring; $\theta_0 = 1.22\lambda/D$ with λ the wavelength and D the telescope diameter) of *Spitzer* and VLT/VISIR are compared for the MIR regime. The latter is an order of magnitude better. At shorter wavelengths the spatial resolution of a ground-based telescope is limited to lower than the diffraction-limited values because of the atmospheric seeing. The seeing can be approximated by the Roddier formula (seeing $\propto \lambda^{0.2}$) by derivation from the spatial coherence radius in the telescope beam. Fig. 3.3 shows that at wavelengths greater than $10\,\mu$m, observations are diffraction-limited for good seeing in the optical ($0.5''$).

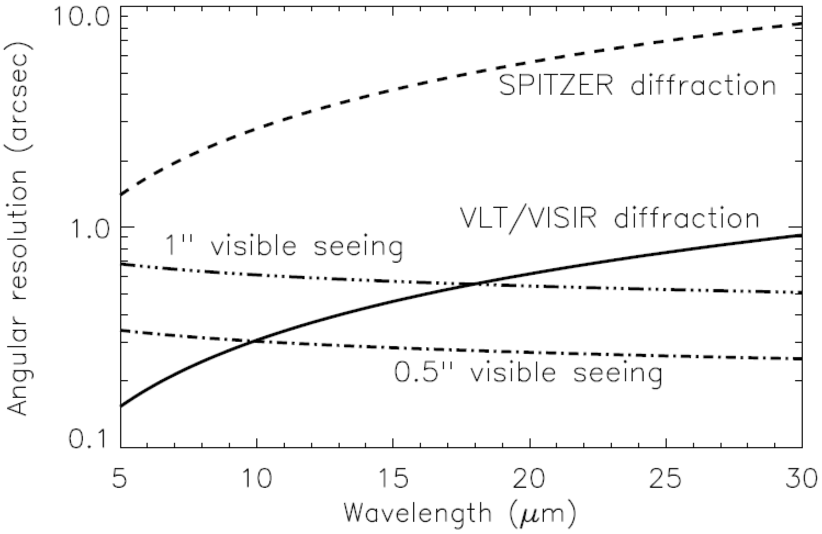

Figure 3.3: VLT diffraction limit (solid line) versus seeing for the MIR. The *Spitzer* diffraction limit (dashed line) is shown for comparison. The Roddier dependence is shown from two optical seeings (dashed-dotted line). Reproduced from Smette and Vanzi (2007).

On the other hand, sensitivities will be lower from the ground than from space, and special observing techniques are needed to deal with the high backgrounds (described Sect. 3.2.1). However, an increasing number of AGN studies demonstrate the power of ground-based MIR instruments to isolate the AGN from surrounding starbursts (e.g., Gorjian et al. 2004; Galliano et al. 2005; Haas et al. 2007; Siebenmorgen et al. 2008; Ramos Almeida et al. 2009).

3.2.1. Chopping and nodding

The basic idea to deal with the extremely high MIR background is to perform differential imaging using the combined techniques of chopping and nodding (Fig. 3.4).

The chopping technique consists of taking two exposures, one centered on the science target (and background) and another one containing only background (first row in Fig. 3.4). By subtracting the second exposure from the first, in principle the background should be canceled out. This only works if the pairs of exposures are taken at a frequency faster than the background fluctuates (or the detector characteristics change). In practice, the chopping is done by moving the secondary mirror at a frequency of 0.25 to 0.5 Hz. In order to increase the time efficiency of these technique it is possible to choose a chopping throw that is small enough such that the science target remains on the detector in an offset position. This leads to two sub-images in the subtracted image, one positive from the first exposure and an offset negative from the second exposure (second row in Fig. 3.4).

While the chopping technique cancels out most of the background, some residuals remain because the optical path is not exactly the same in both chopping positions. Fortunately this residual background varies on longer timescales than the sky fluctuations. Therefore the nodding technique can be used for their cancellation, which is performed by moving, or "nodding," the whole telescope slightly to an off-source position and repeating the chopping pattern. The corresponding nodding throw can again be chosen such that the science target is still visible in the off-source exposures, which leads to four sub-images on the final combined image (two positive and two negative). Usually the orientation of the chopping throw direction and the nodding throw direction can be either perpendicular (with the sub-images forming a square on the detector) or parallel (with the sub-images forming a line on the detector and the positive beams combined atop one another, Fig. 3.4 third row). The sizes of the chopping and nodding throw of course restrict the effective field of view without overlapping source images to one half of their size.

3.2.2. VLT/VISIR

The main instrument for this study is the VLT Imager and Spectrometer for the InfraRed, VISIR, (Lagage et al. 2004) which is mounted on UT3, one of the four 8-meter telescopes that comprise the VLT on Cerro Paranal, Chile (Fig. 3.5). It provides imaging and spectroscopy in the N- and Q-band in various modes, with the imager and the spectrograph having separate light paths, optics and detectors. VISIR's cryogenic optical bench is enclosed in a vacuum vessel with most of the structure cooled to 33 K, the optics to < 15 K and the detectors cooled down to 5 K. Both detectors have 256×256 pixels. The imager offers two fields of view (FOV), the small FOV ($19.2'' \times 19.2''$) with a pixel scale of $0.075''$, and the intermediate FOV ($32.5'' \times 32.5''$) with a pixel scale of $0.127''$. A large set of twenty different filters is available for N-band observations although nine of them have not been fully characterized yet. Sensitivity measurements and bandpasses are displayed for the other eleven in Fig. 3.6. The reasonable sensitivity limit (for 1 hour of on-source integration time) with a signal-to-noise (S/N) of 10 is around 10 mJy for all filters.

The VISIR data acquisition works with a high detector readout rate, operating on a timescale of a few milliseconds. In order to keep the memory usage reasonable, all exposures belonging to one chop are co-added and only the resulting frame is saved. The raw data is saved in data cubes in the Flexible Image Transport System (FITS) file format containing the frames of every chop belonging to one nod. For example, an observation of 6 minutes total length contains four individual nods and thus results in 4 raw data cubes, each containing around 20 chopping frames. The individual pixel values represent a flux density and its unit is ADU/s.

3.2.3. Gemini/Michelle

The other instrument used for this study is the Michelle MIR imager and spectrograph (Glasse et al. 1997) mounted on the Gemini North telescope on Mauna Kea in Hawaii, USA (Fig. 3.7). Instrument and telescope have similar characteristics to the VLT and VISIR. Michelle has a 320×240-pixel detector and offers only one FOV ($32'' \times 24''$) with a pixel scale of $0.1005''$and a maximum chopping throw of $15''$. It offers nine N-band filters with various bandpasses, which are mostly wider than the ones offered for VISIR (Fig. 3.8). The sensitivities are comparable

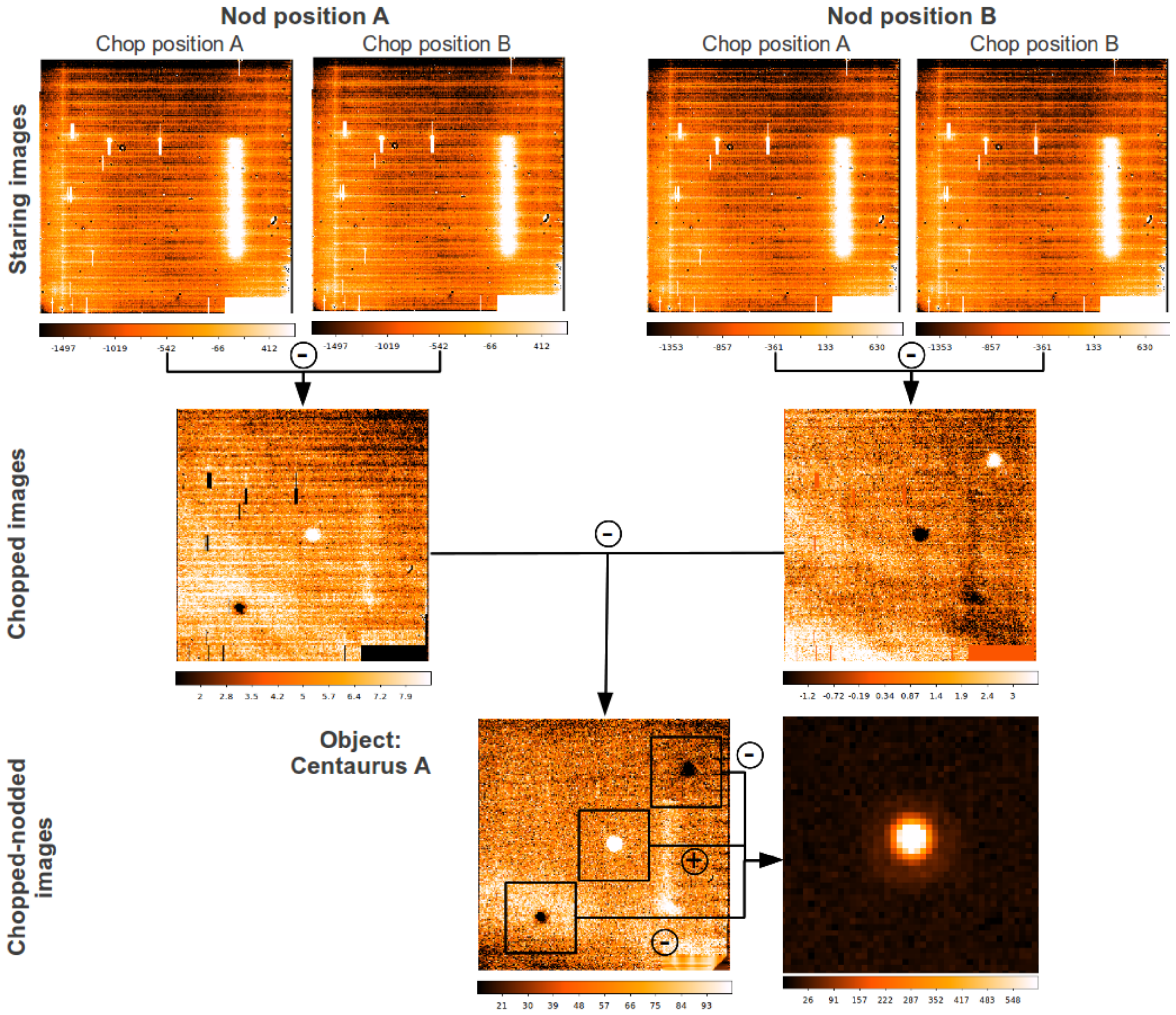

Figure 3.4: Principle of the chopping and nodding technique. VISIR data from this work is used as an example (Cen A). Here the chopping and nodding direction are parallel. The staring images (top row) are dominated by the high background noise and instrument artifacts, while the observed source remains invisible. Only after subtraction of two chopped images (middle row), the target becomes visible as a positive and negative sub-image. By subtracting two nodding positions (bottom row) the final image is created by extracting and combining the three sub-images. See text for further explanation.

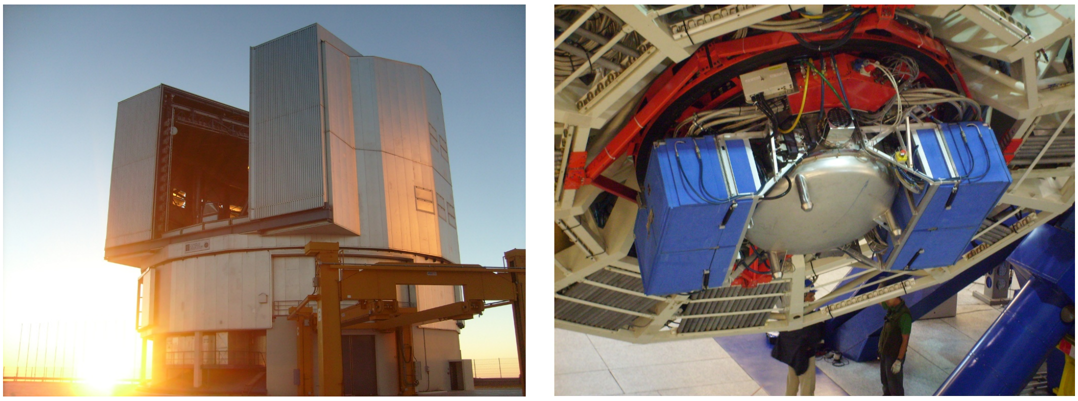

Figure 3.5: Left: UT 3 Melipal belonging to the VLT on Paranal, Chile. Right: VISIR mounted at the Cassegrain focus of UT3 underneath the primary mirror. Both pictures were taken in October 2009 by the author.

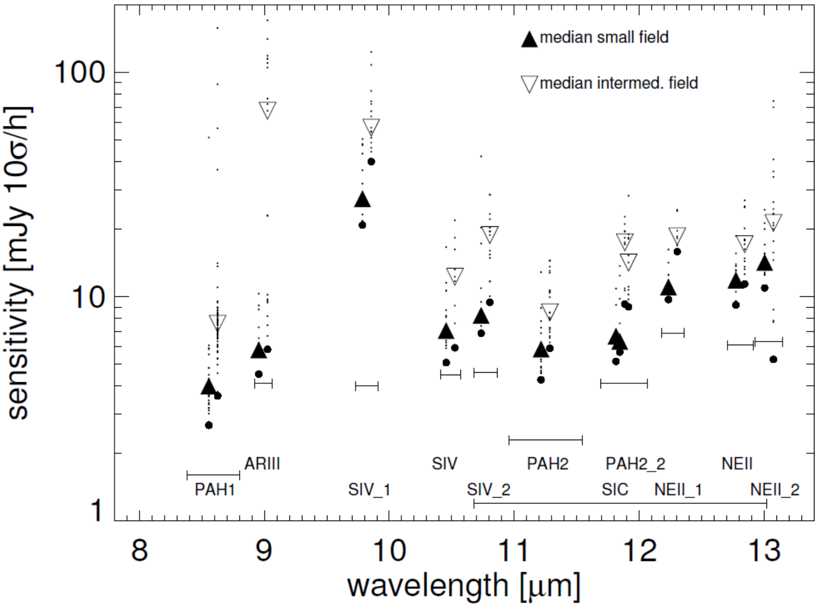

Figure 3.6: Sensitivities for the VISIR imager *N*-band filters. The individual filter bandpasses are marked by horizontal bars. Background noise limits are indicated by their vertical position. Reproduced from Smette and Vanzi (2007).

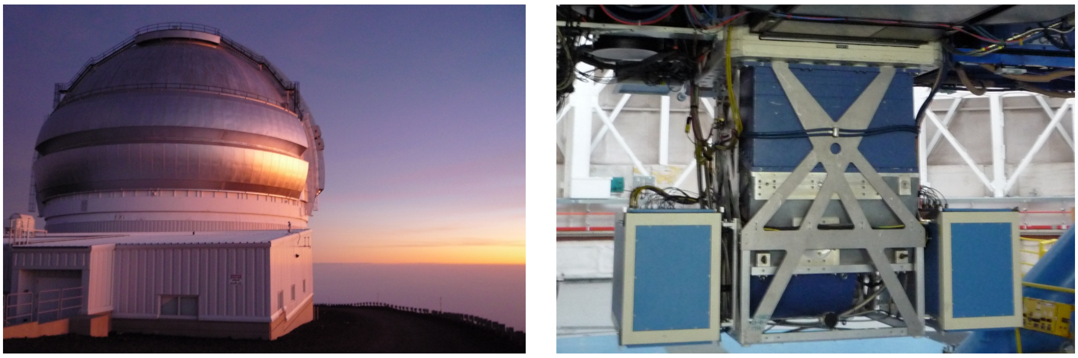

Figure 3.7: Left: Gemini North on Mauna Kea, Hawaii. Right: Michelle mounted at the Cassegrain focus of Gemini North underneath the primary mirror. Both pictures were taken in February 2010 by the author.

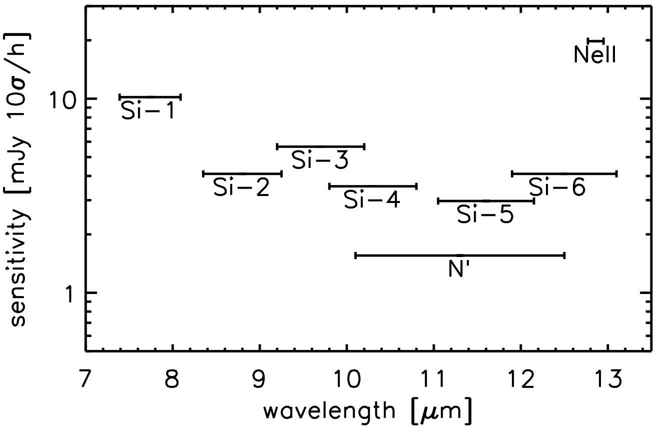

Figure 3.8: Sensitivities for the Michelle imager N-band filters. The individual filter bandpasses are marked by horizontal error bars. Different to Fig. 3.6, here the y position marks the sensitivity of the filter itself.

to those of VISIR, while the off-source chopping positions are not guided by the telescope. Therefore only the positive sub-images are usable and parallel nodding automatically combines them.

The data acquisition in Michelle is comparable to that of VISIR, except that only one FITS file is created for the whole observation, containing one extension for each nod. Each of those extensions contains 3 images: one for each chopping position with all exposures co-added, and the difference image of both chopping positions. Hence, the data belonging to each individual chop is not saved or reconstructible for Michelle.

3.3. Data reduction

The observations undertaken for this work are described in detail in Chapters 4 and 5. All programmes consist of N-band imaging using VLT/VISIR and Gemini/Michelle. The first step in the data reduction consists of combining the raw data of the individual nods, and has been performed by using the observatory delivered pipelines. Those pipelines also take care of some detector cosmetics. The following data reduction has been continued in a uniform way for both instruments with a custom-made IDL software package (based on Hönig et al. 2010). This package does the flux calibration of the data, the flux measurement and creates the final images of the science targets. Previously observed AGN appeared as point sources in the MIR with, at most, weak non-nuclear emission sources if star formation is present in the host galaxies.

For the absolute photometric calibration of the science targets, a standard star (STD) is observed within two hours before or after the science observation in the same filter and usually with a maximum airmass difference of 0.2. These STDs have been selected from the MIR standard catalog from Cohen et al. (1999) with given absolute fluxes in the individual filters. The uncertainties on these values are $\leq 10\,\%$ and often much lower.

In order to maintain consistency, both science and STD data are processed in exactly the same way: 2D Gaussians are fitted to the point-spread-functions (PSF) of the point sources in all sub-images. By subtracting the constant term from the fit, we are able to extract the unresolved flux from the local background. Consequently, this method is not heavily affected by the residual background as long as it is locally smooth. The full width at half maximum (FWHM) of the Gaussian is a good measure for the actually achieved angular resolution θ_0 of the individual observation, it corresponds to $\sim 0.99\lambda/D$. Owing to the chosen chop throw, the emission structures extended over more than half of the throw, e.g., the diffuse emission of the host galaxy or weak extended star-formation regions overlap and are at least partially subtracted. Detecting extended sources with ground-based MIR instruments is particularly difficult for MIR-faint galaxies, of which many are targeted here. Additional complications arise because of fast local sky background variations of the atmosphere in the MIR and various instrument artifacts that are mostly not understood for both VISIR and Michelle. The 2D Gaussian fit yields an integrated number of counts that is then used with the given STD fluxes to compute a conversion factor with the unit Jy/(ADU/s). For the VISIR images, all sub-images (positive and negative) can be used and a statistical error can be derived by comparing the Gaussian fits of the single beams for each target. This standard deviation is a good measure of the precision of the observation. In addition, the residual emission (original - fit) is calculated and can be used to estimate the measurement precision by comparing the residual for the STD and the science target. Finally, in the case of the VISIR images, the sub-images are combined by using Gaussians centers for proper positioning.

It is well known that the MIR PSF varies on ~minute timescales or even faster because of turbulence in the atmosphere. These can lead to a PSF widening of point sources in long exposures or different PSF shapes in science and STD observations. Additional instabilities in the VISIR and Michelle PSFs are caused by instrumental effects, as described in Horst et al.

(2009) and on the Michelle web pages. Hence, in particular for faint targets (as in this work), the PSF-scaling method, as commonly used in the literature (e.g., Ramos Almeida et al. 2009; Reunanen et al. 2010), can be improper for the MIR flux measurement. On the other hand, comparison of the Gaussian method used with the classical aperture method used in Horst et al. (2008) yields consistent results within the uncertainties.

For the faintest detections, it might be necessary to smooth the input images (STD and science target) before proceeding with the fit. In those cases, the measurement of the angular resolution of the individual observation is of course slightly larger, but will be used in order to be able to compare STD and science target.

For objects surrounded by extended emission, the FWHM of the Gaussian fit can be fixed to the value from the corresponding STD which prevents the extended emission from affecting the point-source measurement to a first order. More sophisticated would be the combined fitting of the extended and the unresolved emission with the combination of two functions, e.g., two Gaussians. However, the improvement of such a method is estimated to be $\lesssim 10\%$ and is not applied here because extended emission occurs in very few of the observed objects.

For non-detected nuclei, I have proceeded with the following procedure: A 2D Gaussian with the full-width-half-maximum (FWHM) of the standard star and an amplitude of $2\sigma_{\mathrm{BG}}$ of the local background (50x50 pixel) in the image center is integrated, resulting in the flux upper limit. This method was tested and verified by simulating similar beams on very many artificial and real science images. In all cases the artificial beam is clearly visible and these calculated values therefore represent upper limits with a confidence of $\geq 99\,\%$. In addition, they agree with expectations based on the exposure time and the sensitivity measured from the standard star during the observations.

4. Low-luminosity AGN in the mid-infrared

This chapter describes the first of the two large projects forming to this work, namely MIR HR photometry of a sample LLAGN. Part of this study (the VISIR sample) has already been published in Asmus et al. (2011).

4.1. Goals

The goal of this observational programme is to investigate the existence and properties of nuclear point sources in LLAGN and measure their 12 μm continuum emission with a suitable narrow-band filter (Sect. 4.4). Because of the intrinsic faintness of this type of AGN, emission due to stellar processes, mainly star formation, can be of comparable brightness. Therefore, it is important to estimate the amount of non-AGN contamination to the point-like MIR emission (Sect. 4.5.1). In order to constrain the former, a second filter centered on the PAH 11.3 μm emission feature is used. Once, the LLAGN MIR emission is determined, the position of the LLAGN with respect to the MIR–X-ray correlation can be tested (Sect. 6.4).

4.2. Sample properties

In order to reach the goals described above, two samples of LLAGN have been selected for observations, one in each hemisphere. The southern sample of 18 LLAGN has been chosen according to the following main criteria: *i)* observable from Paranal (DEC < 25°), *ii)* a nuclear X-ray detection in the 2-10 keV band with a corrected $L_{2-10\mathrm{keV}} \lesssim 10^{42}$ erg/s, *iii)* optical classification as active nucleus, and *iv)* an expected flux density at 12 μm of $F_\nu(12\,\mu\mathrm{m}) \geq 10$ mJy, assuming that the objects follow the MIR–X-ray correlation as found by Horst et al. (2008), or that they follow the trend of MIR excess (or X-ray deficit) seen for the three LINERS in the same work. A flux of 10 mJy is roughly the lowest unresolved 12 μm flux density that VLT/VISIR can detect in a narrow-band filter in a reasonable amount of execution time ($\sim$ 1 h) under average conditions. In addition, there are 9 objects for which the selection criteria apply, but which have sufficient VISIR *N*-band imaging data available in the literature (e.g., Cen A and M 87). These objects have not been observed again but are included in the latter part of this analysis.

For observations with Gemini/Michelle on the northern hemisphere, another sample of 15 LLAGN has been selected according to a similar set of criteria: *i)* observable from Mauna Kea (DEC $> -25°$), *ii)* a nuclear X-ray detection in the 2-10 keV band with a corrected $L_{2-10\mathrm{keV}} \lesssim 10^{42}$ erg/s, *iii)* an expected flux density $F_\nu(12\,\mu\mathrm{m}) \gtrsim 10$ mJy, assuming that the objects follow the MIR–X-ray correlation, *iv)* so far unobserved with ground-based MIR instruments on 8 m-class telescopes, *v)* optically classified as Seyfert nucleus in the Palomar optical spectroscopic survey of nearby galaxies (Ho et al. 1997). This Palomar survey represents a well-studied sample of LLAGN with accurate optical classifications of weak nearby AGN and still coves a large range of bolometric luminosities at the same time (10^{40} erg/s $\lesssim L_\mathrm{bol} \lesssim 10^{44}$ erg/s). Although already included in the southern LLAGN sample, we have included M 58 again in order to compare the Michelle and VISIR performance and constrain any bias that might exist between the flux calibration in the 2 different filter systems.

In total, 33 LLAGN have been selected for new MIR observations and has been combined with the data of another 9 LLAGN, yielding 42 LLAGN that are analyzed in this work. Their fundamental properties are listed in Table A.4 while their host galaxy properties can be found in Table A.1. In the following, no further distinction is made between the samples but they are treated exactly in the same way.

4.2.1. Optical classification

The optical classification scheme according to observed emission line strength ratios is widely used throughout the literature, and is used here as well despite the disadvantages arising from extinction in the optical. However, for most of the work I distinguish only between the following 3 main types: type 1 (Sy 1.0-1.5), type 2 (Sy 1.8-2.0 and 1h, 1li) and LINERs. The AGN classification of Véron-Cetty and Véron (2010) have been used in all cases where available. NGC 3125, NGC 5363, NGC 5813, and NGC 7626 are not in this catalog, but have been classified as LINERs by Carrillo et al. (1999) and Ho et al. (1995). Note that some objects have multiple different classifications (as either Seyfert or LINER) in the literature (e.g. NGC 1097, M 81, and NGC 7213). Note further that NGC 5033 and NGC 5273 have been classified as Sy 1.5 by Ho et al. (1997) while in Véron-Cetty and Véron (2010) they are listed as Sy 1.8 and Sy 1.9. This might arise from the fact that the transition between the classifications are continuous and these objects are either located close to the borders or even have different classifications in the individual BPT diagrams. Finally, NGC 1404 is not classified as AGN in the optical but as a narrow-emission-line galaxy (NELG). However, the discovery of a nuclear hard X-ray source in this object makes the presence of a weak or obscured AGN very likely (Grier et al. 2011).

In summary the LLAGN sample comprises 42 LLAGN with 12 LINERs, 3 type 1 Seyferts, 26 type 2 Seyferts, and 1 NELG. The optical classification of individual objects can be found in Table A.4 in Appendix A.

4.2.2. Distances

Because the selected LLAGN are very nearby in a cosmological sense ($\sim 20\,\mathrm{Mpc}$), the motion caused by local gravity potentials can dominate the Hubble flow. Therefore it can be necessary for many nearby galaxies to use redshift-independent distance measurements. I use three different distance collections: a) for comparison the redshift-based luminosity distances D_L from the NASA/IPAC Extragalactic Database (NED) using redshifts corrected for the Earth motion relative to the cosmic microwave background reference frame with $H_0 = 73, \Omega_\mathrm{m} = 0.27$, and $\Omega_\mathrm{vac} = 0.73$, b) the distances given by Tully (1988) employing the Tully-Fisher (TF) relation, D_TF and c) distances of various methods with preference for the most precise and recent measurements, D_best. Here, highest priority is given to direct Cepheid-based distance measurements and next to the surface brightness fluctuation method (see Jacoby et al. 1992 for a review and comparison). If not available, the values based on the TF method or D_L are used. Note that there is no Tully-Fisher distance available for NGC 1667, NGC 3125 and NGC 7626. The individual distances and the corresponding references are listed in Table. A.1. However, unless noted otherwise, distance set c) is used.

The average distance and redshift of the whole LLAGN sample are $\langle D_\mathrm{best} \rangle = 21\,\mathrm{Mpc}$ with $\sigma_D = 12\,\mathrm{Mpc}$, and $\langle z \rangle = 0.005$ with $\sigma_z = 0.003$.

4.3. MIR observations

4.3.1. VISIR observations

For each target, we have chosen a set of two filters, such that the bandpass of one contains only continuum emission around $12\,\mu$m, while the other contains the PAH emission feature at $11.3\,\mu$m. Because all objects are at very low redshifts, the NeIIref1 ($\lambda_\mathrm{c} = 12.27\,\mu$m, half-band width $= 0.18\,\mu$m) and PAH2 ($\lambda_\mathrm{c} = 11.25\,\mu$m, half-band width $= 0.59\,\mu$m) filters have been used for all southern LLAGN.

The VLT/VISIR observations have been carried out in service mode between April and September 2009 (ESO period P83, Progr. ID 083.B-0536). Most observations have fulfilled the required observing conditions (airmass ≤ 1.3, optical seeing $\leq 0.8''$, MIR photometric sensitivity within 20% of expected values). An exception is IC 1459, which has been observed in conditions that have resulted in a much poorer sensitivity. Note that NGC 676 has been observed again in P86 with longer exposure times and the more sensitive PAH2ref2 filter ($\lambda_\mathrm{c} = 11.88\,\mu$m, half-band width $= 0.37\,\mu$m). These data are used here instead of the NeIIref1 data from P83.

Standard chopping-and-nodding observing mode with a chop throw of $8''$ on the small FOV has been performed. Therefore, all four beams fall on the detector – for science targets the two positive ones top of each other (parallel mode), ensuring the highest possible signal-to-noise (S/N) for this observing mode. After consulting *Spitzer*/IRAC $8\,\mu$m images (or 2MASS if the former has not been available), we have chosen the chopping throw and angle for each individual object such that overlap of the nucleus with non-nuclear emission regions is avoided. The flux level of the diffuse host emission at a distance of 8″ drops to less than 10% compared to the nucleus in 80% of the cases. Accordingly, possible contamination through chopping induced overlaps is estimated to be < 10%. The most severe exception is NGC 7590, which shows very complex extended MIR morphologies in IRAC. Therefore, it has been observed with the generic nodding template using offset of 30″, but it remains undetected with VISIR. For each science target, a photometric standard star has been observed within two hours beforehand or afterward. The observational data are summarized in Table 4.1.

The observations and MIR properties of the archival objects are described in detail in the literature (Reunanen et al. 2010 for NGC 1386, M 87, and Circinus; G09 for ESO 005-G004; Horst et al. 2008 for M 61, M 49, NGC 4698, and Cen A; and Horst et al. 2006 for M 58), except NGC 1052 (program ID: 382.A-0604, PI: Treister). For all those objects the available raw data have been re-reduced in exactly the same way as described above.

4.3.2. Michelle observations

Similar to the southern LLAGN, the low redshifts of the northern LLAGN allow to use the same two filters for all objects: the Si-5 filter ($\lambda_c = 11.6\,\mu$m, half-band width = $0.55\,\mu$m) for the PAH and Si-6 filter ($\lambda_c = 12.5\,\mu$m, half-band width = $0.60\,\mu$m) for the continuum. The imaging has also been performed in standard chopping-and-nodding mode in parallel configuration, such that the two positive beams are combined in the center of the raw image. Note that the negative beams are not guided in Michelle observations and therefore is not used in this analysis. We have chosen chopping throws between 8 and 15″, and chopping angles such that overlapping of emission regions, visible in *Spitzer*/IRAC images, is avoided (similar to the VISIR observations).

The observations have taken place in Feb. 2010 and have severely been affected by bad weather conditions. Therefore only 13 of the 15 objects could be observed and 5 of them only in one filter. Owing to high wind speeds and an under-average MIR seeing, the images are not diffraction limited, and the sensitivity is decreased as well. For the the two unobserved objects (NGC 2655 and NGC 3976), I use upper limits for the fluxes by applying synthetic photometry to the *Spitzer*/IRS *N*-band spectra (using the Si-5 and Si-6 filter transfer functions).

The observational data from Michelle is listed in Table 4.2.

4.4. MIR morphology and photometry of the newly observed LLAGN

Out of the 31 newly observed LLAGN, 18 have been detected in both filters, while the other 13 have not been detected in any filter. Corresponding linearly scaled images of the detected LLAGN in all observed filters are presented in Fig. 4.1 for VISIR and in Fig. 4.2 for Michelle.

Table 4.1.: Observational parameters and reduction results for the P83 VISIR LLAGN sample.

Object	Obs. date	Filter	λ_{rest}[a]	Exp. time[b]	FWHM [″]		Flux dens.
	(YY-MM-DD)		μm	[s]	STD[c]	Obj.	[mJy]
IC 1459	2009-06-05	PAH2	11.18 ± 0.59	362	0.29	…	≤ 20
		NeIIref1	12.20 ± 0.18	1443	0.32	…	≤ 30
NGC 676	2010-12-22	PAH2	11.19 ± 0.59	1448	0.32	…	≤ 9
		PAH2ref2	11.82 ± 0.37	1448	0.33	…	≤ 6
NGC 1097	2009-07-14	PAH2	11.20 ± 0.59	997	0.39	0.49	60 ± 10
	2006-08-07	NeIIref1	12.22 ± 0.18	2524	0.32	0.40	27 ± 4
NGC 1404	2009-07-15	PAH2	11.18 ± 0.59	544	0.57	…	≤ 35
	2009-09-06	NeIIref1	12.19 ± 0.18	1992	0.38	…	≤ 18
NGC 1566	2009-09-06	PAH2	11.19 ± 0.59	362	0.37	0.46	101 ± 12
		NeIIref1	12.21 ± 0.18	1443	0.33	0.42	95 ± 13
NGC 1667	2009-09-06	PAH2	11.08 ± 0.58	362	0.37	…	≤16
		NeIIref1	12.09 ± 0.18	1803	0.38	…	≤15
NGC 3125	2009-06-17	PAH2	11.21 ± 0.58	902	0.30	0.72	45 ± 15
	2009-06-16	NeIIref1	12.22 ± 0.18	1992	0.32	0.74	65 ± 13
NGC 3312	2009-07-15	PAH2	11.14 ± 0.59	725	0.38	…	≤ 24
	…	NeIIref1	12.15 ± 0.18	…	…	…	…
NGC 4235	2009-06-07	PAH2	11.16 ± 0.59	362	0.29	0.38	38 ± 6
		NeIIref1	12.17 ± 0.18	1443	0.33	0.37	33 ± 4
NGC 4261	2009-06-16	PAH2	11.17 ± 0.59	544	0.30	0.39	12 ± 2
		NeIIref1	12.18 ± 0.18	1992	0.36	0.48	15 ± 2
M 58	2005-04-30	PAH2ref2	11.82 ± 0.37	542	0.33	0.35	68 ± 6
		NeIIref1	12.23 ± 0.59	541	0.34	0.35	63 ± 7
M 104	2009-06-17	PAH2	11.21 ± 0.59	362	0.30	…	≤ 11
		NeIIref1	12.23 ± 0.18	902	0.33	…	≤ 17
NGC 4941	2009-05-11	PAH2	11.21 ± 0.59	725	0.36	0.33	68 ± 5
	2006-04-19	NeIIref1	12.22 ± 0.18	1620	0.35	0.35	75 ± 4
NGC 5363	2009-05-10	PAH2	11.21 ± 0.59	544	0.33	…	≤ 11
		NeIIref1	12.22 ± 0.18	1443	0.34	…	≤ 18
NGC 5813	2009-05-10	PAH2	11.18 ± 0.59	181	0.33	…	≤ 21
		NeIIref1	12.19 ± 0.18	181	0.34	…	≤ 51
NGC 7213	2009-05-17	PAH2	11.18 ± 0.59	181	0.28	0.30	232 ± 5
		NeIIref1	12.20 ± 0.18	181	0.31	0.32	228 ± 15
NGC 7590	2009-06-04	PAH2	11.19 ± 0.59	362	0.32	…	≤ 16
		NeIIref1	12.21 ± 0.18	902	0.34	…	≤ 28
NGC 7626	2009-06-04	PAH2	11.12 ± 0.58	181	0.32	…	≤ 24
		NeIIref1	12.13 ± 0.18	721	0.34	…	≤ 26
NGC 7743	2009-07-05	PAH2	11.19 ± 0.59	362	0.29	…	≤ 11
		NeIIref1	12.20 ± 0.18	1443	0.32	…	≤ 13

[a]: central filter wavelength in the restframe with half-band width

[b]: on-source exposure time excluding any overheads

[c]: FWHM of the photometric standard star

Table 4.2.: Observational parameters and reduction results for the Michelle LLAGN sample.

Object	Obs. date	Filter	λ_{rest}[a]	Exp. time[b]	FWHM [″]		Flux dens.
	(YY-MM-DD)		μm	[s]	STD[c]	Obj.	[mJy]
M 81	10-02-04	Si-5	11.60 ± 0.55	156	0.43	0.50	168 ± 22
	10-02-04	Si-6	12.50 ± 0.60	141	0.42	0.49	157 ± 23
NGC 3147	10-02-05	Si-5	11.49 ± 0.54	259	0.51	0.51	22 ± 2
	10-02-05	Si-6	12.38 ± 0.59	282	0.53	0.53	20 ± 5
NGC 3486	10-02-04	Si-5	11.57 ± 0.55	363	0.42	...	≤ 4
	10-02-04	Si-6	12.47 ± 0.60	376	0.43	...	≤ 5
NGC 3982	10-02-05	Si-5	11.56 ± 0.55	518	0.43	0.44	24 ± 3
	10-02-05	Si-6	12.45 ± 0.60	517	0.44	0.51	31 ± 3
NGC 4051	10-02-02	Si-5	11.57 ± 0.55	156	0.43	0.47	457 ± 63
NGC 4138	10-02-02	Si-5	11.57 ± 0.55	259	0.43	0.43	17 ± 3
M 106	10-02-04	Si-5	11.58 ± 0.55	156	0.49	0.46	146 ± 18
	10-02-04	Si-6	12.48 ± 0.60	141	0.45	0.50	138 ± 15
NGC 4395	10-02-05	Si-6	12.49 ± 0.60	612	0.40	0.40	6 ± 2
NGC 4501	10-02-02	Si-5	11.51 ± 0.55	518	0.49	...	≤ 5
M 58	10-02-04	Si-5	11.54 ± 0.55	156	0.38	0.51	70 ± 7
	10-02-04	Si-6	12.44 ± 0.60	141	0.40	0.51	74 ± 14
NGC 5033	10-02-02	Si-5	11.57 ± 0.55	518	0.48	0.47	16 ± 3
M 51a	10-02-04	Si-5	11.58 ± 0.55	518	0.53	0.53	20 ± 9
	10-02-04	Si-6	12.48 ± 0.60	517	0.54	0.54	26 ± 13
NGC 5273	10-02-02	Si-5	11.56 ± 0.55	259	0.49	0.49	19 ± 7
	10-02-04	Si-6	12.46 ± 0.60	282	0.40	0.40	24 ± 11

[a]: central filter wavelength in the restframe with half-band width
[b]: on-source exposure time excluding any overheads
[c]: FWHM of the photometric standard star

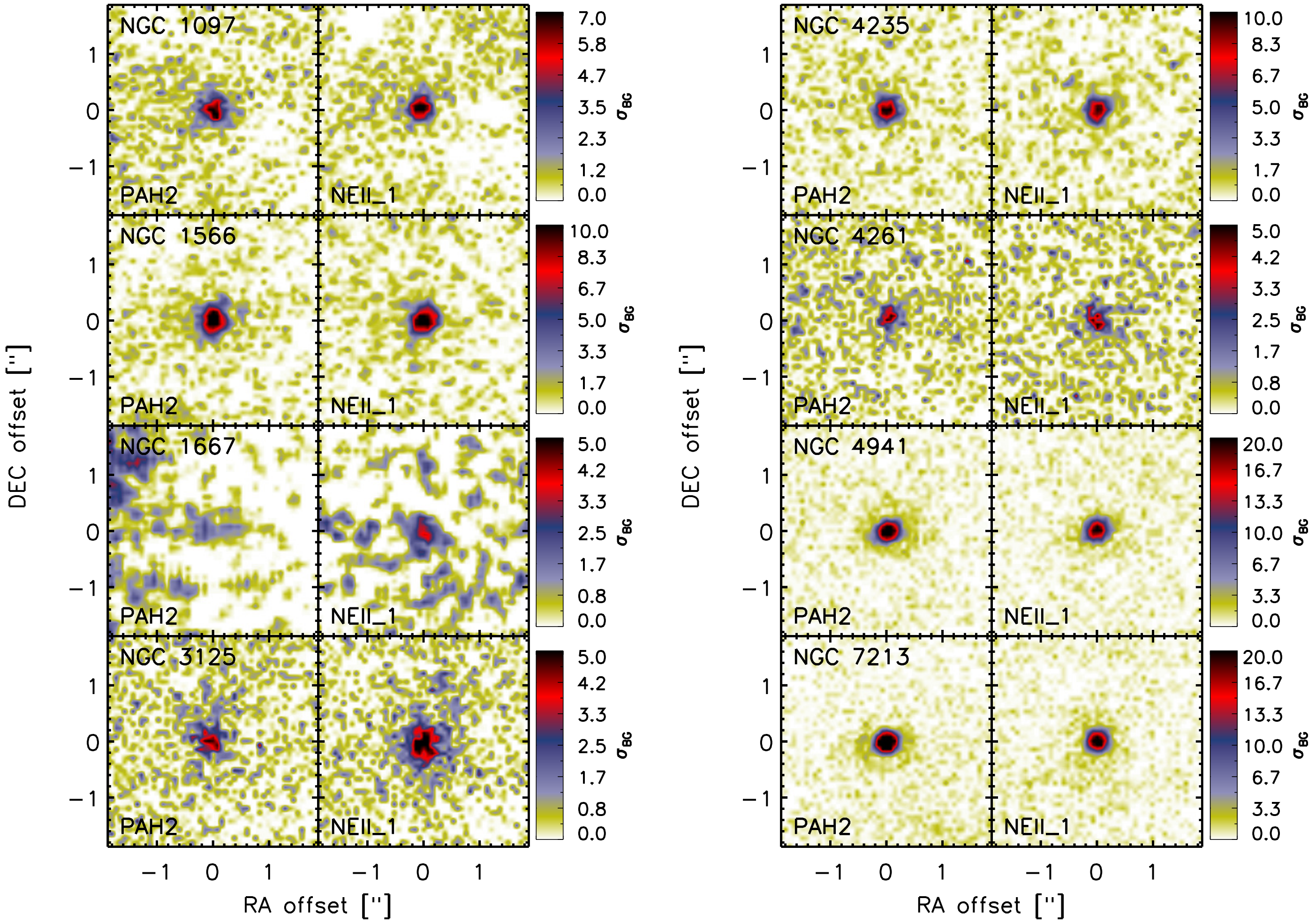

Figure 4.1: VISIR images of the detected LLAGN (except M 58). The linear scaling is indicated in the individual color bars in units of $\sigma_{\rm BG}$ with white corresponding to the mean background value ($\langle$BG$\rangle$). The images of NGC 1667 were smoothed to increase the visibility of this low-S/N detection.

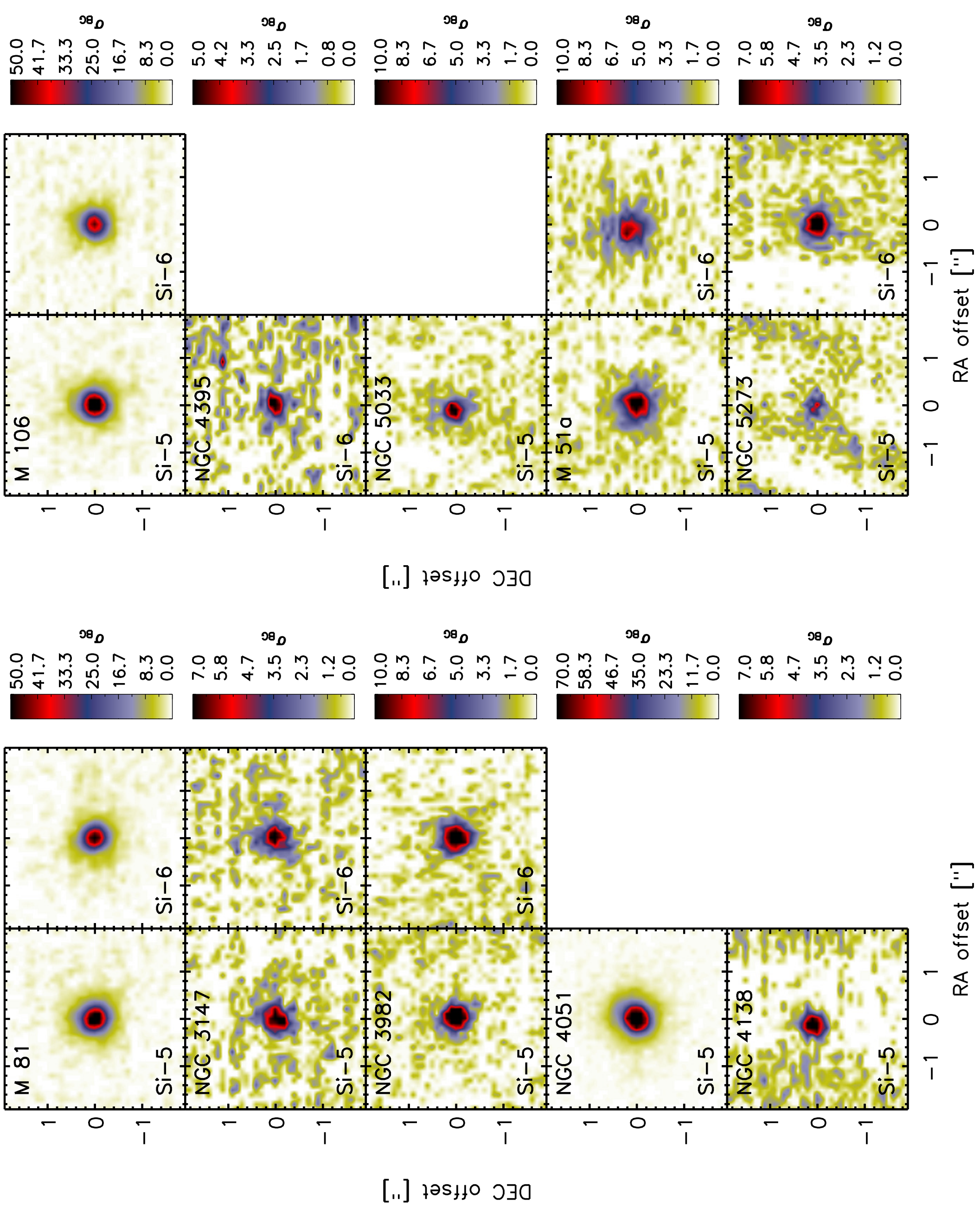

Figure 4.2: Michelle images of the detected LLAGN (except M 58). Description is similar to Fig. 4.1.

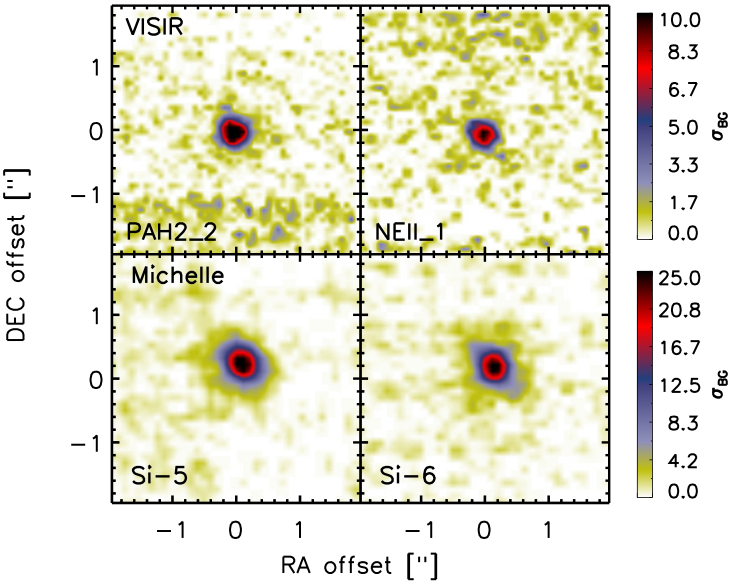

Figure 4.3: VISIR and Michelle images of M 58. Description is similar to Fig. 4.1.

In addition, all HR MIR data of M 58 are presented in Fig. 4.3 combined, for comparison of VISIR and Michelle (see below), while the HR images of the other detected LLAGN from the archive are displayed in Fig. A.1. For the VISIR data, these images are created by co-adding sub-images (50 × 50 pixels) of the negative beams (with changed sign) to the sub-image of the central double beam, while for the Michelle data, only a cut-out (40 × 40 pixels) of the central beam is used. In general, all detected LLAGN show a point-like central source which is in most cases detected with a significance of $\geq 7\sigma_{\mathrm{BG}}$. Here, σ_{BG} signifies the standard variation of the local background (4″). Within the pointing accuracy of the instruments, all point-source positions are consistent with the ones derived for the galaxy nuclei based on other observations (e.g., 2MASS or radio interferometry). I consequently infer that the observed point sources are in fact the MIR imprint of the LLAGN. In addition, no other emission sources of any nature are detected within 8″ around the nuclei.

The faintest detections are NGC 3125, NGC 4261, and NGC 4395. In addition, NGC 3125 seems to be the only object of the newly observed LLAGN that shows extended emission in any filter, although the emission is still acceptably fitted by a Gaussian. On the other hand, the detection is at a low σ-level (≤ 5), which additionally complicates a reliable measurement of its extension. Note that of the archival LLAGN, NGC 1386 and Circinus show extended MIR emission, which is further discussed in Appendix C. Note as well that the dusty disk with 1.7″ extent in the center of NGC 4261 has not been detected (compare Fig. 2.4). Another special case is NGC 1667, for which the individual beams have been detected only at a 2 σ_{BG}-level, on the other hand all three beams are located at the expected positions with respect to the chopping parameters. This raises the detection significance to $3.7\sigma_{\mathrm{BG}}$ for the smoothed combined image (as displayed in Fig. 4.1). However, the measured fluxes of NGC 1667 are formally treated as upper limits throughout this work. NGC 676 has not been detected, but a foreground star is superposed 5″ south of the galaxy center. The latter has been detected in both filters ($5\sigma_{\mathrm{BG}}$, 8 mJy in PAH2ref2), constraining the flux of the AGN to 6 mJy in PAh2ref2 ($3\sigma_{\mathrm{BG}}$ upper limit). For NGC 4941 and NGC 7213, the Airy rings are evident in the PAH2 images, indicating that the diffraction limit has been reached during the exposure in those cases. Because of the bad weather conditions during the Michelle observations, none of the Michelle images is diffraction limited. Instead of Airy rings, the brightest Michelle detections, M 81, NGC 4051, and M 106, weakly show the trefoil shape in the extensions of the PSF (displayed in green) that is characteristic for this instrument (compare Michelle web pages).

Furthermore, the science targets show a ∼ 20% higher FWHM compared to the STDs, both in the VISIR (Table 4.1) and Michelle data (Table 4.2). As already mentioned in Sect. 3.3, this is related to the PSF instabilities affecting the PSF in the much longer exposure times of the science observations. In principle, this could be quantified and corrected for by comparing and discarding the worst chopping frames in the raw data. However, this is not possible for the LLAGN because they are too faint to be visible in the individual chop frames (sometimes even nod frames). Therefore, comparisons between STD and science observations are of limited use even if both have been performed under similar atmospheric conditions. The same PSF instabilities probably also cause the asymmetric PSF shapes evident in many of the LLAGN images.

Finally, for M 58, we can directly compare the VISIR and Michelle data (Fig. 4.3). Note that the VISIR data is taken from the archive but also listed in Table 4.1. Interestingly, the detection significance of the nucleus is more than twice as high in the Michelle data as in VISIR, despite the three times shorter exposure time. The data of the other LLAGN rather imply comparable sensitivities for both instruments. On the other hand, in the VISIR observations of M 58, the diffraction limit has almost been reached (FWHM = 0.35″), indicating good observing conditions, while for Michelle the FWHM is only 0.5″. However, the data of both instruments shows a point-like MIR nucleus in M 58 in all filters. Again, the asymmetric extended PSF shape is evident in the Michelle data together with a slight elongation of the core, which is most likely caused by the strong winds during the observation. Unfortunately, not the same filters are available both for Michelle and VISIR, instead the Michelle filters have different central wavelengths and wider bandpasses than the VISIR filters. However, the structure of M 58 looks very similar in all filters and the measured fluxes also agree within the uncertainties (Table 4.1 and Table 4.2 and Fig. 4.4). Despite being tested only for one object, the similarity implies that a systematic correction between the Michelle and VISIR flux measurements is not be necessary for this work. This conclusion is also based on the low sensitivity and restricted precision ($\lesssim$ 10%) of the presented observations and therefore, no further correction is the applied to the HR MIR photometry of the LLAGN.

In summary, there is no evidence for extended emission (except NGC 3125), non-nuclear discrete sources or elongation in most LLAGN, instead all the observed MIR emission originates in a region unresolved by the HR instruments. The nuclear MIR emission fluxes (and upper limits for non-detections) of the new LLAGN observations are listed in Table 4.1 and Table 4.2, while the measured fluxes of the LLAGN with archival data can be found in Table A.2. These objects are included in the following sections without any further distinction.

4.5. Comparison to *Spitzer*/IRS

A comparison of the HR photometry with lower angular resolution MIR data enables to characterize the amount of non-AGN emission contributing at those resolutions and assess the importance of HR for AGN investigations. For this purpose, I compare the HR data in particular with *Spitzer*/IRS *N*-band spectra (similar to Horst et al. 2009). This is especially interesting because *Spitzer* data is widely used in the literature for examinations of AGN properties. In addition, such a comparison is also important in order to infer the MIR properties of higher redshift objects, where even sub-arcsec resolution is insufficient to separate the nuclear from the host emission.

Most of the LLAGN with HR photometry have also been observed with *Spitzer*/IRS (36 of 40), which enables a more detailed comparison of the innermost 4″. Post-BCD spectra are available in the archive, created by a point-source profile extraction. They are well-calibrated (uncertainty $\lesssim 10\%$) and are sufficient for a rough comparison with the nuclear properties. It is important to note, however, that these IRS spectra can deviate significantly from other studies, because of two possible reasons: for extended objects the extraction profile underweights the extended emission, or the flux might be significantly lower because of bigger extraction areas (e.g. 20″ in Gallimore et al. (2010)). Nevertheless, for the 7 objects in common, the post-BCD spectra generally agree with those published by Diamond-Stanic and Rieke (2010) where very small extraction areas have been used.

The data are displayed in Fig. 4.4, for clarity without the flux uncertainties of the IRS spectra ($\lesssim 10\%$). For NGC 676, NGC 3312, and NGC 5363, no IRS spectra are available in the archive. Furthermore, for NGC 1667, NGC 4594, NGC 7590 and NGC 7626, the IRS spectra are in high-resolution mode with a low S/N, although in some cases a strong PAH feature ($11.3\,\mu$m) is still evident. Commonly occurring MIR emission lines are indicated by vertical dashed lines, from left to right: [ArIII] ($8.99\,\mu$m), H_2 ($9.67\,\mu$m), [SIV] ($10.5\,\mu$m), PAH ($11.3\,\mu$m) and [NeII] ($12.81\,\mu$m). In addition, archival VISIR imaging data along with the photometric measurements of Ramos Almeida et al. (2009) and Mason et al. (2007) are shown for comparison. They agree well with the new measurements within the uncertainties. Only NGC 7213 shows different fluxes ($\gtrsim 10\%$) in both NeIIref1 and PAH2 over a time of about three years. The reason for this is unknown but might indicate variability.

For a quantitative comparison with the HR photometry, $F_\nu^{\mathrm{HR}}(11\,\mu\mathrm{m})$ and $F_\nu^{\mathrm{HR}}(12\,\mu\mathrm{m})$, the IRS spectra were convolved with the normalized filter transfer functions of the corresponding Michelle and VISIR filters. The resulting flux densities, $F_\nu^{\mathrm{IRS}}(11\,\mu\mathrm{m})$ and $F_\nu^{\mathrm{IRS}}(12\,\mu\mathrm{m})$, are displayed in Table A.3 for all LLAGN. Furthermore, the ratios between the HR and IRS flux densities have been computed, $R(\mathrm{PAH}) = F_\nu^{\mathrm{HR}}(11\,\mu\mathrm{m})/F_\nu^{\mathrm{IRS}}(11\,\mu\mathrm{m})$ and $R(\mathrm{cont}) = F_\nu^{\mathrm{HR}}(12\,\mu\mathrm{m})/F_\nu^{\mathrm{IRS}}(12\,\mu\mathrm{m})$, and are displayed in Fig. 4.5 in logarithmic space for all LLAGN with detections in both filters (16). Most of them display significantly lower flux densities in the continuum filter ($\log R(\mathrm{cont}) < 0$) and also in the PAH filter ($\log R(\mathrm{PAH}) < 0$) at HR than with *Spitzer*/IRS. Especially NGC 1097, ESO 005-G004, NGC 4261, and M 51a exhibit very low ratios. This is also true for the upper limits derived for NGC 1667, M 104 and NGC 3486 and implies that in those objects large amounts of hot dust are distributed in extended diffuse

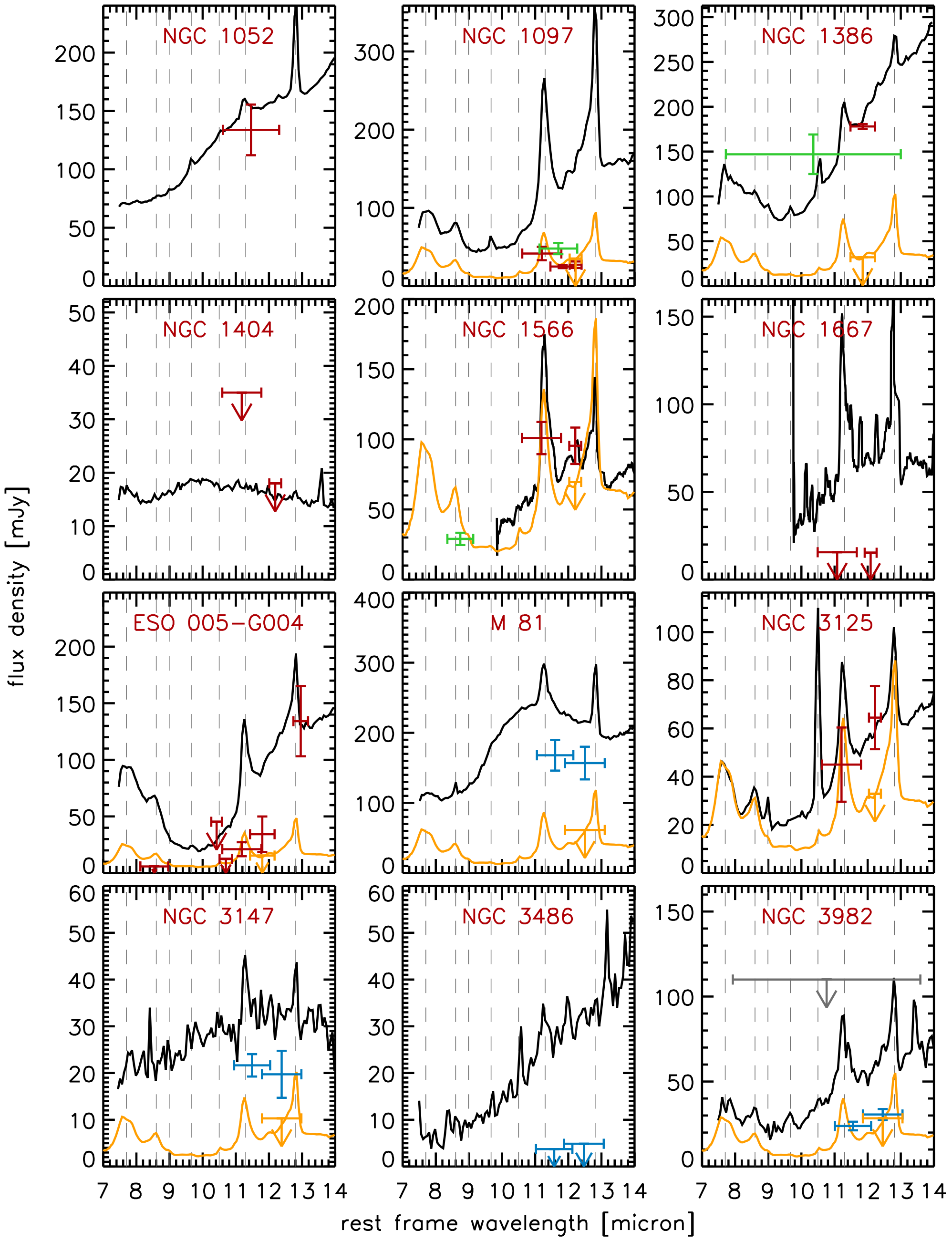

Figure 4.4: Comparison of HR photometry (VISIR: red symbols, Michelle: blue symbols) and *Spitzer*/IRS spectra (black line) for the LLAGN. Displaying errors in the spectra was omitted to maintain clarity, they are of the order of 10%. For comparison, HR photometry from literature is also plotted in grey (MIRLIN; Gorjian et al. 2004) and green (T-ReCS; Mason et al. 2007; Ramos Almeida et al. 2009), see Horizontal error bars correspond to the filter pass band. Commonly occurring emission lines are indicated by the dotted lines. In addition, the scaled starburst template SED (displayed as orange line) are shown as well as the derived upper limit for the starburst contribution to the continuum filter measurement (orange symbols), see Sect. 4.5.1 for details.

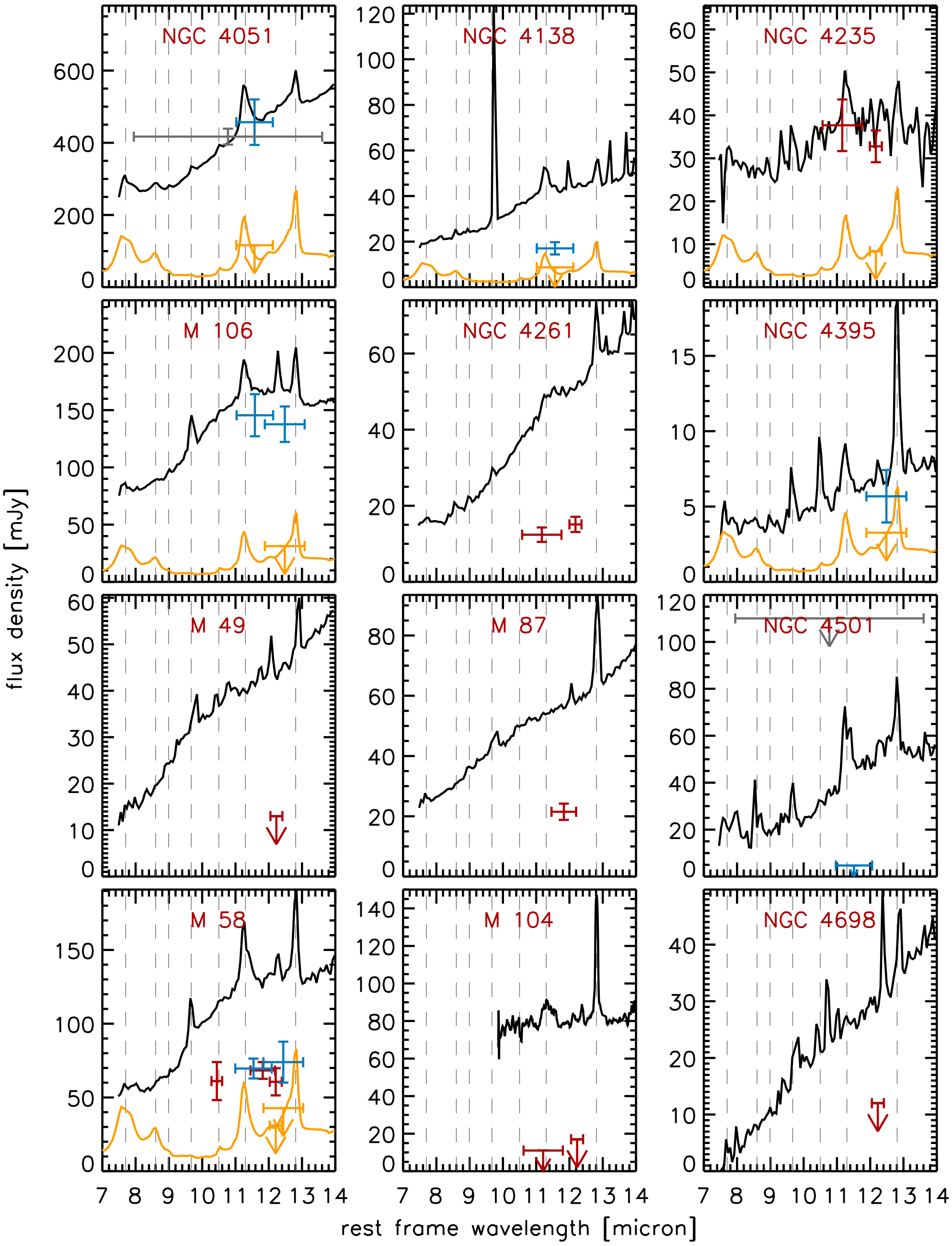

Figure 4.4: continued.

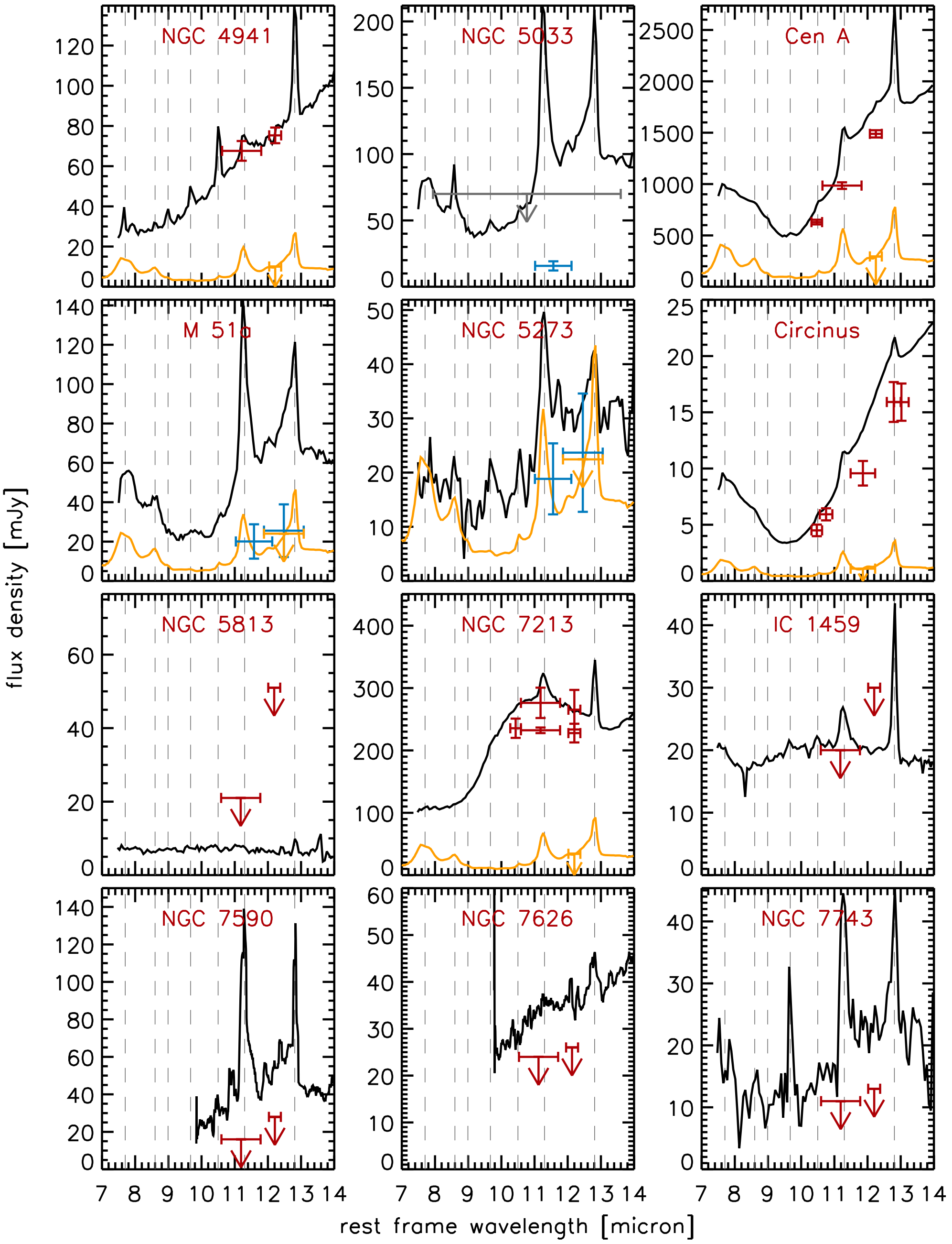

Figure 4.4: continued.

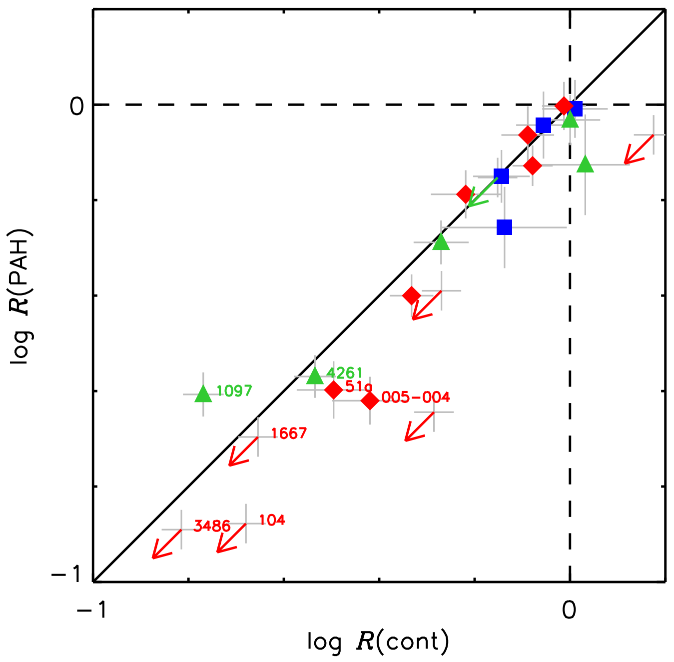

Figure 4.5: Comparison of the continuum ratio *R*(cont) and the PAH ratio *R*(PAH) for type 1 (blue), type 2 LLAGN (red), and LINERs (green) in logarithmic space. The solid black line marks the one to one correspondence line while the dashed lines mark ratios with a value of 1. See text for further explanation.

regions around the nucleus. Owing to their faintness, the latter are probably resolved-out in the HR instruments and consequently not visible. Unfortunately, the S/N of the images is not high enough to constrain these emission regions well, e.g., the missing flux density of ~ 35 mJy of NGC 4261 extended over a region of 0.75″ diameter would become undetectable in VISIR, which agrees with the non-detection of the dusty disk (visible in the HST image) in this object.

However, for some of other objects (NGC 1566, NGC 3125, NGC 4235 and NGC 4941), the HR and IRS continuum flux densities are very similar, indicating that in these cases no additional significant MIR source surrounds the nucleus at arcsec scale. NGC 1566 is an especially interesting case because it exhibits the same strong PAH emission both in IRS and at HR, which indicates that strong star formation is dominating its nuclear emission. On the other hand, the weak PAH emission features present in the IRS spectra of NGC 4235 and NGC 4941 cannot be verified in the VISIR data because the measurement uncertainties are too high.

Most of the LLAGN with measurements in both continuum and PAH emission lie along the diagonal in Fig. 4.5, which implies that, despite lower flux densities, the 10.5-12.5 μm SED shape (and the PAH emission strength) remains largely similar at HR compared to lower resolution. However, ESO 005-G004, NGC 3125, NGC 3982, Cen A, M 51a, and NGC 5273 are significantly under-luminous at HR around 11 μm, i.e. exhibit relatively less PAH emission than in the IRS spectra. Only NGC 1097 lies above the diagonal with strong PAH emission both in VISIR and in the IRS data. It is known that this object harbors a nuclear star cluster (Storchi-Bergmann et al. 2005) that contributes significantly to, and presumably dominates, the MIR emission of the nucleus (Mason et al. 2007).

In summary, most LLAGN exhibit lower flux densities at HR than in *Spitzer*/IRS and tend to have only weak or absent PAH emission (apart from NGC 1097 and NGC 1566). This indicates that this feature, which is typical for star-formation, usually does not originate in the very nucleus of LLAGN, but in the circum-nuclear surroundings (at scales larger than 100 pc), as was already noticed by Hönig et al. (2010) for brighter Seyfert galaxies. These diffuse emission regions are likely very extended, so that they are resolved-out on most HR images.

I examine in the next section the most extreme possible case, i.e., that all PAH emission visible in the IRS spectra originates in the unresolved nucleus. This allows to better constrain any star-formation contamination of the HR data.

4.5.1. Constraining the nuclear star-formation contamination

One of our main concerns is whether the measured 12 μm continuum is contaminated by non-AGN emission, e.g. circum-nuclear star-formation. This contamination would increasingly affect the measurements at lower luminosities as it is the case for the LLAGN. It could indeed explain the MIR excess that some LLAGN show (Sect. 1.5). I use the following assumption in order to better constrain the individual star-formation contamination: the 12 μm continuum emission in SF regions scales with the PAH 11.3 μm line emission. The validity of this assumption can be proven by examining such a relation for a typical sample of starburst galaxies, e.g., the IRS spectra from Brandl et al. (2006). They have been made available electronically by the *Spitzer*/IRS Atlas project (Hernán-Caballero and Hatziminaoglou 2011). Starburst galaxies are objects with a high rate of current SF in either various large regions or the whole galaxy, which are triggered through galaxy interactions or mergers, leading to large concentrations of cold gas. The global emission of starburst galaxies is dominated by SF, particularly in the infrared, and hence they are optimal subjects for the study of SF on galactic scales. The relation between the 12 μm continuum and the PAH 11.3 μm emission line flux is displayed in Fig. 4.6 for the Brandl et al. sample. Here, the 12 μm continuum, $F_\nu(12\,\mu\mathrm{m})$, is measured by synthetic photometry using the NeIIref1 filter function, while the PAH 11.3 μm emission line flux is measured by area under a Gaussian that is fitted to the spectral feature. During the fitting the underlying continuum approximated by a polynomial of first order and then subtracted. The resulting precision of this line flux measurement method is usually $\leq$ 10% and thus sufficient for the current purpose. Fig. 4.6 indeed demonstrates a strong correlation between $F_\nu(12\,\mu\mathrm{m})$ and $F(\mathrm{PAH}11.3\mu\mathrm{m})$ for SF regions: the Spearman rank correlation coefficient for the Brandl et al. sample is $\rho = 0.98$ with a null-hypothesis probability $\log p = -7.1$. For comparison, I also plot M 82 which is a nearby prototypical starburst galaxy. It agrees well with the found correlation. Note that one of the starburst galaxies belonging to the Brandl et al. sample is actually the LINER NGC 1097 (marked as green triangle). However, its global MIR emission is totally dominated by the star formation, mainly occurring in a ring-like structure of kiloparsec extent surrounding its nucleus. This is verified by its position in Fig. 4.6. On the

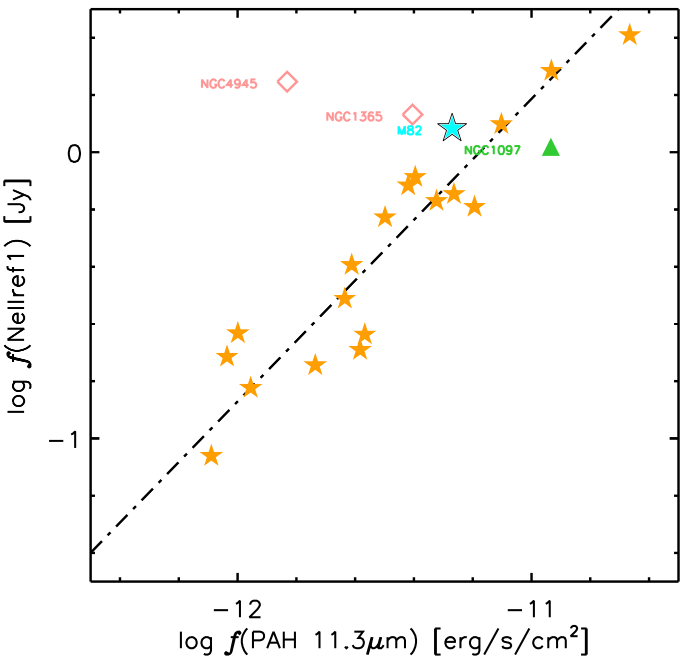

Figure 4.6: 12 μm continuum emission versus the PAH 11.3 μm emission line flux for the starburst galaxies from Brandl et al. (2006) displayed as orange stars. The measurement errors are of the order of 10% and thus smaller than the plotted symbols. In addition, the prototypical starburst galaxy M 82 (cyan star) is plotted as well as the Sy 2 galaxies NGC 1365 and NGC 4945 (red diamonds), and the LINER NGC 1097 (green triangle). The dot-dashed line represents the power-law fit given in Eq. 4.1.

other hand, this sample also includes 2 starburst galaxies with Seyfert nuclei, NGC 1365 and NGC 4945 (red diamonds). Both deviate significantly from the correlation showing an excess of 12 μm continuum emission, which is most likely caused by their active nuclei. Therefore, both galaxies were excluded from the correlation analysis. A bisector fit (Isobe et al. 1990) to the remaining starburst galaxies in logarithmic space yields:

$$\begin{aligned}\log\left(\frac{F_\nu(\mathrm{NeIIref1})}{\mathrm{Jy}}\right) &= (11.82 \pm 0.91) \\ &+ (1.06 \pm 0.08)\log\left(\frac{F(\mathrm{PAH11.3}\mu\mathrm{m})}{\mathrm{erg\,s^{-1}cm^{-2}}}\right). \qquad (4.1)\end{aligned}$$

A comparable correlation has recently been found also by Diamond-Stanic (2011).

With this correlation being verified, we can compare the LLAGN data to a SF template SED that is scaled by the $F(\mathrm{PAH11.3}\mu\mathrm{m})$ from the LLAGN IRS spectra and determine the maximum possible SF contribution to $F_\nu(12\,\mu\mathrm{m})$.

For this purpose, we first have to create such a SF template SED. Again, I use the Brandl et al. IRS spectra, more precisely, a sub-sample of 13 starburst spectra with the highest S/N selected by the authors. These 13 starburst spectra are normalized by their PAH 11.3 μm

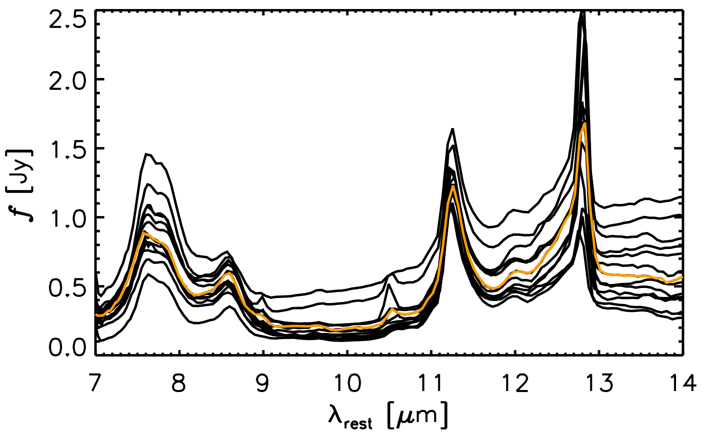

Figure 4.7: Median IRS *N*-band spectrum (orange) of the 13 starburst galaxies with the highest S/N from Brandl et al. (2006). The individual spectra (black) are normalized by *F*(PAH11.3μm). Uncertainties are omitted for clarity.

emission line flux, which results in a scatter of approximately 30% (0.13 dex) for the 12 μm flux in the individual spectra (Fig. 4.7). The median of the individual starburst spectra is used as SF template SED and then is scaled for each individual LLAGN by its PAH 11.3 μm emission line flux. Next, synthetic photometry is computed for the scaled SF SED in the corresponding HR filter containing the PAH 11.3 μm emission feature (PAH2 for VISIR and Si-5 for Michelle in most cases). If this synthetic flux density is higher than the corresponding real HR measurement, then the SF SED is further scaled down by the ratio of the flux densities. This is the case for NGC 1097, ESO 005-G004, NGC 3982, M 51a, and NGC 5273, where the HR photometry is of higher constrain than the IRS spectrum. Finally, the corresponding 12 μm flux density of the scaled SF is determined by convolution with the continuum filter function (NeIIref1 for VISIR and Si-6 for Michelle in most cases). By these means it is possible to estimate the maximum contamination by SF in the measured continuum of the unresolved LLAGN at HR.

The measured total PAH 11.3 μm emission line fluxes, *F*(PAH11.3μm), are given in Table A.3 for all LLAGN with evident PAH emission, the typical measurement error is $\lesssim$ 10%. The scaled starburst template spectra for those LLAGN are plotted in orange in Fig. 4.4. The corresponding calculated 12 μm continuum flux densities, $F_\nu^{\mathrm{SF}}(12\mu\mathrm{m})$, are indicated by orange upper limits and stated in Table A.3 as well. Note that NGC 1052 is not included because it was not observed in the VISIR filter B11.4, for which the transmission function is unknown (private communication with Y. Momany) and thus no synthetic photometry could be computed. Although this filter includes the PAH emission feature in its bandpass, the emission is very weak in the IRS spectrum of NGC 1052. Furthermore, no significant PAH emission could be detected in the IRS spectra for the detected LINERs NGC 4261 and M 87. This makes any significant contribution of star-formation to the HR data of NGC 1052, NGC 4261 and NGC 4486 very unlikely.

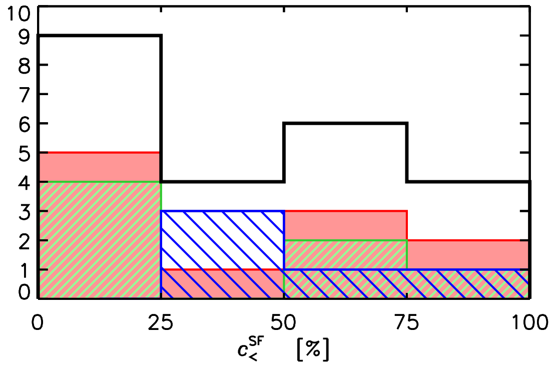

Figure 4.8: Distribution of the maximum star formation contribution $c_<^{\mathrm{SB}}$ to the 12 μm continuum (black line) for all LLAGN. Contributions of the individual classes are displayed for Sy 1 (blue), Sy 2 (red) and LINER (green).

Note that NGC 4051, NGC 4138 and NGC 5033 were only observed in the Si-5 filter, which is used as a measure for $F_\nu(12\,\mu\mathrm{m})$ although it contains the PAH feature. This is reasonable at least for NGC 4051 and NGC 4138, where the PAH emission is relatively weak in the IRS spectra, and thus still a meaningful upper limit for the $F_\nu^{\mathrm{SF}}(12\mu\mathrm{m})$ could be derived.

Unlike the LINERs, some low-luminosity Seyferts exhibit strong PAH emission (NGC 1097, NGC 3982, M 51a, NGC 5273) in their IRS spectra, which leads to their estimated maximum star-formation contribution $c_<^{\mathrm{SF}}$ being very high ($> 90\%$). However, the PAH emission feature is weak in many other cases (NGC 1386, M 81, NGC 4235, M 106, NGC 4941, Cen A, and NGC 7213), so that $c_<^{\mathrm{SF}}$ can often be constrained to much less than 30%.

The distribution of $c_<^{\mathrm{SF}}$ for the LLAGN (and the different sub-types) is displayed in Fig. 4.8. It does not show any strong trends neither for individual optical classes nor for all LLAGN combined. Of course the number of objects per bin is very small. Still it is interesting that the distributions of the Sy 2 and LINER are exactly similar and only weakly favor small $c_<^{\mathrm{SF}}$, while the Sy 1 all have $c_<^{\mathrm{SF}} > 25\%$.

In summary, a major contribution by star-formation to the nuclear 12 μm continuum (at 0.4″ scale) can be excluded for the majority of LLAGN (57%). Furthermore, it is very unlikely that the entire PAH emission originates in the unresolved nucleus (as assumed in this section). Consequently, the real SF contribution is probably much lower in all cases – as long as the PAH 11.3 μm remains a valid tracer of the star-formation. It is not verified that the hard AGN radiation not only destroys the PAH molecules but also quenches star-formation. On the other hand, PAH molecules might survive in the dense clumpy clouds inside the torus itself for significant timescales. In addition, young massive star clusters emit hard radiation fields that could destroy the PAH molecules (see e.g. Snijders et al. 2006). At least, recent findings suggest that the PAH 11.3 μm remains on average a good star-formation tracer, also in circum-nuclear environments of AGN (e.g. Diamond-Stanic and Rieke 2010).

I conclude this chapter about the first major observational project of this work by summarizing that a sample of 42 LLAGN has been selected for HR MIR photometry and 40 have successfully been observed. The detected MIR emission is unresolved at $0.4''$ scale and dominated by the LLAGN itself in the majority of cases. Hence, the extracted $12\,\mu$m emission can be used (without any further correction) for multiwavelength analysis and in particular the MIR–X-ray correlation in Chapter 6. However, prior to this, I describe the second observational project in the next chapter.

5. Mid-infrared properties of an uniform AGN sample

One of the largest weaknesses of the current investigation of the MIR–X-ray correlation is the incompleteness and non-uniformity of the samples used. Usually, AGN samples are selected due to their optical properties, e.g. their emission line strengths. However, the optical emission of the AGN is easily extincted by dust in the line of sight between us and the AGN. Obscuration can happen already at nuclear scale, e.g., by the torus, circum-nuclear clouds (e.g., star formation regions) or somewhere further away in the host galaxy. Many well-studied AGN show in fact high obscuration that dramatically affects the observed properties and the appearance of the source throughout the electromagnetic spectrum. These obscuration effects lead also to a bias in the selection of AGN samples disfavoring obscured objects, which might even be completely unidentified as possessing an active nucleus. Actually, heavily obscured ($N_\mathrm{H} > 10^{22}\,\mathrm{cm}^{-2}$) AGN might represent the largest fraction of the whole AGN population (e.g. Daddi et al. 2007).

But in order to understand the AGN structure and evolution, in particular to test the unification scheme, it is critical to uniformly examine a representative and sufficiently large sample of AGN. In the following section, I present such an unbiased complete sample of local AGN and our corresponding MIR observational programme.

5.1. The BAT AGN sample

There are only two wavelength regions for which the obscuring material around AGN is mostly optical thin (apart from the CT case) and the AGN is intrinsically bright enough for reliable detection. These bands are the hard X-rays ($> 20\,\mathrm{keV}$) and the MIR ($5 - 50\,\mu\mathrm{m}$). However, the MIR selection of AGN is hampered by strong contaminating emission from star forming regions and the lack of an unique MIR signature. Therefore, a MIR selection can suffer from many contaminations and non-AGN objects. On the other hand, non-AGN contamination is not a problem at hard X-rays, as only AGN provide sufficient physical conditions for producing significant hard X-ray emission on extragalactic scale and over long time periods. Even moderately CT sources can be detected, while their intrinsic emission probably is underestimated. At these wavelengths different problems arise however, namely the focusing and the low number of the high-energy photons. These practical problems prevented past telescopes/instruments from performing a sufficiently deep wide-angle survey of the local universe, as needed for an unbiased and complete sample of AGN.

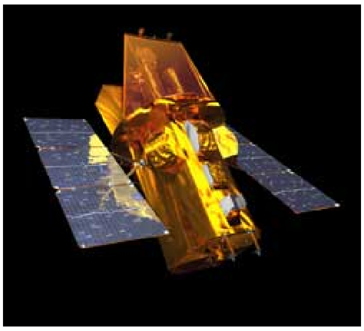

Figure 5.1: Artist view of the *Swift* spacecraft. It weights 1470 kg and orbits the earth in 90 min at a height of 600 km. The original mission length of 6 years is already surpassed. Reproduced from Wikipedia (`http://en.wikipedia.org/wiki/Swift_Gamma-Ray_Burst_Mission`). Credit: NASA.

In 2004, the situation changed with the launch of the robotic spacecraft *Swift* , a NASA mission for the gamma-ray burst research (Fig. 5.1). *Swift* (Gehrels et al. 2004) carries three instruments that were developed to observe the afterglows of gamma-ray bursts at different wavelengths, the UltraViolet/Optical Telescope (UVOT), the X-Ray Telescope (XRT) and the Burst Alert Telescope (BAT). Gamma-ray bursts are extremely short-lived (0.01 to 40 sec) bright events randomly distributed in the sky. Their origin is still unclear (and was the major reason for the *Swift* mission). Theories try to explain them with beamed emission from massive supernovae and the merger of binary neutron stars. I refer the interested reader to Vedrenne and Atteia (2009) for more information about gamma-ray bursts. The BAT (Barthelmy et al. 2005) continuously scans the whole sky at energies between 14 and 195 keVwith an extremely wide field of view and arcmin resolution. Whenever an object is detected, e.g., a gamma-ray burst or an AGN, the XRT immediately performs follow-up observations at $0.2 - 10$ keV, locating the source to a precision of ~ 2 arcsec. Therefore, for every detected object, data covering the whole X-ray range become available. In addition, all the BAT exposures can be combined and correlated, and by these means, it is possible to construct deeper and deeper maps of the whole sky as long as BAT keeps observing. Because of these characteristics *Swift*/BAT is optimal for AGN surveys, and first results have already been published after three months of BAT observations (Markwardt et al. 2005). Later on, after nine months of BAT observations Tueller et al. (2008) have assembled a catalog of local AGN that have been detected at $> 4.8\sigma$ with BAT and which could be identified with optical counterparts, i.e. the host galaxies. This sample of ~ 150 local AGN is flux-complete down to $\sim 2 \cdot 10^{-11}$erg cm^{-2}s^{-1} with all-sky coverage. In order to construct an uniform sample of AGN, Winter et al. (2009a) have excluded all objects that are lying behind or close to the galactic plane ($|b| < 15°$) or known to have beamed emission. The first criterion is used to prevent confusion of emission from AGN with galactic objects like supernova remnants, while the second criterion ensures that the observed emission is the intrinsic one and is not dominated by a jet orientated towards the observer. By these means, an uniform AGN sample of 104 local objects has been created with an average redshift of $\bar{z} = 0.03$. In the following, I refer to this sample simply as the “BAT AGN sample”. A complete list of the individual objects and their relevant properties is given in App. B in

Table B.5 with their host galaxy properties in Table B.1.

Interestingly, some of the BAT AGN show extreme obscuration properties. They might even form a new sub-class of AGN, as indicated by follow-up X-ray spectroscopy using the Suzaku satellite (Ueda et al. 2007). They possess abnormally low scattering fractions of soft X-rays, which is unexpected by the unification model. The easiest explanation would be an extremely thick torus structure with a narrow opening angle ($< 20°$). Winter et al. (2009a) have estimated that these 'buried AGN' might represent up to 20% of the whole AGN population. It will be important to examine whether the buried AGN are indeed a new class and how they affect the theories of AGN evolution in general, and the torus models in particular.

5.2. Goals

The BAT AGN are the first uniform sample of AGN that represents well obscured AGN and therefore, it is perfectly suited for testing the MIR–X-ray correlation. In addition, a HR MIR survey of these objects might lead to important conclusions for the whole AGN population. For this reason, we aimed at observing all the BAT AGN with ground-based MIR instruments mounted on 8-meter class telescopes in order (i) to probe the 12μ continuum emission at sub-arcsec resolution, (ii) to constrain the 10μ silicate feature and (iii) to constrain the PAH 11.3μ emission feature for estimation of star formation contamination. For this purpose, observations in at least three narrow-band filters, one centered on each of these features, are necessary. By these means, it will be possible to investigate intrinsic differences between the AGN types in the MIR.

5.3. MIR observations

5.3.1. New observations

All attempts to observe the part of the BAT AGN sample that is only visible from the northern hemisphere (either with Subaru/COMICS or Gemini/Michelle) have failed so far because no observing time was granted. On the other hand, we have been able to observe all BAT AGN accessible from the the southern hemisphere using VLT/VISIR on Cerro Paranal. Out of the 104 BAT AGN, 72 are observable from Paranal (DEC $< +25°$) and 31 objects had already been observed with VLT/VISIR in a sufficient set of filters. Six more had archival VISIR N-band imaging data available but not in all necessary filters, leaving 35 with no VISIR N-band photometry at all. Therefore, we have observed those 41 BAT AGN (with all filters, or the remaining ones) with VISIR between 2009 and 2010 in service mode (Progr. ID 084-B.0606). Owing to the different redshifts, different filters had to be chosen for the individual objects. For 3 objects (2MASX J06403799, 2MASX J09180027 and NGC 4074), the expected source brightness has been so low that observations had to be limited to one filter, with the maximal on-source exposure time of 1980 s. The required ambient conditions have been: an airmass ≤ 1.3, an optical seeing ≤ 0.8″, and a sky transparency of “clear”, which were fulfilled for most observations. However, some observations have been performed under worse than demanded weather conditions. This affects especially NGC 235A, Pictor A, ESO 548-G081, 2MASX J06403799 and 2MASX J03565655, all observed in the same night. The standards observed during this night show low sensitivities and a high FWHM. The standard chopping and nodding observing mode with a chop throw of 8″ on the small field of view (0.075″/pixel; 19.2″ × 19.2″) was been used. Similar to previous VISIR observations of local AGN, the diffuse host galaxy contribution in the *N*-band has been less than 10% at a distance of 8″ from the nucleus, and therefore negligible for this investigation. In addition, owing to the chop throw, the maximum size of the sub-images without overlap is restricted to the inner 4″ around the nucleus. For each science target, a photometric standard star has been observed before or after within 2 hours.

5.3.2. Data from the archive

Out of the BAT AGN, 31 have sufficient VISIR photometric data available from previous observations. Most of these observations have been presented in the literature (Horst et al. 2006, 2009; Gandhi et al. 2009; Hönig et al. 2010; Reunanen et al. 2010). In general, these AGN have been observed with similar settings, e.g., the small FOV and small chop throws, enabling the usage of all positive and negative beams. Only NGC 6240 has solely been imaged with the large FOV (0.127″/pixel; 32″ × 32″). Many objects have been observed in several filters that are spread over the whole *N*-band range, and some even have VISIR low-spectral resolution spectroscopy available, which is included in the later analysis.

Of the Northern BAT AGN (DEC > +25°), only few objects have HR MIR photometry available, and none in 3 settings covering the continuum, silicate and PAH features. Three of them (NGC 4051, NGC 4138 and NGC 4395) were observed in our LLAGN programme with Gemini/Michelle. In addition, Mrk 3 is the only other BAT AGN with Michelle data but no VISIR coverage.

In total, 77 of the 104 BAT AGN have HR MIR imaging data available.

5.4. Sample properties

5.4.1. Optical classification and morphologies

Roughly half of the 77 BAT AGN are classified in the optical as type 1 AGN, and the other half are treated as type 2 AGN, including those that do not have any optical AGN classification. This is motivated by thigh probability of heavy obscuration in those sources that would lead to the invisibility of their nuclear activity at lower energies. Similar to the LLAGN project, again I only distinguish between type 1 (1.0-1.5) and type 2 (1.8-2.0 and 1h, 1li) AGN and use the classifications from Véron-Cetty and Véron (2010) whenever available. For all other cases, the classification from Tueller et al. (2008) is used instead. One exception is NGC 4992, which is

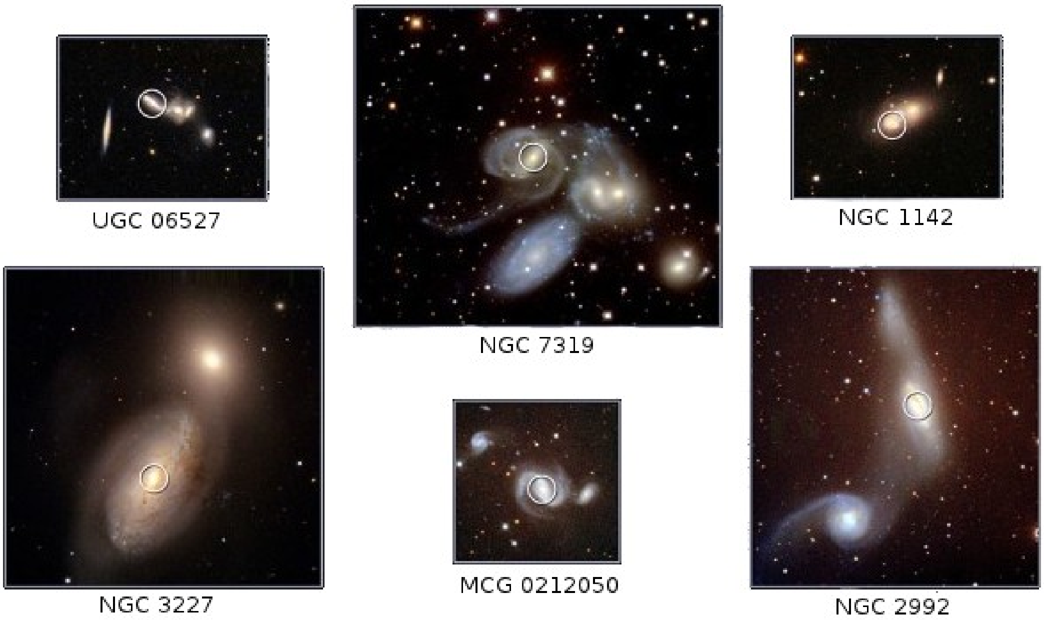

Figure 5.2: Optical images of the host galaxies of a selection of BAT AGN. The white circles mark the location of the hard X-ray source detected by *Swift*. Reproduced from NASA (`http://www.nasa.gov/mission_pages/swift/media/smoking-gun.html`). Credit: NASA, *Swift*, NOAO, M. Koss and R. Mushotzky.

treated as type 2 AGN (contrary to Véron-Cetty and Véron 2010) because of its very high N_H. The LINERs Pictor A and NGC 7213 are treated as type 1 AGN, while NGC 6240 is counted as type 2. Note that the classifications of NGC 235A, NGC 526A and Mrk 1018 in Winter et al. (2009a) and Véron-Cetty and Véron (2010) are not consistent. In addition, Véron-Cetty and Véron (2010) use different Seyfert classifications for 11 objects (not changing the type though) with respect to the ones adopted by Tueller et al. (2008). However, for NGC 235A, NGC 526A and Mrk 1018, the classifications do not agree and they have a different type in Véron-Cetty and Véron (2010).

Summarizing, the total sample corresponds to 41 Sy 1-1.5 and 48 Sy 1.8-2.0 and the individual classifications are listed in Table B.5.

Many of the BAT AGN reside in interacting or merging host galaxies, leading to disturbed morphologies and, in many cases, intense star formation (see Fig. 5.2 for some examples). In particular, NGC 6240 is an ultra-luminous infrared galaxy.

5.4.2. Distances

With respect to the LLAGN sample, many BAT AGN have significantly higher distances and therefore no redshift-independent distance measurements available. I have selected redshifts from the NED database for all objects except 2MASX J06403799, for which the redshift has been derived by using an EMMI spectrum, retrieved from the archive, and XSS J12389-1614, for which I have used the redshift given by Tueller et al. (2008). For the majority of BAT AGN, the luminosity distances given by NED are adopted. These are based on redshifts corrected for the Earth motion relative to the cosmic microwave background reference frame with $H_0 = 73, \Omega_\mathrm{m} = 0.27$, and $\Omega_\mathrm{vac} = 0.7$. However, for 11 nearby objects, I use redshift-independent measurements for the same reason as for the LLAGN sample: NGC 931 (Tully et al. 2009); NGC 3516 (Tully 1988); NGC 4151 (Mundell et al. 2003); NGC 4388 (Russell 2002); NGC 7314, NGC 7582 (Springob et al. 2009); and ESO 005-G004, NGC 4051, NGC 4138, NGC 4395, and Cen A (see Sect. 4.2.2).

5.5. MIR imaging

All but 2 of the 77 BAT have been detected in at least one of the N-band filters and show a point-like MIR source at a position consistent with the AGN coordinates from other observations (mainly 2MASS). Only NGC 612 and PGC 13946 remain undetected in all filters. For some objects, data from additional filter settings are available in the archives and are included, enabling a more detailed reconstruction of the N-band SED (Sect. 5.6). The observational details and measured fluxes are listed in Table B.2. Many objects have been detected only at a low S/N, leading to large ($\lesssim 70\%$) uncertainties in the flux measurements. Nine objects have been detected only at $\lesssim 5\sigma_\mathrm{BG}$ (NGC 235A, ESO 297-G018, Mrk 1018, ESO 416-G002, NGC 1142, 3C 105, 2MASX J03565655, ESO 121-G028 and 2MASX J06403799). In particular, for some of the lowest-S/N detections (ESO 297-G018 in all filters, NGC 1142 in SIV, 2MASX J03565655 in SIVref2 and NEIIref1, 3C 105 in NEIIref1, and MCG -01-13-025 in NEIIref1), it has been necessary to smooth the VISIR images prior to the fitting process.

The combined, co-added VISIR and Michelle images of the central 3″ around the nuclei of the BAT galaxies are presented in Fig. 5.3 and Fig. B.1. The scaling is linear in units of σ_BG, and the median of the background is subtracted. For the objects detected at the highest S/N and under good ambient conditions, the first Airy rings are visible (e.g., NGC 2110, NGC 3281, NGC 3783, NGC 4507, and NGC 4593). The MIR images show a wide range of S/N, some BAT AGN are detected barely above $3\sigma_\mathrm{BG}$ and others at more than $100\sigma_\mathrm{BG}$. Similar to the LLAGN MIR imaging, most point sources detected in the galactic nuclei have a FWHM that is slightly larger than the corresponding one of the standard stars. The highest FWHM ratios are exhibited by objects detected at the lowest S/N. Therefore, a detailed investigation of the FWHM stability during the observation of these faint targets is impossible: the point source is not visible in the individual raw images but only in the combined image. The short-term variability of the MIR seeing is also demonstrated by some observations that show the opposite effect: the FWHM of the standard stars is larger than the one of the science target (e.g., NGC 526A, NGC 985, ESO 198-G024, Ark 120, EXO 055620, and Mrk 509).

In addition to the larger FWHM, 4 objects show slightly elongated beam shapes (MCG -03-34-064, IC 4329A, IC 5063, and MR 2251-178) similar to Horst et al. (2009), who attribute this elongation to instrumental effects. However, see also the discussion in Hönig et al. (2010), who attribute the elongation in MCG -03-34-064 and IC 5063 to extended MIR emission from dust in the NLR. As for the FWHM, the true cause remains unclear.

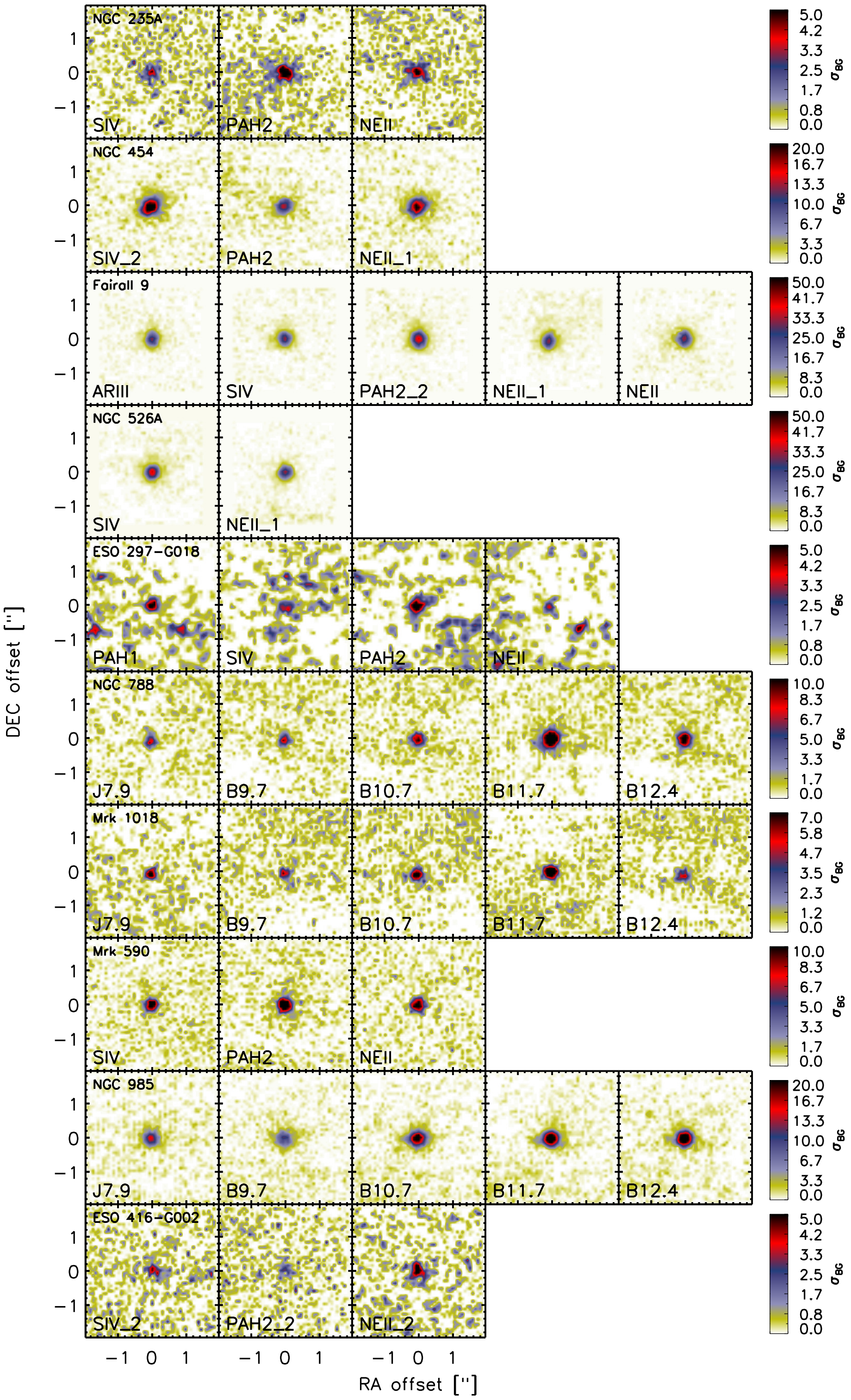

Figure 5.3: VISIR images of the first 10 BAT AGN in different filters. Each row shows one object sorted by right ascension. White corresponds to the mean background value (⟨BG⟩) The remaining BAT AGN are displayed in Appendix B in Fig. B.1.

We clearly detect extended emission around the nuclear point source in NGC 6240, and possibly in NGC 1365, NGC 4388, and NGC 6814. However, for most objects, the low S/N and the blending with the possibly existing first Airy ring prevent clear detections of resolved nuclear MIR emission. In addition, off-nuclear emission is also detected in NGC 6240 (the second nucleus) and in NGC 7469 (as already found by Horst et al. 2009).

In summary, the nuclear MIR emission in the large majority of BAT AGN is unresolved, and no off-nuclear sources are evident in the surrounding 4″-region.

5.6. Average MIR spectral energy distributions

The *N*-band multi-filter photometry of the BAT AGN can be used to assemble rough MIR SEDs for the first time at 0.4″-resolution. By these means, it is possible to verify whether spectral features such as the silicate (at $\sim 10\,\mu$m) and the PAH (at $11.3\,\mu$m) belong to the AGN emission itself, or originate at $> 0.4''$-scale around the nucleus. The individual SEDs are displayed in Fig. 5.4 as thin lines for all objects that have been observed in multiple filters. The SEDs are in general rising in flux density towards longer wavelengths. However, there is large scatter between the SED shapes of individual objects, even if they have the same AGN type.

I compute the average *N*-band SED shapes for type 1 and type 2 AGN by binning the photometric measurements and using their mean and standard deviation. As expected from the large scatter, the differences between the individual objects belonging to either type are dominating and the standard deviations of the average SEDs overlap in all bins. However, the type 1 AGN possess slightly higher fluxes around $10\,\mu$m than the type 2, which is consistent with the silicate feature being in emission in type 1 and in absorption in type 2. This exactly matches the prediction of the unification scheme: in type 1 AGN, the torus is orientated roughly face-on with respect to the observer, and the directly illuminated hot dust is visible, leading to the silicate being observed in emission. On the other hand, in type 2 AGN, the torus is orientated rather edge-on, and view onto the hottest dust is obscured, leading to silicate being in absorption. Therefore, it is very plausible that, despite the large scatter, both average SEDs are indeed different. Furthermore, a possible reason for the large scatter in the type 1 and 2 SEDs is that some objects are "miss-classified" in the optical due to extinction by dust outside the torus, or that the optical classification does not correlate with the intrinsic MIR properties of the AGNs. This is illustrated by NGC 2110, being an Sy 2 but showing the strongest silicate emission in the whole sample (topmost red thin line in Fig. 5.4), as has already been noted in Hönig et al. (2010).

5.6.1. Comparison with torus models

The average *N*-band SED shapes can be combined with available average VISIR *N*-band spectra (Fig. 5.5). The spectra have been computed by taking the data from Hönig et al. (2010) (with NGC 2110 and NGC 4593 being excluded because of incomplete *N*-band coverage).

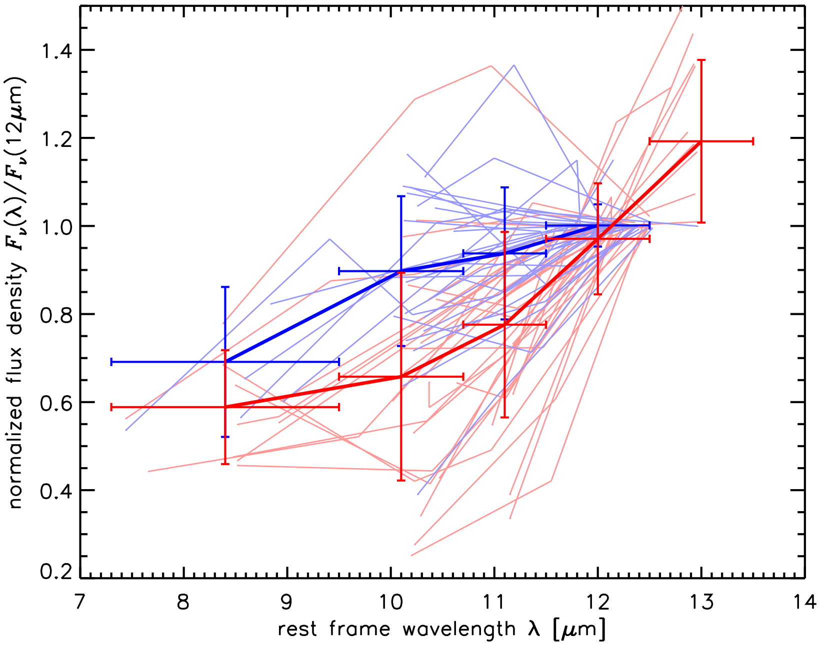

Figure 5.4: Average N-band SED shape (thick lines) for type 1 (blue) and type 2 BAT AGN (red). The individual N-band photometry is displayed as thin light-colored lines and has been normalized by the individual 12 μm continuum flux.

The photometry and spectra reasonable agree, the photometry being only higher in the shortest wavelength bin. The differences are presumably caused by the much smaller number of individual objects used for computing the average spectra (8 compared to 35).

Now, we can compare both the photometric and spectroscopic average SEDs with models for clumpy dust tori in order to probe whether the observed nuclear MIR SED can be explained with emission from such a torus. I use the models from Hönig et al. (2006) with typical parameters (average number of clouds in the equatorial line of sight: $N_0 = 7.5$; total number of clouds: $N_{\text{tot}} = 18010$; outer radius in units of the sublimation radius: $r_{\text{out}} = 300$; power-law index of the cloud density distribution: $\alpha = -1$; and the opening angle in degrees: $\Theta_0 = 45$) for two different orientation angles. For type 1 AGN, an inclination angle of 45° is used while it is 90° for type 2 AGN. Further description and comparison of these torus models with observational data can be found in Hönig and Kishimoto (2010). The model SEDs agree well with the photometry and the average spectra, at least in the 10 to 12 μm range. At shorter wavelengths, the torus models predict higher fluxes than the spectra and the type 2 photometry, which particularly affects again the shortest wavelength bin. However, note that at those wavelengths, only the archival VISIR photometry has been available and thus the coverage is much smaller here than at longer wavelengths. In addition, the model parameters have not been varied to better fit the data. Therefore, I conclude that, in general, the HR photometry is consistent with the torus model SEDs and reproduces the expected orientation-dependent difference of the AGN types. This indicates (although not proofs) that the MIR emission of

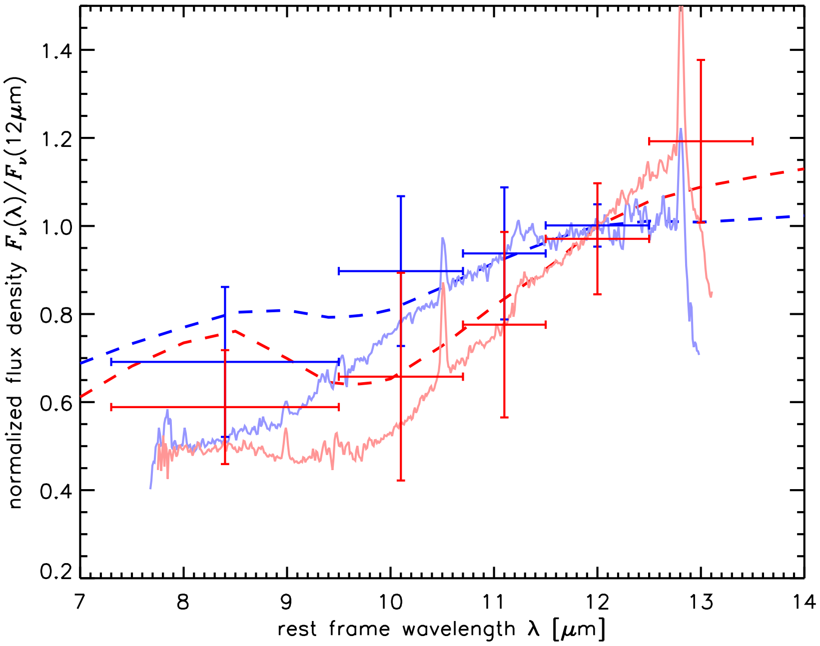

Figure 5.5: Comparison of the average N-band SED shapes for type 1 (blue) and type 2 BAT AGN (red) with average VISIR spectra and torus models. The average N-band photometry is similar to Fig. 5.4 and displayed as symbols with error bars. The average VISIR N-band spectra are displayed as light-colored lines and the torus model SEDs as dashed lines. Every SED has been normalized to its 12 μm flux.

most of the BAT AGN is indeed dominated by a clumpy torus at 0.4″-scale.

5.7. Comparison to *Spitzer*/IRS

Similar to the LLAGN, the HR photometry of the BAT AGN is also compared with the corresponding *Spitzer*/IRS spectra. For 7 out of 77 BAT AGN, no *Spitzer*/IRS spectra covering the N-band are available. All IRS spectra used are post-BCD products taken from the *Spitzer* archive, and have been performed in the low-resolution staring mode with background subtraction. Only 7 objects (NGC 1142, 3C 105, ESO 362-G018, MCG -06-30-015, NGC 6860, MR 2251-178, and NGC 7582) have been observed in mapping mode, in which cases the spectrum with the slit centered on the nucleus has always been used. Many of the IRS spectra of BAT AGN have been analyzed in Weaver et al. (2010), but only the ion emission line properties are presented. Hence, no direct comparison of the N-band continuum and PAH emission properties is possible.

The data are displayed in Fig. 5.6 and Fig. B.2. I also plot VISIR spectra from Hönig et al. (2010) as blue lines for all sources in common . A detailed comparison of the IRS and VISIR spectra is presented in that work and therefore not repeated here. The main difference between the IRS and VISIR spectra is that the latter exhibit lower flux levels in many cases, and, in particular, the PAH features are much weaker or even absent. On the other hand, the VISIR spectra show very good agreement with the HR photometry.

To compare the HR photometric fluxes, $F_\nu^{\mathrm{HR}}(11\,\mu\mathrm{m})$ and $F_\nu^{\mathrm{HR}}(12\,\mu\mathrm{m})$ respectively, with the *Spitzer*/IRS spectra, synthetic photometric fluxes are computed by convolving the IRS spectra with the corresponding VISIR filter transmission curves, yielding $F_\nu^{\mathrm{IRS}}(11\,\mu\mathrm{m})$ and $F_\nu^{\mathrm{IRS}}(12\,\mu\mathrm{m})$ similar to Sect. 4.5. The comparison is quantitatively displayed in Fig. 5.7 and Table B.3 for the filters measuring the PAH 11.3 μm feature and the 12 μm continuum (where available). Note that for three objects (NGC 788, Mrk 1018 and NGC 985), the corresponding filter transmission curves are not available and therefore these objects are not included. Displayed are the ratios $R(\mathrm{PAH}) = F_\nu^{\mathrm{HR}}/F_\nu^{\mathrm{IRS}}(11\,\mu\mathrm{m})$ and $R(\mathrm{cont}) = F_\nu^{\mathrm{HR}}/F_\nu^{\mathrm{IRS}}(12\,\mu\mathrm{m})$: Out of 70 BAT AGN, 31 exhibit lower continuum fluxes in HR than in IRS ($\log R(\mathrm{cont}) < 0$), i.e. are left of the vertical dashed line. The most extreme cases are ESO 297-G018, NGC 1142, NGC 1365, 3C 105, ESO 005-G004, NGC 5728, NGC 6240, and NGC 7582 with more than a factor of 2 lower fluxes. In additional 6 cases (Mrk 590, ESO 362-G018, NGC 2110, NGC 3227, NGC 4388, and NGC 4507), the continuum shape agrees between both instruments, but the PAH emission is much weaker or absent in the HR photometry (objects close to the vertical dashed line, but below the diagonal). On the other hand, for 5 AGN (NGC 454, MCG -01-24-012, NGC 3281, NGC 5252 and Mrk 926), the VISIR fluxes are higher compared to those of the IRS spectrum. The reason for this seems to be improper centering of the IRS slit on the nuclei of these galaxies as evident from the slit position images in the *Spitzer* archive. In the remaining 28 cases, the HR photometry and IRS spectra have consistent flux levels within the uncertainties. For most objects, the flux at 11 μm scales with to the continuum and they lie along the diagonal solid line, i.e. the SED shape is similar. However, some AGN possess relatively weaker PAH emission at HR and therefore are below the diagonal. Finally, a couple objects have blue SED slopes in VISIR, non-compatible with the red slope in their IRS spectra (lying above the diagonal). Of those, ESO 297-G018 and MR 2251-178 are the most extreme cases.

In summary, the MIR SED properties in $\sim 50\%$ of the BAT AGN are significantly different on 0.4″-scale (probed by VISIR and Michelle) than on 4″-scale (probed by *Spitzer*/IRS. It is interesting to note that, in general, the type 2 AGN show the largest differences between HR and IRS (Fig. 5.7).

5.7.1. Constraining the nuclear star-formation contamination

The previous section has indicated that also many BAT AGN have non-nuclear MIR emission on 4″-scale that is not visible in the HR photometry but significantly affects the IRS spectra. Therefore, it is possible that the HR photometry is also contaminated by non-nuclear emission on 0.4″-scale. However, in Sect. 4.5.1 I have already shown that the HR photometry of the majority of LLAGN is not significantly affected by star formation. In brighter AGN, as the BAT AGN are, the intrinsic scale of the AGN is relatively larger, and the AGN itself is comparably brighter than in the low-luminosity regime. Thus, I do not expect significant SF contribution to the HR MIR emission in the BAT sample either. On the other hand, many BAT

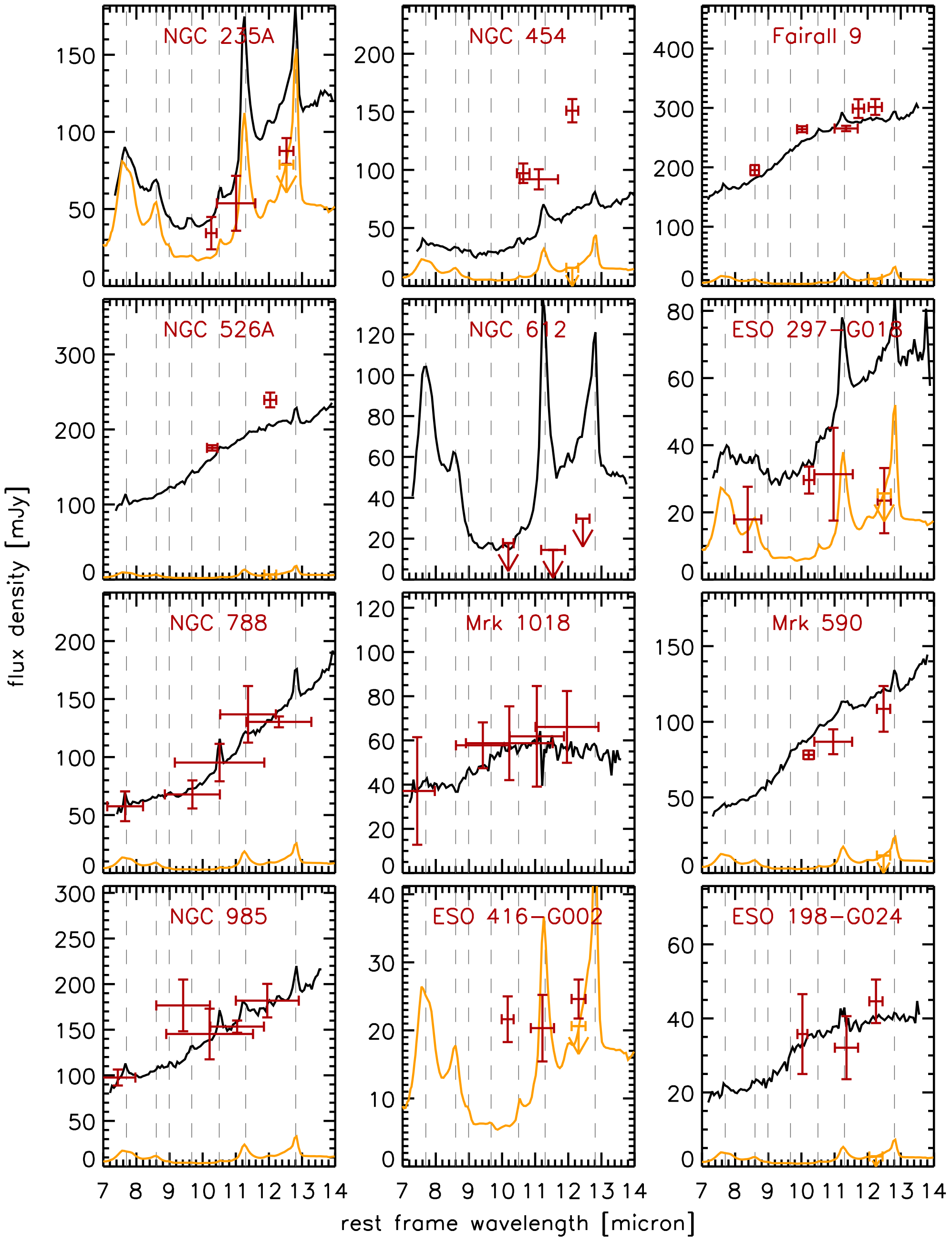

Figure 5.6: Comparison of HR photometry (red symbols) and *Spitzer* IRS spectra (black line) and VISIR spectra where available (blue line) for the first 24 BAT AGN. The remaining sources are displayed in Fig. B.2. Displaying errors in the spectra was omitted to maintain clarity. They are of the order of 10% for both IRS and VISIR. Horizontal error bars correspond to the filter pass band. Commonly occurring emission lines are indicated by the dotted lines. In addition, the scaled starburst template SED (displayed as orange line) are shown as well as the derived upper limit for the starburst contribution to the continuum filter measurement (orange symbols), see Sect. 5.7.1 for details.

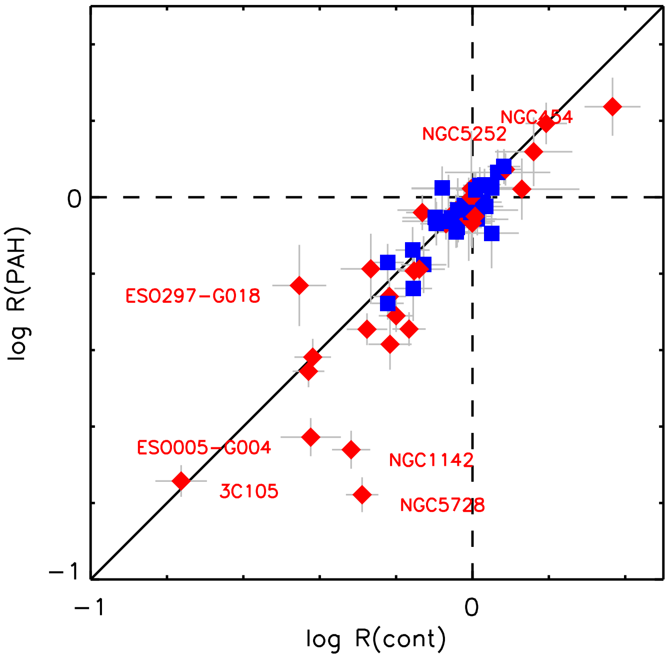

Figure 5.7: Comparison of the continuum ratio R(cont) and the PAH ratio R(PAH) for type 1 (blue) and type 2 BAT AGN (red) in logarithmic space. The solid black line marks the one to one correspondence line while the dashed lines mark ratios with a value of 1. See text for further explanation.

AGN are residing in interacting host galaxies ,which show a lot of stellar activity, sometimes also in the MIR. Hence, I apply the same method of fitting the 11.3 μm PAH emission feature as in Sect. 4.5.1 in order to constrain the maximum SF contribution.

The PAH emission is absent in the IRS spectra of 12 BAT AGN (XSS J05054, EXO 055620, 3C 105, Mrk 3, ESO 121-G028, MR 2251-178, Mrk 1018, NGC 4992, Pictor A, NGC 3281, ESO 103-G035, IC 5063). Furthermore, the VISIR spectra of 4 additional objects (NGC 3783, NGC 4507, IC 4329A, NGC 7213) do not show PAH emission (although present in their IRS spectra). For the other objects with VISIR spectra (NGC 3227, NGC 7469 and NGC 7582), the PAH emission feature is present but much weaker. In those cases, the VISIR spectra are used for the SF contamination estimate instead of the IRS data. According to the present assumption, therefore no significant star formation is happening in the nuclei of these galaxies (in Table B.3). Therefore, 57 BAT AGN are remaining with either multiple HR filters and/or IRS spectra. For those, the 11.3 μm PAH emission feature flux, F(PAH11.3μm), is measured (Table B.3), and the correspondingly scaled SF template spectra are displayed in Fig. 5.6 (and Fig. B.2) as orange lines, with the maximum contribution of SF to the 12 μm continuum indicated by orange upper limits. These maximum SF contributions, $c_{<}^{\mathrm{SF}}$, are listed as well in Table B.3 for all objects with visible PAH emission or multiple HR filter measurements. For 9 objects, those HR photometric settings, that include the PAH feature in their filter bandpass, further constrain the PAH emission (NGC 235A, NGC 1142, NGC 1365, ESO 005-G004, NGC 2992, CGC 041-020, NGC 5728, NGC 6240, UGC 11871). I apply the same method as

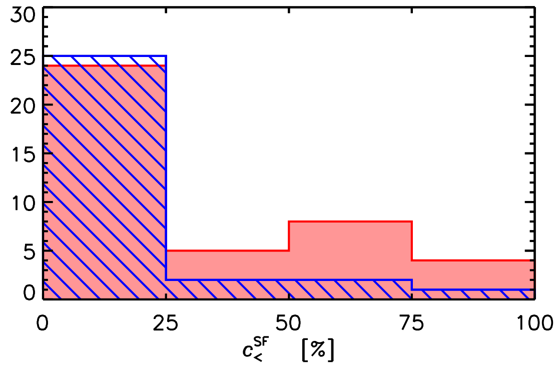

Figure 5.8: Distribution of the maximum possible star formation contribution to the 12 μm continuum for type 1 (blue) and type 2 BAT AGN (red).

well to the 5 objects with solely HR photometry (and no IRS spectra) but with a filter that includes the PAH feature (ESO 416-G002, 2MASX J03565655, 1H 0419-577, 1RXS J112716, and XSS J12389-1614). The resulting $c_{<}^{SF}$ for those objects are very high ($\gtrsim$ 75%). However, in all 5 cases, a third filter measuring the 10 μm range shows fluxes very similar to the one measuring the PAH feature. Therefore, the PAH feature, if present at all, is probably much weaker than assumed for the SF contribution estimation, and consequently the $c_{<}^{SF}$ is severely overestimated. The total distribution of the SF contribution is displayed in Fig. 5.8, separated for type 1 and 2 BAT AGN. Both AGN type show roughly the same distribution, although $c_{<}^{SF}$ is on average higher in type 2 AGN. For all BAT AGN combined, in general, $c_{<}^{SF}$ is $\leq$ 25% in $\sim$ 67% (49 of 73) for objects detected in more than one HR filter, and $\leq$ 50% in $\sim$ 79% (58 of 73). If one ignores the 5 objects without any spectra, there are only 2 objects with a possible SF contribution of $\geq$ 75%.

Therefore, we can conclude that SF does not significantly affect the HR photometry of the BAT AGN sample, in agreement with the LLAGN sample. Finally, no difference with the optical classification is evident, which is a very noticeable result because type 2 are generally hosted in more actively star forming galaxies. Thus, this indicates that the HR photometry is not biased against host properties, but indeed isolates well the AGN emission.

5.8. The 12 μm continuum

For the further analysis, I just concentrate on the 12 μm continuum only, which has to be extracted from the HR photometry. Most objects have been observed in a suitable narrow-band filter to directly measure the 12 μm emission, and no additional correction is necessary for those. However, a few objects have not been observed in a suitable filter for different reasons. 2MASX J09180027 could only be measured at a restframe wavelength of $\lambda_{\mathrm{rest}} = 10.3\,\mu$m because of its relatively high redshift. Hence, I apply a correction factor to this measurement by using the average slope of Sy 2 galaxies determined from the other objects ($\approx$ 1.48).

NGC 3081, NGC 4388 and ESO 103-G035 have only been observed in PAH2 ($\lambda_{\rm rest} \approx 11.1\,\mu$m) and NeIIref2 ($\lambda_{\rm rest} \approx 12.9\,\mu$m), and thus, the 12 μm continuum is extracted by interpolating these two filter measurements. Finally, NGC 7314 has only been measured in the SIV ($\lambda_{\rm rest} = 10.4\,\mu$m) and PAH2 ($\lambda_{\rm rest} = 11.2\,\mu$m) filters. On the other hand, the HR photometry agrees very well with the IRS spectrum and hence, I perform synthetic photometry, using the NeIIref1 filter ($\lambda_{\rm rest} = 12.2\,\mu$m), for determination of the 12 μm continuum.

In addition to the HR photometry, I combine the data set with lower angular resolution photometry in order to reach a larger coverage for the whole BAT AGN sample. Gorjian et al. (2004) have observed a large number of local Seyfert galaxies on the northern hemisphere with Palomar/MIRLIN in a broad N-band filter ($\lambda_{\rm c} = 10.6 \pm 2.83\,\mu$m). As the angular resolution of $0.5''$ is only slightly worse than the one from our HR photometry, we can use their photometry for those BAT AGN without HR coverage. These are 4 additional objects (Mrk 348, NGC 931, Mrk 79, and NGC 4253). However, their fluxes have to be corrected for the broad-band filter, which is done by computing a correction factor (of 1.33 ± 0.44) from the 10 overlapping sources with both HR and MIRLIN photometry. In addition, the standard deviation of this correction factor is added to the total flux error. No other work in the literature provides MIR photometry of comparable angular resolution on any additional BAT AGN. Only low angular resolution MIR photometry can be found for a few more BAT AGN and is included as upper limits for objects with no other MIR photometric coverage. For example, Siebenmorgen et al. (2004) have used ISOCAM on board of the *ISO* space observatory for 12 μm photometric observations of a number of objects from the revised third Cambridge catalogue of radio sources (3CR). ISOCAM provides an angular resolution of $\sim 6''$ and a relatively broad filter. These data provide upper limits for 2 more BAT AGN (3C 390.3 and 3C 452). In addition, Rieke (1978) have observed 53 local Seyferts with the 61 inch and 90 inch telescopes of the University of Arizona with angular resolutions of $5.7''$ and $3.9''$ respectively. These measurements were also performed using a broad-band filter ($\lambda_{\rm c} = 10.6 \pm 2.83\,\mu$m), and provide upper limits for 5 additional BAT AGN (Mrk 352, Mrk 6, NGC 3516, Mrk 279, and Mrk 290). Finally, N-band photometry for 3C 382 is presented in Heckman et al. (1983), obtained also with the 61 inch telescope and the broad-band N filter. Again, I apply the correction factor for the different bandpass to these measurements.

By including the MIRLIN photometry and the upper limits from lower-angular resolution data, the 12 μm continuum coverage is increased to 89 out of 104 BAT AGN. These data can now be used to perform further multiwavelength analysis, in particular the MIR–X-ray correlation in the next chapter.

6. The MIR–X-ray correlation

In the two previous chapters, we have dealt with the MIR observational programmes of a large number of local AGN of all types, and I have presented their MIR properties at HR. It has been demonstrated that this HR MIR emission is dominated by the AGN and might mainly be produced by the dusty torus structure. Now these data are used for comparison with the hard X-ray properties of these AGN samples. This X-ray emission is an important intrinsic tracer of the accretion processes in AGN (see Sect. 2.4). As already mentioned in Sect. 1.4, a strong correlation between the MIR and X-ray emission has already been found previously. This correlation is very useful, e.g., it can enable to assess the bolometric IR luminosity of AGN when no high-resolution IR data are available (e.g. Mullaney et al. 2011). One major goal of this work is to test and verify the existence and properties of this correlation for more complete AGN samples, which is presented now.

I construct HR monochromatic 12 μm luminosities, $\lambda L_\lambda(12\,\mu\mathrm{m})$, from the flux densities determined in Chapter 4 and Chapter 5 and the corresponding object distances given in the Sections 4.2.2 and 5.4. The resulting $\lambda L_\lambda(12\,\mu\mathrm{m})$ are listed in Table A.4 for the individual LLAGN and in Table B.5 for the individual BAT AGN. I account for the different filter central wavelengths and finite bandpasses by assuming a flat MIR SED around 12 μm (in λL_λ) without any K-correction. Owing to the low redshifts of the samples, the latter effect is negligible.

6.1. X-ray properties of the LLAGN

First, I select X-ray luminosities in the 2-10 keV energy band for the LLAGN sample of Chapter 4 from the literature and correct them for the distances adopted in each case. In the selection process, I have preferred the most recent observations with X-ray telescopes that had a high angular resolution, a large effective area, broad band energy coverage or the best combination of these. In many cases, there are several measurements available that fulfill these criteria. For these objects, I use the average of the published values after correcting for the different distances used. The detailed selection process for the individual LLAGN is reported in Appendix C. It is important to note that extinction can be very high in the 2-10 keV band, and therefore only absorption-corrected luminosities $L_{2-10\mathrm{keV}}$ are used. However, the true amount of absorption measured in N_H is basically always unknown, and hence the observational X-ray data has to be modeled in order to determine N_H and the corresponding $L_{2-10\mathrm{keV}}$. A detailed description of these X-ray spectral models is beyond the scope of this work but can be found in, e.g., Turner and Miller (2009). Often different models fit the observational data equally well while having completely different physical consequences. This mostly affects highly obscured and Compton-thick ($N_{\mathrm{H}} > 1.5 \cdot 10^{24}\,\mathrm{cm}^{-2}$) objects, and a number of LLAGN turned out to be such CT candidates. Their X-ray spectra are often dominated by scattered or extended emission and consequently appear to be unabsorbed with a much lower luminosity than predicted by CT obscuration. Depending on the model assumed, this leads to intrinsic 2-10 keV luminosity estimates differing by several orders of magnitude (e.g., for NGC 7743).

To identify the "true" nature of the Compton-thick candidates, it is useful to compare the estimated X-ray luminosity to other intrinsic indicators, such as luminosities of the forbidden emission lines [OIII] $\lambda 5007\,\text{Å}$ and [OIV] $\lambda 25.89\,\mu$m. In Panessa et al. (2006), a correlation between the 2-10 keV and [OIII] luminosities has been found, which can be used to predict the intrinsic X-ray luminosity for the Compton-thick candidates. There is also evidence for significant absorption of [OIII] in the narrow-line region (NLR; Haas et al. 2005). But the [OIV] is almost unabsorbed, which makes it a powerful tool (Meléndez et al. 2008). Diamond-Stanic et al. (2009) present an extended sample of local Seyferts with measured [OIV] and observed X-ray fluxes, whose luminosities correlate well for the 27 unabsorbed sources (Spearman rank $\rho = 0.84$ with $\log p = -7.3$). A bisector fit to these objects yields

$$\log\left(\frac{L_{2-10\,\mathrm{keV}}}{\mathrm{erg\,s^{-1}}}\right) = -0.44 \pm 3.46 + (1.06 \pm 0.09)\left(\frac{L_{\mathrm{[OIV]}}}{\mathrm{erg\,s^{-1}}}\right). \tag{6.1}$$

Both luminosity correlations, X-ray–[OIII] and X-ray–[OIV], are used to predict the intrinsic X-ray luminosity of the CT candidates and, thus, to distinguish between the Compton-thin or -thick scenario.

In addition, it is well known that AGN can show huge X-ray flux variations, either intrinsic or caused by a change of obscuration/absorption in the innermost region (e.g. Murphy et al. 2007; Risaliti et al. 2007). To account for this, I have assumed an error of factor 2 (0.3 dex) in all cases where variation is evident or only one high-spatial resolution X-ray observation is available, while I have applied 0.6 dex for CT candidates. In particular, it is important to note that X-ray luminosities of the following objects have been significantly revised since the sample was initially selected: for NGC 5813 only *ROSAT* data were available, inferring a much higher X-ray luminosity ($\log L_{2-10\mathrm{keV}} = 42.1$, Schwope et al. (2000)) than has been found later by *Chandra* ($\log L_{2-10\mathrm{keV}} = 38.77$). Similarly, for NGC 7590 the *ASCA* data yielded $\log L_{2-10\mathrm{keV}} = 40.78$ (Bassani et al. 1999) and later *XMM-Newton* $\log L_{2-10\mathrm{keV}} = 39.70$ (Shu et al. 2010a). This has led to a severe overestimation of the MIR flux density and, thus, an underestimation of the VISIR exposure times for these objects.

The intrinsic X-ray luminosities $L_{2-10\mathrm{keV}}$ with corresponding column densities N_{H} are listed in Table A.4 for the distance set D_{best}.

6.2. X-ray properties of the BAT AGN

As for the LLAGN, I concentrate on the 2-10 keV range first and only refer to the hardest X-rays (14-195 keV) again in Sect. 6.7. The X-ray properties of the BAT AGN, in particular in the 2-10 keV range, have been studied by Winter et al. (2009a) with uniform methods and non-complex models by using data from various X-ray satellites. On the one hand, new X-ray observations with modern satellites have become available since then, and on the other hand, owing to their high obscuration or strong variability, many BAT AGN benefit from a more detailed and complex modeling. Therefore, I have collected additional 2-10 keV measurements from the recent literature and used averages of several published absorption-corrected 2-10 keV luminosities when applicable. A comparison of both set of X-ray luminosities, $L_{2-10\mathrm{keV}}$(Winter) and $L_{2-10\mathrm{keV}}$(altern.) is listed for individual objects in Table B.4. Indeed some objects have 2-10 keV luminosities differing by orders of magnitude in both sets. Thus, we have to investigate whether these differences affect the MIR–X-ray correlation in Sect. 6.3.

6.3. 12 μm–2-10 keV correlation for the BAT AGN

Although the LLAGN programme has chronologically been planned and executed before the BAT AGN programme, I concentrate on the latter first in order to calibrate the MIR–X-ray correlation with this uniform AGN sample, before comparing the LLAGN to it in the next section.

The MIR–X-ray correlation strength is measured by using the Spearman rank correlation coefficient, ρ, and the corresponding null-hypothesis probability, p (`r_correlate` in IDL). To quantify the correlation, linear regression in logarithmic space is performed. Because of a variety of systematic uncertainties (see discussion in G09) and a significant number of upper limits, it is useful to compare different fitting methods. Here, the Bayesian based `linmix_err` (Kelly 2007) and the canonical `fitexy` (Press et al. 1992) are used. Both algorithms include treatment of errors on both axes. In addition, `linmix_err` can handle upper limits and intrinsic scatter as well, which makes it the superior algorithm for this investigation. It uses a Markov-chain Monte-Carlo method to draw random parameter sets from the probability distributions given by the measured data. The maxima of the resulting distributions of parameter draws represent the best-fit values (details and comparison tests can be found in Kelly 2007). Here, typically 10^5 of these random draws are used. As the posterior distributions are approximately Gaussians in all examined cases, I use the median and standard deviation of each returned quantity for its estimate and uncertainty. Apart from an estimate of the intrinsic scatter σ_{int}, `linmix_err` also returns a linear correlation strength, comparable to the Spearman rank. On the other hand, the Spearman rank and the `fitexy` are also stated to facilitate a comparison with previous work. Note that the X-ray luminosity is always treated as the independent variable. This is physically motivated, because the X-ray emission originates in the innermost region around the black hole and directly traces the accretion, while the MIR radiation is presumably emitted in UV heated dust farther out.

First, I compare the two X-ray luminosity sets for the BAT AGN in Fig.6.1 with objects in extreme positions being marked. For example NGC 4051, NGC 6814, and MCG -03-34-064 show very different positions in both plots, which demonstrates the difference between the $L_{2-10\mathrm{keV}}$(Winter) and $L_{2-10\mathrm{keV}}$(altern.) data sets. NGC 4138 and NGC 4395 are the two lowest luminosity objects in the BAT AGN sample with the latter being more than one order of

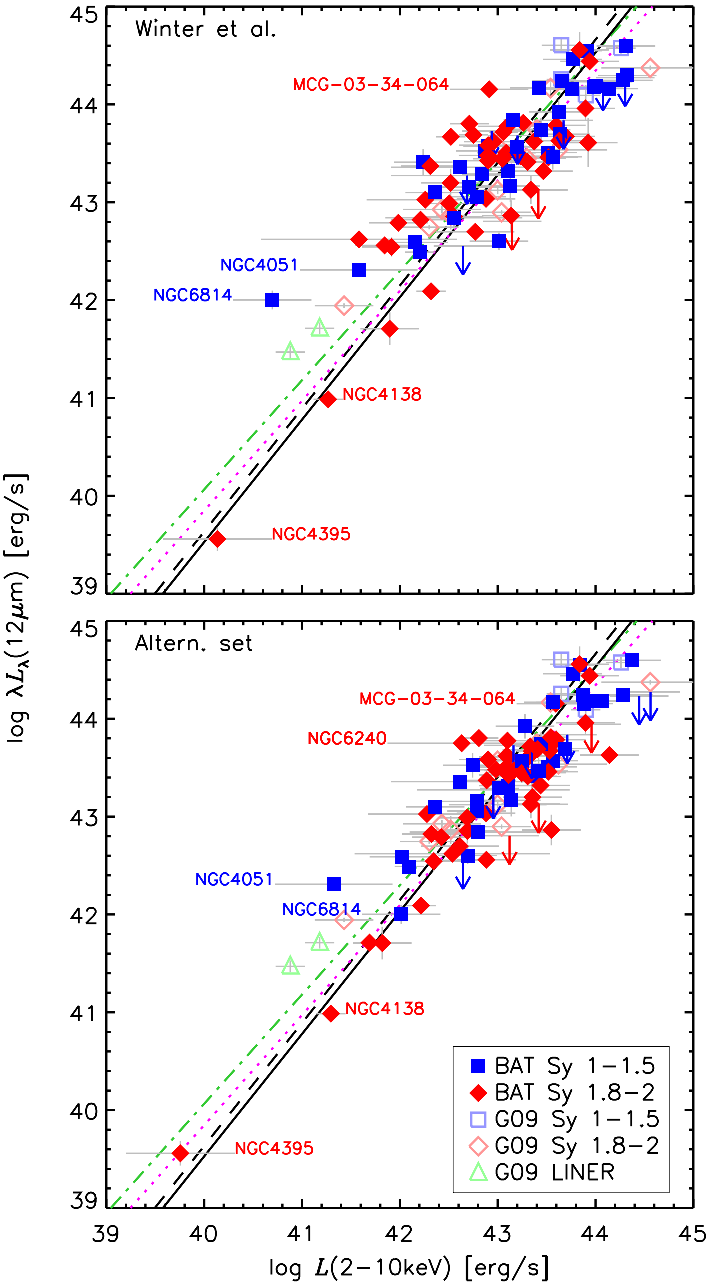

Figure 6.1: Nuclear MIR luminosities vs. absorption-corrected hard X-ray luminosities for BAT AGN (filled symbols) using the $L_{2-10\mathrm{keV}}$(Winter) (top) and the alternative set $L_{2-10\mathrm{keV}}$(altern.) (bottom), and the non-BAT AGN from G09 (empty symbols); blue squares: type 1 Seyferts (type 1.5 or lower), red diamonds: type 2 Seyferts, green triangle: LINERs; solid line: `fitexy` fit to BAT AGN with $L_{2-10\mathrm{keV}}$(altern.); dashed line: `fitexy` fit to BAT AGN with $L_{2-10\mathrm{keV}}$ from Winter et al.; green dot-dashed line: `fitexy` fit from G09; magenta dotted lines: `linmix_err` fit to BAT AGN with $L_{2-10\mathrm{keV}}$(altern.).

magnitude fainter than the rest. For both sets, a strong correlation is present between $L_{2-10\mathrm{keV}}$ and $\lambda L_{\lambda}(12\,\mu\mathrm{m})$, however, the correlation strength is marginally higher for the alternative set ($\rho = 0.84, \log p = -22$) than for the luminosity set from Winter et al. (2009a) ($\rho = 0.83, \log p = -21$). This is also clearly visible in the decreased scatter, $\sigma_{\mathrm{X}}^{\mathrm{M}}$, of the logarithmic luminosity ratio, $R_{\mathrm{X}}^{\mathrm{M}} = \log \lambda L_{\lambda}(12\,\mu\mathrm{m}) - \log L_{2-10\mathrm{keV}}$: $\sigma_{\mathrm{X}}^{\mathrm{M}}$(Winter)= 0.42 and $\sigma_{\mathrm{X}}^{\mathrm{M}}$(altern.)= 0.35. Similarly to G09, `fitexy` has been used for fitting the data and gives very similar results for both $L_{2-10\mathrm{keV}}$ sets. The slope for the alternative set is marginally flatter ($a = 1.25 \pm 0.06$ compared to $a = 1.26 \pm 0.05$). Surprisingly, both are significantly steeper than the fit from G09 ($a = 1.11 \pm 0.04$), which is further examined below. All fit and correlation parameters for the various AGN samples are listed in Table 6.1. Because of the higher correlation strength ρ and the lower scatter $\sigma_{\mathrm{X}}^{\mathrm{M}}$, I concentrate in the following analysis on the alternative luminosity set and discard $L_{2-10\mathrm{keV}}$(Winter).

However, also for $L_{2-10\mathrm{keV}}$(altern.), some outliers become obvious: NGC 4051, NGC 6240, and IC 5063 exhibit high MIR–X-ray ratios ($R_{\mathrm{X}}^{\mathrm{M}} \geq 1.0$). For NGC 4051 and NGC 6240, this might be related to the highly uncertain X-ray luminosities caused by variability in the former, and obscuration in the latter case. In addition, NGC 6240 shows the most complex MIR emission in the inner 4″, and taking into account the fact that this is an ultra-luminous merging galaxy with a double nucleus, a peculiar position is not surprising. On the other hand, ESO 297-G018 and XSS J05054-2348 have very small MIR–X-ray ratios ($R_{\mathrm{X}}^{\mathrm{M}} < -0.5$). ESO 297-G018 has already been observed by G09 and is located in the same peculiar position in their Fig. 1. Both objects have only recently been identified as highly obscured AGN, showing peculiar X-ray properties (Ueda et al. 2007; Eguchi et al. 2009) making them candidates for the buried AGN class (Sect. 5.1). If the nuclei of ESO 297-G018 and XSS J05054-2348 are indeed enshrouded in an extremely thick torus (geometrically and optically) with only narrow opening angles, this would explain its relative weakness in the MIR because then, the torus itself would shield most of the MIR emission.

Compared to the G09 AGN, the BAT AGN have slightly lower $R_{\mathrm{X}}^{\mathrm{M}}$ and $\sigma_{\mathrm{X}}^{\mathrm{M}}$ but also a lower ρ, which is surprising. Both samples follow the same trend. A difference might be possible at the lowest luminosities but remains insignificant because of the small number of objects. It seems as if the slope of the `fitexy` fit for the BAT AGN is significantly influenced by the few BAT AGN at lowest luminosities with small X-ray uncertainties, NGC 4138, Cen A, and ESO 005-G004. On the other hand, even their exclusion from the fitting still yields incompatible results with the G09 fit. It is interesting to note that the low-luminosity objects included in the G09 sample, the LINERs NGC 1097 and NGC 4579 and also NGC 4941, all lie above the correlations, while the low-luminosity BAT AGN (except NGC 4051) all lie below. I come back to this when including the full LLAGN sample.

Furthermore, the `linmix_err` fit is also shown in Fig.6.1 for comparison. In contrast to `fitexy`, it includes the 10 upper limits in the fitting process. It yields the same slope as the G09 `fitexy` fit, however, is again steeper than (but consistent with) the corresponding `linmix_err` fit for the G09 sample (Table 6.1). This effect of flatter slopes (by ∼ 0.1) for `linmix_err` compared to `fitexy` seems to be systematic and gives an idea about the true uncertainty of the slope for the MIR–X-ray correlation. In addition, the intrinsic scatter, σ_{int} determined by `linmix_err` is lower compared to the G09 sample but still incompatible with zero. This implies that some of the differences in the MIR–X-ray properties put in evidence by comparing the correlation properties for different samples are not only caused by measurement uncertainties but by intrinsic differences between the objects. However, the lower dispersion leads to a higher correlation coefficient of `linmix_err` as well, which contradicts the lower Spearman rank and demonstrates that the properties of the MIR–X-ray correlation depend on methods used for their determination.

Hence, the main result from the comparison between the BAT AGN and the G09 samples is that the MIR–X-ray correlation is steeper in the former than in the latter – although for `linmix_err` still in agreement – but not well-determined ($1.05 \leq b \leq 1.3$).

6.4. MIR-X-ray relation for LLAGN

After establishing the $\lambda L_\lambda(12\,\mu\mathrm{m})$–$L_{2-10\mathrm{keV}}$ correlation for an uniform AGN sample in the previous section, we now investigate its existence in the low-luminosity regime ($L_{2-10\mathrm{keV}} \lesssim 10^{42}$ erg/s). For the LLAGN, it is important to take into account the uncertainties in the object distances as explained in Sect. 4.2.2. Different distance measurement methods can yield largely different and often even incompatible values. Therefore, the absorption-corrected X-ray versus MIR luminosities for all LLAGN are displayed in Fig. 6.2 for the 3 different distance sets D_L, D_{TF}, and D_{best}. Clearly, the MIR–X-ray correlation is also present in the LLAGN sample for all three distance sets. Although the LLAGN sample does not extend over a wide luminosity range, the MIR and intrinsic X-ray luminosities are highly correlated. However, individual objects change their position in the MIR–X-ray plane by large factors. The objects in the extreme positions at the high and low luminosity end are marked in Fig. 6.2: Cen A and Circinus are the brightest LLAGN and, when using D_L, even not LLAGN anymore because their X-ray luminosities become almost 10^{43} erg/s. The two faintest LLAGN are M 81 and NGC 4395, both are very nearby (< 5 Mpc). For these, the effect of the distance measurement used is largest, placing, e.g., M 81 for $D_L = 0.66$ Mpc at $\sim 10^{39}$ erg/s and at $> 10^{40}$ erg/s for $D_{\mathrm{best}} = 3.7$ Mpc. There is convincing evidence coming from different independent measurements that M 81 is indeed at a larger distance but moving towards us, which affects D_L and makes it misleading.

On the other hand, there are a couple of outliers with peculiar positions far away from the rest of the distribution. These LLAGN are marked with light colors in Fig. 6.2. In particular there are 5 upper limits that belong to NGC 3976, M 49, NGC 5813, NGC 7590, and NGC 7626. All of them have revised X-ray luminosities (as already mentioned in Sect. 6.1) that are much lower than the values used for the sample selection, rendering them useless for the current investigation. Even worse, they affect the results from the `linmix_err` algorithm, which gives them the same weight as the other upper limits. Hence, they are not considered in the fitting process and the rest of this analysis. In addition, there are two detected LLAGN with offsets > 1 dex toward high MIR (or low X-ray) luminosities: NGC 3125 and M 61. Both turn out to be dominated by young nuclear star clusters as explained in Sect. 6.4.1 and thus are excluded form the correlation and regression analysis as well. Note that the upper limit for the NELG NGC 1404 is consistent with the AGN correlations, and thus it might harbor an

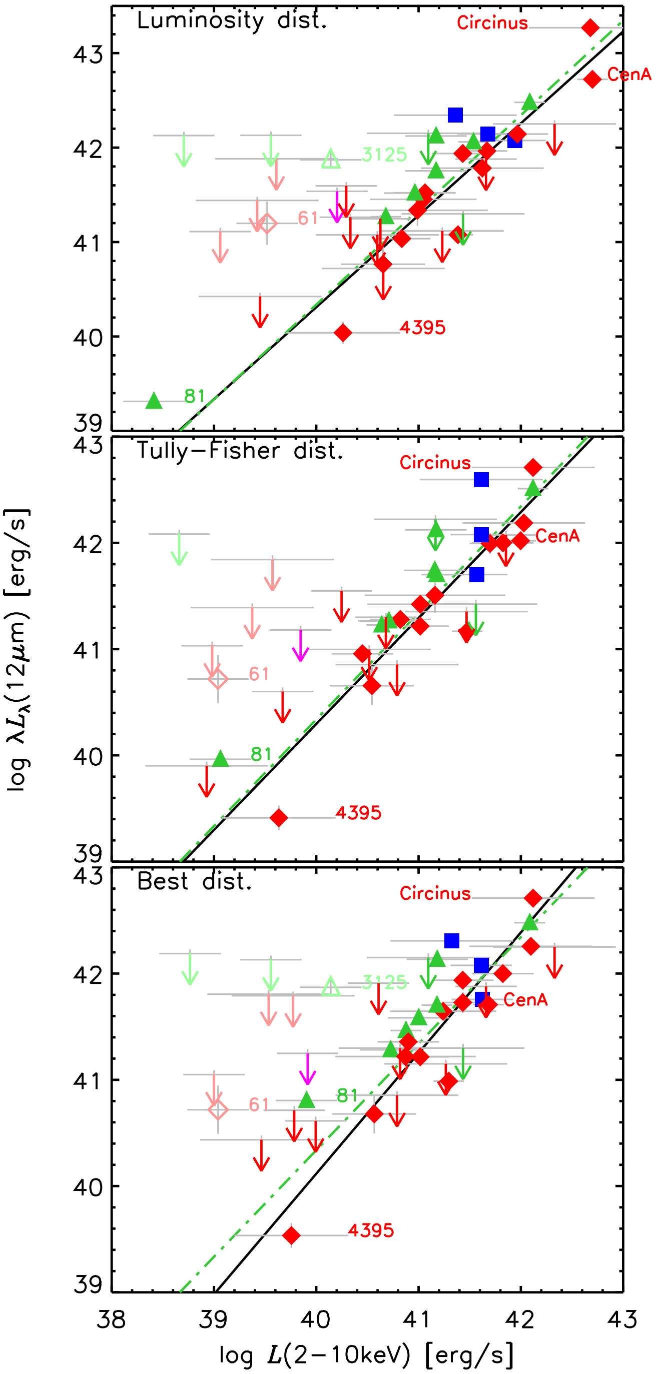

Figure 6.2: Nuclear MIR luminosities vs. absorption-corrected hard X-ray luminosities for the LLAGN using D_L (top), D_{TF} (middle), and D_{best} (bottom); blue squares: type 1 Seyferts (type 1.5 or lower), red diamonds: type 2 Seyferts, green triangle: LINERs, magenta arrow: NGC 1404 (NELG); solid line: `linmix_err` fit to all LLAGN (except the light colored); green dot-dashed line: `linmix_err` fit from G09.

AGN in its center as suggested by Grier et al. (2011). However, NGC 1404 will not regarded anymore in this work.

The Spearman rank coefficient, ρ, for the luminosity relation of the remaining LLAGN varies between 0.85 and 0.89 (null-hypothesis probability $-6.51 \geq \log p \geq -7.89$), depending on the distance set used. The correlation is strongest for D_L, which is a presumably a result of the increased luminosity range that occurs because of the extreme positions of M 81, Cen A and Circinus. However, as already mentioned, we have good reason to believe that these D_L values do not represent the true object distances. Furthermore, the LLAGN luminosities were fitted with the two algorithms described above and are listed as well in Table 6.1. The `linmix_err` fits are displayed as solid lines in Fig. 6.2. The results of both fitting algorithms generally agree, while again `linmix_err` gives systematically flatter slopes and larger uncertainties for the parameters for these samples. Note that although the Compton-thickness of some objects (e.g. NGC 5363 and NGC 7743) remains uncertain, they do not significantly affect the results. The reason for this is that they are not detected with VISIR and their upper limits do not constrain the results with either high (absorbed) or low (unabsorbed) intrinsic X-ray luminosities. Furthermore, the fit parameters for the different distance sets do not all agree within the calculated uncertainties: the fit for D_{best} is significantly steeper than the ones of the other two. Interestingly, it is also steeper than the G09 fit and similar to the BAT AGN fit, which is further investigated in Sect. 6.4.2.

In summary, the MIR–X-ray luminosity correlation is certainly valid in the low-luminosity regime, independent of the distance set used. All LLAGN subclasses including the LINER seem to follow one correlation, however, its precise slope depends on the distance set and the fitting algorithm used. Therefore the slope of the MIR–X-ray correlation for LLAGN is generally only constrained to be between ~0.95 and 1.25. As I have argued above, D_{best} likely represents the most accurate distances for the LLAGN and hence I concentrate on this set for the further analysis.

6.4.1. The outliers

Two of the detected LLAGN, NGC 3125 and M 61, exhibit very peculiar positions in Fig. 6.2. Both are detected only very weakly at $\sim 3\sigma_{\text{BG}}$ and were excluded from the correlation and regression analysis because of evidence that their observed fluxes at multiple wavelengths are heavily dominated by non-AGN processes, which I detail in this section for both object separately.

Table 6.1.: Correlation properties between $\log L_{\mathrm{MIR}}$ and $\log L_{\mathrm{X}}$ for various sample populations.

Sample	Method	N	ρ	$\log p$	σ_{int}	a	b	$\langle R_{\mathrm{X}}^{\mathrm{M}} \rangle$	$\sigma_{\mathrm{X}}^{\mathrm{M}}$
G09	fitexy	42	0.88	-14.01	...	0.41 ± 0.03	1.12 ± 0.04	0.30	0.36
G09	linmix_err	42	0.95 ± 0.03	...	0.29 ± 0.19	0.35 ± 0.06	1.00 ± 0.08	0.30	0.36
G09(well-r.)	fitexy	22	0.93	-9.52	...	0.19 ± 0.05	1.11 ± 0.07	0.15	0.23
G09(well-r.)	linmix_err	22	0.99 ± 0.02	...	0.12 ± 0.15	0.18 ± 0.06	1.08 ± 0.09	0.15	0.23
BAT(Winter)	fitexy	77	0.83	-20.20	...	0.41 ± 0.03	1.26 ± 0.06	0.39	0.42
BAT(altern.)	fitexy	79	0.83	-20.90	...	0.27 ± 0.03	1.26 ± 0.05	0.26	0.35
BAT(altern.)	linmix_err	89	0.96 ± 0.02	...	0.24 ± 0.15	0.18 ± 0.04	1.11 ± 0.07	0.26	0.35
BAT(>42)	fitexy	74	0.80	-16.84	...	0.27 ± 0.04	1.25 ± 0.08	0.27	0.33
BAT(>42)	linmix_err	84	0.91 ± 0.04	...	0.25 ± 0.16	0.20 ± 0.05	1.04 ± 0.10	0.27	0.33
BAT\LLAGN	fitexy	73	0.79	-16.06	...	0.24 ± 0.04	1.32 ± 0.09	0.27	0.34
BAT\LLAGN	linmix_err	83	0.91 ± 0.04	...	0.25 ± 0.16	0.19 ± 0.05	1.06 ± 0.11	0.27	0.34
LLAGN(D_L)	fitexy	23	0.89	-7.89	...	0.26 ± 0.13	0.96 ± 0.07	0.38	0.33
LLAGN(D_L)	linmix_err	34	0.95 ± 0.04	...	0.30 ± 0.27	0.23 ± 0.20	0.97 ± 0.11	0.38	0.33
LLAGN(D_{TF})	fitexy	23	0.88	-7.59	...	0.32 ± 0.17	0.99 ± 0.09	0.38	0.33
LLAGN(D_{TF})	linmix_err	33	0.95 ± 0.04	...	0.29 ± 0.26	0.29 ± 0.24	1.00 ± 0.13	0.38	0.33
LLAGN(D_{best})	fitexy	23	0.85	-6.51	...	0.74 ± 0.31	1.25 ± 0.17	0.38	0.33
LLAGN(D_{best})	linmix_err	34	0.94 ± 0.06	...	0.30 ± 0.27	0.52 ± 0.34	1.14 ± 0.19	0.38	0.33
LLAGN(≤ 42)	fitexy	20	0.78	-4.36	...	1.06 ± 0.56	1.41 ± 0.29	0.38	0.35
LLAGN(≤ 42)	linmix_err	30	0.91 ± 0.08	...	0.34 ± 0.30	0.56 ± 0.50	1.16 ± 0.26	0.38	0.35
All AGN	fitexy	113	0.90	-42.09	...	0.35 ± 0.03	1.08 ± 0.03	0.31	0.35
All AGN	linmix_err	134	0.98 ± 0.01	...	0.25 ± 0.13	0.25 ± 0.04	1.00 ± 0.04	0.31	0.35
All AGN(well-r.)	fitexy	43	0.90	-15.53	...	0.14 ± 0.04	1.11 ± 0.07	0.14	0.28
All AGN(well-r.)	linmix_err	43	0.99 ± 0.02	...	0.10 ± 0.13	0.14 ± 0.05	1.08 ± 0.08	0.14	0.28
All AGN($c_{<}^{\mathrm{SF}} \leq 10\%$)	fitexy	59	0.87	-18.10	...	0.38 ± 0.03	1.08 ± 0.05	0.35	0.33
All AGN($c_{<}^{\mathrm{SF}} \leq 10\%$)	linmix_err	59	0.96 ± 0.02	...	0.21 ± 0.13	0.37 ± 0.04	0.93 ± 0.07	0.35	0.33
Pure AGN	fitexy	28	0.92	-11.50	...	0.18 ± 0.06	1.11 ± 0.10	0.20	0.26
Pure AGN	linmix_err	28	0.99 ± 0.03	...	0.11 ± 0.14	0.20 ± 0.07	1.06 ± 0.12	0.20	0.26
Starbursts	bisector	22	0.92	-8.97	...	2.96 ± 0.20	0.97 ± 0.07	3.06	0.25

– *Notes:* Methods: see text for a description; N: number of objects used for the analysis; ρ: linear correlation coefficient (for 'fitexy': Spearman Rank); p: null-hypothesis probability; σ_{int}: intrinsic scatter; a, b: fitting parameters of $\log L_{\mathrm{MIR}} - 43 = a + b(\log L_{\mathrm{X}} - 43)$; $\langle R_{\mathrm{X}}^{\mathrm{M}} \rangle$: average of the luminosity ratio $R_{\mathrm{X}}^{\mathrm{M}}$ with $\sigma_{\mathrm{X}}^{\mathrm{M}}$ its standard deviation.

NGC 3125

The X-ray analysis of Chandra data published by Dudik et al. (2005) indicates an AGN in this object, while Zhang et al. (2009) reports a point-like X-ray nucleus embedded in soft emission based on the same data. On the other hand, this galaxy is known to harbor young and extreme Wolf-Rayet star clusters, two of which have been confirmed by optical and near-infrared observations (Hadfield and Crowther 2006), one directly in its galactic nucleus. In addition, no broad optical emission lines have been detected and it is optically classified as starburst (Kewley et al. 2001). Therefore, it is unclear whether NGC 3125 really harbors an AGN, or if the X-ray emission originates from X-ray binaries or an ultra-luminous X-ray source (ULX) inside or near the star cluster. The MIR emission may either originate from dust heated by an AGN or by the central star cluster on which the VISIR imaging was centered. The latter is favored because this object is also the only LLAGN that was spatially resolved in the HR MIR data. Note that the second and fainter star cluster at $\sim 10''$ to the east was not detected. The VISIR photometry and the IRS spectrum agree well in the continuum, indicating that the emission seen by IRS originates from a compact nucleus. On the other hand, the strong PAH emission feature in the IRS spectrum seems to be absent from the VISIR data. By assuming that the PAH $11.3\,\mu$m emission is still present in the nucleus the maximum contribution of star-formation $c^{\mathrm{SF}}_{<}$ is only $\leq 51\%$. However, complex molecules are probably also destroyed in close proximity of extremely massive young star forming regions. Evidence is strong that the Wolf-Rayet star cluster dominates the MIR emission of NGC 3125, which is the reason for its peculiar position with respect to the luminosity correlation. Hence, the observed MIR flux should be regarded as an upper limit for any dusty-torus emission of a putative AGN in NGC 3125.

M 61

This object has been undetected in Horst et al. (2008). However, a careful re-analysis of the NeIIref1 image reveals a very weak detection at a low $\sigma \sim 2$ (compare Fig. 6.3). Similar to NGC 1667, the negative beams were found at the expected positions. Furthermore, the detection significance increases in the smoothed co-added image to $5\sigma_{\mathrm{BG}}$. Still, the MIR values calculated for this object are unreliable owing to the very low S/N. Because the flux of this object is very low, it will unfortunately be very difficult to improve the S/N with any additional observations. M 61 has been classified as having an HII nucleus by Ho et al. (1995), although the optical line ratios are close to the AGN regime. Its X-ray luminosity is determined by Tzanavaris and Georgantopoulos (2007) also based on Chandra data. They conclude that this object is a good AGN candidate even with a low luminosity and without a detected Fe Kα emission line. Jiménez-Bailón et al. (2003) derive a 0.3 dex lower value from the same data. Both works report a hard X-ray core surrounded by a softer emission environment possibly associated with a circum-nuclear starburst ring. Colina et al. (2002) find evidence for a young star cluster present in the nucleus. This could contribute significantly to or even dominate the MIR emission at these low luminosities. This would explain the object's extreme position in the luminosity plane far off from the correlation. Unfortunately, there is no IRS spectrum

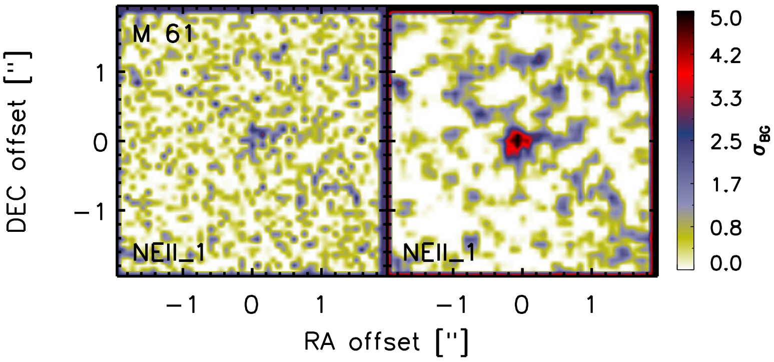

Figure 6.3: HR MIR image (VISIR) of the nucleus of M 61 (left) and smoothed (right), with linear scaling.

covering the N-band region. The nuclear star cluster might easily dominate the observed MIR emission similarly to NGC 3125, which would then lead to the observed excess. Note that off-nuclear young clusters with comparable MIR luminosities are found for example in NGC 1365 (Galliano et al. 2008) and would similarly be unresolved at the distance of M 61.

I conclude that the HR MIR detections for both NGC 3125 and M 61 could be only treated as upper limits for any AGN emission. However, as these upper limits are still very far away from the distribution of the other LLAGN in the luminosity plane, I exclude both objects completely from the rest of the analysis, similar to the upper limits from the X-ray revised objects mentioned above.

6.4.2. Comparison to brighter AGN

One of the main goals of this investigation is to determine whether LLAGN deviate from the MIR–X-ray correlation found for brighter local AGN. The BAT AGN represent the best available reference sample, however it contains a few LLAGN that overlap in both samples and would affect the comparison. Therefore, I exclude those LLAGN from the BAT AGN and use the remaining bright BAT AGN as the reference sample (BAT\LLAGN). The X-ray and MIR luminosities of both samples are displayed in Fig. 6.4. Note that some of the LLAGN turned out to have $L_{2-10\mathrm{keV}} > 10^{42}$ erg/s, namely, NGC 1667, Cen A, Circinus, and NGC 7213, which introduces some overlap of the two samples in this region as visible in Fig. 6.4. However, this does not affect the qualitative results reached in this section as I have tested by making a hard cut at $L_{2-10\mathrm{keV}} = 10^{42}$ erg/s, i.e. excluding NGC 1667 and Circinus, and keeping Cen A and NGC 7213 in the BAT AGN sample. The fit and correlation properties of these two variations are listed as "LLAGN(≤ 42)" and "BAT(> 42)" in Table 6.1.

In general, many LLAGN are offset by ~ 0.3 dex from the fit of the brighter AGN toward higher MIR (or lower X-ray) luminosities, which is in particular true for the LINERs and type 1 AGN. On the other hand, the type 2 LLAGN show a large scatter, so that the average logarithmic luminosity ratio $\langle R^{\mathrm{M}}_{\mathrm{X}} \rangle$ is only 0.1 dex higher than for the BAT\LLAGN. Both samples

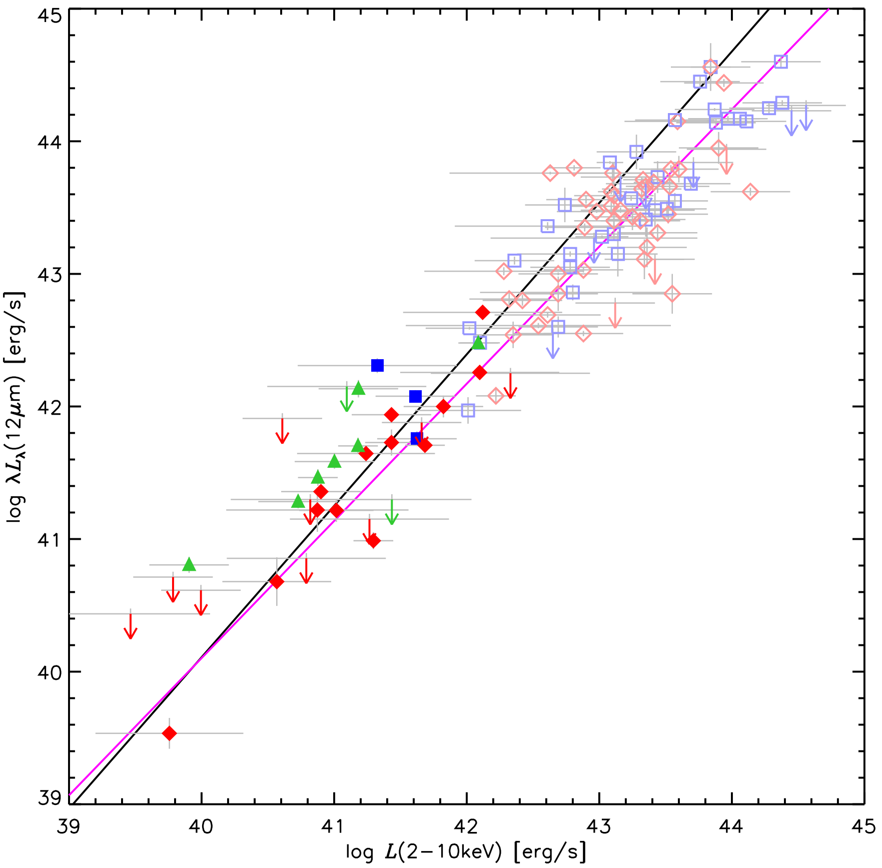

Figure 6.4: Comparison of LLAGN (filled symbols) to the bright BAT AGN (empty symbols) in $\lambda L_\lambda(12\,\mu\mathrm{m})$ versus $L_{2-10\mathrm{keV}}$; blue squares: type 1 Seyferts (type 1.5 or lower), red diamonds: type 2 Seyferts; green triangles: LINERs; black line: `linmix_err` fit to all displayed LLAGN (similar to Fig. 6.2, bottom); magenta line: `linmix_err` fit to all bright BAT AGN (BAT\LLAGN);

have been fitted with the `linmix_err` algorithm, which is also displayed in Fig. 6.4 with all corresponding parameters in Table 6.1. When excluding the LLAGN from the BAT AGN sample, the fit becomes slightly flatter ($b = 1.06 \pm 0.11$), which is mainly caused by the absence of the type 2 LLAGN NGC 4138 and NGC 4395 with low $R^{\mathrm{M}}_{\mathrm{X}}$. On the contrary, the slope of the LLAGN fit is steeper ($b = 1.14 \pm 0.19$). However, the uncertainties of the LLAGN and BAT AGN fit parameters are so large that the 1-σ confidence intervals overlap and the statistical difference between the 2 samples, thus, is insignificant. Visual inspection of Fig. 6.4 supports this fact: the LLAGN align very well with the BAT AGN extending the correlation toward lowest luminosities. Finally, the 7 detected LINERs constrain any possible difference of this class to be < 1 dex in the MIR-X-ray luminosity plane with respect to the Seyferts.

6.5. 12 μm–2-10 keV correlation for all AGN

The previous section has revealed that the LLAGN do not differ significantly from brighter AGN. Therefore, it makes sense to investigate the properties of the combined AGN sample, and for this purpose, I combine all available MIR HR data of local AGN from G09, Hönig et al. (2010) and this work (LLAGN and BAT AGN), leading to a total sample of 134 AGN (113 detected). For all AGN from G09 and Hönig et al. (2010) that are contained neither in the LLAGN nor in the BAT AGN sample, the corresponding luminosities are listed in Table B.7. The relation of the 12 μm versus 2-10 keV luminosities of this sample are plotted in Fig. 6.5 and its properties are listed in Table 6.1 as "All AGN". The correlation strength of the whole AGN sample measured by the Spearman rank coefficient significantly increases from $\rho = 0.83$ to 0.90 with respect to the BAT AGN sample. Also, the correlation coefficient measured by `linmix_err` increases to 0.98 ± 0.01 and the intrinsic scatter estimate remains at a low value and incompatible with 0 ($\sigma_{\mathrm{int}} = 0.25 \pm 0.13$). These resulting properties emphasize that the strongest MIR–X-ray correlation is indeed reached for the combination of all AGN, which is additional evidence for the absence of a significant deviation of the LLAGN as a group. Instead, the fits are remarkably consistent with the MIR–X-ray luminosity correlation found in previous work (G09). In particular, the slope of the `linmix_err` fit is unity, which implies a linear relation ship between $\lambda L_\lambda(12\,\mu\mathrm{m})$ and $L_{2-10\mathrm{keV}}$ with an offset of a factor of ~ 2 (0.25 dex). Therefore, the main result of this section is that the MIR-X-ray correlation extends unchanged down to luminosities of $\lesssim 10^{40}$ erg/s with a small scatter:

$$\log\left(\frac{\lambda L_\lambda(12\,\mu\mathrm{m})}{10^{43}\mathrm{erg\,s^{-1}}}\right) = (0.25 \pm 0.04) + (1.00 \pm 0.04)\log\left(\frac{L_{2-10\mathrm{keV}}}{10^{43}\mathrm{erg\,s^{-1}}}\right). \quad (6.2)$$

6.5.1. Comparison to starburst galaxies

It is interesting to compare the MIR–X-ray properties of the AGN to those of typical starburst galaxies, in which the MIR emission is dominated by star-formation. Here, the galaxy sample of Ranalli et al. (2003) is used, consisting of 22 typical nearby starburst galaxies. All possess measured 2-10 keV X-ray luminosities presented in the same work. The hard X-ray emission in these objects originates mainly in X-ray binaries and shock-heated diffuse gas. Because the star-formation in these galaxies is occurring on global and not (only) nuclear scales, large-aperture photometry is used for the comparison, in this case 12 μm photometry from the *IRAS* space observatory (Neugebauer et al. 1984). The starbursts are displayed as orange stars in Fig. 6.5 while the corresponding power-law fit is denoted as orange solid line with parameters listed in Table 6.1. No luminosity uncertainties are given in Ranalli et al. (2003), therefore I use the bisector algorithm for the fit. The starbursts form a strong correlation ($\rho = 0.92$; $\log p = -9.0$) with a high luminosity ratio ($\langle R^{\mathrm{M}}_{\mathrm{X}}\rangle = 3.1$) and a small scatter ($\sigma^{\mathrm{M}}_{\mathrm{X}} = 0.25$) in agreement with Krabbe et al. (2001). They form a population clearly distinct from the AGN. Interestingly, the slope (0.97 ± 0.07) of the power-law fit is comparable to that of the AGN, although the X-ray emission originates from completely different mechanisms. On the other hand, the normalization of the MIR-X-ray correlation for the starburst galaxies differs

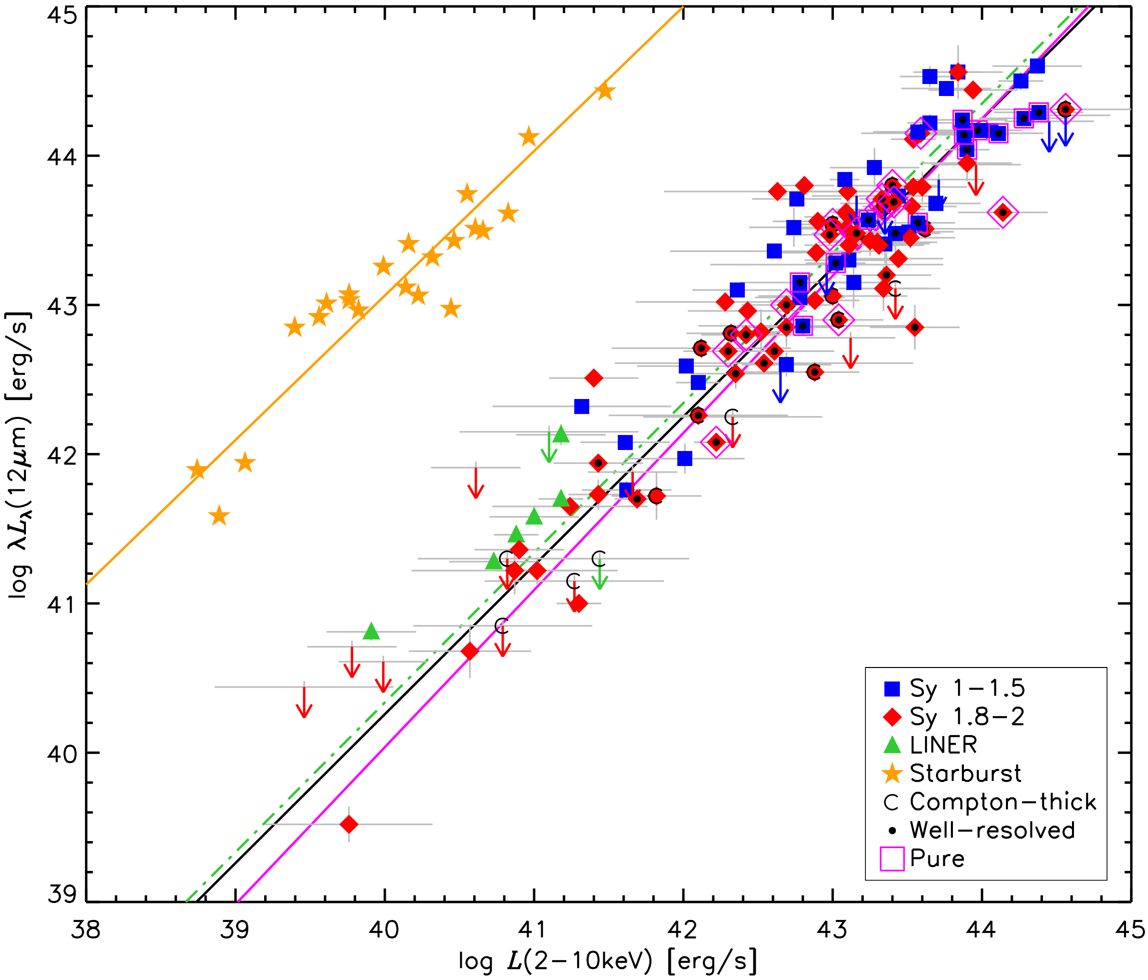

Figure 6.5: Absorption-corrected hard X-ray luminosities vs. the nuclear MIR luminosities for all AGN; blue squares: type 1 Seyferts (type 1.5 or lower), red diamonds: type 2 Seyferts; green triangles: LINERs; objects marked with a C: Compton thick AGNs (X-ray $N_{\mathrm{H}} > 1.5 \cdot 10^{24}\,\mathrm{cm}^{-2}$); objects highlighted with central black-filled circles: "well-resolved" AGN, see Sect. 6.5.2; filled orange stars: starburst galaxies (total luminosities) from Ranalli et al. (2003); solid black line: `linmix_err` fit to all displayed AGN; solid magenta line: `linmix_err` fit to all pure AGN (see Sect. 6.5.3); dot-dashed green line: `linmix_err` fit to all AGN from G09; orange solid line: bisector fit to all starburst galaxies.

by ~ 2.6 orders of magnitude toward higher MIR (or lower X-ray) emission. Note that the two outliers, NGC 3125 and M 61, would in fact be located closer to the starburst than to the AGN correlation, in agreement with our finding in Sect. 6.4.1.

6.5.2. Correlation for well-resolved AGN

The term "well-resolved" has been defined in Horst et al. (2008) for those AGN that have been observed at the highest intrinsic resolutions in the MIR and, hence, should have the least non-AGN contamination in their HR MIR data. Note however that this does not mean that the AGN structure itself, i.e. the torus, is spatially resolved. Instead, a well-resolved AGN is defined by its MIR data having a resolved scale r_0 in units of the dust sublimation radius r_sub that is smaller than a certain threshold ($s_\mathrm{wr} = r_0/r_\mathrm{sub} = 560$). The underlying idea is that the dusty torus structure is scaling in size with the bolometric luminosity of the AGN as explained in Sect. 2.2.3: $r_\mathrm{sub} = 0.45\sqrt{L_\mathrm{bol}/10^{45}\mathrm{erg/s}}\,\mathrm{pc}$. This means that even if an AGN is farther away, it might be studied at the same intrinsically resolved scale r_0/r_sub when it is brighter at the same time. Here, for the sake of simplicity, a constant angular resolution of $\theta_0 = 0.35''$ (corresponding to the one expected for a 8 m telescope at $\lambda = 12\,\mu\mathrm{m}$) is assumed, which in reality slightly depends on the observing wavelength. In addition, the bolometric luminosity is simply approximated by the X-ray luminosity: $L_\mathrm{bol} = 10 L_\mathrm{2-10keV}$. The threshold $s_\mathrm{wr} = 560$ has been determined by a sudden increase of $\langle R^\mathrm{M}_\mathrm{X}\rangle$ and $\sigma^\mathrm{M}_\mathrm{X}$ for objects with $r_0/r_\mathrm{sub} > 560$. This has been verified by G09 for a larger sample by using a 1D Kolmogorov-Smirnov (KS) test (e.g., Press et al. 1992) for finding a maximum sample difference. However, since then, the r_sub–L_bol relation has been slightly modified and some X-ray luminosities have been re-determined with improved data. Therefore, I re-determine the threshold s_wr for the BAT AGN sample and perform a KS test with splitting the AGN sample at each value for the intrinsic scale. The distribution of R^M_X versus r_0/r_sub is displayed in Fig. 6.6. No clear correlation is present ($\rho = 0.25$), but a general trend of increasing R^M_X with increasing r_0/r_sub albeit a dominating scatter (~ 0.3 dex). In this plot, the extremely low R^M_X of ESO 297-G018 and XSS J05054-2348 become obvious once more, while NGC 4051, NGC 6240 and IC 5063 show high R^M_X.

The KS test returns two coefficients that characterize the statistical difference of the R^M_X distributions of the AGN on each side of the chosen threshold: the maximum distance of the cumulative distribution functions, D_KS (magenta line), and the null-hypothesis probability, p_KS (black line). For better visibility they are shifted by +1 and smoothed in Fig. 6.6. If D_KS is high and p_KS low, then the two samples have probably been drawn from different parent distributions. The shapes of D_KS and p_KS are somewhat complex for the given AGN sample, and there is no dominating extremum that would indicate a clear separation between two different populations. Instead, there are three local minima in p_KS of almost equal depth. However, only the first minimum corresponds to a clear local maximum in D_KS at $\log(r_0/r_\mathrm{sub}) = 2.82$ and therefore represents the best candidate for s_wr. Indeed, $\langle R^\mathrm{M}_\mathrm{X}\rangle$ ($\sigma^\mathrm{M}_\mathrm{X}$) increases from 0.13 to 0.39 (0.29 to 0.38) for $\log(r_0/r_\mathrm{sub}) > 2.82$ as visible to the eye in Fig. 6.6. Of course, the corresponding value $s_\mathrm{wr} = 662$ does probably not mark a sharp transition, beyond which the point-like HR MIR emission is significantly contaminated. It rather resembles the best detectable discriminator for the current sample, identifying from a purely geometrical point of

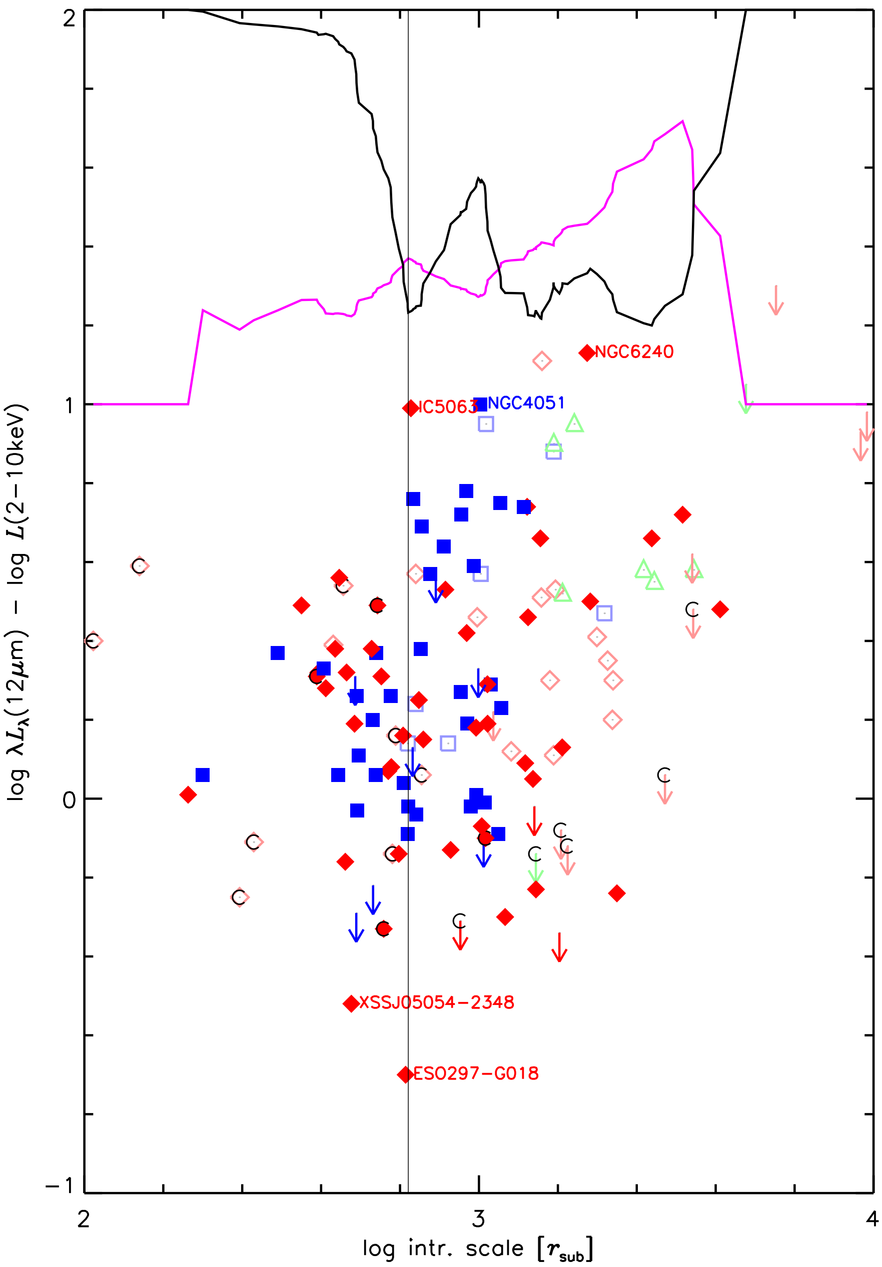

Figure 6.6: Logarithmic ratio of the nuclear MIR and absorption-corrected hard X-ray luminosities for BAT AGN (filled symbols) and the non-BAT AGN from G09 (empty symbols) versus the intrinsic scale r_0/r_{sub}; blue squares: type 1 Seyferts (type 1.5 or lower), red diamonds: type 2 Seyferts, green triangle: LINERs; black line: log p_{KS} + 1 normalized to 1 for visibility, magenta line: D_{KS} + 1.

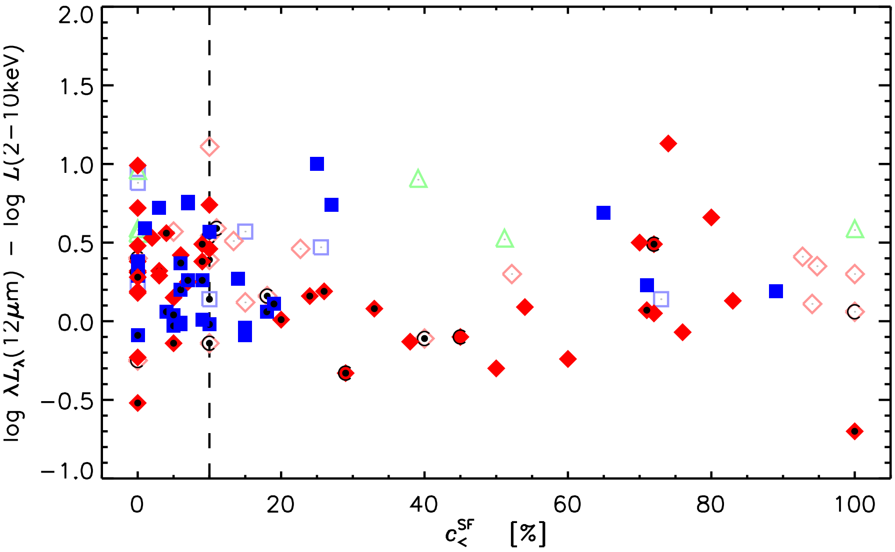

Figure 6.7: Logarithmic ratio of the nuclear MIR and absorption-corrected hard X-ray luminosities for BAT AGN (filled symbols) and the non-BAT AGN from G09 (empty symbols) versus the maximum SF contribution $c_<^{\mathrm{SF}}$; blue squares: type 1 Seyferts (type 1.5 or lower), red diamonds: type 2 Seyferts, green triangle: LINERs; objects marked with a C: Compton thick AGNs ($N_{\mathrm{H}} > 1.5 \cdot 10^{24}\,\mathrm{cm}^{-2}$); objects highlighted with central black-filled circles: well-resolved AGN.

view those objects that are presumably the least non-AGN contaminated. Note that for this reason any connection between the maximum SF contamination estimate $c_<^{\mathrm{SF}}$ and the property of being well-resolved is expected to be weak but still discussed in the next section.

With the newly determined s_{wr}, 43 out of the 113 detected AGN are well-resolved and marked with small filled black circles in Fig. 6.5. Of the LLAGN, only NGC 1386, Cen A and Circinus are well-resolved and, thus, the coverage at low luminosities is poor. Nevertheless, the well-resolved AGN have higher correlation coefficients, ρ, and the lower intrinsic scatter, σ_{int}, than the other AGN samples (compare Table 6.1). In fact, the fit and correlation properties are very similar to the well-resolved AGN from G09 despite the almost doubled sample size.

6.5.3. Correlation for pure AGN

In the Sections 4.5.1 and 5.7.1, I have presented an estimation of the maximum contamination by star formation to the 12 μm continuum in the HR data, $c_<^{\mathrm{SF}}$. Because this is just an upper limit, I have not corrected the HR MIR data for this fraction. However, one can select those sources with a low $c_<^{\mathrm{SF}}$, for example $c_<^{\mathrm{SF}} \leq 10\%$, and examine the MIR–X-ray relation only for these least contaminated AGN. Hence, the relation of the logarithmic luminosity ratio $R_{\mathrm{X}}^{\mathrm{M}}$ with $c_<^{\mathrm{SF}}$ is shown in Fig. 6.7. No dependency of $R_{\mathrm{X}}^{\mathrm{M}}$ with $c_<^{\mathrm{SF}}$ is evident, nor any trend, which is also true for the well-resolved AGN. This implies that the HR MIR data are actually much less SF contaminated than estimated with $c_<^{\mathrm{SF}}$ and the origin of the scatter in $R_{\mathrm{X}}^{\mathrm{M}}$ is caused by phenomena that are not star formation related. Therefore, it is not surprising that the correlation properties for the 59 AGN with $c_{<}^{\mathrm{SF}} \leq 10\%$ (left of the vertical dashed line in Fig. 6.7) do not improve in any way (compare Table 6.1). This result does not depend on the exact threshold chosen for the selection of this AGN sub-sample. Apart from SF, another possibility of non-AGN contamination can be diffuse (hot) dust residing in the host galaxy. This diffuse emission can contribute significantly at least in lower resolution data as the example of NGC 4261 in Sect. 4.5 demonstrates: this object exhibits only a very weak PAH feature (leading to a low $c_{<}^{\mathrm{SF}}$) but, nevertheless, has a much lower $F_\nu^{\mathrm{HR}}(12\,\mu\mathrm{m})$ than $F_\nu^{\mathrm{IRS}}(12\,\mu\mathrm{m})$. In this case, the missing flux arises from the dusty nuclear disk (Fig. 2.4), which might also be present in other objects. On the other hand, this disk does not emit PAH emission indicative of a SF origin as the IRS spectrum shows. Hence, a selection based on only $c_{<}^{\mathrm{SF}}$ unlikely provides those objects with the best isolated AGN emission in the HR MIR data.

However, by combining the criteria of $r_0/r_{\mathrm{sub}} \leq 662$ and $c_{<}^{\mathrm{SF}} \leq 10\%$, a sample of 28 AGN can be selected, which are "well-resolved" (free of host galaxy contribution) and most certainly free of SF contamination. I call these AGN "pure" because their observed HR MIR emission is coming only from the AGN, without any contamination, and mark them with magenta colored frames in Fig. 6.5. Despite the decreased object numbers and luminosity coverage (none of the LLAGN is "pure"), the correlation significance remains as high as for the well-resolved AGN. Also the fitting parameters remain similar and the slope of the `linmix_err` fit (magenta line in Fig. 6.5) is slightly steeper than the fit to all AGN although consistent within the error bars. This pure AGN fit represents the best estimate of the "true" underlying MIR–X-ray correlation free of non-AGN contamination:

$$\log\left(\frac{\lambda L_\lambda(12\,\mu\mathrm{m})}{10^{43}\mathrm{erg\,s^{-1}}}\right) = (0.20 \pm 0.07 + (1.06 \pm 0.12)\log\left(\frac{L_{2-10\mathrm{keV}}}{10^{43}\mathrm{erg\,s^{-1}}}\right). \tag{6.3}$$

6.5.4. Correlation in flux space

As we have seen in Sect. 6.4, the object distance influences the spread of the MIR and X-ray luminosities along the diagonal in logarithmic space. This can, in principle, introduce artificial correlations (with a slope of 1) that are caused just by the included distance term on both axis. Therefore, it is important to verify any luminosity correlation also in flux space. Horst et al. (2008) and G09 have already shown that the MIR–X-ray correlation is present also in flux space although of lower statistical significance. With the largely increased sample size, it is worth to have another look (Fig. 6.8). The intrinsic 2-10 keV flux is calculated with the alternative set of luminosities for the BAT AGN. Most of them are distributed at higher fluxes both in X-rays and MIR, but there are some type 2 AGN at the lowest fluxes as well. The two brightest objects in terms of flux are NGC 1068 and Circinus, almost one order of magnitude brighter than any other AGN. Interestingly, there are almost no type 1 AGN at low fluxes ($F_{2-10\mathrm{keV}} < 10^{-11}$ erg/s/cm^2).

The formal correlation strength of $F_\nu(12\,\mu\mathrm{m})$ and $F_{2-10\mathrm{keV}}$ is weaker ($\rho = 0.77; \log p = -23.1$), because of the decreased range in orders of magnitude compared to the luminosity space.

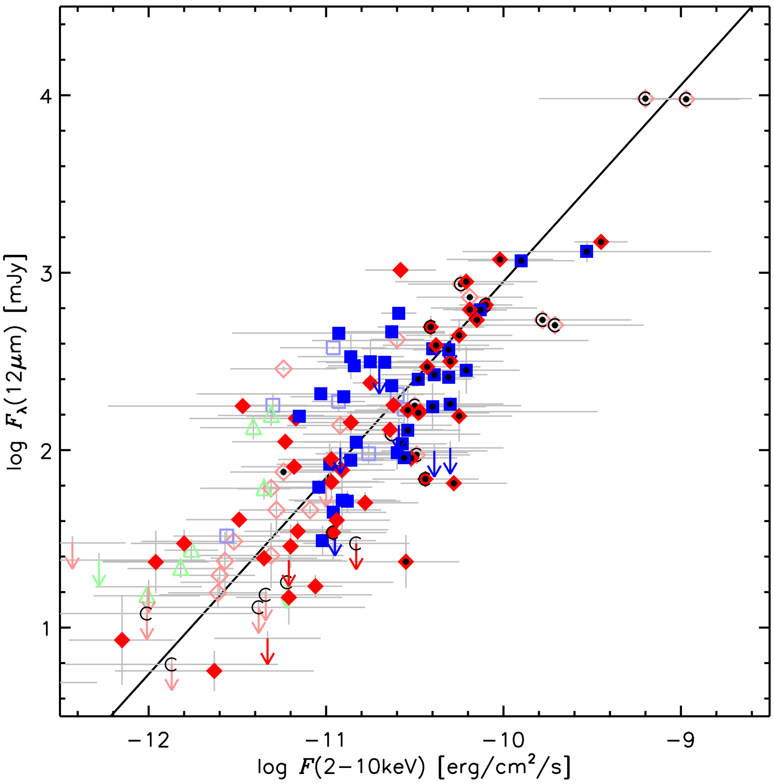

Figure 6.8: Nuclear MIR vs. absorption-corrected hard X-ray fluxes for BAT AGN (filled symbols) and the non-BAT AGN (empty symbols); blue squares: type 1 Seyferts (type 1.5 or lower), red diamonds: type 2 Seyferts, green triangle: LINERs; objects marked with a C: Compton thick AGNs ($N_\mathrm{H} > 1.5 \cdot 10^{24}\,\mathrm{cm}^{-2}$); objects highlighted with central black-filled circles: well-resolved AGN; solid line: `linmix_err` fit all displayed AGN.

However, the slope flux correlation is comparable to that of the luminosity correlation for the combined sample (using `linmix_err`):

$$\log\left(\frac{F_\nu(12\,\mu\mathrm{m})}{10^2\,\mathrm{mJy}}\right) = (0.95 \pm 0.07) + (1.11 \pm 0.08)\log\left(\frac{F_{2-10\mathrm{keV}}}{10^{-10}\,\mathrm{erg\,s^{-1}cm^{-2}}}\right), \qquad (6.4)$$

whereas again no K-correction is applied. The strong flux correlation and its consistent slope prove that the luminosity correlation is not a consequence of a selection bias related to distance.

6.6. 2-10 keV–14-195 keV correlation

The BAT AGN sample has been selected in the hardest X-ray band, 14-195 keV because at these energies AGN that are totally obscured at longer wavelengths are still visible and have only low obscuration at hardest X-rays. Therefore, the 14-195 keV X-ray luminosities,

$L_{14-195\mathrm{keV}}$, are not dependent on the spectral modeling as those at 2-10 keV. The modeling dependency and partially high obscuration introduce major uncertainties in $L_{2-10\mathrm{keV}}$, which dominate the scatter in the 12 μm–2-10 keV correlation and the uncertainties in the fitting parameters. Consequently, the average $L_{14-195\mathrm{keV}}$ might be a more robust measure of the AGN power output and, thus, a comparison with $\lambda L_\lambda(12\,\mu\mathrm{m})$ is useful. However, first I compare $L_{2-10\mathrm{keV}}$ to $L_{14-195\mathrm{keV}}$, similar to Winter et al. (2009a) but using the alternative $L_{2-10\mathrm{keV}}$ collection and updated $L_{14-195\mathrm{keV}}$. For this purpose, I take the observed 14-195 keV fluxes, $F_{14-195\mathrm{keV}}$, from Tueller et al. (2008) and Tueller et al. (2010) with preference to the latter. I estimate the uncertainty of the individual fluxes by the difference in both catalogs because flux variations of factors of several have to be expected. Note however, that the $F_{14-195\mathrm{keV}}$ listed in these catalogs represent already the average values for 9 and 22 months of observations respectively. Surprisingly, seven of the observed BAT AGN from the 9-month catalog are not in the 22-month catalog (NGC 454, Mrk 590, 2MASX J03565655, MCG -01-13-025, ESO 121-G028, 2MASX J06403799, and 2MASX J09180027), i.e. are not detected above 4.8 σ_{BG} anymore. The reason for this might be long term variations or outbursts in the affected objects. For them, I use the fluxes from Tueller et al. (2008) but adopt an uncertainty of 0.3 dex. The corresponding $L_{14-195\mathrm{keV}}$ are listed in Table B.5 for individual objects. First, I examine the relation of the X-ray emission in both energy bands in flux space Fig. 6.9. Note that the $F_{2-10\mathrm{keV}}$ are absorption-corrected, while $F_{14-195\mathrm{keV}}$ are observed quantities. In addition, some of the non-BAT AGN have $F_{14-195\mathrm{keV}}$ available in the 22-month catalog from Tueller et al. (2010): NGC 1068, ESO 263-G013, ESO 323-G077, NGC 6300, ESO 141-G055, 3C 445, NGC 7674 (from G09 and Hönig et al. (2010); and NGC 1052, NGC 4235 and Circinus from the LLAGN. Note that NGC 6300 has already been detected in the 9-month catalog but has been discarded by Winter et al. (2009a) because it is close to the galactic plane. All these 10 non-BAT AGN are also shown in Fig. 6.9. Interestingly, the two brightest AGN in terms of $F_{2-10\mathrm{keV}}$ are significantly offset toward lower $F_{14-195\mathrm{keV}}$ with respect to the other AGN, which is probably the reason why these two usually bright AGN have not been detected in the 9-month BAT AGN catalog. The same is true for NGC 7464 from the G09 AGN sample. The reason for this offset is most likely related to the Compton-thickness of both objects: for $N_{\mathrm{H}} > 1.5 \times 10^{24}\mathrm{cm}^{-2}$, even at energies > 20 keV extinction is dominating, leading to orders of magnitude lower observed $F_{14-195\mathrm{keV}}$. This is also evident for the other CT objects in Fig. 6.9 by their location on or above the correlation. For this reason, I exclude the CT non-BAT AGN (NGC 1068, Circinus and NGC 7674) from the following correlation analysis.

For the remaining 97 AGN (of which 87 are detected), the Spearman rank is $\rho = 0.75$ ($\log p = -16.3$) and the `linmix_err` algorithm yields the following fit:

$$\log\left(\frac{F_{2-10\mathrm{keV}}}{10^{-10}\,\mathrm{erg\,cm^{-2}s^{-1}}}\right) = (-0.50 \pm 0.04) + (1.20 \pm 0.12)\log\left(\frac{F_{14-195\mathrm{keV}}}{10^{-10}\,\mathrm{erg\,cm^{-2}s^{-1}}}\right), \tag{6.5}$$

with $\rho = 0.92 \pm 0.05$ and a $\sigma_{\mathrm{int}} = 0.16 \pm 0.12$. This result does not depend on the choice of the AGN sample, i.e. BAT AGN only, or all AGN. It is remarkable that all objects at the low $F_{2-10\mathrm{keV}}$ end exhibit an excess of $F_{14-195\mathrm{keV}}$. In particular, 4 objects (2MASX J06403799, 2MASX J09180027, NGC 4395, and 3C 105) are significantly over-luminous, which is also the reason why they have been detected by BAT at all – the flux-limit for the 9-month catalog

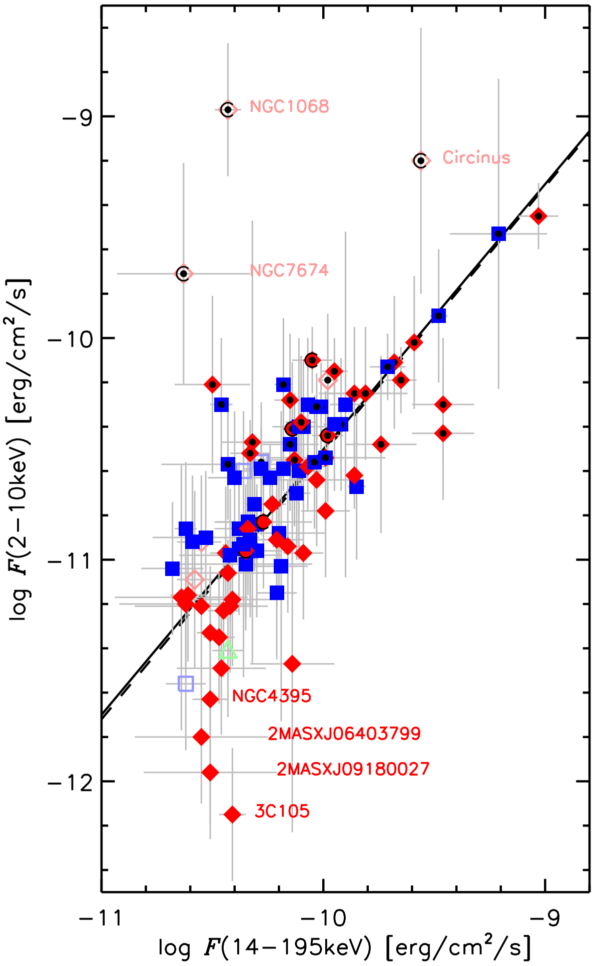

Figure 6.9: Absorption-corrected 2-10 vs. 14-195 keV X-ray fluxes for BAT AGN (filled symbols) and the non-BAT AGN (empty symbols); blue squares: type 1 Seyferts (type 1.5 or lower), red diamonds: type 2 Seyferts, green triangle: LINERs; objects marked with a C: Compton thick AGNs ($N_\mathrm{H} > 1.5 \cdot 10^{24}\,\mathrm{cm}^{-2}$); objects highlighted with central black-filled circles: well-resolved AGN; solid line: `linmix_err` fit to all displayed AGN (except NGC 1068, Circinus and NGC 7674); dashed line: `linmix_err` fit to all BAT AGN.

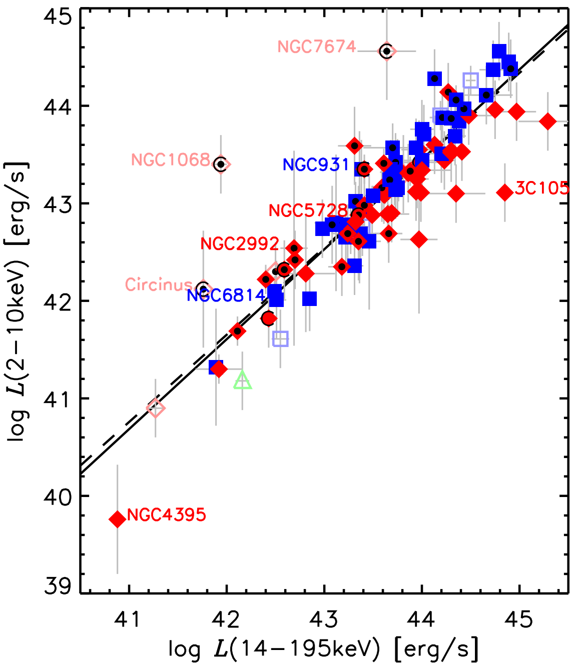

Figure 6.10: Absorption-corrected 2-10 vs. 14-195 keV X-ray luminosities for BAT AGN (filled symbols) and the non-BAT AGN (empty symbols); description is similar to Fig. 6.9.

is $\log(F_{14-195\mathrm{keV}}/\mathrm{erg\,cm^{-2}s^{-1}}) \sim -10.7$. The reason for this $F_{14-195\mathrm{keV}}$ excess is unknown, at least in 3C 105, additional emission could be caused by synchrotron emission from the jet in this radio-loud object.

Fig. 6.10 shows the 2-10 keV–14-195 keV relation in luminosity space. Here, the Spearman rank is again increased ($\rho = 0.88$; $\log p = -29.8$) and the `linmix_err` fit is

$$\log\left(\frac{L_{2-10\mathrm{keV}}}{10^{43}\,\mathrm{erg\,s^{-1}}}\right) = (-0.49 \pm 0.05) + (0.94 \pm 0.04)\log\left(\frac{L_{14-195\mathrm{keV}}}{10^{43}\,\mathrm{erg\,s^{-1}}}\right), \tag{6.6}$$

with $\rho = 0.99 \pm 0.04$ and a $\sigma_{\mathrm{int}} = 0.13 \pm 0.11$, which is significantly flatter than the fit in flux space and also the fit given by Winter et al. ($b = 1.06 \pm 0.05$). Note that the disagreement becomes even larger when using the BAT AGN only (dashed line). Unfortunately, the exact algorithm used to obtain this value is not given in the latter work. Therefore, it is hard to judge where the discrepancy arises. It commonly happens that different algorithms give inconsistent results, for example because the choice of the independent variable and treatment of error can have large influence.

The outliers in Fig. 6.9 remain also in extreme positions in Fig. 6.10. However, only one of them (2MASX J09180027) is also an outlier in Fig. 6 in Winter et al. (2009a), while their other outliers, NGC 931, NGC 2992, NGC 5728, and NGC 6814, are here in perfect agreement with the correlation and tend to exhibit even higher than average $L_{2-10\mathrm{keV}}/L_{14-195\mathrm{keV}}$ ratios. The reason for this is on the one hand because of the updated $L_{14-195\mathrm{keV}}$ but on the other hand mainly because of the alternative $L_{2-10\mathrm{keV}}$ selection that has been used here.

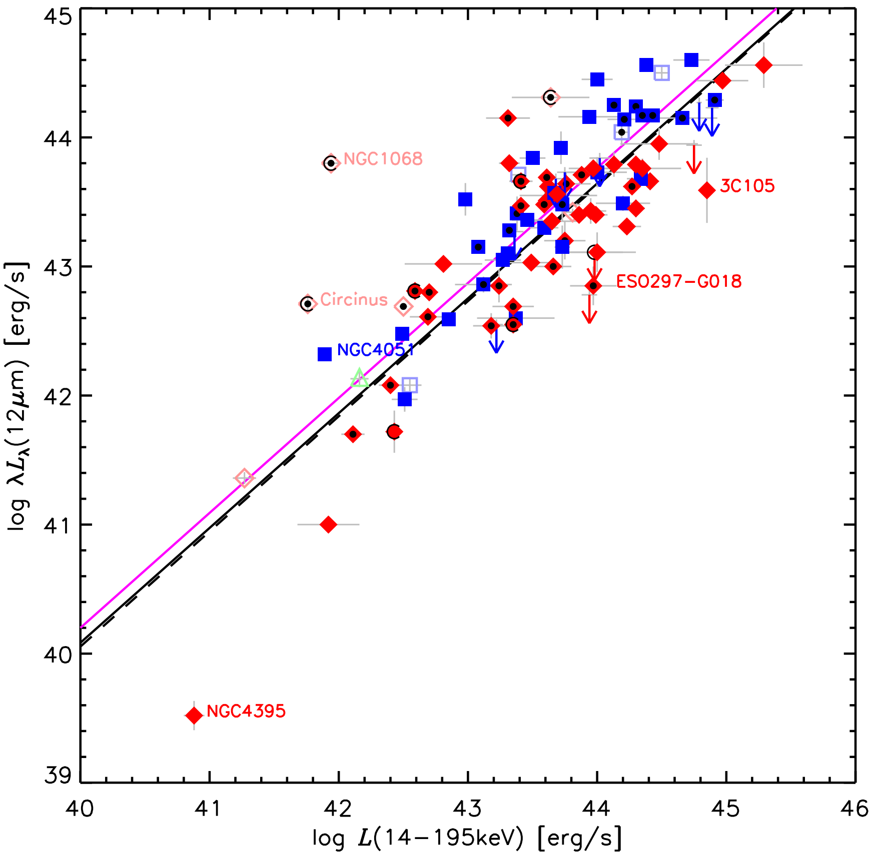

Figure 6.11: Observed nuclear MIR vs. 14-195 keV X-ray luminosities for BAT AGN (filled symbols) and the non-BAT AGN (empty symbols); description is similar to Fig. 6.9, and the solid magenta line is a `linmix_err` fit to all well-resolved AGN (except NGC 1068, Circinus and NGC 7674).

6.7. 12 μm–14-195 keV correlation

The previous section verified the 2-10 keV–14-195 keV correlation for local AGN. Given the strong correlations of the 2-10 keV with the 12 μm and 14-195 keV luminosities, one should also expect a strong correlation for the observed 12 μm an 14-195 keV luminosities as well (Fig. 6.11). In the 12 μm–14-195 keV plane, the Spearman rank is in fact lower, $\rho = 0.81$ ($\log p = -20.5$), than the one for the two X-ray bands. Here, NGC 1068, Circinus and NGC 7674 have been excluded again for the reason given above. Despite the LLAGN (NGC 4138 and NGC 4395) showing an $L_{14-195\mathrm{keV}}$ excess, the `linmix_err` algorithm yields a fit that is flatter than in previous relations:

$$\log\left(\frac{\lambda L_\lambda(12\,\mu\mathrm{m})}{10^{43}\mathrm{erg\,s^{-1}}}\right) = (-0.24 \pm 0.06 + (0.89 \pm 0.06)\log\left(\frac{L_{14-195\mathrm{keV}}}{10^{43}\mathrm{erg\,s^{-1}}}\right). \tag{6.7}$$

This result is surprising because from the previous correlations one would expect the slope to be larger than in Eq. 6.6. I assume that the fit is dominated by the objects with the smallest

X-ray uncertainties. The average logarithmic luminosity ratio, $\langle R^{\mathrm{M}}_{\mathrm{HX}} \rangle$, is -0.27 ± 0.42 and the intrinsic scatter $\sigma_{\mathrm{int}} = 0.43 \pm 0.19$. These values slightly improve when only the 36 well-resolved AGN with BAT detection are used: $\langle R^{\mathrm{M}}_{\mathrm{HX}} \rangle$ becomes bigger (-0.20 ± 0.37) and ρ increases to 0.82 while σ_{int} decreases (0.34 ± 0.19). However, it is remarkable that the correlation strength is so high and the scatter so low taking into account that $\lambda L_{\lambda}(12\,\mu\mathrm{m})$ and $L_{14-195\mathrm{keV}}$ are both observed quantities without any absorption correction.

Note that some of the outliers in the 12 μm–2-10 keV plane are closer to the other AGN in the 12 μm–14-195 keV plane. In particular, XSS J05054, NGC 4051, NGC 6240, and IC 5063 exhibit $R^{\mathrm{M}}_{\mathrm{HX}}$ that are closer to the average than in the 12 μm–2-10 keV plane. This indicates that the 2-10 keV luminosity of XSS J05054 might be estimated as too low, and too high for the other three. On the other hand, ESO 297-G018 remains at an extreme luminosity ratio, and in addition, some other objects exhibit extreme $R^{\mathrm{M}}_{\mathrm{HX}}$: MCG -03-34-064 with $R^{\mathrm{M}}_{\mathrm{HX}} = 0.84$; and 3C 105, NGC 4395, and PG 13946 with $R^{\mathrm{M}}_{\mathrm{HX}} < -1.1$. Additional 14-195 keV data, also from other instruments (like *INTEGRAL*), will be needed in order to verify the extreme ratios for these outliers. One has to keep in mind, that the number of photons decreases extremely fast toward higher X-ray energies, and flux variabilities can have high amplitudes for individual objects as well, in particular at 14-195 keV.

However, I conclude that, despite the lower range of orders of magnitude in flux and luminosity compared to the 12 μm–2-10 keV plane, there is a strong correlation present for the 12 μm–14-195 keV plane as well. The correlation in luminosity space is at least as strong as the one with the X-ray luminosities at lower energies, although the 14-195 keV is not absorption-corrected.

In this chapter, I have demonstrated that the HR 12 μm emission of AGN correlates very strongly with their X-ray emission in the two energy bands, 2-10 and 14-195 keV, with a slope that is close to unity and a scatter of the order of 0.3 dex. All different AGN types including LLAGN and LINERs can be described well by one correlation that is valid in flux and luminosity space and extends over the whole probed range for 2-10 keV. Finally, the $\lambda L_{\lambda}(12\,\mu\mathrm{m})$–$L_{2-10\mathrm{keV}}$ correlation is by at least two orders of magnitude distinct from a similar correlation for typical starburst galaxies.

7. Discussion

The last chapters have presented the HR MIR observational results for two local AGN samples and their comparison to the X-ray properties of these objects, leading to a strong empirical correlation between both wavelength regions. In this chapter, I want to discuss these results with respect to the AGN models presented in Chapter 2 and try to investigate the physical origin of the observed MIR emission, in particular in the low-luminosity regime. Section 5.6.1 already demonstrated that for brighter AGN, the observed MIR SEDs at HR are consistent with clumpy torus models. This explanation is supported by fitting of high-spatial resolution spectrophotometry with clumpy torus models (Hönig et al. 2010; Alonso-Herrero et al. 2011).

7.1. Intrinsic AGN-type difference

One of the major open questions in AGN research is whether the unification model (Sect. 2.2) indeed holds for all types of AGN without further modification, i.e., whether the only difference between type 1 and type 2 AGN is the orientation of the AGN with respect to the observer, or if there is an intrinsic difference at least for some type 2 AGN. Winter et al. (2009a) have found such a difference in the 9-month BAT AGN sample: the type 2 AGN are on average intrinsically fainter in the X-rays than the type 1 AGN.

I test this finding here for the observed BAT and non-BAT AGN (using the alternative $L_{2-10\mathrm{keV}}$ set). Fig.7.1 shows the distribution of $L_{2-10\mathrm{keV}}$ for all observed AGN. While Winter et al. have combined all intermediate Seyfert classes as a separate intermediate class, I consider Sy 1.5 as type 1 AGN and Sy 1.8-1.9 as type 2 AGN. Owing to this differentiation and the fact that some BAT AGN from the northern hemisphere are missing here (mainly type 1 AGN), the majority of AGN with HR MIR data are type 2 AGN. Most of these are distributed among the lower X-ray luminosities, while the number density drops fast towards highest luminosities ($L_{2-10\mathrm{keV}} \gtrsim 10^{43.5}$ erg/s) as visible in the histogram. On the other hand, the type 1 AGN have a maximum number density at higher luminosity, and in particular at $L_{2-10\mathrm{keV}} \gtrsim 10^{43.5}$ erg/s, they become the majority of all AGN, which is exactly what Winter et al. have found before. This result is also valid for the combined sample including all AGN, although the KS test yields moderate numbers $D_{\mathrm{KS}} = 0.29$ and $p_{\mathrm{KS}} = 0.02$. Reasons for this might be the missing BAT AGN or the different classification distinction used with respect to Winter et al.

Because every histogram shape partly depends on the choice of the binning, I have verified this results for different bin numbers and borders, and, in addition, plotted the normalized cumulative distribution function in Fig.7.1. The latter shows that for the combined sample, the growth rate is comparable between $L_{2-10\mathrm{keV}} \approx 10^{42.1}$ erg/s and $L_{2-10\mathrm{keV}} \approx 10^{43.6}$ erg/s. This

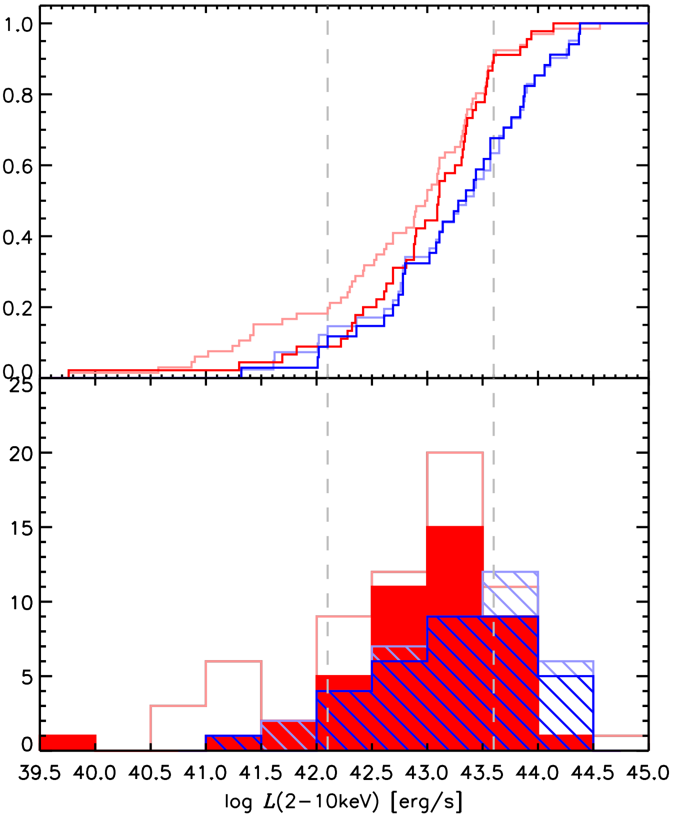

Figure 7.1: Distribution of absorption-corrected 2-10 keV X-ray luminosities as normalized cumulative function (top) and histogram (bottom). The distribution for BAT AGN only are in solid blue (type 1 AGN) and solid red (type 2 AGN), while the distributions for all AGN are in light colors. The vertical dashed gray lines indicate the region with roughly similar growth of the cumulative distribution function for all AGN.

region of X-ray luminosities would be best suited for a comparison of the AGN types with respect to other data like the HR MIR photometry. Note that the distribution of $L_{14-195\mathrm{keV}}$ is qualitatively similar with an over-density of type 2 AGN at lower luminosities and an over-density of type 1 AGN at higher luminosities, although the significance of this trends is much lower: a KS-test finds no statistical difference between the samples.

Owing to the selection technique used for the BAT AGN, their distribution should be much less biased against highly obscured objects compared to previous studies (except CT AGN). The difference in the $L_{2-10\mathrm{keV}}$ distribution might not be caused by a selection effect but indicate an intrinsic difference between the AGN types. On the contrary, when including the non-BAT AGN, of which many are CT (from G09), the KS significance for the difference becomes much weaker as stated above. Indeed, the Compton-thick population of AGN is not well represented in the BAT AGN sample because, as indicated in Sect. 6.7, the observed 14-195 keV emission is severely affected by CT obscuration. Therefore, the difference that Winter et al. have found, might arise from the missing CT AGN, and thus might not be intrinsic. Further tests will be necessary to verify or dismiss this possibility.

However, the next sections discuss the possibility of any differences in the MIR–X-ray luminosity relation with the AGN type and related properties.

7.2. Dependencies of the MIR–X-ray ratio

The dispersion in the found MIR and X-ray correlations is of the order of 0.4 dex (Chapter 6). What is causing this dispersion? Is it related to any other object property like the optical AGN classification? Does the MIR–X-ray luminosity relation reveal any intrinsic differences between the AGN types?

Because this relation can approximately be described as linear (Sect. 6.5), one can instead simply examine the logarithmic luminosity ratios $R^{\mathrm{M}}_{\mathrm{X}}$ and $R^{\mathrm{M}}_{\mathrm{HX}}$ and their dispersion in order to investigate these questions. In addition, I define the logarithmic X-ray luminosity ratio $R^{\mathrm{X}}_{\mathrm{HX}} = \log L_{2-10\mathrm{keV}} - \log L_{14-195\mathrm{keV}}$.

7.2.1. Expectations form the torus model

In the clumpy torus models from Hönig and Kishimoto (2010), the MIR luminosity drops with increasing inclination of the torus with respect to the observer. This can be understood with the following illustration: for low inclinations (and hence low N_{H}) the hot accretion-disk-facing side of the dusty clouds can be seen by the observer, leading to higher observed MIR emission, while for increasing inclination (and N_{H}), the probability is increasing that the direct view of these hottest dust is blocked by another optically thick cloud on the close side of the torus. Fig. 7.2 demonstrates this effect for such a model with typical parameters. In particular, $F_\nu(12\,\mu\mathrm{m})$ (and $\lambda L_\lambda(12\,\mu\mathrm{m})$) is 0.3 dex lower for the edge-on case than in the face-on case. Note however that the clouds are randomly distributed following a statistical distribution function. Hence, for individual objects, there is always a certain chance for an unobscured view onto the central region, even for high torus inclinations. Furthermore $L_{2-10\mathrm{keV}}$ should be corrected for the increased absorption with increasing torus inclination because I use the absorption-corrected X-ray luminosities, while the observed $L_{14-195\mathrm{keV}}$ are in general only marginally affected. Therefore, the clumpy torus torus scenario predicts that, in a statistical sense, the MIR–X-ray ratios should also decrease with increasing torus inclination and, thus, type 2 AGN should have on average ~ 0.3 dex lower ratios than type 1 AGN. Note, however, that this predicted difference depends slightly on on the model parameters used. For example, for lower covering fractions and more compact radial cloud distributions, the difference is only ~ 0.2 dex (Hönig et al. 2011), while for different parameter values it can be as large as ~ 0.4 dex. In any case, the chosen parameters represent values that have found to be in good agreement for observational data of typical Seyferts (Hönig et al. 2010).

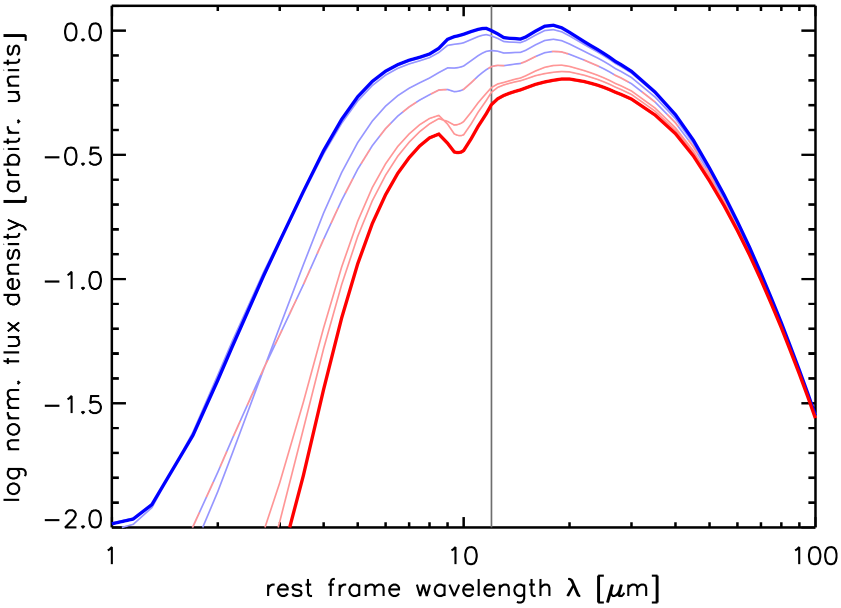

Figure 7.2: Calculated infrared SED for the clumpy torus models from Hönig and Kishimoto (2010) for different orientations of the torus with respect to the observer. The thick blue line is for the case of a face-on orientation (inclination = 0°), the thin light-blue lines with decreasing intensities have 15° and 30°, the thin light-blue-red dashed line 45°, and the thin light- red lines 60° and 75°. The thick red line is for the edge.on orientation (90°). All SEDs are normalized by the $F_\nu(12\,\mu\mathrm{m})$ of the face-on SED. The other model parameters are similar for all SEDs: $N_0 = 7.5$, $N_{\mathrm{tot}} = 18010$, $r_{\mathrm{out}} = 300$, $\alpha = -1$, $\Theta_0 = 45$. See Sect. 5.6.1 for their explanation. The thin black line marks $12\,\mu$m.

7.2.2. Dependency on the optical AGN class

The dependency of the AGN optical classification (listed in Tables A.4, B.5 and B.7) for the luminosity ratios and the contributing luminosities is displayed in Fig. 7.3. To examine the effect of the intermediate Seyfert classes, all classes are plotted separately. The distributions of the $12\,\mu$m and 2-10 keV luminosities for the individual classes show again the difference between type 1 and type 2 objects which is particularly strong for Sy 1.0 compared to Sy 2.0. The former are distributed only over a narrow range of one order of magnitude, while the latter spread over the whole range of several orders of magnitude. The LINER are, of course, distributed only at low luminosities. This characteristics are also present in $L_{14-195\mathrm{keV}}$ but to a lesser extent. The distribution of the mean values and their standard deviations looks roughly similar for all luminosities, on the contrary, the ratios reveal some differences between the different luminosity distributions. Sy 1.2 exhibit the highest $R^{\mathrm{M}}_{\mathrm{X}}$ while it is lowest for the Sy 1.0. This might indicate a different inclination of the clumpy torus with respect to the observer. However, the difference between Sy 1.0 and Sy 1.2 or 1.5 is presumably not related to obscuration effects but is rather dependent on the metallicity (chemical composition) of the line emitting gas, which controls the optical emission line ratios used for the Sy classification. Therefore, no significant difference between the luminosity ratios of Sy 1.0 to 1.5 is expected,

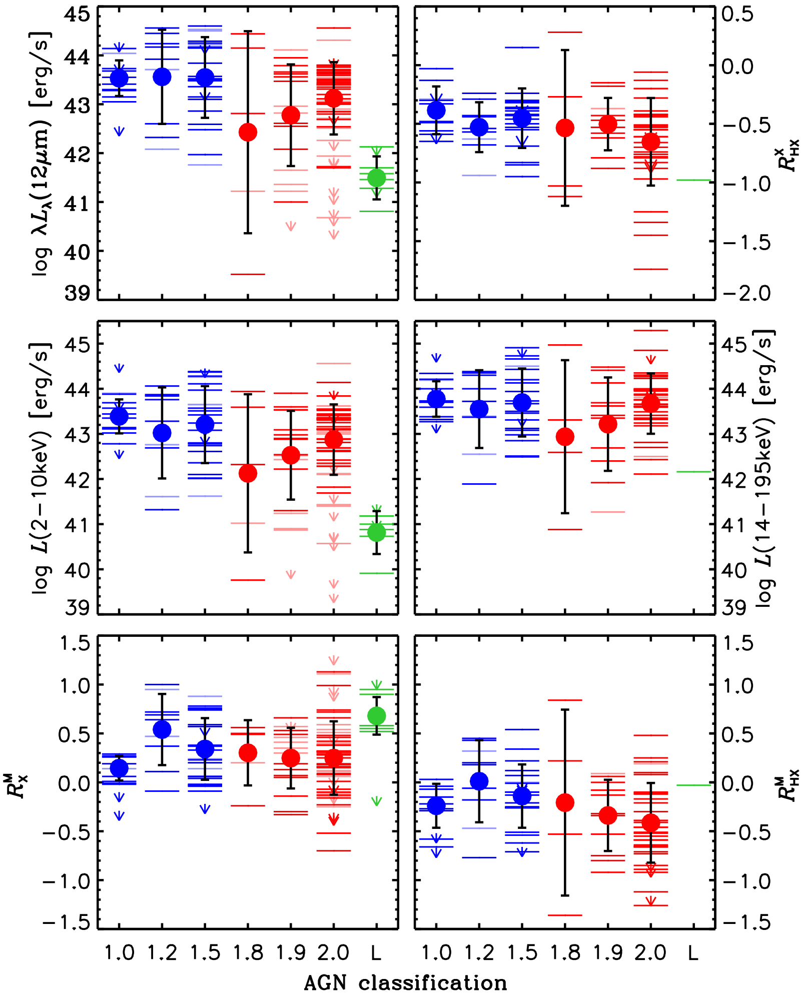

Figure 7.3: Dependencies of the luminosities and ratios on the optical AGN classification (always abscissa): top-left: for $\lambda L_\lambda(12\,\mu\mathrm{m})$; middle-left: for $L_{2-10\mathrm{keV}}$; bottom-left: for $R^{\mathrm{M}}_{\mathrm{X}}$; top-right: for $R^{\mathrm{X}}_{\mathrm{HX}}$; middle-right: for $L_{14-195\mathrm{keV}}$, bottom-right: for $R^{\mathrm{M}}_{\mathrm{HX}}$. Each horizontal line represents one object, arrows are upper-limits. In blue are all classes counted as type 1 AGN, and in red all type 2 AGN; green are LINERs. The filled circle marks the mean of each distribution and the black error bar its standard deviation.

and the reason for the low $R^{\mathrm{M}}_{\mathrm{X}}$ of the Sy 1.0 remains unknown.

On the other hand, the more obscured Sy 1.8-2.0 should have lower $\langle R^{\mathrm{M}}_{\mathrm{X}} \rangle$ and $\langle R^{\mathrm{M}}_{\mathrm{HX}} \rangle$ in the clumpy torus model by ~ 0.3 dex (Sect. 7.2.1). Indeed, the ratios are lower for Sy 1.8-1.9, but Sy 2.0 surprisingly exhibit a higher observed $R^{\mathrm{M}}_{\mathrm{X}}$, which is in contradiction to this picture. An explanation for this might be either additional sources of MIR emission in Sy 2.0 (i.e. an intrinsic difference), or the uncertainties in the X-ray absorption correction. We have to remember that most Sy 2.0 are highly obscured and sometimes also CT.

Anyway, the standard deviations of all Sy classes overlap and hence any statistical significant difference between them can only be indicated by a KS test. When comparing $R^{\mathrm{M}}_{\mathrm{X}}$ for all type 1 AGN (Sy 1.0-1.5; $R^{\mathrm{M}}_{\mathrm{X}} = 0.34 \pm 0.32$) to all type 2 (Sy 1.8-2.0; $R^{\mathrm{M}}_{\mathrm{X}} = 0.26 \pm 0.035$), the test yields $D_{\mathrm{KS}} = 0.20$; $p_{\mathrm{KS}} = 0.25$ and hence a high probability that both samples have been drawn from the same parent distribution. On the other hand, if taking into account only Sy 1.0 ($R^{\mathrm{M}}_{\mathrm{X}} = 0.14 \pm 0.13$) and Sy 2.0 ($R^{\mathrm{M}}_{\mathrm{X}} = 0.26 \pm 0.37$), then the difference becomes somewhat significant ($D_{\mathrm{KS}} = 0.49$; $p_{\mathrm{KS}} = 0.025$). This is the largest statistical difference between the Sy classes for $R^{\mathrm{M}}_{\mathrm{X}}$. Finally, LINERs exhibit a significantly higher $R^{\mathrm{M}}_{\mathrm{X}}$ (0.68 ± 0.19) than the other classes, i.e. the KS-test between Sy and LINERs yields $D_{\mathrm{KS}} = 0.76$ with $p_{\mathrm{KS}} = 0.001$. This result implies that LINERs are indeed a special class that is dominated by an additional MIR emission source, e.g., a jet or an ADAF.

All these results are also valid for the ratio with the 14-195 keV luminosities, $R^{\mathrm{M}}_{\mathrm{HX}}$, only that here $\langle R^{\mathrm{M}}_{\mathrm{HX}} \rangle$ for the Sy 2.0 is lowest in agreement with the clumpy torus picture. This also leads to a significant difference between type 1 and 2 AGN ($D_{\mathrm{KS}} = 0.41$ with $p_{\mathrm{KS}} = 0.0009$), the ratios are $R^{\mathrm{M}}_{\mathrm{HX}} = -0.13 \pm 0.33$ for type 1 and $R^{\mathrm{M}}_{\mathrm{HX}} = -0.38 \pm 0.45$ for type 2 AGN. Therefore, it is quite likely that the high $\langle R^{\mathrm{M}}_{\mathrm{X}} \rangle$ for the Sy 2.0 is indeed caused by insufficient absorption correction.

Looking at the X-ray ratio $R^{\mathrm{X}}_{\mathrm{HX}}$, it seems on first glance that there is as well a significant difference between Sy 1.0 ($\langle R^{\mathrm{X}}_{\mathrm{HX}} \rangle = -0.39 \pm 0.20$) and Sy 2.0 ($\langle R^{\mathrm{X}}_{\mathrm{HX}} \rangle = -0.65 \pm 0.37$) with $D_{\mathrm{KS}} = 0.42$ and $p_{\mathrm{KS}} = 0.09$. However, this is caused by the outliers identified in Sect. 6.6, 3C 105, 2MASX J06403799, and 2MASX J09180027. If they and NGC 6240, which has large uncertainties in $L_{2-10\mathrm{keV}}$, are excluded, the luminosity ratio for the Sy 2.0 becomes $\langle R^{\mathrm{X}}_{\mathrm{HX}} \rangle = -0.53 \pm 0.27$ and the KS difference significance drops to $D_{\mathrm{KS}} = 0.25$ with $p_{\mathrm{KS}} = 0.15$. And therefore, there is no significant difference in $R^{\mathrm{X}}_{\mathrm{HX}}$ for the different Seyfert classes, or AGN types in general. Of the LINERs, only NGC 1052 was detected so far by BAT, and hence no statement can be made for their relation with $R^{\mathrm{M}}_{\mathrm{HX}}$ or $R^{\mathrm{X}}_{\mathrm{HX}}$.

In summary, there are no large differences in the 12 μm–2-10 keV luminosity ratio for the different Seyfert classes (except Sy 1.0). Instead, a difference of 0.25 dex is indicated in the 12 μm–14-195 keV ratio, which is of the same order as expected from the clumpy torus models. On the other hand, there is no evidence for an intrinsic difference between type 1 and 2 AGNs, instead all Seyferts exhibit surprisingly uniform luminosity ratios. However, the results for the LINERs indicate a significant deviation from the Seyfert class in general.

7.2.3. Luminosity-dependency

Another way to look at the relation of the luminosity ratios with the classification and the total luminosity is by plotting $R^{\mathrm{M}}_{\mathrm{X}}$, $R^{\mathrm{M}}_{\mathrm{HX}}$, and $R^{\mathrm{X}}_{\mathrm{HX}}$ over the X-ray luminosity in either 2-10 keV or 14-195 keV (Fig. 7.4). Note that plotting functions of the same quantity on the abscissa and ordinate can result in artificial correlations due to correlations of the errors. Indeed a weak anti-correlation might be present for $R^{\mathrm{M}}_{\mathrm{X}}$ and $R^{\mathrm{M}}_{\mathrm{HX}}$ with the X-ray luminosity (Spearman rank: $\rho \approx -0.26$ and $p \approx 0.007$) in Fig. 7.4, which is attributed to this effect. Again, the Sy 1.0 span a narrow range in ratio and luminosity in all three plots, while the Sy 2.0 are scattered over the whole range. Furthermore, it becomes visible, in particular in the $R^{\mathrm{M}}_{\mathrm{HX}}$ plot (middle), that the Sy 1.2-1.5 exhibit the highest ratios and are distributed toward the highest luminosities (apart from a few Sy 2.0). At these high X-ray luminosities ($\gtrsim 10^{44}$ erg/s), $R^{\mathrm{M}}_{\mathrm{X}}$ and $R^{\mathrm{M}}_{\mathrm{HX}}$ seem to decline with a slope ~ 1, while $R^{\mathrm{X}}_{\mathrm{HX}}$ is declining much slower in the same range. Therefore, $\lambda L_{\lambda}(12\,\mu\mathrm{m})$ would be the main driver for this effect, if it is real and not caused by an selection effect. Such an effect could be expected by the concept of a receding or flattening of the torus with increasing luminosity (Sect. 2.2.3), leading to a lower covering factor and, thus, less MIR emission at the same bolometric luminosity. The result would be an under-density of type 2 AGN at high luminosities as observed in the BAT sample. However, the current data are insufficient for testing this scenario, and instead, I can only constrain the negative slope of any AGN global dependency of $R^{\mathrm{M}}_{\mathrm{X}}$ with $L_{2-10\mathrm{keV}}$ to be ≥ 0.17 at 3σ confidence.

7.2.4. Dependency on the nuclear obscuration

An increasing angle between the vertical axis of the putative torus and the line of sight implies an increasing amount of obscuration by additional clouds intersecting the view of the observer toward the AGN. Therefore, the nuclear obscuration, measured, e.g., by the hydrogen column density N_{H} from X-ray data, should be a better indicator of the torus inclination than the optical classification. Of course, most objects with a large nuclear obscuration are classified as type 2 AGN in the optical, and the other way around for type 1 with the low N_{H}. However, there is not a one-to-one correspondence between N_{H} and the AGN type. As already mentioned, the torus models predict a dependency of the MIR–X-ray luminosity ratio with the inclination of the torus and thus with N_{H}. Hence, a statistical sample of AGN should exhibit some kind of dependency of the luminosity ratios on N_{H} (listed in Tables A.4 for the LLAGN, in B.5 for the BAT AGN, and in B.7 for the other AGN). Neither Horst et al. (2008) nor G09 have found evidence for such a dependency. However, their samples were much smaller, thus, I investigate once more the relations of $R^{\mathrm{M}}_{\mathrm{X}}$, and also $R^{\mathrm{M}}_{\mathrm{HX}}$ and $R^{\mathrm{X}}_{\mathrm{HX}}$, with N_{H} (Fig. 7.5). In general, the column density roughly separates type 1 and 2 AGN, with the latter having on average higher N_{H}. Nevertheless, apart from the Sy 1.0, all other classes are distributed over many orders of magnitude in N_{H}.

In addition, some objects with peculiar N_{H} values are noticed: NGC 235A is the only Sy 1.0 with a high N_{H} ($10^{23.5}\mathrm{cm}^{-2}$), which is from Winter et al. (2009a), who also classify this object as Sy 2.0, contrary to Véron-Cetty and Véron (2010). On the other hand, its luminosity ratio is in perfect agreement with the other Sy 1.0. Unfortunately, there is not other N_{H} measurement

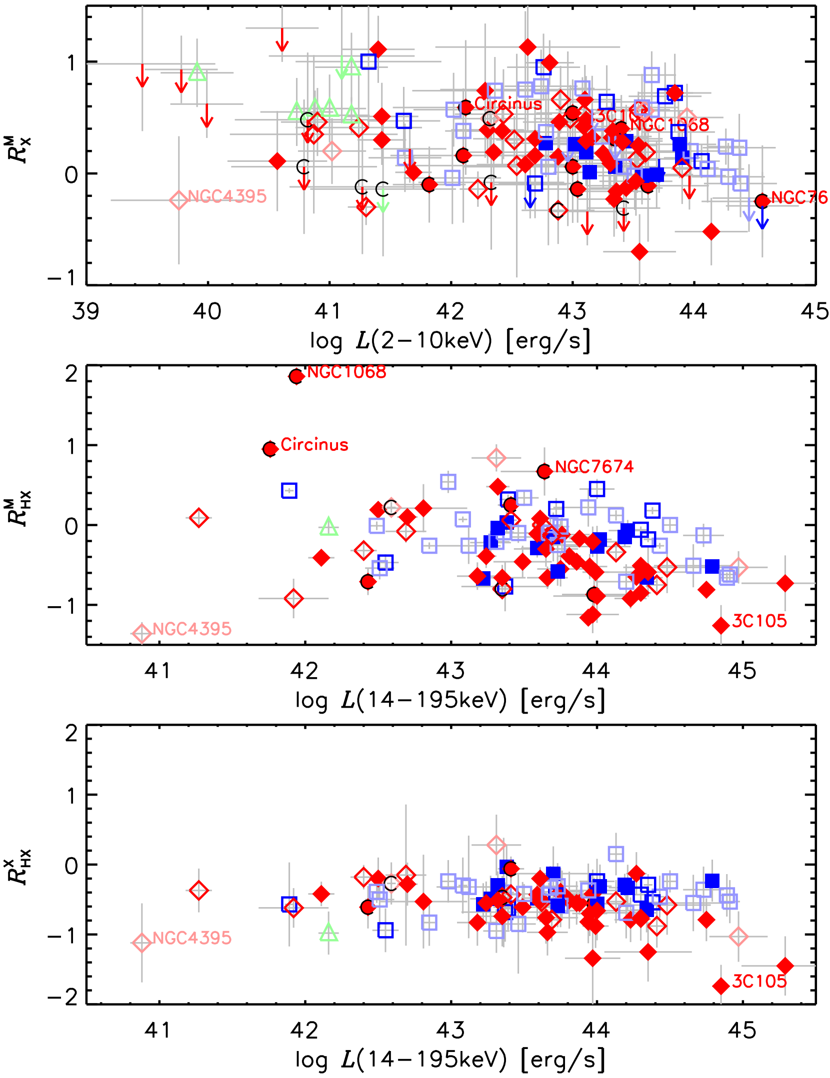

Figure 7.4: Dependencies of the luminosity ratios on the X-ray luminosities. Top: for R_X^M versus $L_{2-10\mathrm{keV}}$; middle: R_{HX}^M versus $L_{14-195\mathrm{keV}}$; bottom: R_{HX}^X versus $L_{14-195\mathrm{keV}}$. Blue squares are type 1 AGN: Sy 1.0 (filled), Sy 1.2 (open), Sy 1.5 (light-blue open); red diamonds are type 2 AGN: Sy 1.8 (light-red open), Sy 1.9 (open), Sy 2.0 (filled); green triangles are LINERs.

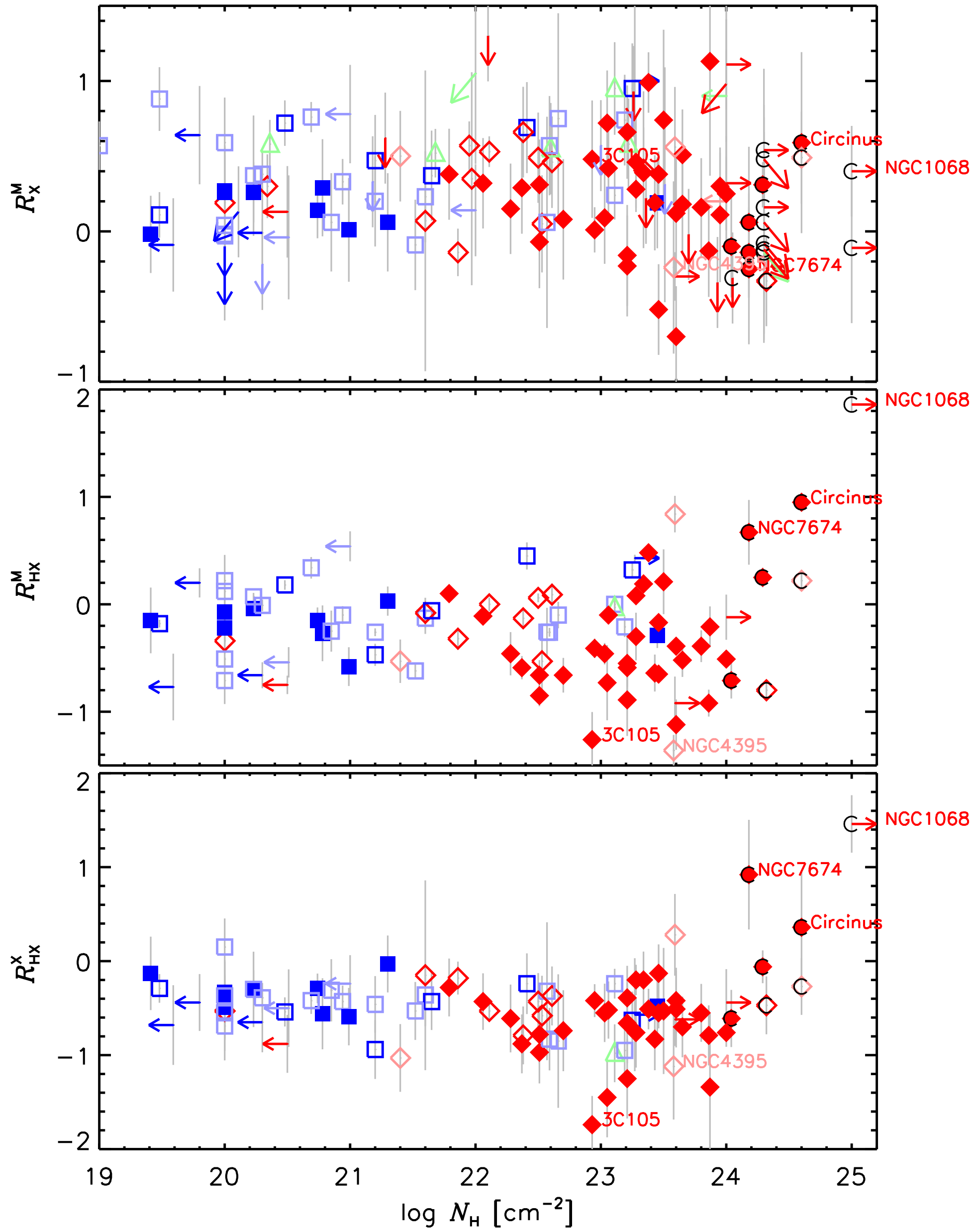

Figure 7.5: Dependencies of the luminosity ratios on the X-ray column density N_H. Top: for R_X^M; middle: R_{HX}^M; bottom: R_{HX}^X. Blue squares are type 1 AGN: Sy 1.0 (filled), Sy 1.2 (open), Sy 1.5 (light-blue open); red diamonds are type 2 AGN: Sy 1.8 (light-red open), Sy 1.9 (open), Sy 2.0 (filled); green triangles are LINERs.

published, which would allow confirmation of the X-ray properties. Furthermore, of the Sy 1.2, ESO 323-G077 and NGC 4051 also have exceptionally high N_H ($10^{23.3}$ and $10^{23.27}\mathrm{cm}^{-2}$). The value for ESO 323-G077 is taken from Hönig et al. (2010) based on the average from Beckmann et al. (2006) and Malizia et al. (2007). Taking into account its peculiar position in Fig. 7.5, it is likely that the its "true" N_H is much closer to the low value given in the latter work ($N_\mathrm{H} = 10^{22.8}\mathrm{cm}^{-2}$), or even lower: the authors argue that an unabsorbed fit as well gives good results. NGC 4051 is a special case because of its enormous X-ray variability: while its 2-10 keV emission is modeled by Winter et al. (2009a) without any obscuration component, it is interpreted to be CT by Panessa et al. (2006) and also has a high obscuration in Brightman and Nandra (2011), which is adopted here. Note as well that Winter et al. (2009a) classify it as Sy 1.5 contrary to Véron-Cetty and Véron (2010) again.

Furthermore, some type 2 AGN are located on the low N_H side: in particular, the three Sy 1.9, Mrk 1018, ESO 416-G002, and NGC 7679, exhibit $N_\mathrm{H} \leq 10^{20.5}\mathrm{cm}^{-2}$. The values of the former two are taken from Winter et al. (2009a) with Mrk 1018 being classified as Sy 1.5 in the same work. The peculiarity of NGC 7679 has already been discussed in Horst et al. (2008). However, as these objects exhibit luminosity ratios very close to the average, I do not further investigate these cases. Finally, NGC 7582 is the Sy 2.0 with the lowest N_H ($10^{21.79}\mathrm{cm}^{-2}$) which is an average from Dadina (2007) and Brightman and Nandra (2011).

Surprisingly, neither R^M_X ($\rho = -0.02$; $p = 0.8$) nor R^M_HX ($\rho = -0.13$ and $p = 0.2$) show any significant correlation with the column density for the AGN population as a whole. Furthermore, the 3σ upper limit on the slope of a global R^M_X-dependency on $\log N_\mathrm{H}$ is -0.09 (-0.14 for R^M_HX). The only evident trend is that all objects exhibiting low R^M_X and R^M_HX also have high column densities $N_\mathrm{H} \gtrsim 10^{23}\mathrm{cm}^{-2}$. Nevertheless, $\langle R^\mathrm{M}_\mathrm{X} \rangle$ is similar for both low-obscuration AGN ($\log N_\mathrm{H} \leq 21.5$) and high-obscuration AGN ($\log N_\mathrm{H} \geq 23$), which does not depend on the exact chosen N_H-threshold. Also the KS-test reveals no difference between any sub-samples that have been made with cuts for various column densities.

The same is true for R^X_HX, which is constant for all AGN, except for some Sy 2.0 at $N_\mathrm{H} \gtrsim 10^{23}\mathrm{cm}^{-2}$ that either show extremely low or high ratios. This indicates that in the high ratio cases the $L_{14-195\mathrm{keV}}$ is significantly absorbed, while in the low-ratio cases, either the absorption-correction for $L_{2-10\mathrm{keV}}$ might be overestimated leading to too high $L_{2-10\mathrm{keV}}$, or these objects are affected by exceptionally changes in $F_{14-195\mathrm{keV}}$.

Based on the 3σ upper limit of $R^\mathrm{M}_\mathrm{X} \propto -0.1 \log N_\mathrm{H}$, I conclude that the MIR–X-ray luminosity ratio of AGN is independent of the nuclear obscuration measured with the X-ray hydrogen column density. Although this contradicts expectations from current torus models, it might be possible to modify the latter to account for this now verified observational result.

7.2.5. The role of the accretion rate

Another intrinsic AGN property that can obviously have an influence on the MIR–X-ray emission ratio is the accretion rate of the SMBH. In fact, it is presumably the most important parameter, determining the structure of the accretion disk and, thus, also affecting the whole SED of the AGN (Sect. 2.3). Therefore, one would clearly expect the accretion rate to influence the MIR and X-ray emission and their ratio as well.

Unfortunately, the accretion rate is difficult to measure because current technology does not allow to resolve the accretion disks. Instead, I use the Eddington ratio, $\eta_{\mathrm{Edd}} = L_{\mathrm{Bol}}/L_{\mathrm{Edd}}$, as a proxy of the accretion rate. The X-ray luminosity is often used to estimate L_{Bol} (e.g., Vasudevan and Fabian 2007; Vasudevan et al. 2009), where $L_{\mathrm{Bol}} = 10L_{2-10\,\mathrm{keV}}$ is a reasonable choice, and the exact value of the bolometric correction factor does not affect the qualitative results of this section.

The required black hole masses of the AGN have been compiled from the literature with preference given to the most recent and precise determinations. They are listed in the Tables A.4 for the LLAGN, Table B.5 for the BAT AGN, and inTables B.7 for the other AGN. In most cases, the only available mass estimate comes from using the empirical M_{BH}–σ_* relation (Gebhardt et al. 2000; Ferrarese and Merritt 2000; Tremaine et al. 2002), and in those cases the given reference is for the stellar velocity dispersion, σ_*. Furthermore, the newest determination of the relation (Graham et al. 2011) is used, for which the intrinsic scatter is estimated to be 0.37 dex for elliptical galaxies, and 0.36 dex for spirals. Here, these values will be adopted as general uncertainty for those cases where M_{BH} is determined from σ_*. Finally, for many of the lesser known BAT AGN, not even σ_*-measurements are available, so that I use the M_{BH} estimates from Winter et al. (2009a) from the K-band magnitudes, and adopt a conservative generic uncertainty of 0.5 dex for those objects.

Fig. 7.6 shows the distributions of the luminosity ratios, $R^{\mathrm{M}}_{\mathrm{X}}$, $R^{\mathrm{M}}_{\mathrm{HX}}$ and $R^{\mathrm{X}}_{\mathrm{HX}}$ versus the computed accretion rate. In general, the Seyferts are populating a large range in η_{Edd} from ~ 1 to $\sim 10^{-4}$, while type 1 AGN have a slight over-density at high accretion rates $\eta_{\mathrm{Edd}} \gtrsim 0.05$. This has already been found by Winter et al. (2009a) and results from the $L_{2-10\mathrm{keV}}$ distribution, when M_{BH} is approximately equally distributed for type 1 and 2 AGN. However, the two objects accreting at the maximum accretion rate ($\eta_{\mathrm{Edd}} \approx 1$) are both CT type 2 AGN (IC 3639 and NGC 7674). Furthermore, there seems to be no general relation between $R^{\mathrm{M}}_{\mathrm{X}}$ or $R^{\mathrm{M}}_{\mathrm{HX}}$ and η_{Edd} for the Seyferts or any of their sub-classes.

On the contrary, all AGN with $\eta_{\mathrm{Edd}} \lesssim 10^{-4}$, in particular the LINERs (M 87, M 81, NGC 4261, NGC 1097, and NGC 1052), exhibit a high $R^{\mathrm{M}}_{\mathrm{X}}$. Indeed, the maximum, statistically significant, difference is yielded with the KS-test when splitting the AGN at $\eta_{\mathrm{Edd}} = 10^{-3.8}$ with $D_{\mathrm{KS}} = 0.82$ and $p_{\mathrm{KS}} = 0.0004$. This implies that around this η_{Edd} value something changes in the MIR emitting AGN structure. Note that for all LINERs except NGC 1097, we can exclude SF as a possible cause (Sect. 4.5.1 and Table A.3). For $R^{\mathrm{M}}_{\mathrm{HX}}$, this is also indicated for the 4 objects detected by BAT with $\eta_{\mathrm{Edd}} < 10^{-3.8}$. The appearance of an additional component that contributes significantly to the MIR emission, leading to a high $R^{\mathrm{M}}_{\mathrm{X}}$ and $R^{\mathrm{M}}_{\mathrm{HX}}$, seems very likely. It is well-known that, in particular, LINERs have strong jets that are bright at least at radio and sub-mm wavelengths (Sect. 2.3). The synchrotron emission from these jets can easily also dominate the MIR region as demonstrated for, e.g., M 87 (Perlman et al. 2007), which is as well the observed AGN with by far the lowest η_{Edd}, The case of M 87 is further discussed in Sect. 7.4.1. Also from the theoretical point of view, Falcke and Markoff (2000) have argued that the jet might dominate the AGN emission at low accretion rates and have

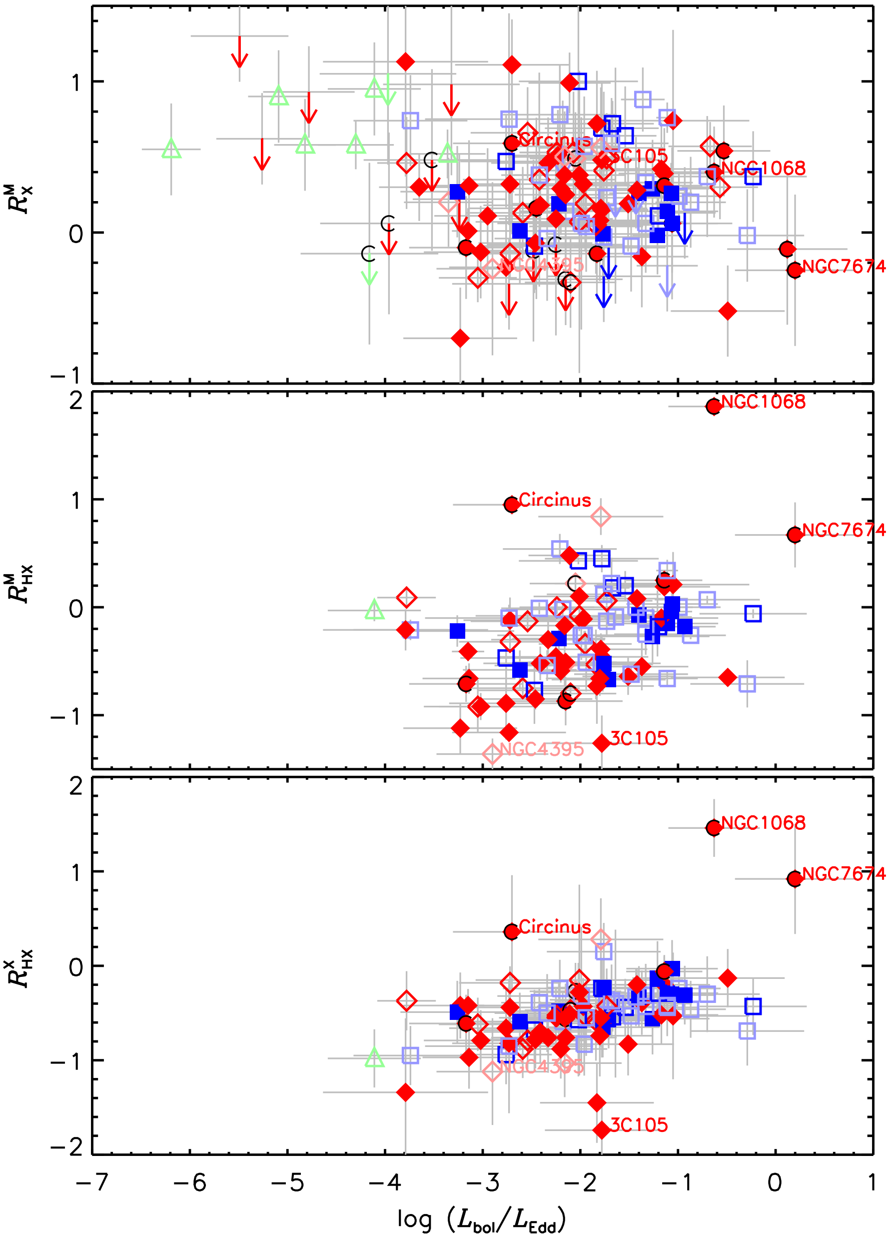

Figure 7.6: Dependencies of the luminosity ratios on the accretion rate measured with the η_{Edd}. Top: for R_X^M; middle: R_{HX}^M; bottom: R_{HX}^X. Blue squares are type 1 AGN: Sy 1.0 (filled), Sy 1.2 (open), Sy 1.5 (light-blue open); red diamonds are type 2 AGN: Sy 1.8 (light-red open), Sy 1.9 (open), Sy 2.0 (filled); green triangles are LINERs.

presented a jet model that explains the observed SED of Sgr A*. A similar model was used by Markoff et al. (2008) to fit the extensive multiwavelength data of M 81 successfully, the object with the second-lowest η_{Edd} in the our sample. Note that most of the MIR synchrotron emission is expected to originate in the base of the jet that is much smaller than the resolved scale r_0 of the presented HR MIR observations. In addition, Yuan and Cui (2005) predict that the jet (if present) should even dominate the X-ray emission at rates below $\eta_{\mathrm{Edd}}^{\mathrm{crit}} \approx 10^{-5}$. In our LLAGN sample, this would be the case for M 87, M 104 and IC 1459, while, e.g., NGC 1052, NGC 4261 and M 58 should be ADAF dominated. All these objects are also included in the sample of Yuan et al. (2009), who have successfully tested the above prediction by SED fitting. These authors have not included a torus model though, and instead, the MIR emission is mainly produced by the ADAF. In this case, the MIR-X-ray luminosity ratio is predicted to be roughly one for the ADAF-dominated sources and to be significantly higher for the jet-dominated sources M 87 and M 104. However, this difference in $R_{\mathrm{X}}^{\mathrm{M}}$ is not evident in Fig. 7.6, and the predicted MIR flux is much lower than the observed one, as is further discussed in Sect. 7.4.1 for M 87. A better coverage at these lowest accretion rates will be necessary in order to distinguish between these ADAF and jet models.

In summary, the MIR–X-ray ratio is constant ($R_{\mathrm{X}}^{\mathrm{M}} = 0.28 \pm 0.34$) for all AGN with moderate or high accretion rates ($10^{-3.8} < \eta_{\mathrm{Edd}} \lesssim 1$), while it is significantly higher ($R_{\mathrm{X}}^{\mathrm{M}} = 0.71 \pm 0.20$) for all low-accretion rate objects ($\eta_{\mathrm{Edd}} \leq 10^{-3.8}$). Nevertheless, no anti-correlation is found to be valid over the whole range of η_{Edd} (Spearman rank $\rho = -0.10; p = 0.28$).

Finally, the X-ray ratio, $R_{\mathrm{HX}}^{\mathrm{X}}$, seems to follow an increasing trend with increasing accretion rate ($\rho = 0.51; p \approx 10^{-7}$) with a slope of $\sim 0.17 \pm 0.06$ and a very low intrinsic scatter ($\sigma_{\mathrm{int}} = 0.08 \pm 0.08$). However, one has to keep in mind again that the scatter in $L_{2-10\mathrm{keV}}$ on both axis might correlate, leading to an artificial correlation with positive slope. Nevertheless, when using $\lambda L_\lambda(12\,\mu\mathrm{m})$ instead of $L_{2-10\mathrm{keV}}$ for the computation of L_{bol}, the correlation still remains significant albeit becoming weaker ($\rho = 0.41; p \approx 10^{-5}$). Therefore, I conclude that the ratio of the 2-10 keV to the 14-195 keV emission indeed weakly depends on the accretion rate. Its origin is clearly related to the accretion disk and the innermost region around the SMBH, whose investigation is beyond the scope of this work, though.

All together, these results verify the importance of the accretion rate as one of the most fundamental parameters in AGN, influencing also the MIR and X-ray emission relations to some extend.

7.2.6. Influence of the host galaxy

The investigation of relations between the MIR and X-ray emission of AGN with some of the important nuclear properties has yielded only weak dependencies. In this section, I will conclude this exploration of the AGN luminosity ratios with a comparison to the basic properties of the host galaxies, i.e. morphology and inclination.

Although the presented MIR observations have been performed at HR, it is still possible that non-AGN related emission or absorption is affecting the data, which might be the case, in particular, for highly inclined host galaxies. In those cases, our line of sight toward the nucleus is passing through the galactic disk (if the host is a spiral), which usually contains large amounts of obscuring material and emission regions. But also for lower inclination angles, i, obscuring material located in the bulge or circum-nuclear region could be affecting the observed nuclear X-ray and MIR emission. Therefore, one would expect that edge-on galaxies have a higher probability to harbor AGN that are highly obscured (high N_H), and exhibit also a higher MIR–X-ray luminosity ratio. But then, no correlation has been found between the AGN type (or the orientation of the obscuring torus) and the orientation of the host galaxy. In addition, the majority of AGN appear to exist in earlier type galaxies, i.e. ellipticals (E) or bulge-dominated galaxies (S0; e.g., Ho 2008).

I have collected the host galaxy morphologies and inclinations from the Hyperleda data base (Paturel et al. 2003) and list them for individual objects in the Tables A.1, B.1 and B.6 whenever available. Note that some of the lesser known (and often farther away) BAT AGN do not have determinations of their morphology or inclination. For many other objects both properties are quite uncertain, which can be quantified by the uncertainty in the revised de Vaucouleurs morphological types. The latter is a numerical coding scheme with negative numbers for elliptical and early-type galaxies (−5 to 0) and with rising positive numbers for increasing prominence of spiral arms. Finally, dwarf galaxies and irregulars have the highest numbers (8-10). I use this scheme here as well.

As expected, the host galaxy inclination and morphology for all AGN are randomly distributed, with the average morphological type being relatively early (0.94 ± 2.85), as shown in Fig. 7.7. Type-1-AGN host galaxies are marginally earlier (lower) in type than those of type 2 AGN, but without statistical significance. Instead, the host morphologies are equally distributed for all AGN optical classifications. Apart from the dwarf (NGC 4395) and the irregular (NGC 985) galaxy, all AGN have de Vaucouleurs types $\lesssim 5$. Furthermore, there is no preferred inclination, neither for all AGN, nor for any of the sub-classes. However, 77% of the edge-on galaxies host AGN with $N_\mathrm{H} > 10^{22}\mathrm{cm}^{-2}$. In addition, the average column density for galaxies with $i \geq 80^\circ$ is $\langle \log N_\mathrm{H} \rangle = 22.74 \pm 1.56$, while it is $\langle \log N_\mathrm{H} \rangle = 22.17 \pm 2.76$ for AGN hosted in less-inclined galaxies. In particular, almost 30% of all type 2 AGN with a morphological type ≥ -2 have an inclination of 90°, compared to only 5% for the type 1 AGN. This implies that for a significant number of type 2 AGN the obscuration is caused by material outside the nucleus somewhere in the galactic disk. Such a relation could have important implications for studies of the AGN type dichotomy. Further tests for a much larger sample will be required, in addition to more detailed studies of the type 2 AGN with $i = 90^\circ$. However, for smaller host inclinations the AGN optical classification is independent of the basic host properties.

Finally, I compare the luminosity ratios with the host morphology (Fig. 7.8). No general correlation of the luminosity ratios with the morphological type are evident. The marked spirals with high inclinations, on the other hand, show a declining trend in R^M_X and R^M_HX with increasing de Vaucouleurs type, but of low significance (Spearman rank $\rho = -0.40$; $p = 0.18$).

I conclude that, apart from an over-density of type 2 AGN being hosted in edge-on galaxies, the MIR and X-ray luminosity ratios are in general unaffected by the host galaxy properties, and at least the HR MIR data do not suffer from any significant contaminating emission of

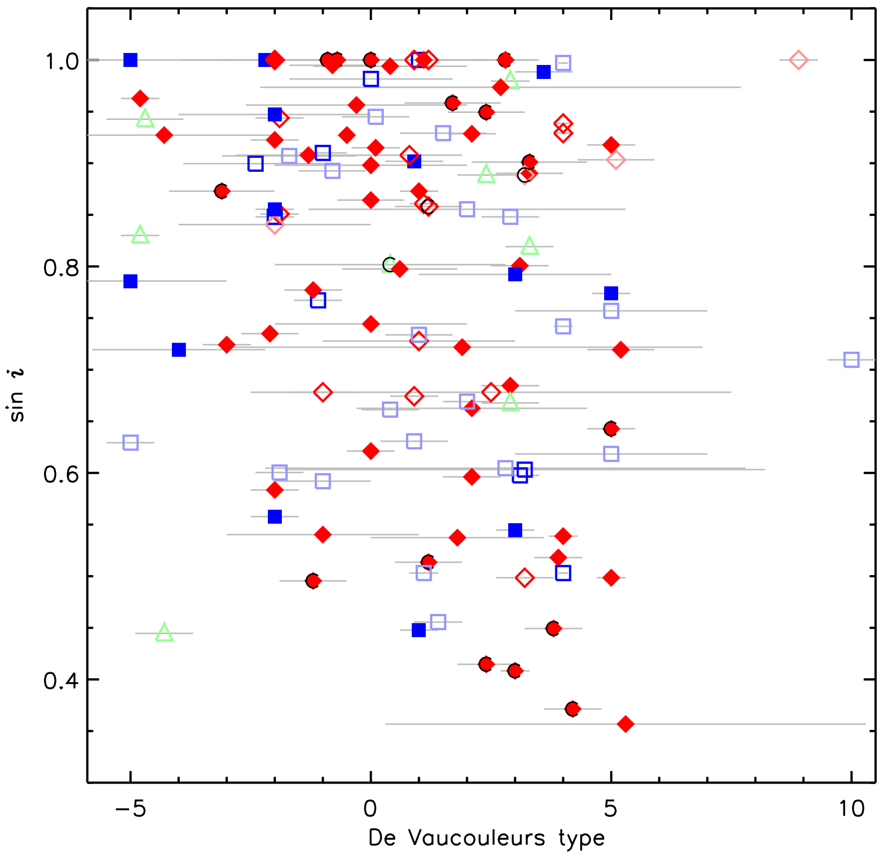

Figure 7.7: Relation of the host inclination *i* with the host morphology for the different AGN types. Blue squares are type 1 AGN: Sy 1.0 (filled), Sy 1.2 (open), Sy 1.5 (light-blue open); red diamonds are type 2 AGN: Sy 1.8 (light-red open), Sy 1.9 (open), Sy 2.0 (filled); green triangles are LINERs.

foreground regions in the host galaxy spirals.

7.3. Comparison to global MIR emission

In the previous chapters, I have demonstrated that the HR 12 μm emission is dominated by the AGN. For isolating its emission, the HR is of critical importance, as the comparisons with lower resolution data in Sect. 4.5 and 5.7 has already indicated. Therefore, it has to be expected that non-AGN emission increasingly affects objects, the more distant they are. However, studying and characterizing high-redshift AGN is very important for developing and testing AGN and galaxy evolution theories. For this reason, it is very useful to develop a diagnostic for determining the AGN contribution to the total 12 μm emission of galaxies. And the obtained HR data give a good opportunity for such an investigation.

The global 12 μm luminosity of galaxies, $\lambda L_\lambda^\mathrm{G}(12\,\mu\mathrm{m})$, can be measured by using the large-aperture *IRAS* photometry ($\theta_0 \approx 30''$), taken either from Sanders et al. (2003) or the NED

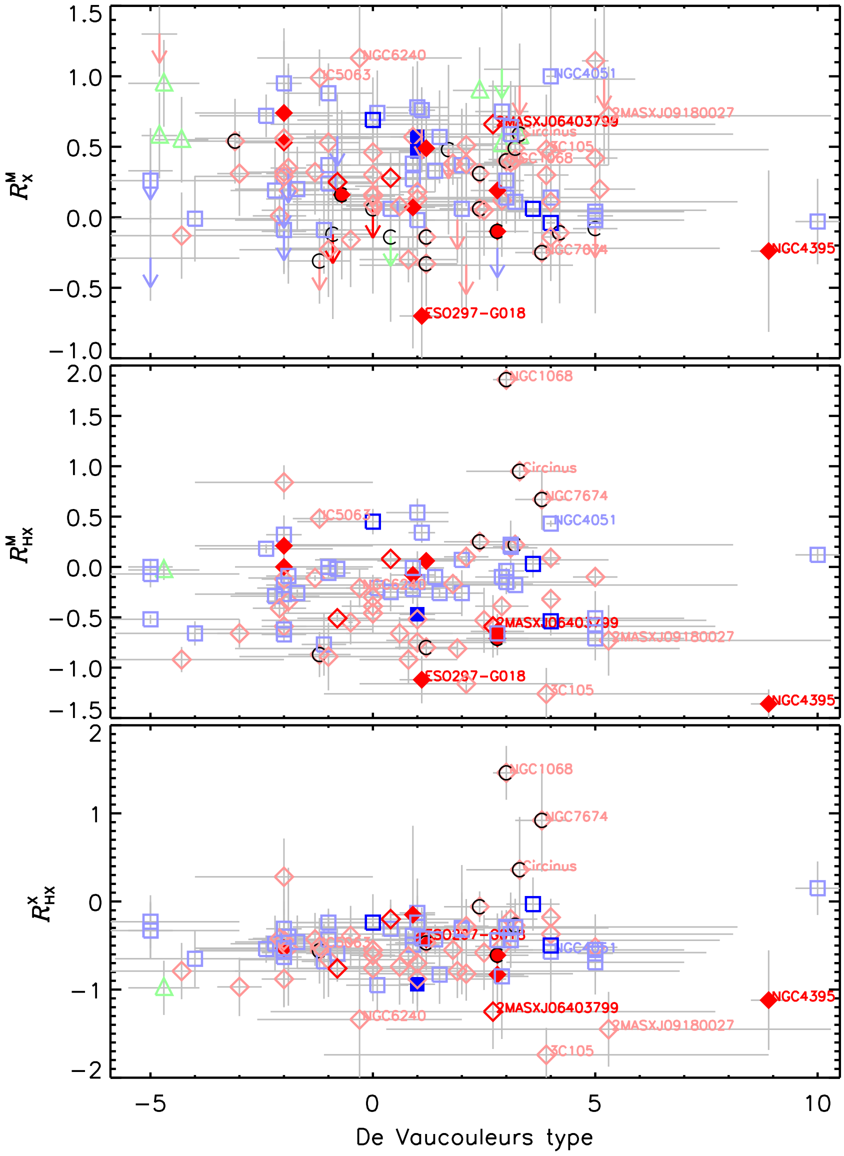

Figure 7.8: Dependencies of the luminosity ratios on the host morphological type. Top: for $R^{\mathrm{M}}_{\mathrm{X}}$; middle: $R^{\mathrm{M}}_{\mathrm{HX}}$; bottom: $R^{\mathrm{X}}_{\mathrm{HX}}$. Blue squares are type 1 AGN, red diamonds are type 2 AGN and green triangles are LINERs with filled symbols mark spirals (type ≥ −2) having $i = 90°$ and normal colored open symbols spirals with $i \geq 75°$.

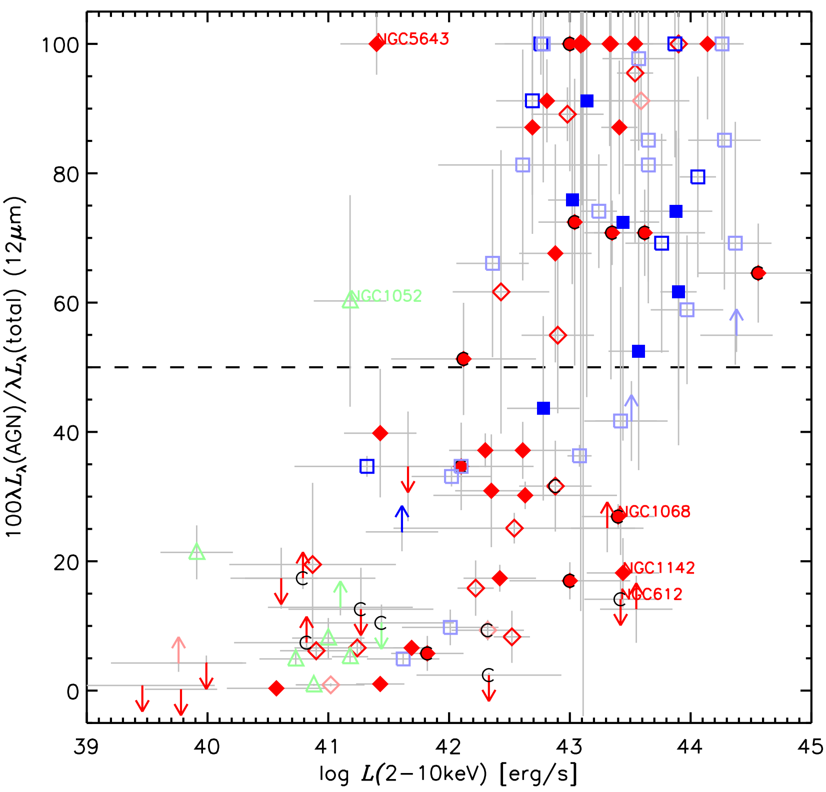

Figure 7.9: Fraction of total 12 μm luminosity that is emitted by the nucleus. It is measured by the ratio of HR to global luminosities versus the absorption-corrected hard X-ray luminosity. Blue squares are type 1 AGN: Sy 1.0 (filled), Sy 1.2 (open), Sy 1.5 (light-blue open); red diamonds are type 2 AGN: Sy 1.8 (light-red open), Sy 1.9 (open), Sy 2.0 (filled); green triangles are LINERs. $\lambda L_\lambda^{\mathrm{G}}(12\,\mu\mathrm{m})$ of all objects above the dashed line is AGN dominated.

database. For some fainter objects, only upper limits (or no *IRAS* photometry at all) are available. A few of those objects (2MASX J03565655, 3C 105, MCG -01-13-025, XSS J05054-2348, ESO 121-G028, 2MASX J06403799, and ESO 511-G030), however, have already been successfully observed with the new *WISE* space observatory (Wright et al. 2010), and for these I use the photometry available in the preliminary point-source catalog. $\lambda L_\lambda^{\mathrm{G}}(12\,\mu\mathrm{m})$ is listed for individual sources in the Tables A.1, B.1 and B.6, while Fig. 7.9 shows the ratio of the nuclear to global 12 μm luminosities over the absorption-corrected X-ray luminosities for all observed AGN. Note that for three objects (ESO 138-G001, XSS J05054-2348, and NGC 4507), $\lambda L_\lambda^{\mathrm{G}}(12\,\mu\mathrm{m})$ is significantly lower than the HR $\lambda L_\lambda(12\,\mu\mathrm{m})$, which is caused by the much wider filter band-passes ($\sim$ 8 to 15 μm) of *IRAS* and *WISE*. They include large parts of the shorter wavelength SED, which always has lower flux densities because of the red continuum and the commonly occurring silicate absorption. Therefore, I set $\lambda L_\lambda^{\mathrm{G}}(12\,\mu\mathrm{m}) := \lambda L_\lambda(12\,\mu\mathrm{m})$ for all objects that exhibit a higher MIR luminosity at HR than in *IRAS* and *WISE*.

In general, the nuclear fraction of the total MIR luminosity is increasing with increasing X-ray luminosity but with a large scatter of a factor ~ 2.5. Still, the correlation is significant: the

Spearman rank is $\rho = 0.65$ ($\log p = -10.82$). Consequently, the total MIR emission of many galaxies is dominated by non-nuclear emission and the AGN contribution dominates only at X-ray luminosities $\gtrsim 10^{43.6}$ erg/s. This finding agrees well with the results from Vasudevan et al. (2010) and emphasizes once more the need for high spatial resolution to isolate the AGN from surrounding processes. In particular, at $L_{2-10\mathrm{keV}} \sim 10^{42}$ erg/s the host contribution to the MIR is already 3 to 10 times higher than that of the nucleus. The only exceptions are NGC 1052 and NGC 5643 that are AGN dominated, although having $L_{2-10\mathrm{keV}} < 10^{42}$ erg/s. The lowest MIR ratios occur in NGC 1097, NGC 3486, NGC 4501, NGC 5033, and M 51a with $\lambda L_\lambda(12\,\mu\mathrm{m}) < 0.01 \lambda L_\lambda^\mathrm{G}(12\,\mu\mathrm{m})$. All of them are late-type spiral galaxies (de Vaucouleurs type > 3) with large star-forming regions.

In addition, $\sim 2/3$ of all type 1 AGN dominate $\lambda L_\lambda^\mathrm{G}(12\,\mu\mathrm{m})$, while this is the case for only half of the type 2 AGN. This effect appears stronger than expected from the unequal $L_{2-10\mathrm{keV}}$ distribution and indicates that many of the type 2 AGN are hosted in galaxies with high stellar activity, i.e. star formation. In particular, the Sy 2.0 in NGC 612, NGC 1142 and NGC 1068 contribute less than 30% to the total MIR emission, although the intrinsic powers of their AGN are quite high ($L_{2-10\mathrm{keV}} > 10^{43.4}$ erg/s).

The large scatter in the MIR emission fraction for AGN to the total emission over the whole range of X-ray luminosities prohibits the determination of an useful correction factor that could be used to determine the AGN contribution to the observed MIR emission for very distant or lowly resolved objects. However, as a rule of thumb, one can expect that the AGN dominates the global MIR emission when $L_{2-10\mathrm{keV}} \gtrsim 10^{43.6}$ erg/s.

7.4. Nature of the nuclear MIR emission

The MIR observations of local AGN presented here comprise the highest available angular resolution available with single-dish telescopes to the present day. Still, the nuclear emission has not been resolved, and its nature and origin have to be inferred indirectly instead. A powerful possibility to infer the nature of the point-like MIR emission is the characterization of its SED with multiple-band photometry, and spectroscopy (when the source is sufficiently bright in terms of flux). The other possibilities of measuring the light polarization or using infrared interferometers are difficult, either due to lack of facilities, or lack of sensitivity.

This thesis represents only the first step in measuring the AGN SEDs at HR with photometry in a few filters and comparison to spectra where available. Many AGN exhibit highly variable emission at various wavelengths, possibly even over the whole electromagnetic range. Variability cannot be taken into account here, but I would like to point out that, so far, variability in the MIR has been found to be of the order of 13% (and always $\lesssim 30\%$) in AGN (Neugebauer and Matthews 1999; but see Gorjian et al. 2004). On the contrary, much stronger variability (> 50%) is observed in the non-thermal emission from the innermost region of the accretion disk and jet at other wavelengths (e.g., X-rays or radio). Hence, at least the bulk of the MIR emission cannot have the same origin, but must originate much farther away from the SMBH.

On the other hand, we know from the obscuration observed at short wavelengths (optical to X-rays) that large amounts of dust have to exist around the accretion disk. As explained already in Sect. 2.2.3, this dust is heated by absorbing the UV emission from the accretion disk. Hence, the simplest explanation for the MIR emission is the thermal radiation from the obscuring dust, whichever spatial distribution it has. This is strongly supported by the presence of the silicate feature in the averaged HR data (Sect. 5.6). Furthermore, the absence of strong variability is a natural consequence of this scenario because the dust is distributed presumably in complex structures, e.g., clouds or filaments, surrounding the accretion disk on larger scale. Owing to this structure, any MIR response to the variable UV emission from the disk will be smoothed and stretched, resulting in overlap and weakening of the variability signal in the MIR.

Dust is also generated and massively heated by stellar processes, either in star forming regions or by old stellar populations, erupting dusty shells. Although many galaxy centers harbor SF regions and such stars, we could rule out SF as the origin of the MIR emission by comparison with lower resolution MIR spectra (Sect. 4.5.1 and 5.7.1). Furthermore, the independence of the MIR emission from the host properties (Sect. 7.2.6), and in particular, the extremely small scatter in the MIR–X-ray correlation strongly favor the AGN as the heating source for the dust.

The fact that this correlation holds over the whole probed range of luminosities indicates that the same heating process is working for all AGN, and, at least in MIR–X-ray space, there is no characteristic change evident for any luminosity (Sect. 6.5). Interestingly, the optical AGN class of the LINERs might be offset from the correlation at maximum 1 dex but follows the same slope as the Seyferts. The reason for this is clearly related to the accretion rate (Sect. 7.2.5) which seems to be the critical parameter deciding on the AGN structure rather than the absolute luminosity in any band. I attribute the systematically higher MIR–X-ray ratios that are exhibited by the lowest accretion rate objects to an additional (most likely) non-thermal component like the ADAF or jet. SF can be excluded because of the absence of PAH emission in these sources (Sect. 4.5.1). Thus, these objects might be intrinsically different to the other AGN and will need further investigation. Consequently, the LLAGN definition might not be applicable and one should rather define the low-accretion rate AGN (LARAGN; $\eta_{\mathrm{Edd}} \lesssim 10^{-3.8}$) as distinct group.

However, I conclude that all AGN (including the LARAGN) possess a significant MIR emission component caused by thermal radiation of AGN-heated dust. So far, only two AGN components are known to contain dust, the torus and the narrow-line region. It is likely that both structures are not clearly separated but interacting and overlapping. This connects to the model of Elitzur and Shlosman (2006), which combines the different components in one large clumpy (outflowing) structure. On the other hand, for most AGN, significant contribution to the 12 μm continuum by the NLR has been considered unlikely in the literature (Groves et al. 2006; Mor et al. 2009), while the dusty torus models reproduce the observed infrared SEDs quite well (Sect. 5.6.1; Hönig and Kishimoto 2010). In particular, the silicate feature is a key element for the success of these models: Smooth dust distributions predict this feature to be in strong emission for type 1 AGN contrary to observations which found it only in weak emission if at all in type 1 objects. Clumpy torus models on the other hand reproduce this observational results because the averaged emission of the individual clouds (with some having silicate in emission and others in absorption depending on their orientation toward the observer) always produces weak features. In addition, smooth dust distributions predict a difference in brightness of one order of magnitude depending on the viewing angle of the torus, which is contradicting the narrow scatter in the MIR–X-ray correlation with the at best small difference between type 1 and 2 objects. Hence, these results clearly favor a clumpy structure for the obscuring dust that seems to exist in all observed AGN, including those at lowest luminosities. Consequently, the unification model might still hold for LLAGN, as already suggested by, e.g., Panessa et al. (2006) and Maoz (2007).

Furthermore, Elitzur and Ho (2009) recently determined a threshold for the disappearance of the torus at very low accretion rates depending on the bolometric luminosity. None of the detected AGN is below this threshold. On the other hand, if there were no torus in the LARAGN at all and the MIR emission were completely caused by the jet or ADAF, the agreement between the slope (and normalization) with the MIR–X-ray correlation for brighter (torus-dominated) AGN seems surprising.

7.4.1. The case of M 87

M 87 is probably the best studied LINER, and indeed the observed MIR emission can be explained solely with synchrotron emission of different jet components (Perlman et al. 2007). However, this object lies close to the MIR–X-ray correlation. Here, one has to keep in mind, that the correlation lies in logarithmic space and thus an offset by 0.3 dex still agrees with a brighter synchrotron component in addition to the putative torus. To illustrate this rarely regarded possibility of the coexistence of a jet and a torus in LINERs, I show the SED for M 87 in Fig. 7.10. For the SED, data has been compiled from different sources: low-resolution data from Baes et al. (2010) and Cotton et al. (2009) covering the the far-infrared to radio wavelength region, the IRS MIR spectrum from Perlman et al. (2007), and HR data from Eracleous et al. (2010), Reunanen et al. (2010) and this work. The significant difference between the high and low resolution data becomes immediately obvious, and it is clear that the fit from Baes et al. (2010) is not describing the nuclear emission of M 87 but is dominated by the well-known extended jet in this object. On the other hand, Nemmen et al. (2011) has used the HR data (except the MIR) to fit a current AGN model to the whole SED. It consists of a jet and an ADAF component and reproduces the data well.

However, the MIR data was not taken into account in this fit, and the IRS spectrum indicates that this model might under-predict the MIR flux significantly, in particular, as the HR VISIR photometry gives the same fluxes. Therefore, an additional component might be needed to explain this emission, namely the torus. To motivate this, the 12 μm flux has been predicted from the MIR–X-ray correlation and used to normalize a typical torus model SED from Hönig and Kishimoto (2010), which is shown in Fig. 7.11 in more detail. In addition to the data and fits from Fig. 7.10, the best fit from Perlman et al. (2007) to the *Spitzer* spectrum consisting of several synchrotron components is shown as well. Finally, the sum of the torus SED and the best fit from Nemmen et al., scaled to the difference of the observed and predicted 12 μm emission, is shown. In particular in the *N*-band, it yields a better fit to the data and demonstrates

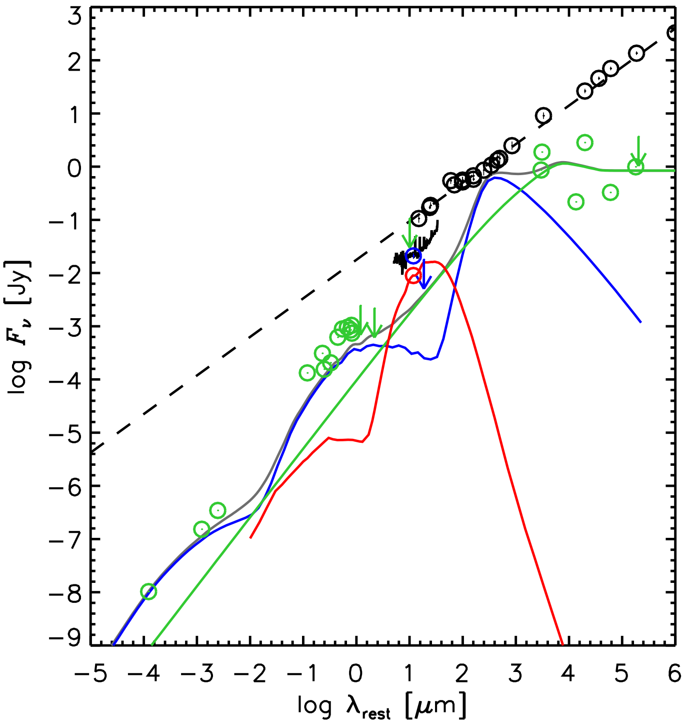

Figure 7.10: SED of M 87 in units of flux density versus restframe wavelength. Black open circles mark the far-infrared, sub-mm and radio data taken from Baes et al. (2010) and Cotton et al. (2009); the black dashed line represents a power-law fit to this data. The green circles are photometry taken from Eracleous et al. (2010) and the green (jet) and blue (ADAF) line represent a fit to these data from Nemmen et al. (2011); the gray line is their sum. The black solid line is the *Spitzer*/IRS spectrum from Perlman et al. (2007) and the blue data points are VISIR photometry from this work and Reunanen et al. (2010). The red circle marks the 12 μm flux predicted from the MIR–X-ray correlation and the red line is a clumpy torus model SED from Hönig and Kishimoto (2010) normalized to this flux.

that indeed a significant dust emission component cannot be excluded in M 87. In fact the SED in the N-band might indicate silicate in emission. The SED at shorter and higher wavelengths is significantly under-predicted indicating the possible presence of additional emission components. However, note that no fit with a combined model of jet, ADAF and torus was performed here, and hence significant improvement of the modeled SED might be possible.

Whether the clumpy torus model is the only explanation for the thermal MIR emission and/or needs modification is beyond the scope of this work. But I note, that the predicted dependency of the MIR–X-ray ratio with the inclination of the torus (measured by $N_{\rm H}$) could not be clearly verified. Instead, the MIR–X-ray correlation is exactly the same for unobscured and highly obscured AGN. On the other hand, it is remarkable that the type 1 AGN (or unobscured objects) show actually the strongest correlation with the least scatter, while type 2 objects are much more scattered. Together with the weak relation of the type 2 class and the

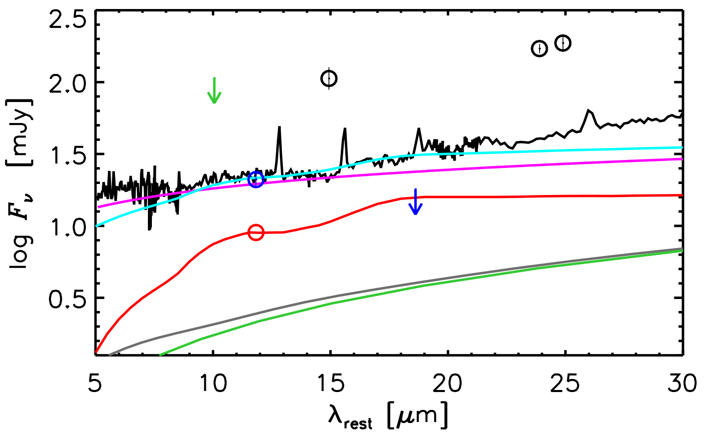

Figure 7.11: MIR SED of M 87 in units of flux density versus restframe wavelength. Black open circles mark the far-infrared, sub-mm and radio data taken from Baes et al. (2010) and Cotton et al. (2009). The green line represent the jet component from the fit of Nemmen et al. (2011) and the gray line the total of the fitting components. The black solid line is the *Spitzer*/IRS spectrum from Perlman et al. (2007) and the magenta line is the best fit from the same work. The blue data points are VISIR photometry from this work and Reunanen et al. (2010). The red circle marks the 12 μm flux predicted from the MIR–X-ray correlation and the red line is a clumpy torus model SED from Hönig and Kishimoto (2010) normalized to this flux. The cyan line represents the sum of the torus SED and the scaled fit from Nemmen et al..

nuclear obscuration with the host properties, this implies that type 2 AGN are a “mixed bag” of different objects, for which the obscuration is of different origin and happening on different scales. Hence, the type 1 objects might be the better candidates for a detailed follow-up study of the origin of the MIR emission and the nature of the torus.

8. Summary and future work

In this work, I have presented high-angular resolution mid-infrared imaging of two samples of local active galactic nuclei. The study of this local population of AGN is of fundamental importance for developing a general understanding of AGN phenomenon and will yield important constraints on the current theoretical AGN models. In particular, the MIR regime allows to measure unique spectral properties of AGN, and is mostly unaffected by obscuration at the same time (Sect. 7.2.4). Previous HR studies of local AGN have revealed a strong correlation between the MIR and X-ray emission of AGN, which seemed to be independent of all other object properties. Therefore, the main motivation for this work has been to test this correlation and to examine its properties for an uniform sample of local AGN. At the same time, the coverage of the AGN powers has been extended into the low-luminosity regime, which is of special interest because of the predicted AGN structural changes (Sect. 2.3). For this purpose, we have planned and performed a large number of new observations with VLT/VISIR and Gemini/Michelle, using narrow filters in the *N*-band (Chapt. 3). The HR provided by these 8 m-class telescopes is of critical importance for the work presented here. Indeed, it has been possible to perform most of the imaging with an angular resolution of $\sim 0.4''$, and hence observe close to the diffraction limit.

The first sample consists of 42 nearby low-luminosity AGN, which have been selected by their 2-10 keV X-ray brightness (Chapt. 4). They represent the bulk of all observable LLAGN with current ground-based MIR instrumentation and extend the X-ray coverage down to luminosities of $L_{2-10\mathrm{keV}} \approx 10^{40}$ erg/s. The main goal for this observational programme has been to investigate the existence of nuclear point sources in those LLAGN and characterize their $12\,\mu$m emission and morphology. The detection rate has only been $\sim 2/3$ for this sample, which is attributed to the severe uncertainties in $L_{2-10\mathrm{keV}}$, in particular, for the non-detected objects. Furthermore, the Michelle observations have suffered from bad weather conditions and, thus, remained incomplete. However, all detected LLAGN exhibit point-like MIR emission (Sect. 4.4), whose position coincides with the AGN positions determined from other data (radio interferometry or 2MASS). The only exception is NGC 3125, which has turned out to be dominated by a young nuclear star cluster in the MIR, and hence has been excluded from the analysis (as for M 61, Sect. 6.4.1). Apart from the AGN associated point-source, no additional emission source has been detected in the surrounding $4''$-region.

The second sample has been selected from the 9-month BAT sample of 104 local AGN (see Chapt. 5). Because of its unique all-sky flux selection in the hardest X-ray band (14-195 keV), this sample represents well the highly-obscured (but not Compton-thick) AGN population for the first time, which makes it perfectly suitable for studies of the MIR–X-ray correlation (Sect. 5.4). However, it was only possible to observe those BAT AGN that are visible from

Paranal. All AGN observed, except two, have been detected. The data quality is moderate for many observations in many cases because of under-average weather conditions or intrinsic object faintness. Nevertheless, basically all BAT AGN appear point-like with no clear evidence for extended emission, similarly to the previously studied AGN and LLAGN (except NGC 6240 and NGC 7469). By combining the data with previous observation also from other MIR instruments, it has been possible to increase the total HR MIR coverage to 89 out of 104 BAT AGN (Sect. 5.8). Many of the BAT AGN have been observed with three or more filters, covering large parts of the N-band, which has been allowed by the higher MIR fluxes compared to the LLAGN. By these means average N-band SEDs have been constructed, which, despite large scatter, show the silicate $10\,\mu$m feature in emission for type 1 AGN and in absorption for type 2 AGN (Sect. 5.6). This feature provides direct evidence of dust that is presumably located close to the accretion disk. These average SEDs also agree reasonable well with current clumpy torus models (Sect. 5.6.1), which also supports a dusty origin for the observed MIR emission.

Both AGN samples have been compared to lower-angular resolution N-band spectra from *Spitzer*/IRS taken from the archive (Sect. 4.5 and 5.7). These spectra exhibit higher fluxes and, in some cases, also different spectral properties than the HR photometry. In particular, the PAH $11.3\,\mu$m emission feature is often much weaker, or even absent, in the HR data. Therefore, the PAH emission likely originates in diffuse circum-nuclear emission regions that are over-resolved in the HR images. In general, there is no correlation between the $F_\nu^{\mathrm{HR}}(12\,\mu\mathrm{m})$ and $F_\nu^{\mathrm{IRS}}(12\,\mu\mathrm{m})$ flux densities, emphasizing the importance of HR for AGN investigations.

Furthermore, the PAH $11.3\,\mu$m emission line flux is commonly regarded as a SF indicator, and its flux scales with the $12\,\mu$m continuum emission in starburst galaxies (Sect. 4.5.1). I have used this correlation to derive upper limits for the SF contribution to the $12\,\mu$m continuum of the AGN HR photometry. For this purpose, I have scaled a SF template SED by the PAH flux measured in the *Spitzer*/IRS spectra and further constrained it with the HR photometry in the filter that covered this feature. Imaging in such a matching filter has been performed for all sufficiently bright AGN. Next, synthetic photometry of the scaled SF template yields upper limits for the SF contribution to the HR photometry. This turns out to be below 50% for the majority of the objects (57% of the LLAGN, Sect. 4.5.1; and 79% of the BAT AGN, Sect. 5.7.1), often much lower. On the other hand, there are a few exceptional cases (in particular LLAGN) where all of $F_\nu(12\,\mu\mathrm{m})$ possibly arises from SF processes. However, it is very unlikely that all the PAH emission detected on $4''$-scale indeed comes from the $0.4''$-nuclear region and, hence, the true SF contamination is presumably much lower. Therefore, we can safely exclude SF as the main origin of the observed nuclear MIR emission in AGN.

With the AGN origin of the MIR emission being confirmed, the MIR–X-ray correlation has been investigated, after selecting absorption-corrected 2-10 keV X-ray luminosities for all AGN from the literature (Sect. 6.1 and6.2). Firstly, the correlation for the BAT AGN has been determined to be comparable in scatter and significance, with the one found in G09, while its slope is steeper although depending on the fitting algorithm used (Sect. 6.3). In addition, the LLAGN follow the correlation as well independent of the distance measurement set used, which implies that LLAGN in general are similar to brighter AGN (Sect. 6.4). In fact, a higher correlation strength is found for the combined samples and verifies that the MIR–X-ray correlation extends over a luminosity range of, at least, 10^{40} to 10^{45} erg/s (Sect. 6.5).

It is noteworthy that local starburst galaxies with globally measured MIR and X-ray luminosities show a similar correlation with the same slope but with $\sim$ 2.6 orders of magnitude difference in normalization (Sect. 6.5.1).

For the hardest X-ray energies (14-195 keV), a strong correlation is found with the 2-10 keV and the 12 μm emission as well (Sect. 6.7). This is expected, because the emission in both X-ray bands is presumably caused by similar processes in the same region close to the SMBH.

An additional improvement of the correlation strength is yielded by selecting either the well-resolved or pure AGN only (Sect. 6.5.2 and 6.5.3). These AGN are expected to be the least contaminated by non-AGN emission because of the intrinsically high spatial resolution they have been observed at; and because the maximum SF contribution has been estimated to be negligible, respectively. The resulting, MIR–X-ray correlation has a slope of 1.08 ± 0.08 and represents the best estimate of the true underlying correlation for AGN, possibly without any intrinsic scatter (0.10 ± 0.13). This value will be an important constraint for the physical modeling of the AGN structures in future applications.

The generally low intrinsic scatter (0.25 dex) in the correlation for all AGN provides further evidence that the MIR emission originates in a structure that is directly heated by the accretion disk radiation. Furthermore, this structure, presumably the dusty torus, exists in all of the observed AGN over the whole luminosity range. In addition, the difference of 0.25 dex in the MIR–X-ray luminosity ratio between type 1 and 2 AGN roughly agrees with the predictions of the scenario of differently orientated clumpy tori (Sect. 7.2.2). On the contrary, the MIR–X-ray luminosity is independent of the nuclear obscuration (N_{H}), which is regarded as a superior tracer for the putative torus inclination (Sect. 7.2.4). It will have to be investigated in future work whether these empirical results can be incorporated in the current torus models.

On the other hand, by comparison with the host galaxy morphology and inclination, an over-density of type 2 AGN located in edge-on galaxies has been found (Sect. 7.2.6). This implies that in a significant number of cases, the obscuration of our line of sight towards the AGN core happens outside the galactic nucleus, far away from the AGN. In general, type 2 AGN show a much larger scatter in the investigated properties, especially in the luminosity ratios. Therefore, this population of AGN contains objects with various intrinsic differences, contrary to the very homogeneous type 1 AGN.

Finally, it is debated in the literature whether the LINER class has a similar structure as the brighter AGN, or is intrinsically different, possibly not even SMBH-powered at all. Indeed, LINERs posses significantly higher MIR–X-ray luminosity ratios than Seyferts, although they deviate from the global MIR–X-ray correlation by less than 1 dex. This difference is connected to the accretion rate: while the MIR–X-ray ratio is independent of the accretion rate for all AGN with an Eddington-ratio $\gtrsim 10^{3.8}$, for objects with lower rates (mainly LINERs), the average ratio is significantly higher (Sect. 7.2.5). Hence, the non-thermal contribution by another AGN component (accretion disk or jet) becomes significant (or even dominating) for these objects, in addition to the thermal emission from the dust torus (Sect. 7.4).

In any case, the MIR–X-ray correlation represents a powerful observational tool for converting between MIR and X-ray powers, irrespective of the nature of the individual AGN. This is particularly interesting for observations of very distant (high-redshift) objects, for which the angular resolution is insufficient to separate AGN and host MIR emission. The latter indeed causes significant contamination, and the AGN only dominates the global MIR emission at $\gtrsim 10^{43.6}$ erg/s with a large scatter (Sect. 7.3).

The major achievements of this work are, on the one hand, the demonstration of the existence of hot dust in the nuclei all local AGN classes, and on the other hand, the verification of a strong MIR–X-ray correlation valid for all those classes. The fact that all AGN (Seyferts and LINERs) can be described well by a sole correlation demonstrates the existence of a fundamental physical connection between the processes causing the emission in both bands. This connection must be relatively uniform and, in particular, independent of any other AGN property. Owing to this uniformity and the low absorption in the MIR, the nuclear MIR luminosity might be the best indicator of the intrinsic AGN power by providing a time-averaged measure of the accretion-related total luminosity. The AGN emission at all other wavelengths is affected by either strong variability or possibly high obscuration.

8.1. Future work

As summarized above, many additional questions arise from the results and conclusions presented. Therefore, from this point, two major directions for future research become obvious: a more detailed investigation of the lowest-accretion rate objects, and additional tests on the difference between the Seyfert classes and the cause for obscuration in those objects.

Both investigations will benefit from taking into account additional multiwavelength data. In particular, the radio emission of AGN seems to introduce an additional dichotomy between radio-quite and radio-loud objects, which is debated in the literature (e.g, Sikora et al. 2007; Broderick and Fender 2011). This radio emission is of synchrotron nature and produced in the jet, which is known to be present and strong in many of the BAT AGN and LLAGN. In case this synchrotron significantly contributes to the MIR (as indicated for the LINERs), it should have influence on the MIR–X-ray correlation and possibly explain some of its scatter.

In addition, other intrinsic luminosity indicators as the forbidden emission lines [OIII] and [OIV] will help to better understand the nuclear properties of the AGN (compare Sect. 6.1). Furthermore, a detailed comparison of all these indicators (including X-rays and the 12 μm continuum emission) will be of great interest because determining the bolometric luminosity of AGN is still very complicated but of uttermost importance for AGN models.

Regarding the LLAGN, gathering HR MIR data of additional objects, in particular, the lowest accretion rate objects, the LARAGN, would be important to further verify the luminosity ratio difference and thus tighter constrain the nature of their MIR emission. Unfortunately, current MIR facilities either lack the sensitivity or spatial resolution necessary to observe most LLAGN. A different possibility is to instead gather additional HR photometry at other (infrared) wavelengths for the already detected objects, and a corresponding observational programme has already be successfully completed. The detailed analysis of this data, including comparison to models of the different AGN components will help to determine those that significantly contribute to the observed MIR emission. Finally, fitting of the complete multi-wavelength SED with self-consistent models will benefit a lot from the HR infrared data.

Finally regarding the Seyfert galaxies and apparent intrinsic differences, it will be important to take into account the CT AGN population. These AGN are not included into the otherwise uniform BAT AGN sample, however, this work has indicated that they might affect the results on intrinsic differences (Sect. 7.1). In addition, it has to be clarified which influence the host galaxies have onto the findings and whether for type 2 AGN one can distinguish somehow between those that are obscured on nuclear scale and those with obscuration on galactic scale. This is particularly interesting for the putative new class of buried AGN (Sect. 5.4).

To investigate these issues, the upgraded VISIR will create a formidable opportunity to obtain HR *N*-band spectra of large numbers of AGN in a reasonable amount of time. By these means, the MIR emission and especially the molecular features can be characterized in detail for a statistical sample of type 1 and 2 AGN, helping to constrain intrinsic differences and torus models.

Appendix A.

LLAGN: tables and figures

Table A.1.: Relevant host galaxy properties for the whole LLAGN sample.

Name	Morph.	Incl. [°]	Redshift	D_L [Mpc]	$D_{\rm TF}$ [Mpc]	$D_{\rm best}$ [Mpc]	Ref.	r_0 [pc]	Global $\log \lambda L_\lambda^{\rm G}(12\,\mu{\rm m})$ [erg/s]
NGC 676	S0-a	90	0.005	16.7	19.5	19.5 ± 8.7	Tu	33	≤ 41.61
NGC 1052	E4	70	0.005	17.8	17.8	18.0 ± 2.4	Je	31	42.35 ± 0.04
NGC 1097	SBb	37	0.0042	15.2	14.5	19.1 ± 4.2	Wi	32	43.51 ± 0.01
NGC 1386	S0-a	90	0.0029	10.6	16.9	18.3 ± 1.4	Ma	31	42.72 ± 0.02
NGC 1404	E	39	0.0065	25.5	16.9	18.3 ± 1.4	Ma	31	42.00 ± 0.16
NGC 1566	SABb	48	0.005	20.6	13.4	14.3 ± 5.9	Av	24	43.07 ± 0.01
NGC 1667	SABc	40	0.0152	62.6	0.0	62.6 ± 4.3	Lu	106	43.87 ± 0.02
ESO 005-G004	Sb	90	0.0062	26.4	22.4	22.4 ± 10.0	Tu	38	42.96 ± 0.01
NGC 2655	S0-a	66	0.0047	19.5	24.4	19.5 ± 10.9	TF	33	42.34 ± 0.06
M 81	Sab	59	-0.0001	0.7	1.4	3.7 ± 0.5	NE	6	41.48 ± 0.02
NGC 3125	E	56	0.0037	19.8	0.0	19.8 ± 1.4	Lu	34	42.56 ± 0.03
NGC 3147	Sbc	30	0.0093	39.5	40.9	30.1 ± 4.9	Am	51	43.72 ± 0.01
NGC 3312	Sb	78	0.0096	44.7	48.5	44.7 ± 3.1	NE	76	≤ 43.04
NGC 3486	SABc	46	0.0023	13.5	7.4	13.7 ± 2.4	Tu	23	42.54 ± 0.02
NGC 3976	SABb	82	0.0083	39.4	37.7	36.1 ± 6.4	Sp	61	42.89 ± 0.06
NGC 3982	SABb	30	0.0037	17.6	17.0	22.0 ± 2.2	NE	37	42.83 ± 0.02
NGC 4051	SABb	30	0.0023	12.7	17.0	12.2 ± 2.2	Tu	21	42.78 ± 0.01
NGC 4138	S0-a	65	0.003	15.3	17.0	13.8 ± 1.8	To	23	. . .
NGC 4235	Sa	90	0.008	38.0	35.2	35.2 ± 15.7	Tu	60	≤ 42.69
M 106	SABb	72	0.0015	9.0	6.8	7.4 ± 0.8	NE	13	42.57 ± 0.05
NGC 4261	E	56	0.0075	35.7	35.2	29.4 ± 2.7	Je	50	42.67 ± 0.10
M 61	SAB bc	18	0.0052	26.4	15.2	15.2 ± 3.1	Tu	26	43.36 ± 0.01
NGC 4395	SBm	90	0.0011	8.0	3.9	4.5 ± 1.1	NE	8	≤ 40.89
M 49	E2/S0	50	0.0032	18.4	16.8	17.1 ± 0.6	Me	29	≤ 42.25 ± 0.08
M 87	E	26	0.0044	22.5	16.8	17.1 ± 0.6	Me	29	42.59 ± 0.03
NGC 4501	Sb	63	0.0076	36.0	16.8	19.1 ± 5.8	NE	32	43.40 ± 0.01
M 58	SABb	39	0.0051	25.4	16.8	16.8 ± 3.4	Tu	29	42.98 ± 0.02
M 104	Sa	79	0.0034	18.8	20.0	9.1 ± 0.8	Je	15	41.98 ± 0.07
NGC 4698	SA ab	51	0.0034	18.4	16.8	23.8 ± 6.4	Sp	40	≤ 42.43
NGC 4941	SABa	37	0.0037	19.8	6.4	19.8 ± 1.4	Lu	34	42.34 ± 0.08
NGC 5033	Sc	65	0.0029	15.2	18.7	18.7 ± 4.2	Sp	32	43.27 ± 0.01
Cen A	S0	47	0.0018	11.0	4.9	3.4 ± 0.2	Fe	6	42.89 ± 0.01
M 51a	Sbc pec	33	0.0015	8.7	7.7	7.9 ± 0.9	NE	13	43.13 ± 0.01
NGC 5273	S0	58	0.0035	17.5	21.3	15.3 ± 2.0	Je	26	41.93 ± 0.08

Table A.1.: continued.

Name	Morph.	Incl. [°]	Redshift	D_L [Mpc]	D_{TF} [Mpc]	D_{best} [Mpc]	Ref.	r_0 [pc]	Global $\log \lambda L_\lambda^{\mathrm{G}}(12\,\mu\mathrm{m})$ [erg/s]
NGC 5363	S0-a	53	0.0038	19.4	22.4	19.4 ± 1.4	Lu	33	42.28 ± 0.07
Circinus	SA(s)b?	64	0.0014	8.0	4.2	4.2 ± 0.0	TF	7	43.00 ± 0.02
NGC 5813	E1-2	90	0.0066	29.9	28.4	32.1 ± 2.8	Bl	54	≤ 41.97
NGC 7213	Sa	39	0.0058	21.2	22.0	21.2 ± 1.5	Lu	36	42.91 ± 0.03
IC 1459	E3	73	0.006	21.1	20.0	30.3 ± 4.2	Bl	51	42.67 ± 0.07
NGC 7590	Sbc	70	0.0053	18.3	17.3	27.4 ± 6.0	Wi	47	43.19 ± 0.02
NGC 7626	E	47	0.0114	41.9	0.0	41.9 ± 2.9	Lu	71	≤ 42.42
NGC 7743	S0-a	90	0.0057	18.5	24.3	19.2 ± 1.6	Je	33	42.05 ± 0.15

– *Notes:* Morph.: galaxy morphology from NED; Incl: galaxy inclination i from the Hyperleda database (Paturel et al. 2003); Ref.: references for D_{best}: Am: Amanullah et al. (2010); Av: average of Tully (1988), Willick et al. (1997) and D_L from NED; Bl: Blakeslee et al. (2001); Fe: Ferrarese et al. (2007); Je: Jensen et al. (2003); Ma: Madore et al. (1999); Me: Mei et al. (2007); NE: average of redshift-independent measurements from NED; Lu: D_L from NED; Sp Springob et al. (2007); TF: Tully-Fisher distance from NEd; T8: Tully (1988); T9: Tully et al. (2009); To: Tonry et al. (2001); Wi: Willick et al. (1997); r_0: spatial scale corresponding to the theoretical diffraction limit for a 8 m telescope at 12 μm; Global $\lambda L_\lambda^{\mathrm{G}}(12\,\mu\mathrm{m})$: total monochromatic 12 μm luminosity of the galaxy (host+AGN), measured with *IRAS* taken from NED or Sanders et al. (2003).

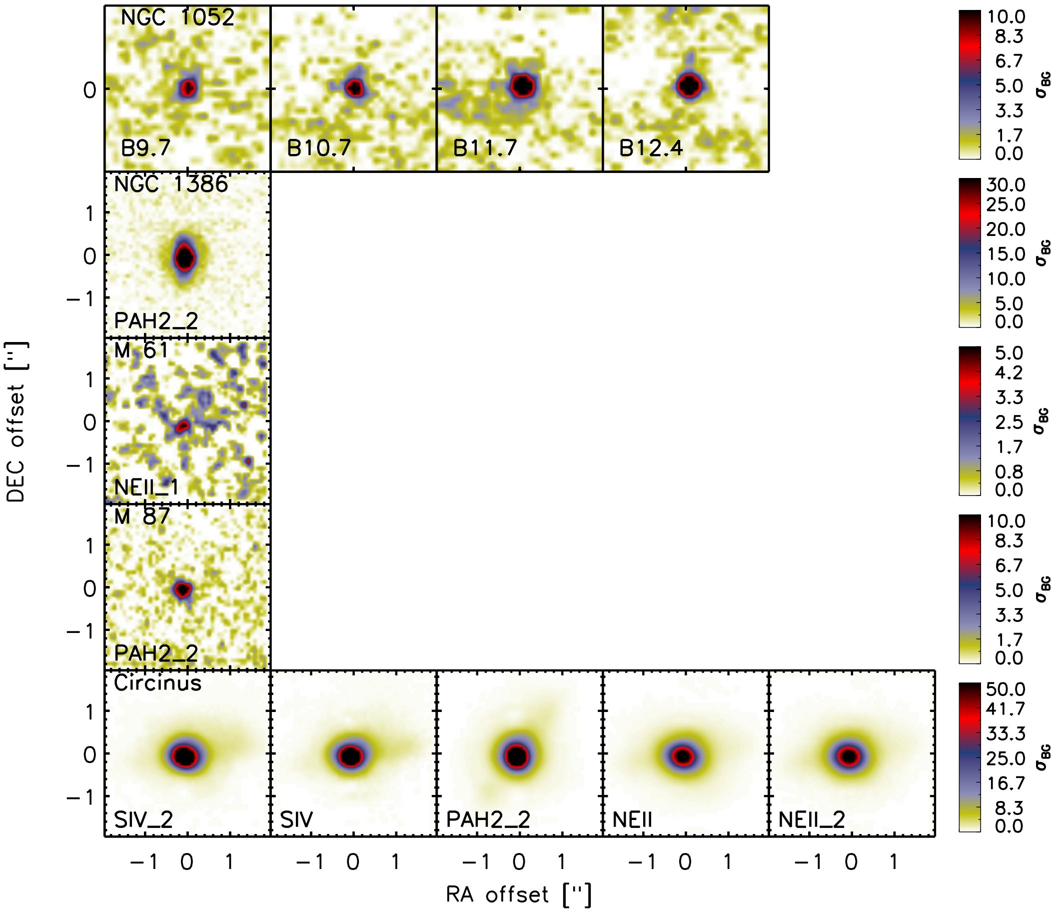

Figure A.1: VISIR images of the detected archival LLAGN (except ESO 005-G004 and Cen A, see Fig. B.1). The linear scaling is indicated in the individual color bars in units of σ_{BG} with white corresponding to the mean background value ($\langle\mathrm{BG}\rangle$). Note that the PAH2_2 image of Circinus has been recorded with an orientation angle of 45°.

Table A.2.: Observational parameters and reduction results for the archival VISIR LLAGN.

Object	Obs. date	Filter	λ_{rest}	Exp. time	FWHM [″]		Flux dens.
	(YYYY-MM-DD)		μm	[s]	STD	Obj.	[mJy]
NGC 1052	2008-09-18	J7.9	7.72 ± 0.55	361	0.33	. . .	≤ 15
	2008-09-18	B9.7	9.77 ± 0.84	362	0.36	0.38	128 ± 21
	2008-09-18	B10.7	10.60 ± 1.37	181	0.35	0.37	121 17
	2008-09-18	B11.7	11.46 ± 0.85	180	0.36	0.38	136 25
	2008-09-18	B12.4	12.41 ± 0.99	362	0.38	0.37	137 18
NGC 1386	2006-08-17	PAH2_2	11.85 ± 0.37	542	0.36	0.36	178 72
M 61	2006-04-15	NEII_1	12.21 ± 0.18	2524	0.40	0.40	7 ± 1
M 49	2006-04-18	NEII_1	12.23 ± 0.18	2524	0.35	. . .	≤ 6
M 87	2006-05-17	PAH2_2	11.83 ± 0.37	1986	0.32	0.34	21 ± 2
NGC 4698	2006-04-18	NEII_1	12.23 ± 0.18	2524	0.35	. . .	≤ 6
Circinus	2006-09-13	SIV	10.41 ± 0.16	717	0.33	0.38	4496 ± 75
	2006-09-13	SIV_2	10.69 ± 0.19	722	0.34	0.44	5925 ± 175
	2006-06-05	PAH2_2	11.86 ± 0.37	541	0.34	0.42	9575 ± 235
	2006-09-14	NEII	12.7915 ± 0.21	538	0.36	0.52	15913 ± 472
	2006-09-15	NEII_2	12.94 ± 0.22	541	0.36	0.53	15898 ± 502

– *Notes:* Description similar to Table 4.1. The data of ESO 005-G004 and Cen A are listed in Table B.2.

Table A.3.: Comparison between HR photometry and *Spitzer*/IRS flux densities.

Object	$F_\nu^{\mathrm{HR}}(11\,\mu\mathrm{m})$ [mJy]	$F_\nu^{\mathrm{IRS}}(11\,\mu\mathrm{m})$ [mJy]	$R(11\,\mu\mathrm{m})$	$F_\nu^{\mathrm{HR}}(\mathrm{cont})$ [mJy]	$F_\nu^{\mathrm{IRS}}(\mathrm{cont})$ [mJy]	$R(\mathrm{cont})$	$\log F(\mathrm{PAH}11.3\mu\mathrm{m})$ [erg/s/cm^2]	$F_\nu^{\mathrm{SF}}(12\mu\mathrm{m})$ [mJy]	$c_<^{\mathrm{SF}}$ %
NGC 1052	133.8 ± 21.7	...	...	133.8 ± 21.7	...	...	-12.93	...	...
NGC 1097	41.6 ± 8.6	168.4	0.2	27.3 ± 4.2	160.3	0.2	-11.95	35.2	100
NGC 1386	...	...	...	178.0 ± 2.7	181.9	1.0	-12.48	32.1	18
NGC 1404	≤ 35.0	17.5	≤ 2.0	≤ 18.0	15.5	≤ 1.2	-9.93	...	...
NGC 1566	100.9 ± 11.5	103.0	1.0	95.4 ± 13.0	93.1	1.0	-12.22	69.6	72
NGC 1667	≤ 15.6	77.5	≤ 0.2	≤ 15.3	69.0	≤ 0.2	-12.43	...	...
ESO 005-G004	21.0 ± 6.2	87.7	0.2	34.3 ± 15.7	90.1	0.4	-12.37	15.4	45
M 81	168.0 ± 21.8	237.4	0.7	156.8 ± 23.3	218.4	0.7	-12.42	61.3	39
NGC 3125	45.0 ± 15.4	60.1	0.7	64.5 ± 13.1	59.9	1.1	-12.54	32.9	51
NGC 3147	21.6 ± 2.4	33.4	0.6	19.7 ± 5.0	32.6	0.6	-13.18	10.3	52
NGC 3486	...	...	...	≤ 4.9	31.8	≤ 0.2	-13.19	...	...
NGC 3982	23.8 ± 2.5	59.9	0.4	30.6 ± 3.2	65.7	0.5	-12.48	28.4	92
NGC 4051	456.9 ± 62.9	478.1	1.0	456.9 ± 62.9	478.1	1.0	-12.06	116.3	25
NGC 4138	17.1 ± 2.7	44.8	0.4	17.1 ± 2.7	44.8	0.4	-13.19	8.7	51
NGC 4235	37.7 ± 6.0	41.6	0.9	32.8 ± 3.7	37.3	0.9	-13.13	8.4	25
M 106	145.5 ± 18.4	168.5	0.9	137.7 ± 15.5	168.8	0.8	-12.71	31.2	22
NGC 4261	12.4 ± 1.9	46.0	0.3	15.1 ± 2.0	51.7	0.3	-13.07	...	...
NGC 4395	...	...	...	5.7 ± 1.7	8.4	0.7	-13.69	3.3	57
M 49	...	...	...	≤ 13.0	44.3	≤ 0.3	...	...	0
M 87	...	...	...	21.5 ± 2.7	56.0	0.4	...	...	0
NGC 4501	...	...	...	≤ 4.7	50.7	≤ 0.1	-12.71	...	...
M 58	...	...	...	60.6 ± 9.2	140.6	0.4	-12.57	31.0	51
M 104	≤ 11.0	83.0	≤ 0.1	≤ 17.0	81.3	≤ 0.2	-13.12	...	...
NGC 4698	...	...	...	≤ 12.0	30.8	≤ 0.4	...	...	0
NGC 4941	67.6 ± 4.9	68.0	1.0	75.3 ± 3.9	77.5	1.0	-13.06	10.1	13
NGC 5033	...	...	...	15.7 ± 3.5	121.3	0.1	-12.07	...	...
Cen A	984.8 ± 32.1	1322.4	0.7	1488.7 ± 35.1	1783.4	0.8	-11.60	295.1	19
M 51a	20.1 ± 8.7	79.4	0.3	25.5 ± 13.4	79.9	0.3	-12.24	24.0	94
NGC 5273	18.8 ± 6.5	34.1	0.6	23.7 ± 10.9	32.5	0.7	-12.74	22.4	94
Circinus	...	...	...	9.6 ± 1.1	12.7	0.8	-10.94	1.1	11
NGC 5813	≤ 21.0	7.4	≤ 2.8	≤ 51.0	6.3	≤ 8.1	-14.03	...	...
NGC 7213	276.2 ± 24.3	297.4	0.9	265.2 ± 31.7	265.0	1.0	-12.52	34.2	12
IC 1459	≤ 20.0	23.1	≤ 0.9	≤ 30.0	20.0	≤ 1.5	-13.41	...	...

Table A.3.: continued.

Object	$F_\nu^{\mathrm{HR}}(11\,\mu\mathrm{m})$ [mJy]	$F_\nu^{\mathrm{IRS}}(11\,\mu\mathrm{m})$ [mJy]	$R(11\,\mu\mathrm{m})$	$F_\nu^{\mathrm{HR}}(\mathrm{cont})$ [mJy]	$F_\nu^{\mathrm{IRS}}(\mathrm{cont})$ [mJy]	$R(\mathrm{cont})$	$\log F(\mathrm{PAH}11.3\mu\mathrm{m})$ [erg/s/cm^2]	$F_\nu^{\mathrm{SF}}(12\mu\mathrm{m})$ [mJy]	$c_<^{\mathrm{SF}}$ %
NGC 7590	≤ 16.0	70.5	≤ 0.2	≤ 28.0	54.0	≤ 0.5	-12.38	…	…
NGC 7626	≤ 24.0	34.1	≤ 0.7	≤ 26.0	36.9	≤ 0.7	-13.77	…	…
NGC 7743	≤ 11.0	27.0	≤ 0.4	≤ 13.0	24.2	≤ 0.5	-12.82	…	…

– *Notes:* The given IRS fluxes are extracted from the post-BCD spectra convolved with the normalized HR filter transfer functions; the 11 μm fluxes contain not only the PAH feature at 11.3 μm but also the underlying continuum; $R(11\,\mu\mathrm{m})$ and $R(\mathrm{cont})$ give the flux ratios ($F_\nu^{\mathrm{HR}}/F_\nu^{\mathrm{IRS}}$) for the corresponding filters. $c_<^{\mathrm{SF}}$ signifies the maximum SF contribution (in percent) to the nuclear 12 μm continuum flux (at 0.4″scale).

Table A.4.: Relevant nuclear properties for the whole LLAGN sample.

Name	AGN type	log N_{H} [cm^{-2}]	log $L_{2-10\mathrm{keV}}$ [erg/s]	log $\lambda L_{\lambda}(12\,\mu\mathrm{m})$ [erg/s]	log M_{BH} [$M_{\odot}$]	Ref.
NGC 676	2.0	≥ 24.3	40.79 ± 0.60	≤ 40.85	7.65 ± 0.37	H09
NGC 1052	L	23.1	41.18 ± 0.30	42.13 ± 0.07	8.19 ± 0.37	H09
NGC 1097	L	20.4	40.88 ± 0.15	41.46 ± 0.06	8.08 ± 0.44	L06
NGC 1386	2.0	≥ 24.3	42.10 ± 0.60	42.26 ± 0.01	7.45 ± 0.36	Hyp
NGC 1404	NELG	≤ 22.0	39.92 ± 0.30	≤ 41.25	8.56 ± 0.37	Hyp
NGC 1566	1.5	≤ 22.0	41.62 ± 0.30	41.76 ± 0.06	6.67 ± 0.36	Hyp
NGC 1667	2.0	≥ 24.3	42.33 ± 0.60	≤ 42.25	7.48 ± 0.36	Hyp
ESO 005-G004	2.0	24.0	41.82 ± 0.30	42.00 ± 0.08	7.89 ± 0.50	W09
NGC 2655	2.0	23.4	41.66 ± 0.30	≤ 41.88	7.80 ± 0.37	H09
M 81	L	≤ 24.0	39.91 ± 0.30	40.81 ± 0.06	7.90 ± 0.09	D03
NGC 3125	L	21.7	40.14 ± 0.30	41.87 ± 0.08	5.77 ± 0.31	D05
NGC 3147	2.0	24.0	41.43 ± 0.20	41.73 ± 0.10	7.98 ± 0.36	H09
NGC 3312	L	≤ 22.0	41.10 ± 0.60	≤ 42.15	7.97 ± 0.36	Hyp
NGC 3486	2.0	≤ 24.0	39.46 ± 0.60	≤ 40.44	5.68 ± 0.36	H09
NGC 3976	2.0	23.2	39.53 ± 0.60	≤ 41.81	7.70 ± 0.36	H09
NGC 3982	1.9	23.3	41.24 ± 0.52	41.65 ± 0.04	5.90 ± 0.36	H09
NGC 4051	1.2	23.3	41.32 ± 0.60	42.31 ± 0.06	6.24 ± 0.11	D10
NGC 4138	1.9	22.9	41.30 ± 0.15	40.99 ± 0.06	7.25 ± 0.37	H09
NGC 4235	1.2	21.2	41.61 ± 0.30	42.08 ± 0.05	7.27 ± 0.36	H09
M 106	1.9	22.6	40.90 ± 0.30	41.36 ± 0.05	7.58 ± 0.001	H05
NGC 4261	L	23.2	41.00 ± 0.30	41.58 ± 0.05	8.72 ± 0.10	F96
M 61	2.0	≤ 22.0	39.04 ± 0.30	40.72 ± 0.23	6.16 ± 0.36	H09
NGC 4395	1.8	23.0	39.76 ± 0.56	39.53 ± 0.12	5.56 ± 0.12	P05
M 49	2.0	≤ 22.0	39.00 ± 0.30	≤ 41.05	8.99 ± 0.37	H09
M 87	L	22.6	40.73 ± 0.30	41.28 ± 0.05	9.82 ± 0.03	G11
NGC 4501	2.0	23.3	39.78 ± 0.30	≤ 40.71	7.46 ± 0.36	H09
M 58	L	21.7	41.18 ± 0.15	41.70 ± 0.06	7.44 ± 0.36	H09
M 104	1.9	21.3	39.99 ± 0.30	≤ 40.61	8.15 ± 0.36	H09
NGC 4698	2.0	≥ 24.3	40.82 ± 0.60	≤ 41.30	7.24 ± 0.36	H09
NGC 4941	2.0	23.7	41.43 ± 0.30	41.94 ± 0.02	6.56 ± 0.36	Hyp
NGC 5033	1.8	≤ 24.0	41.02 ± 0.28	41.22 ± 0.09	7.27 ± 0.36	H09
Cen A	2.0	23.0	41.69 ± 0.15	41.71 ± 0.01	7.74 ± 0.07	C09
M 51a	2.0	24.0	40.57 ± 0.41	40.68 ± 0.18	6.42 ± 0.36	H09
NGC 5273	1.9	22.0	40.87 ± 0.69	41.22 ± 0.16	6.19 ± 0.37	H09
NGC 5363	L	≥ 24.3	41.44 ± 0.60	≤ 41.30	8.50 ± 0.37	H09
Circinus	2.0	24.6	42.12 ± 0.60	42.71 ± 0.05	7.72 ± 0.07	G03
NGC 5813	L	21.1	38.77 ± 0.30	≤ 42.19	8.60 ± 0.37	H09
NGC 7213	L	20.3	42.09 ± 0.15	42.48 ± 0.03	7.42 ± 0.36	Hyp
IC 1459	2.0	22.1	40.61 ± 0.30	≤ 41.91	9.00 ± 0.40	C02
NGC 7590	2.0	≤ 22.0	39.77 ± 0.60	≤ 41.79	6.36 ± 0.36	G05
NGC 7626	L	≤ 22.0	39.56 ± 0.30	≤ 42.13	8.88 ± 0.37	H09
NGC 7743	2.0	≥ 24.3	41.27 ± 0.60	≤ 41.15	6.65 ± 0.37	H09

– *Notes:* For references on optical AGN classification see Sect. 4.2.1; References for $L_{2-10\mathrm{keV}}$ and N_{H} in Appendix C. $\lambda L_{\lambda}(12\,\mu\mathrm{m})$ from the HR data presented in this work; References on M_{BH}: C02 Cappellari et al. (2002); C09 Cappellari et al. (2009); D03 Devereux et al. (2003); D05 Dudik et al. (2005); D10 Denney et al. (2010); F96 Ferrarese et al. (1996); F07 Ferrarese et al. (2007); G05 Garcia-Rissmann et al. (2005); G11 Gebhardt et al. (2011); H09 Ho et al. (2009); Hyp Hyperleda database (Paturel et al. 2003); L06 Lewis and Eracleous (2006); P05 Peterson et al. (2005); W09 Winter et al. (2009a).

Appendix B.

BAT AGN: tables and figures

Table B.1.: Basic host properties for all BAT AGN used in this work.

BAT ID	Object	Morphology	Incl. [°]	Redshift	D [Mpc]	Ref.	r_0 [pc]	Global $\log \lambda L_\lambda(12\,\mu\mathrm{m})$ [erg/s]
1	NGC 235 A	S0	90	0.0222	89	D_L	144	…
2	Mrk 348	S0-a	68	0.015	58	D_L	96	…
3	Mrk 352	S0	34	0.0149	58	D_L	95	…
4	NGC 454	S0	90	0.0122	49	D_L	80	…
5	Fairall 9	S0	64	0.047	199	D_L	319	…
6	NGC 526A	S0	90	0.0191	77	D_L	125	43.61 ± 0.06
7	NGC 612	S0-a	30	0.0298	122	D_L	195	43.96 ± 0.07
8	ESO 297-G018	Sa	90	0.0252	103	D_L	166	≤ 43.75
9	NGC 788	S0-a	38	0.0136	53	D_L	87	43.20 ± 0.08
10	Mrk 1018	S0	71	0.0424	176	D_L	277	…
12	Mrk 590	Sa	27	0.0264	107	D_L	173	43.83 ± 0.08
15	NGC 931	Sbc	81	0.0167	55	T09	94	…
16	NGC 985	I	45	0.0431	180	D_L	282	44.32 ± 0.07
17	ESO 416-G002	Sa	47	0.0591	251	D_L	380	…
18	ESO 198-G024	E	46	0.0455	192	D_L	299	…
20	NGC 1142	E	68	0.0288	118	D_L	190	44.05 ± 0.06
24	NGC 1365	Sb	63	0.0055	21	D_L	36	43.84 ± 0.01
25	ESO 548-G081	Sba	64	0.0145	59	D_L	97	43.41 ± 0.09
27	PGC 13946	Sab	42	0.0365	154	D_L	243	…
28	2MASX J03565655	S?	43	0.0748	324	D_L	477	43.76 ± 0.02
29	3C 105	S?	?	0.089	389	D_L	558	43.54 ± 0.06
31	1H 0419-577	?	?	0.104	462	D_L	643	44.76 ± 0.07
32	3C 120	S0	65	0.033	138	D_L	221	44.40 ± 0.06
34	MCG -01-13-025	S0-a	50	0.0159	66	D_L	108	42.64 ± 0.01
36	XSS J05054-2348	?	?	0.035	148	D_L	234	43.53 ± 0.01
38	Ark 120	E	52	0.0327	138	D_L	219	44.27 ± 0.04
39	ESO 362-G018	S0-a	71	0.0124	52	D_L	86	43.28 ± 0.06
40	Pictor A	S0	71	0.0351	149	D_L	236	43.87 ± 0.06
45	NGC 2110	E-S0	46	0.0078	33	D_L	55	43.06 ± 0.04
47	EXO 055620-3820	S0-a	79	0.0339	144	D_L	229	44.61 ± 0.06
49	ESO 005-G004	Sb	90	0.0064	22	T88	38	42.96 ± 0.01
50	Mrk 3	S0	36	0.0135	56	D_L	92	…
51	ESO 121-G028	S0-a	33	0.0405	173	D_L	271	43.08 ± 0.03
53	2MASX J06403799	S?	77	0.06	258	D_L	390	43.76 ± 0.02

Table B.1.: continued.

BAT ID	Object	Morphology	Incl. [°]	Redshift	D [Mpc]	Ref.	r_0 [pc]	Global $\log \lambda L_\lambda(12\,\mu\mathrm{m})$ [erg/s]
55	Mrk 6	S0-a	63	0.0188	78	D_L	128	…
56	Mrk 79	Sb	37	0.0097	94	D_L	153	…
64	2MASX J09180027	S?	21	0.1564	724	D_L	918	…
65	MCG -01-24-012	SABc	67	0.0196	87	D_L	141	43.26 ± 0.12
68	NGC 2992	Sa	90	0.0077	29	D_L	48	43.21 ± 0.02
69	MCG -05-23-016	S0-a	65	0.0082	40	D_L	66	…
70	NGC 3081	S0-a	60	0.008	38	D_L	63	…
71	NGC 3227	SABa	68	0.0039	20	D_L	34	43.07 ± 0.01
72	NGC 3281	Sab	72	0.0107	49	D_L	81	43.81 ± 0.02
77	NGC 3516	S0	37	0.0088	39	T88	66	…
78	1RXS J112716.6+	?	?	0.1055	474	D_L	657	…
79	NGC 3783	SBa	27	0.0097	45	D_L	65	43.70 ± 0.03
82	2MASX J11454045	Sc	49	0.0329	144	D_L	229	≤ 43.87
83	CGCG 041-020	S0-a	48	0.036	157	D_L	248	≤ 44.00
85	NGC 4051	SABb	30	0.0023	12	T09	21	42.78 ± 0.01
86	NGC 4074	S0-a	64	0.0224	98	D_L	160	…
88	NGC 4138	S0-a	65	0.003	14	T01	23	…
89	NGC 4151	SABa	42	0.0033	13	M03	23	…
90	NGC 4253	SBa	47	0.0129	58	D_L	95	…
91	NGC 4388	Sb	90	0.0084	19	R02	33	43.05 ± 0.01
92	NGC 4395	Sm	90	0.0011	4	mean	8	≤ 40.89
94	NGC 4507	Sab	33	0.0118	53	D_L	88	43.59 ± 0.04
95	ESO 506-G027	S0-a	84	0.025	110	D_L	176	43.74 ± 0.08
96	XSS J12389-1614	?	?	0.0367	155	D_L	245	…
97	NGC 4593	Sb	33	0.009	42	D_L	75	43.40 ± 0.06
102	NGC 4992	Sa	61	0.0251	110	D_L	176	…
103	MCG -03-34-064	S0	57	0.0165	73	D_L	120	44.19 ± 0.02
104	Cen A	S0	47	0.0018	3	F07	6	42.88 ± 0.01
105	MCG -06-30-015	Sab	59	0.0079	36	D_L	60	43.11 ± 0.06
106	NGC 5252	S0	67	0.023	100	D_L	162	…
108	IC 4329A	S0-a	66	0.0161	71	D_L	116	44.23 ± 0.06
109	Mrk 279	S0	59	0.0305	129	D_L	205	…
110	NGC 5506	Sa	90	0.0062	29	D_L	49	43.52 ± 0.01
112	NGC 5548	S0-a	41	0.0172	75	D_L	122	43.86 ± 0.06
113	ESO 511-G030	Sc	51	0.0224	97	D_L	157	43.19 ± 0.01
115	NGC 5728	Sa	59	0.0094	42	D_L	70	43.05 ± 0.07
116	Mrk 841	S?	?	0.0364	157	D_L	248	44.17 ± 0.05
117	Mrk 290	E	39	0.0296	125	D_L	200	…
120	NGC 6240	S0-a	73	0.0245	103	D_L	166	44.28 ± 0.02
125	3C 382	E	90	0.0579	247	D_L	375	…
126	ESO 103-G035	S0-a	84	0.0132	55	D_L	91	43.75 ± 0.03
127	3C 390.3	S?	37	0.0561	240	D_L	365	…
129	NGC 6814	SABb	86	0.0052	19	D_L	31	42.98 ± 0.01
133	NGC 6860	SBb	58	0.0149	61	D_L	100	43.45 ± 0.06
136	4C +74.26	?	?	0.104	460	D_L	641	…
137	Mrk 509	S?	37	0.0344	141	D_L	224	44.27 ± 0.06
138	IC 5063	S0-a	51	0.0113	45	D_L	75	43.84 ± 0.01
144	UGC 11871	?	?	0.0266	107	D_L	171	43.82 ± 0.06

Table B.1.: continued.

BAT ID	Object	Morphology	Incl. [°]	Redshift	D [Mpc]	Ref.	r_0 [pc]	Global $\log \lambda L_\lambda(12\,\mu\mathrm{m})$ [erg/s]
145	NGC 7172	Sa	53	0.0087	32	D_L	54	43.12 ± 0.03
146	NGC 7213	Sa	39	0.0058	21	D_L	36	42.94 ± 0.06
147	NGC 7314	SABb	70	0.0048	21	S09	36	42.88 ± 0.06
149	3C 452	S?	46	0.0811	350	D_L	509	...
151	MR 2251-178	S0	?	0.064	271	D_L	407	≤ 44.55
152	NGC 7469	Sa	30	0.0163	63	D_L	103	44.28 ± 0.01
153	Mrk 926	Sc	38	0.0469	194	D_L	302	...
154	NGC 7582	SBab	68	0.0053	23	S09	39	43.56 ± 0.01

– *Notes:* Morph.: galaxy morphology from NED; Incl: galaxy inclination i from the Hyperleda database (Paturel et al. 2003); Ref.: references for the distance : D_L: luminosity distance from NED F07: Ferrarese et al. (2007); mean: average of redshift-indep. measurements from NED; M03: Mundell et al. (2003); R02: Russell (2002); S09: Springob et al. (2007); T01: Tonry et al. (2001); T88: Tully (1988); T09: Tully et al. (2009); r_0: spatial scale corresponding to the theoretical diffraction limit for a 8 m telescope at $12\,\mu$m; Global $\lambda L_\lambda(12\,\mu\mathrm{m})$: total monochromatic $12\,\mu$m luminosity of the galaxy (host+AGN), measured with *IRAS* taken from NED or Sanders et al. (2003), if not available then taken from the *WISE* point-source catalog.

Table B.2.: Observational parameters and reduction results for the HR MIR data.

BAT	Object	Obs. date	Filter	λ_rest	Exp. time	FWHM [″]		Flux
ID		(YY-MM-DD)		μm	[s]	STD[1]	Obj.	[mJy]
1	NGC 235A	09-09-30	SIV	10.26 ± 0.16	177	0.31	0.43	34 ± 20
1	NGC 235A	09-09-30	PAH2	11.01 ± 0.58	181	0.36	0.45	54 ± 12
1	NGC 235A	09-09-30	NEII	12.53 ± 0.21	179	0.58	0.45	88 ± 14
4	NGC 454	09-09-30	SIV_2	10.64 ± 0.19	1267	0.35	0.43	97 ± 3
4	NGC 454	09-09-30	PAH2	11.11 ± 0.58	181	0.34	0.41	92 ± 6
4	NGC 454	09-09-30	NEII_1	12.12 ± 0.18	721	0.41	0.44	151 ± 4
5	Fairall 9	10-07-11	ARIII	8.59 ± 0.13	160	0.30	0.35	195 ± 3
5	Fairall 9	05-07-21	SIV	10.02 ± 0.15	177	0.34	0.37	264 ± 2
5	Fairall 9	10-07-11	PAH2_2	11.35 ± 0.35	165	0.35	0.38	265 ± 2
5	Fairall 9	05-07-21	NEII_1	11.72 ± 0.17	361	0.38	0.39	299 ± 2
5	Fairall 9	05-07-21	NEII	12.23 ± 0.20	359	0.41	0.41	302 ± 3
6	NGC 526A	05-07-20	SIV	10.29 ± 0.16	359	0.34	0.34	175 ± 2
6	NGC 526A	05-07-20	NEII_1	12.04 ± 0.18	543	0.44	0.36	239 ± 2
7	NGC 612	09-09-28	SIV	10.19 ± 0.16	177	0.40	...	≤18
7	NGC 612	09-09-28	PAH2_2	11.54 ± 0.36	181	0.44	...	≤14
7	NGC 612	09-09-28	NEII	12.44 ± 0.20	179	0.44	...	≤30
8	ESO 297-G018	07-10-09	PAH1	8.38 ± 0.41	63	0.38	0.30	18 ± 8
8	ESO 297-G018	07-10-09	SIV	10.23 ± 0.16	61	0.38	0.35	30 ± 13
8	ESO 297-G018	07-10-09	PAH2	10.97 ± 0.58	63	0.38	0.40	31 ± 8
8	ESO 297-G018	07-10-09	NEII	12.50 ± 0.20	62	0.38	0.31	23 ± 15
9	NGC 788	08-08-26	J7.9	7.66 ± 0.54	350	0.28	0.31	58 ± 15
9	NGC 788	08-08-26	B9.7	9.69 ± 0.83	361	0.28	0.32	68 ± 9
9	NGC 788	08-08-26	B10.7	10.51 ± 1.35	180	0.31	0.34	95 ± 9
9	NGC 788	08-08-26	B11.7	11.37 ± 0.84	177	0.31	0.41	137 ± 5
9	NGC 788	08-08-26	B12.4	12.30 ± 0.98	361	0.35	0.35	130 ± 8
10	Mrk 1018	08-08-25	J7.9	7.44 ± 0.53	345	0.25	0.27	37 ± 10
10	Mrk 1018	08-08-25	B9.7	9.42 ± 0.81	179	0.28	0.31	58 ± 16
10	Mrk 1018	08-08-25	B10.7	10.22 ± 1.31	117	0.29	0.31	59 ± 11
10	Mrk 1018	08-08-25	B11.7	11.05 ± 0.82	114	0.31	0.31	62 ± 7
10	Mrk 1018	08-08-25	B12.4	11.96 ± 0.95	179	0.34	0.33	66 ± 16
12	Mrk 590	06-08-17	SIV	10.22 ± 0.16	177	0.30	0.31	78 ± 7
12	Mrk 590	06-08-17	PAH2	10.96 ± 0.57	181	0.31	0.32	87 ± 4
12	Mrk 590	06-08-17	NEII	12.48 ± 0.20	179	0.34	0.33	109 ± 6
16	NGC 985	08-09-19	J7.9	7.44 ± 0.53	339	0.33	0.41	98 ± 7
16	NGC 985	08-09-19	B9.7	9.41 ± 0.81	177	0.37	0.48	177 ± 9
16	NGC 985	08-09-19	B10.7	10.21 ± 1.31	115	0.50	0.40	145 ± 4
16	NGC 985	08-09-19	B11.7	11.04 ± 0.81	114	0.45	0.35	153 ± 3
16	NGC 985	08-09-19	B12.4	11.95 ± 0.95	177	0.41	0.37	182 ± 3
17	ESO 416-G002	09-09-28	SIV_2	10.17 ± 0.18	362	0.42	0.39	22 ± 14
17	ESO 416-G002	09-09-28	PAH2_2	11.22 ± 0.35	181	0.44	0.44	20 ± 25
17	ESO 416-G002	09-09-28	NEII_2	12.31 ± 0.21	902	0.42	0.43	25 ± 16
18	ESO 198-G024	09-09-28	SIV	10.03 ± 0.15	177	0.40	0.39	36 ± 14
18	ESO 198-G024	09-09-28	PAH2_2	11.36 ± 0.35	181	0.44	0.30	32 ± 10
18	ESO 198-G024	09-09-28	NEII	12.25 ± 0.20	359	0.44	0.44	45 ± 10
20	NGC 1142	09-10-06	SIV	10.20 ± 0.16	177	0.37	0.39	13 ± 12
20	NGC 1142	09-10-06	PAH2_2	11.55 ± 0.36	181	0.41	0.35	21 ± 15
20	NGC 1142	09-10-06	NEII	12.45 ± 0.20	179	0.36	0.39	50 ± 14
24	NGC 1365	09-09-28	PAH2	11.19 ± 0.59	181	0.42	0.40	423 ± 1

Table B.2.: continued.

BAT	Object	Obs. date	Filter	λ_rest	Exp. time	FWHM [″]		Flux
ID		(YY-MM-DD)		μm	[s]	STD	Obj.	[mJy]
24	NGC 1365	09-09-28	NEII_1	12.20 ± 0.18	180	0.41	0.46	494 ± 3
24	NGC 1365	09-09-28	NEII_2	12.97 ± 0.22	180	0.42	0.45	499 ± 4
25	ESO 548-G081	09-09-30	SIV_2	10.62 ± 0.19	362	0.35	0.49	110 ± 12
25	ESO 548-G081	09-09-30	PAH2	11.09 ± 0.58	181	0.34	0.57	115 ± 8
25	ESO 548-G081	09-09-30	NEII_1	12.09 ± 0.18	180	0.41	0.50	111 ± 15
27	PGC 13946	09-09-30	SIV	10.12 ± 0.15	530	0.34	…	≤7
27	PGC 13946	09-09-30	PAH2_2	11.46 ± 0.36	361	0.38	…	≤9
27	PGC 13946	09-09-30	NEII	12.36 ± 0.20	1076	0.38	…	≤ 9
28	2MASX J03565655	09-09-30	SIV_2	10.02 ± 0.18	362	0.40	0.37	17 ± 15
28	2MASX J03565655	09-09-30	NEII_1	11.42 ± 0.17	541	0.45	0.69	28 ± 23
28	2MASX J03565655	09-09-30	NEII_2	12.13 ± 0.20	902	0.40	0.49	29 ± 28
29	3C 105	09-10-06	SIV_2	9.89 ± 0.17	543	0.35	…	≤8
29	3C 105	09-10-06	NEII_1	11.27 ± 0.17	902	0.35	…	≤ 7
29	3C 105	09-11-19	NEII_2	11.97 ± 0.20	1443	0.38	0.42	9 ± 15
31	1H 0419-577	09-11-29	PAH2	10.19 ± 0.53	181	0.35	0.32	67 ± 6
31	1H 0419-577	09-11-29	NEII_1	11.11 ± 0.16	361	0.37	0.36	62 ± 9
31	1H 0419-577	09-11-29	NEII_2	11.81 ± 0.20	543	0.36	0.39	62 ± 10
32	3C 120	09-10-04	SIV	10.15 ± 0.15	177	0.33	0.39	232 ± 3
32	3C 120	06-12-27	SIC	11.47 ± 2.27	1803	0.34	0.39	259 ± 2
32	3C 120	09-10-04	PAH2_2	11.50 ± 0.36	181	0.40	0.45	254 ± 3
32	3C 120	09-10-04	NEII	12.40 ± 0.20	179	0.41	0.41	266 ± 4
34	MCG -01-13-025	09-11-16	SIV	10.33 ± 0.16	177	0.30	0.35	34 ± 14
34	MCG -01-13-025	09-11-16	PAH2	11.19 ± 0.59	181	0.32	0.40	42 ± 12
34	MCG -01-13-025	09-11-16	NEII_1	12.08 ± 0.18	180	0.38	0.39	31 ± 14
36	XSS J05054-2348	09-09-30	SIV	10.13 ± 0.15	530	0.67	0.54	43 ± 14
36	XSS J05054-2348	09-09-30	PAH2_2	11.48 ± 0.36	542	0.38	0.48	59 ± 7
36	XSS J05054-2348	09-09-30	NEII	12.38 ± 0.20	1256	0.38	0.50	65 ± 8
38	Ark 120	09-10-04	SIV	10.16 ± 0.15	177	0.33	0.32	270 ± 2
38	Ark 120	09-10-04	PAH2_2	11.50 ± 0.36	181	0.40	0.39	255 ± 2
38	Ark 120	09-10-04	NEII	12.40 ± 0.20	179	0.41	0.36	251 ± 3
39	ESO 362-G018	09-11-12	SIV_2	10.64 ± 0.19	905	0.34	0.37	137 ± 2
39	ESO 362-G018	09-11-12	PAH2	11.11 ± 0.58	181	0.34	0.33	132 ± 2
39	ESO 362-G018	09-11-12	NEII_1	12.12 ± 0.18	541	0.38	0.37	155 ± 3
40	Pictor A	09-09-30	SIV	10.13 ± 0.15	177	0.67	0.61	84 ± 21
40	Pictor A	06-12-27	SIC	11.45 ± 2.26	1803	0.34	0.33	82 ± 4
40	Pictor A	09-09-30	PAH2_2	11.48 ± 0.36	181	0.57	0.59	80 ± 15
40	Pictor A	09-09-30	NEII	12.38 ± 0.20	359	0.56	0.61	83 ± 20
45	NGC 2110	06-10-10	PAH1	8.52 ± 0.42	63	0.33	0.34	162 ± 4
45	NGC 2110	06-10-10	ARIII	8.92 ± 0.14	345	0.30	0.30	167 ± 2
45	NGC 2110	06-10-10	PAH2_2	11.79 ± 0.37	361	0.36	0.34	295 ± 1
45	NGC 2110	10-10-20	NEII_1	12.18 ± 0.18	1984	0.33	0.36	365 ± 1
45	NGC 2110	10-10-20	NEII	12.71 ± 0.21	1973	0.34	0.35	388 ± 1
47	EXO 055620-3820	09-09-30	SIV	10.15 ± 0.15	177	0.67	0.48	344 ± 3
47	EXO 055620-3820	09-09-30	PAH2_2	11.49 ± 0.36	181	0.57	0.50	385 ± 2
47	EXO 055620-3820	09-09-30	NEII	12.39 ± 0.20	179	0.56	0.49	465 ± 3
49	ESO 005-G004	10-11-13	PAH1	8.54 ± 0.42	181	0.32	…	≤ 6
49	ESO 005-G004	07-10-09	SIV	10.42 ± 0.16	179	0.69	…	≤45
49	ESO 005-G004	10-11-13	SIV_2	10.70 ± 0.19	361	0.35	…	≤12
49	ESO 005-G004	10-11-22	PAH2	11.18 ± 0.59	906	0.49	0.56	21 ± 18

Table B.2.: continued.

BAT ID	Object	Obs. date (YY-MM-DD)	Filter	λ_rest μm	Exp. time [s]	FWHM [″]		Flux [mJy]
						STD	Obj.	
49	ESO 005-G004	10-11-22	PAH2_2	11.80 ± 0.37	903	0.45	0.43	34 ± 18
49	ESO 005-G004	07-10-09	NEII_2	12.96 ± 0.22	181	0.65	0.87	134 ± 39
50	Mrk 3	10-02-06	Si-5	11.45 ± 0.54	5	0.45	0.45	444 ± 0
51	ESO 121-G028	09-10-04	SIV	10.08 ± 0.15	353	0.33	…	≤ 8
51	ESO 121-G028	09-10-04	PAH2_2	11.42 ± 0.36	361	0.40	0.37	12 ± 19
51	ESO 121-G028	09-10-04	NEII	12.31 ± 0.20	718	0.41	0.35	15 ± 20
53	2MASX J06403799	09-09-30	NEII_2	12.30 ± 0.21	1984	0.61	0.55	30 ± 16
64	2MASX J09180027	10-01-05	PAH2_2	10.27 ± 0.32	1986	0.33	0.39	16 ± 16
65	MCG -01-24-012	09-11-17	SIV	10.29 ± 0.16	177	0.30	0.28	49 ± 8
65	MCG -01-24-012	09-11-17	PAH2	11.03 ± 0.58	181	0.31	0.30	95 ± 7
65	MCG -01-24-012	09-11-17	NEII_1	12.03 ± 0.18	180	0.34	0.37	143 ± 9
68	NGC 2992	09-12-02	PAH2	11.16 ± 0.59	181	0.31	0.37	140 ± 3
68	NGC 2992	09-12-02	NEII_1	12.18 ± 0.18	181	0.39	0.38	165 ± 7
68	NGC 2992	09-12-02	NEII_2	12.94 ± 0.22	181	0.36	0.41	225 ± 6
69	MCG -05-23-016	07-01-30	ARIII	8.92 ± 0.14	350	0.33	0.32	350 ± 1
69	MCG -05-23-016	07-01-30	PAH2_2	11.78 ± 0.37	181	0.36	0.35	633 ± 1
70	NGC 3081	07-12-30	PAH1	8.52 ± 0.42	63	0.31	0.42	78 ± 11
70	NGC 3081	07-12-30	SIV	10.41 ± 0.16	62	0.32	0.33	129 ± 13
70	NGC 3081	07-12-30	PAH2	11.16 ± 0.59	63	0.35	0.37	155 ± 8
70	NGC 3081	07-12-30	NEII_2	12.94 ± 0.22	63	0.37	0.38	180 ± 15
71	NGC 3227	08-03-22	ARIII	8.96 ± 0.14	177	0.33	0.34	187 ± 4
71	NGC 3227	06-12-27	SIC	11.80 ± 2.33	1803	0.37	0.48	359 ± 3
71	NGC 3227	08-03-22	PAH2_2	11.83 ± 0.37	118	0.34	0.38	312 ± 4
72	NGC 3281	08-02-07	PAH1	8.50 ± 0.42	543	0.29	0.32	420 ± 1
72	NGC 3281	08-02-07	PAH2	11.13 ± 0.58	544	0.31	0.35	454 ± 1
72	NGC 3281	08-03-20	SIV	10.38 ± 0.16	538	0.30	0.35	273 ± 3
72	NGC 3281	08-03-20	SIC	11.72 ± 2.32	541	0.33	0.38	641 ± 2
72	NGC 3281	08-02-07	NEII_2	12.90 ± 0.22	541	0.35	0.40	1012 ± 2
78	1RXS_J112716	10-01-26	PAH2	10.18 ± 0.53	362	0.31	0.40	32 ± 9
78	1RXS_J112716	10-01-26	NEII_1	11.10 ± 0.16	1443	0.36	0.44	37 ± 11
78	1RXS_J112716	10-03-23	NEII_2	11.80 ± 0.20	1992	0.38	0.53	41 ± 9
79	NGC 3783	05-04-17	SIV	10.39 ± 0.16	177	0.30	0.32	560 ± 1
79	NGC 3783	05-04-17	PAH2_2	11.77 ± 0.37	181	0.32	0.35	616 ± 1
79	NGC 3783	05-04-17	NEII_1	12.15 ± 0.18	180	0.33	0.35	709 ± 1
82	2MASX J11454045	10-01-08	SIV	10.16 ± 0.15	179	0.31	0.32	60 ± 11
82	2MASX J11454045	10-01-08	PAH2_2	11.50 ± 0.36	181	0.33	0.35	45 ± 16
82	2MASX J11454045	10-01-08	NEII	12.40 ± 0.20	180	0.35	0.33	52 ± 15
83	CGCG 041-020	10-01-27	SIV	10.13 ± 0.15	359	0.30	0.58	25 ± 49
83	CGCG 041-020	10-01-27	PAH2_2	11.47 ± 0.36	181	0.31	0.42	25 ± 14
83	CGCG 041-020	10-01-27	NEII	12.36 ± 0.20	541	0.34	0.38	35 ± 18
85	NGC 4051	10-02-02	Si-5	11.57 ± 0.55	156	0.43	0.47	457 ± 2
86	NGC 4074	10-01-27	NEII	12.53 ± 0.21	1984	0.34	0.40	81 ± 4
88	NGC 4138	10-02-02	Si-5	11.57 ± 0.55	259	0.43	0.43	17 ± 22
89	NGC 4151	09-06-07	PAH1	8.56 ± 0.42	118	0.58	0.48	826 ± 52
89	NGC 4151	10-03-29	PAH1	8.56 ± 0.42	361	0.54	0.42	875 ± 54
89	NGC 4151	07-03-18	Si-5	11.56 ± 0.55	13	0.44	0.44	1315 ± 0
89	NGC 4151	09-06-07	PAH2_2	11.84 ± 0.37	118	0.53	0.58	1294 ± 87
89	NGC 4151	10-03-29	PAH2_2	11.84 ± 0.37	361	0.47	0.49	1404 ± 64
91	NGC 4388	08-03-21	PAH1	8.52 ± 0.42	63	0.38	0.49	145 ± 24

Table B.2.: continued.

BAT	Object	Obs. date	Filter	λ_rest	Exp. time	FWHM [″]		Flux
ID		(YY-MM-DD)		μm	[s]	STD	Obj.	[mJy]
91	NGC 4388	08-03-21	SIV	10.40 ± 0.16	62	0.36	0.39	141 ± 11
91	NGC 4388	08-03-21	PAH2	11.16 ± 0.59	63	0.34	0.49	201 ± 8
91	NGC 4388	08-03-21	NEII_2	12.93 ± 0.22	63	0.37	0.47	434 ± 11
92	NGC 4395	10-02-05	Si-6	12.49 ± 0.60	612	0.40	0.40	6 ± 0
94	NGC 4507	06-04-15	SIV	10.37 ± 0.16	177	0.33	0.33	517 ± 1
94	NGC 4507	06-04-15	PAH2	11.12 ± 0.58	181	0.34	0.33	584 ± 1
94	NGC 4507	06-04-15	NEII_1	12.13 ± 0.18	180	0.35	0.35	620 ± 1
95	ESO 506-G027	10-01-09	SIV	10.23 ± 0.16	179	0.34	0.31	49 ± 10
95	ESO 506-G027	10-01-09	PAH2_2	11.59 ± 0.36	181	0.35	0.35	109 ± 4
95	ESO 506-G027	10-01-09	NEII	12.50 ± 0.20	180	0.36	0.36	179 ± 6
96	XSS J12389-1614	10-01-09	SIV	10.12 ± 0.15	179	0.34	0.35	39 ± 13
96	XSS J12389-1614	10-01-09	PAH2_2	11.46 ± 0.36	181	0.35	0.39	41 ± 14
96	XSS J12389-1614	10-01-09	NEII	12.36 ± 0.20	361	0.36	0.35	40 ± 14
97	NGC 4593	05-04-30	SIV	10.40 ± 0.16	353	0.31	0.32	337 ± 1
97	NGC 4593	05-04-30	PAH2_2	11.77 ± 0.37	361	0.32	0.33	334 ± 1
97	NGC 4593	05-04-30	NEII_1	12.16 ± 0.18	361	0.34	0.35	368 ± 1
102	NGC 4992	08-03-21	PAH1	8.38 ± 0.41	102	0.38	0.36	53 ± 13
102	NGC 4992	08-03-21	SIV	10.23 ± 0.16	101	0.36	0.34	32 ± 25
102	NGC 4992	08-03-21	PAH2	10.97 ± 0.58	102	0.34	0.34	38 ± 15
102	NGC 4992	08-03-21	NEII	12.50 ± 0.20	102	0.33	0.39	77 ± 14
103	MCG -03-34-064	06-04-09	SIV	10.32 ± 0.16	177	0.30	0.42	586 ± 4
103	MCG -03-34-064	06-04-09	PAH2	11.07 ± 0.58	181	0.33	0.45	741 ± 3
103	MCG -03-34-064	06-04-09	NEII_1	12.07 ± 0.18	180	0.35	0.45	890 ± 5
104	Cen A	06-04-09	SIV	10.47 ± 0.16	177	0.30	0.35	638 ± 3
104	Cen A	06-04-09	PAH2	11.23 ± 0.59	181	0.33	0.39	987 ± 2
104	Cen A	06-04-09	NEII_1	12.25 ± 0.18	180	0.35	0.36	1491 ± 2
105	MCG -06-30-015	06-04-14	SIV	10.41 ± 0.16	177	0.30	0.33	313 ± 4
105	MCG -06-30-015	06-04-14	PAH2	11.16 ± 0.59	181	0.34	0.34	365 ± 3
105	MCG -06-30-015	06-04-14	NEII_1	12.17 ± 0.18	180	0.33	0.37	373 ± 7
106	NGC 5252	10-02-21	SIV	10.25 ± 0.16	361	0.30	0.34	90 ± 13
106	NGC 5252	10-02-21	PAH2_2	11.61 ± 0.36	362	0.33	0.35	89 ± 12
106	NGC 5252	10-02-21	NEII	12.52 ± 0.21	724	0.35	0.40	89 ± 19
108	IC 4329A	10-03-12	SIV	10.32 ± 0.16	179	0.36	0.35	925 ± 2
108	IC 4329A	10-03-12	PAH2	11.07 ± 0.58	181	0.36	0.35	1047 ± 1
108	IC 4329A	10-03-12	NEII_1	12.08 ± 0.18	181	0.39	0.38	1168 ± 3
110	NGC 5506	10-02-23	PAH2	11.18 ± 0.59	181	0.33	0.41	870 ± 2
110	NGC 5506	10-02-23	NEII_1	12.19 ± 0.18	181	0.34	0.39	1188 ± 3
110	NGC 5506	10-02-23	NEII_2	12.96 ± 0.22	181	0.36	0.40	1388 ± 3
112	NGC 5548	10-06-27	ARIII	8.84 ± 0.14	177	0.33	0.81	145 ± 16
112	NGC 5548	10-06-27	PAH2_2	11.68 ± 0.36	181	0.39	0.54	176 ± 10
113	ESO 511-G030	10-01-27	SIV	10.26 ± 0.16	179	0.31	0.38	54 ± 30
113	ESO 511-G030	10-01-27	PAH2	11.00 ± 0.58	181	0.31	0.38	60 ± 24
113	ESO 511-G030	10-01-27	NEII	12.53 ± 0.21	180	0.34	0.44	52 ± 21
115	NGC 5728	08-03-21	PAH1	8.51 ± 0.42	63	0.38	…	≤22
115	NGC 5728	08-03-21	SIV	10.39 ± 0.16	62	0.36	…	≤35
115	NGC 5728	10-03-12	PAH2	11.15 ± 0.58	362	0.36	0.39	23 ± 19
115	NGC 5728	10-03-12	NEII_1	12.16 ± 0.18	1448	0.39	0.45	69 ± 19
115	NGC 5728	08-03-21	NEII_2	12.92 ± 0.22	63	0.36	0.37	99 ± 33
116	Mrk 841	10-04-01	SIV	10.12 ± 0.15	177	0.30	0.32	127 ± 12

Table B.2.: continued.

BAT	Object	Obs. date	Filter	λ_rest	Exp. time	FWHM ["]		Flux
ID		(YY-MM-DD)		µm	[s]	STD	Obj.	[mJy]
116	Mrk 841	10-04-01	PAH2_2	11.46 ± 0.36	181	0.33	0.35	162 ± 10
116	Mrk 841	10-04-01	NEII	12.36 ± 0.20	361	0.37	0.38	200 ± 11
120	NGC 6240	05-04-19	PAH2	10.98 ± 0.58	1794	0.38	0.38	97 ± 0
120	NGC 6240	05-04-19	PAH2_2	11.60 ± 0.36	1766	0.53	0.53	177 ± 0
120	NGC 6240	05-04-19	PAH2	10.98 ± 0.58	1794	0.38	0.38	13 ± 0
120	NGC 6240	05-04-19	PAH2_2	11.60 ± 0.36	1766	0.53	0.53	32 ± 0
126	ESO 103-G035	08-03-22	PAH1	8.48 ± 0.41	63	0.28	0.44	257 ± 15
126	ESO 103-G035	08-03-22	SIV	10.35 ± 0.16	62	0.31	0.58	301 ± 23
126	ESO 103-G035	08-03-22	PAH2	11.10 ± 0.58	63	0.35	0.50	399 ± 12
126	ESO 103-G035	08-03-22	NEII_2	12.87 ± 0.22	63	0.36	0.52	657 ± 20
129	NGC 6814	07-10-20	PAH1	8.55 ± 0.42	543	0.37	0.49	55 ± 7
129	NGC 6814	07-10-20	SIV	10.44 ± 0.16	530	0.39	0.53	98 ± 7
129	NGC 6814	07-10-20	PAH2	11.19 ± 0.59	544	0.41	0.45	101 ± 4
129	NGC 6814	07-10-20	NEII_2	12.97 ± 0.22	543	0.41	0.49	97 ± 9
133	NGC 6860	09-09-19	SIV_2	10.61 ± 0.19	543	0.37	0.35	205 ± 5
133	NGC 6860	09-09-19	PAH2	11.09 ± 0.58	181	0.36	0.33	206 ± 6
133	NGC 6860	09-09-19	NEII_1	12.09 ± 0.18	361	0.36	0.36	207 ± 8
137	Mrk 509	06-06-14	SIV	10.14 ± 0.15	177	0.49	0.37	206 ± 8
137	Mrk 509	06-06-14	PAH2	10.88 ± 0.57	181	0.40	0.37	232 ± 5
137	Mrk 509	06-06-14	NEII	12.38 ± 0.20	179	0.41	0.38	257 ± 12
138	IC 5063	05-06-10	SIV	10.37 ± 0.16	177	0.40	0.45	667 ± 6
138	IC 5063	06-05-05	SIV	10.37 ± 0.16	177	0.38	0.49	608 ± 5
138	IC 5063	06-05-05	PAH2	11.12 ± 0.58	181	0.39	0.45	734 ± 3
138	IC 5063	05-06-10	PAH2_2	11.75 ± 0.37	181	0.39	0.42	926 ± 4
138	IC 5063	05-06-10	NEII_1	12.13 ± 0.18	180	0.43	0.47	1103 ± 6
138	IC 5063	06-05-05	NEII_1	12.13 ± 0.18	180	0.38	0.44	1035 ± 3
144	UGC 11871	09-09-19	SIV	10.22 ± 0.16	530	0.38	0.40	59 ± 14
144	UGC 11871	09-09-19	PAH2_2	11.57 ± 0.36	361	0.36	0.42	90 ± 11
144	UGC 11871	09-09-19	NEII	12.48 ± 0.20	897	0.37	0.44	112 ± 10
145	NGC 7172	09-09-20	PAH2	11.15 ± 0.58	181	0.31	0.36	63 ± 19
145	NGC 7172	06-07-09	NEII_1	12.16 ± 0.18	721	0.38	0.45	162 ± 13
145	NGC 7172	09-09-20	NEII_2	12.93 ± 0.22	180	0.36	0.40	192 ± 16
146	NGC 7213	06-07-14	SIV	10.43 ± 0.16	177	0.36	0.34	239 ± 7
146	NGC 7213	09-05-18	PAH2	11.19 ± 0.59	181	0.30	0.31	232 ± 3
146	NGC 7213	09-05-18	NEII_1	12.20 ± 0.18	180	0.32	0.33	230 ± 8
147	NGC 7314	05-07-20	SIV	10.44 ± 0.16	361	0.34	0.39	75 ± 52
147	NGC 7314	05-07-20	PAH2	11.20 ± 0.59	724	0.38	0.39	71 ± 19
151	MR 2251-178	09-09-20	SIV_2	10.12 ± 0.18	181	0.30	0.63	98 ± 57
151	MR 2251-178	09-09-20	PAH2_2	11.17 ± 0.35	181	0.32	0.50	94 ± 29
151	MR 2251-178	09-09-20	NEII_2	12.26 ± 0.21	180	0.36	0.48	90 ± 44
152	NGC 7469	06-07-12	SIV	10.32 ± 0.16	177	0.33	0.40	451 ± 6
152	NGC 7469	06-07-12	PAH2	11.07 ± 0.58	181	0.34	0.43	502 ± 5
152	NGC 7469	06-07-12	NEII_1	12.07 ± 0.18	180	0.35	0.37	592 ± 4
153	Mrk 926	09-09-20	SIV_2	10.29 ± 0.18	181	0.30	0.43	114 ± 22
153	Mrk 926	09-09-20	PAH2_2	11.35 ± 0.35	181	0.32	0.38	125 ± 12
153	Mrk 926	09-09-20	NEII	12.24 ± 0.20	179	0.35	0.42	129 ± 22
154	NGC 7582	08-08-23	ARIII	8.94 ± 0.14	60	0.30	0.34	235 ± 13
154	NGC 7582	08-08-23	PAH2_2	11.82 ± 0.37	63	0.34	0.36	390 ± 11

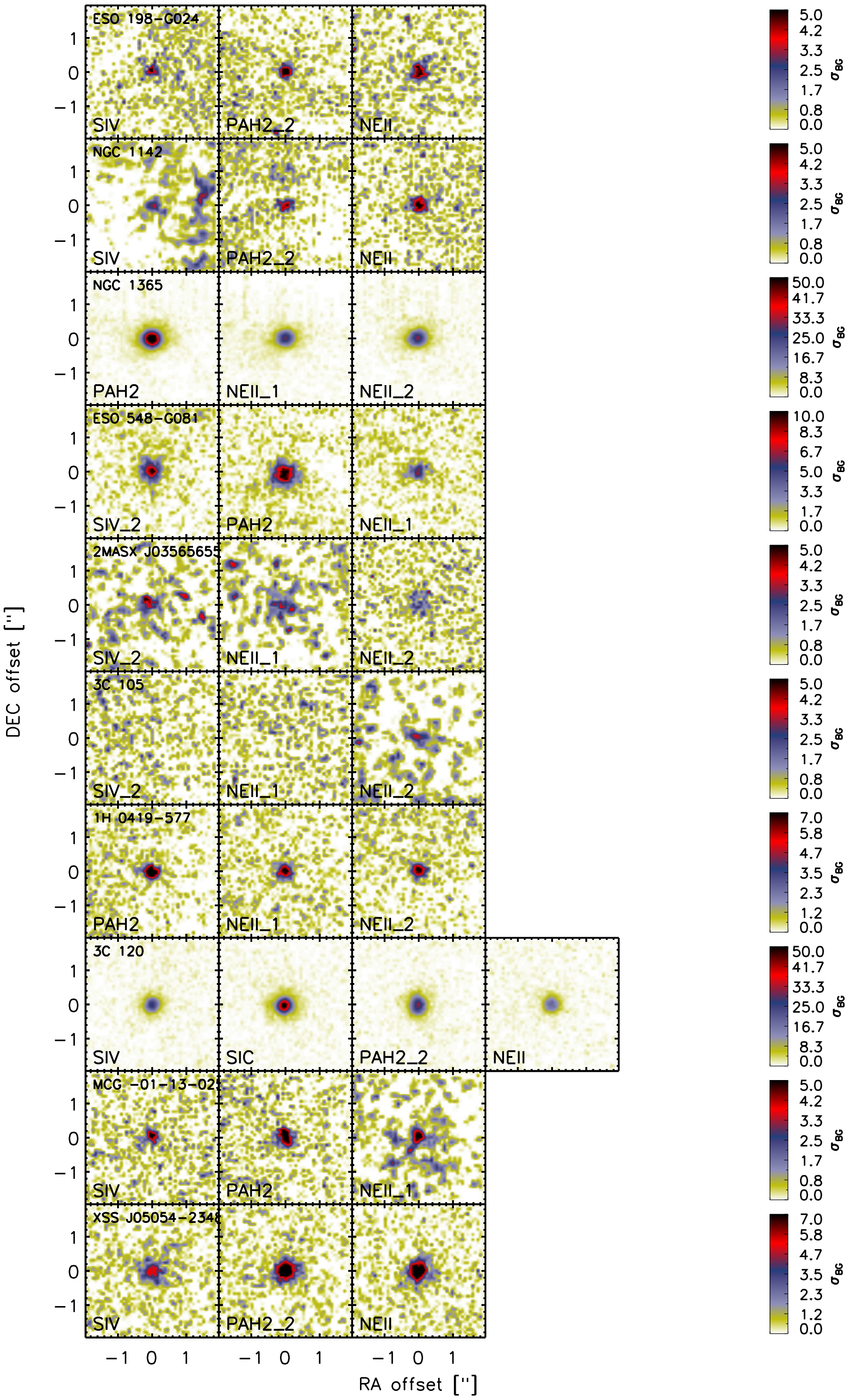

Figure B.1: Remaining MIR images of the BAT AGN in different filters. Each row shows one object sorted by right ascension. White corresponds to the mean background value (⟨BG⟩). The first 10 objects are displayed in Fig. 5.3.

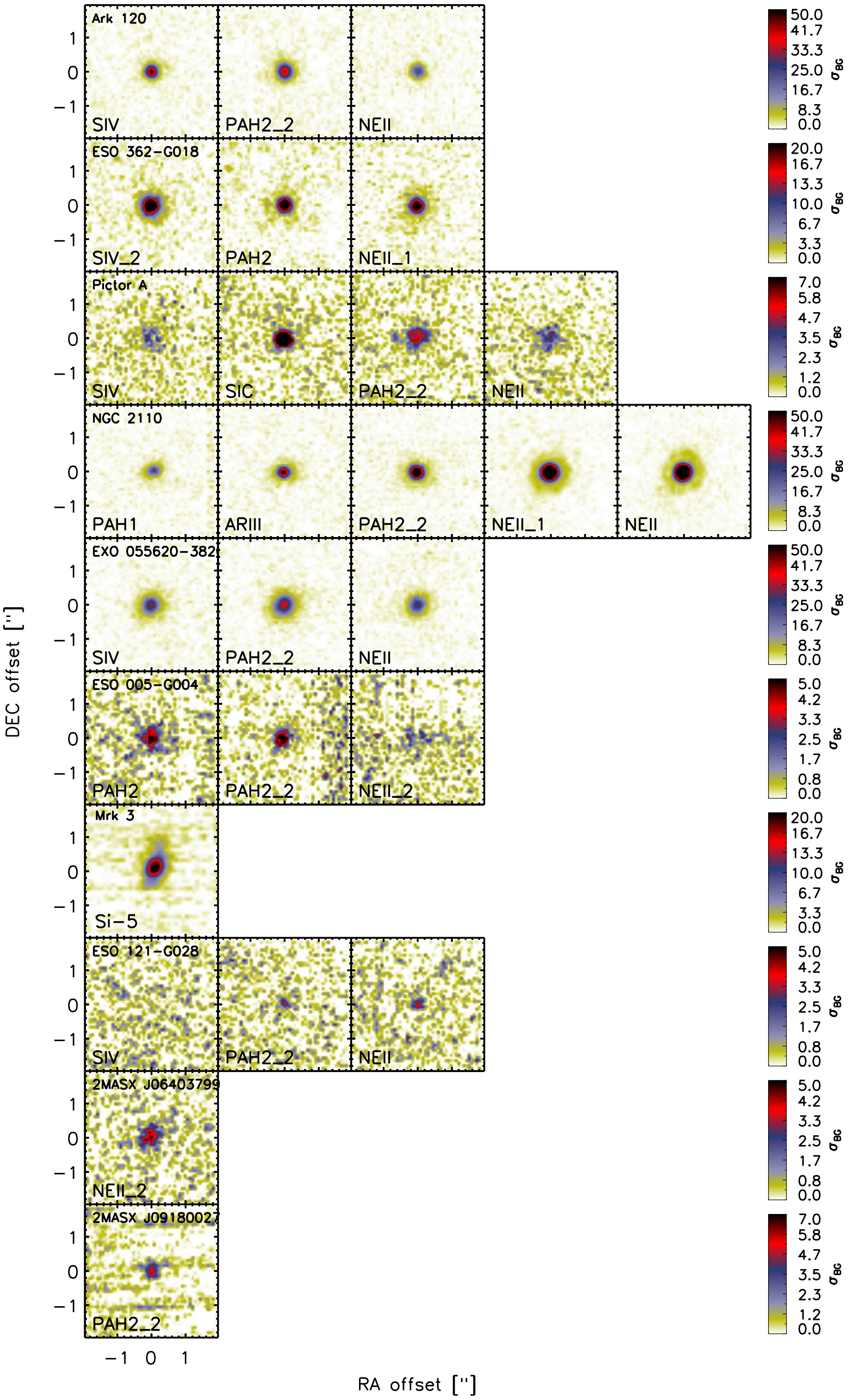

Figure B.1: continued.

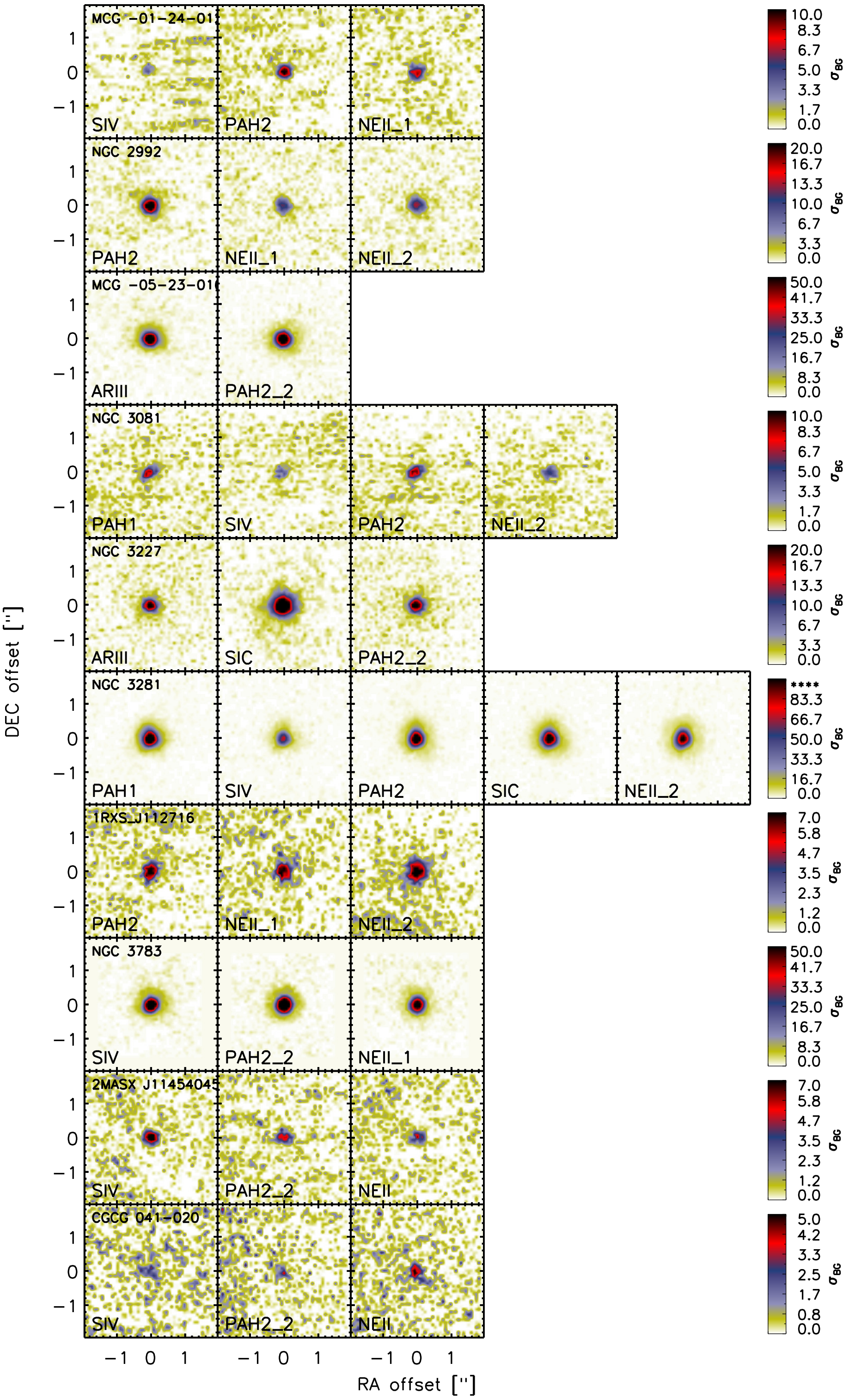

Figure B.1: continued.

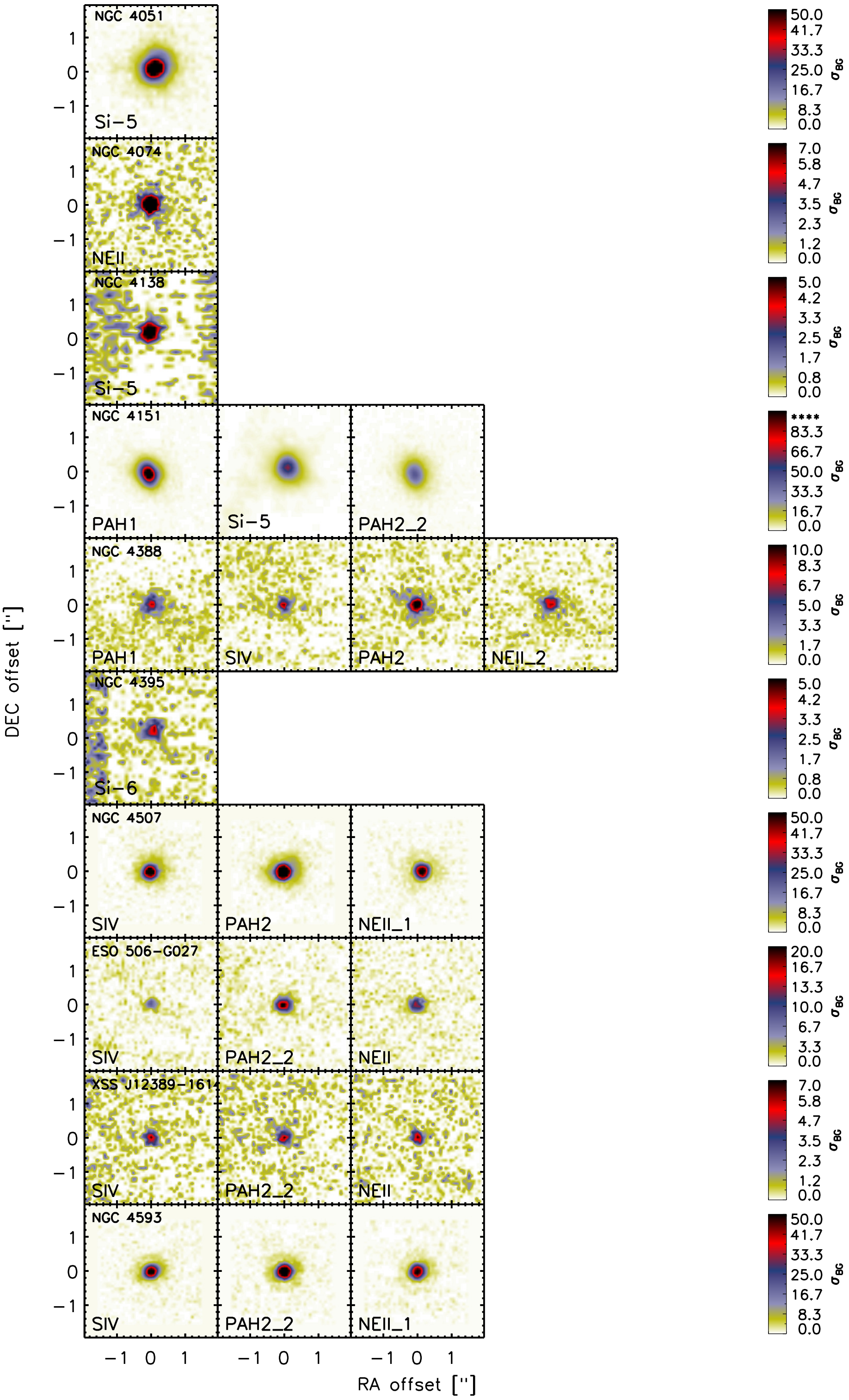

Figure B.1: continued.

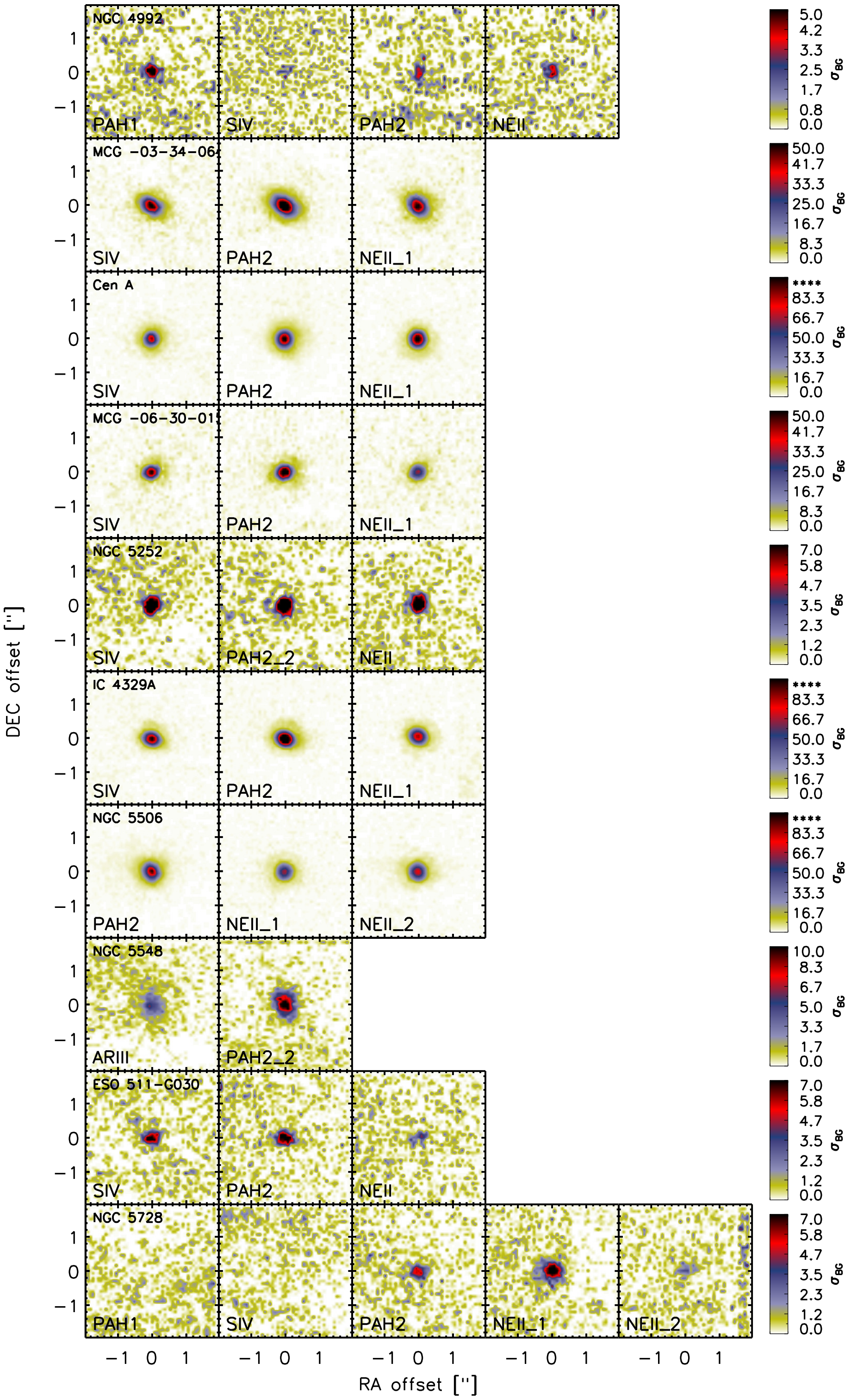

Figure B.1: continued.

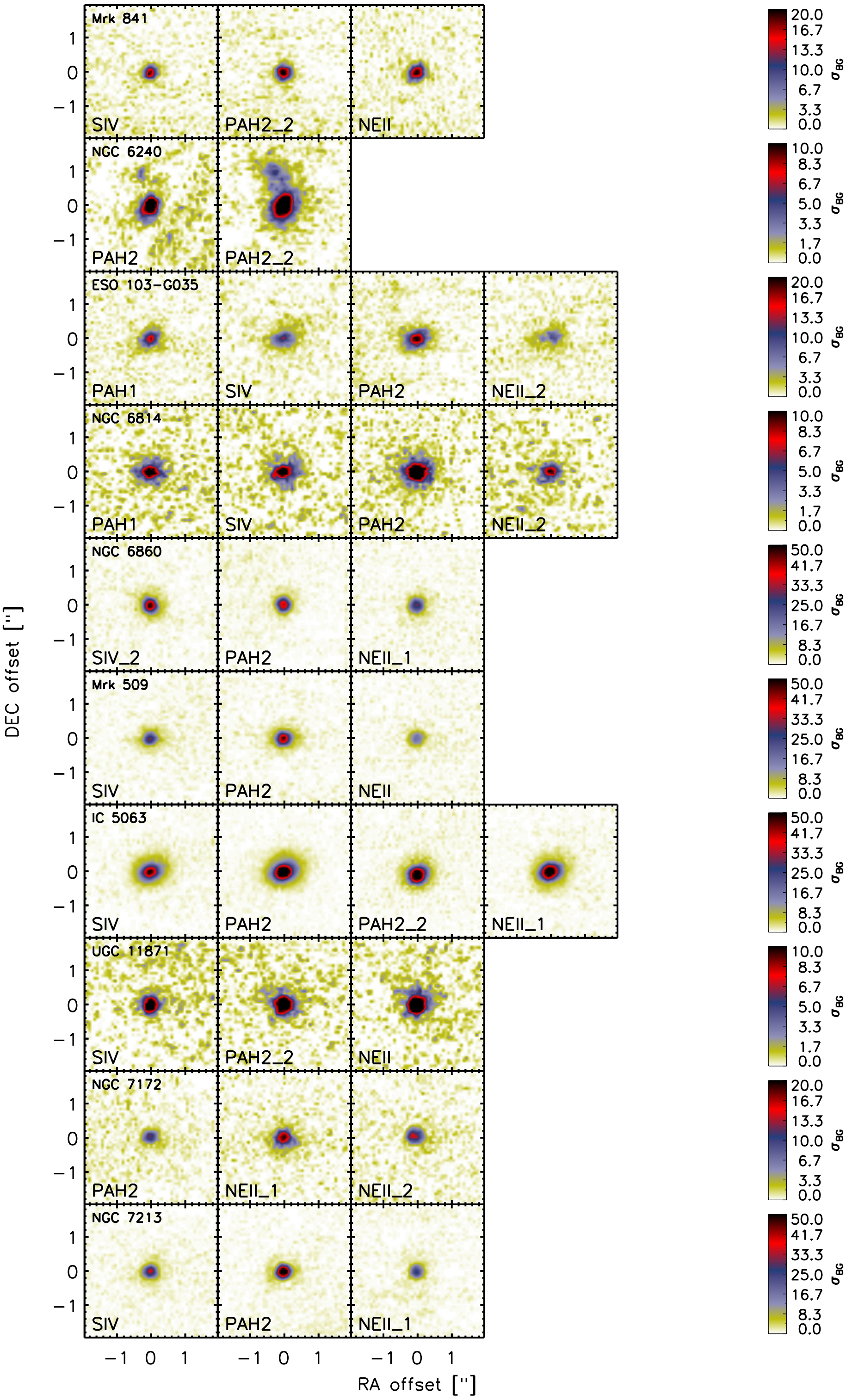

Figure B.1: continued.

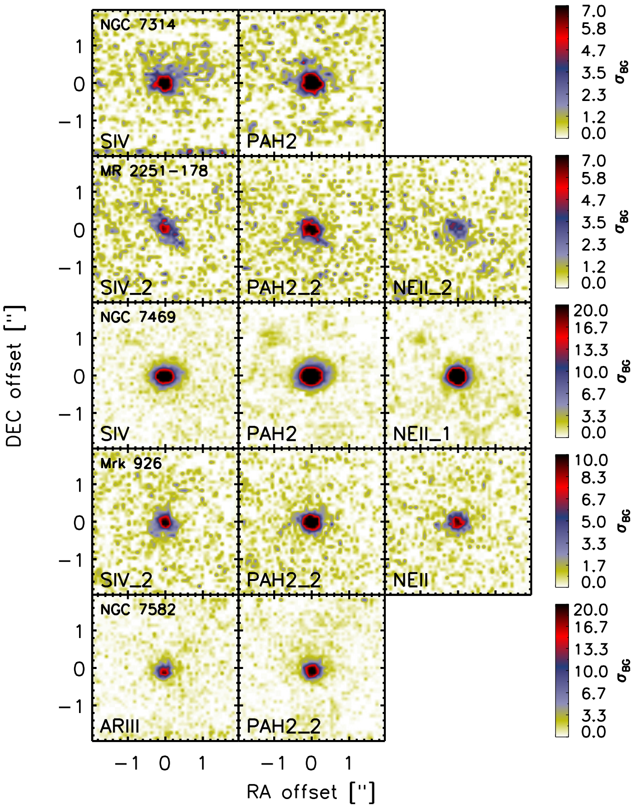

Figure B.1: continued.

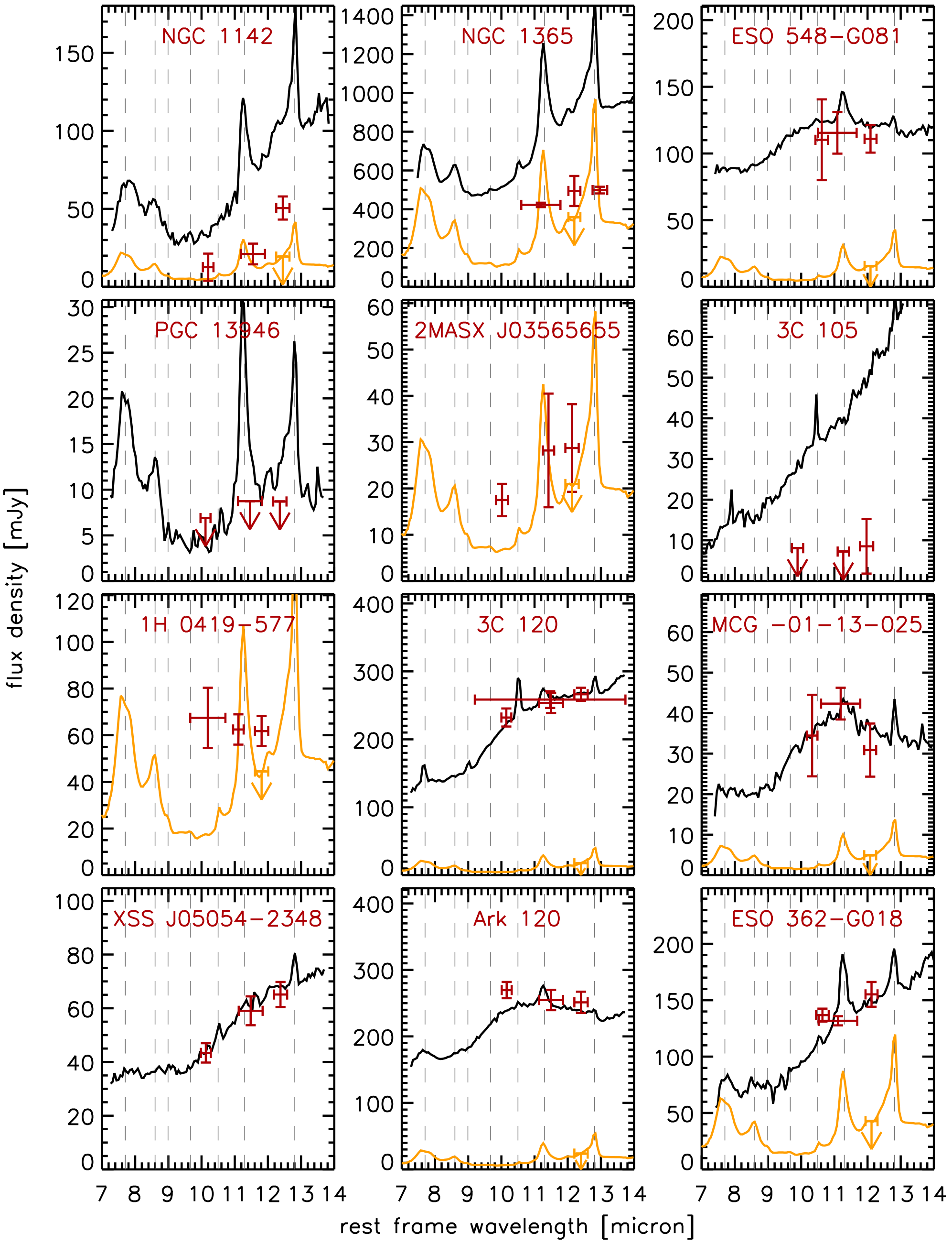

Figure B.2: Comparison of HR photometry (red symbols) and *Spitzer* IRS spectra (black line) and VISIR spectra where available (blue line) for the remaining BAT AGN. Displaying errors in the spectra was omitted to maintain clarity. They are of the order of 10% for both IRS and VISIR. Horizontal error bars correspond to the filter pass band. Commonly occurring emission lines are indicated by the dotted lines. In addition, the scaled starburst template SED (displayed as orange line) are shown as well as the derived upper limit for the starburst contribution to the continuum filter measurement (orange symbols), see Sect. 5.7.1 for details.

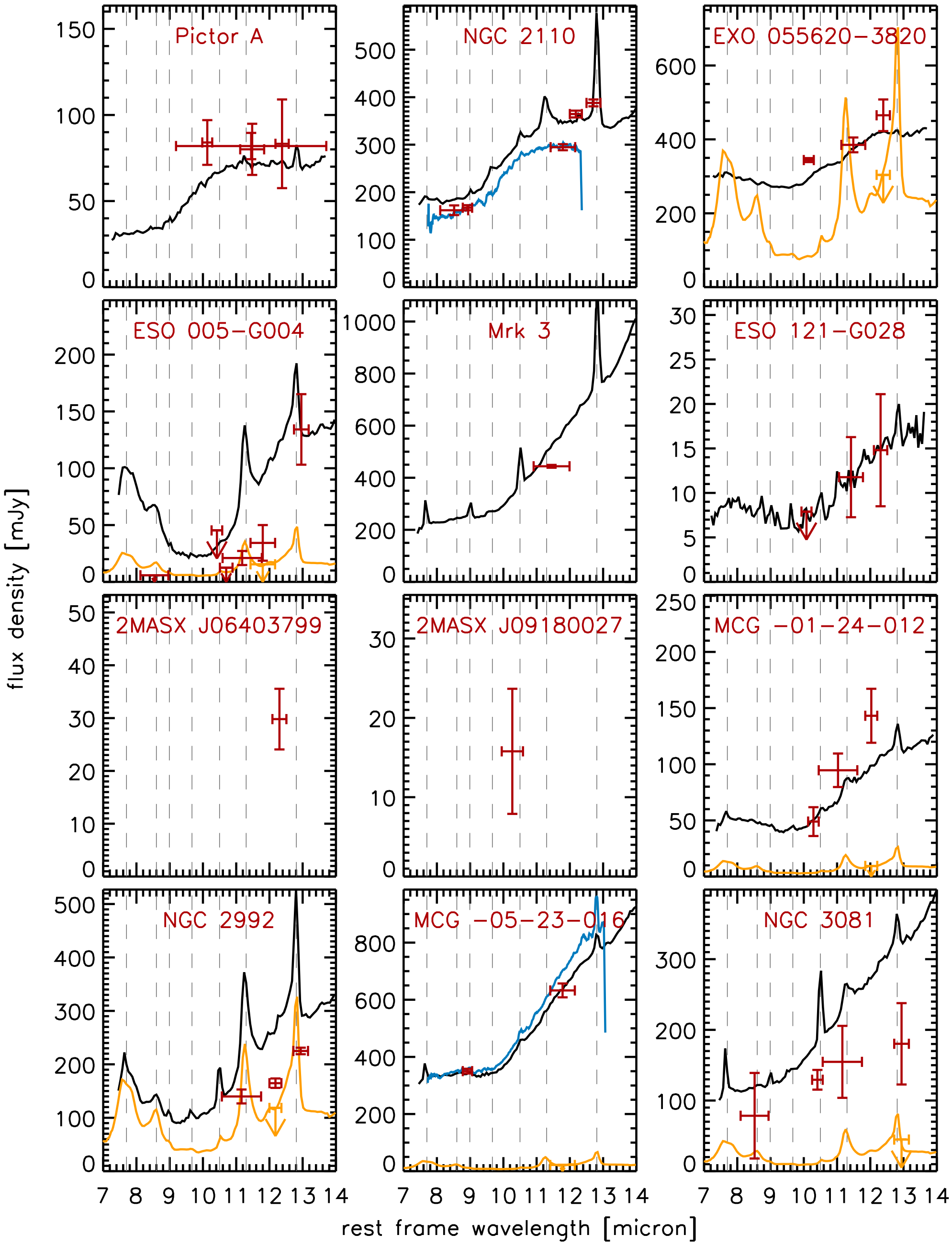

Figure B.2: continued.

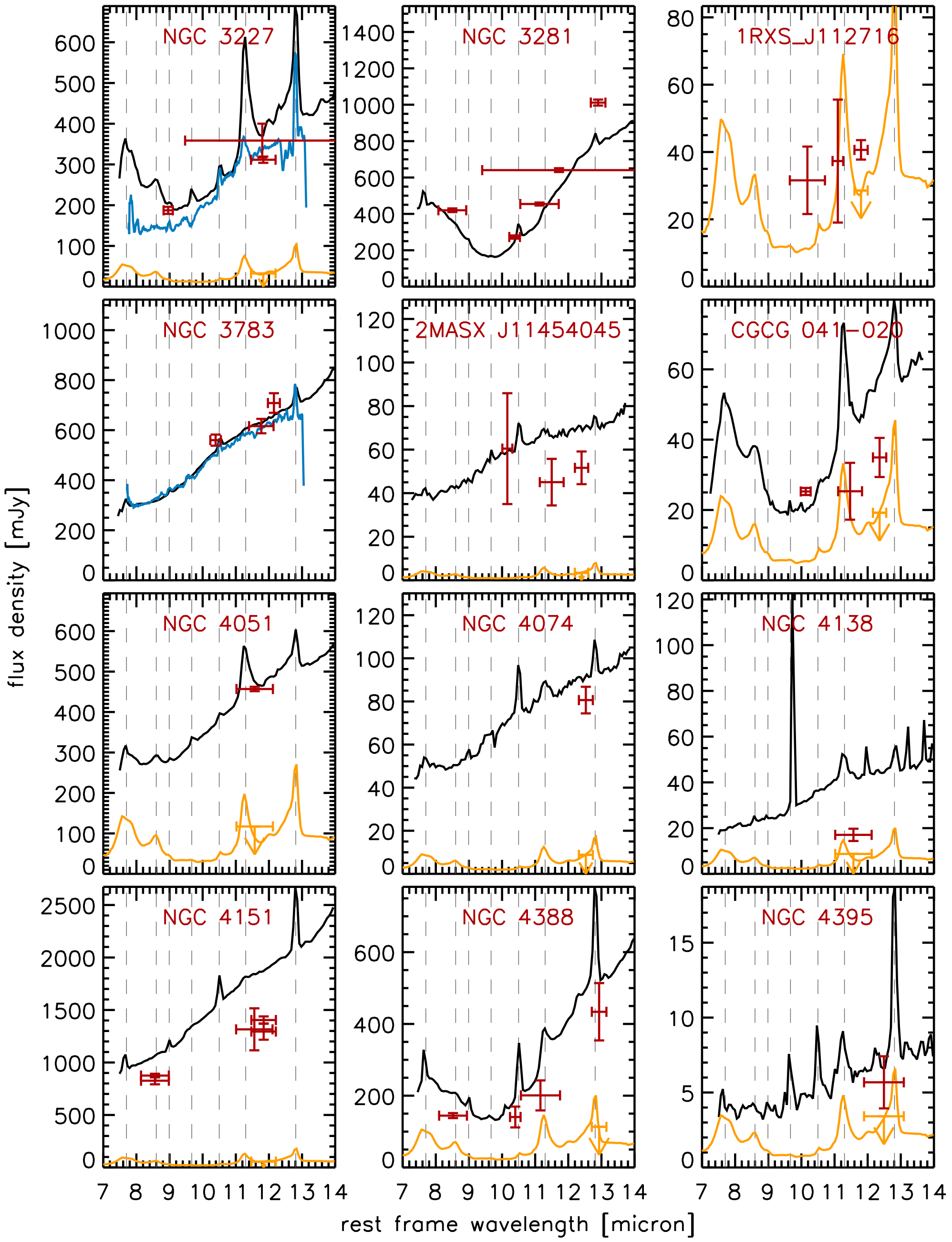

Figure B.2: continued.

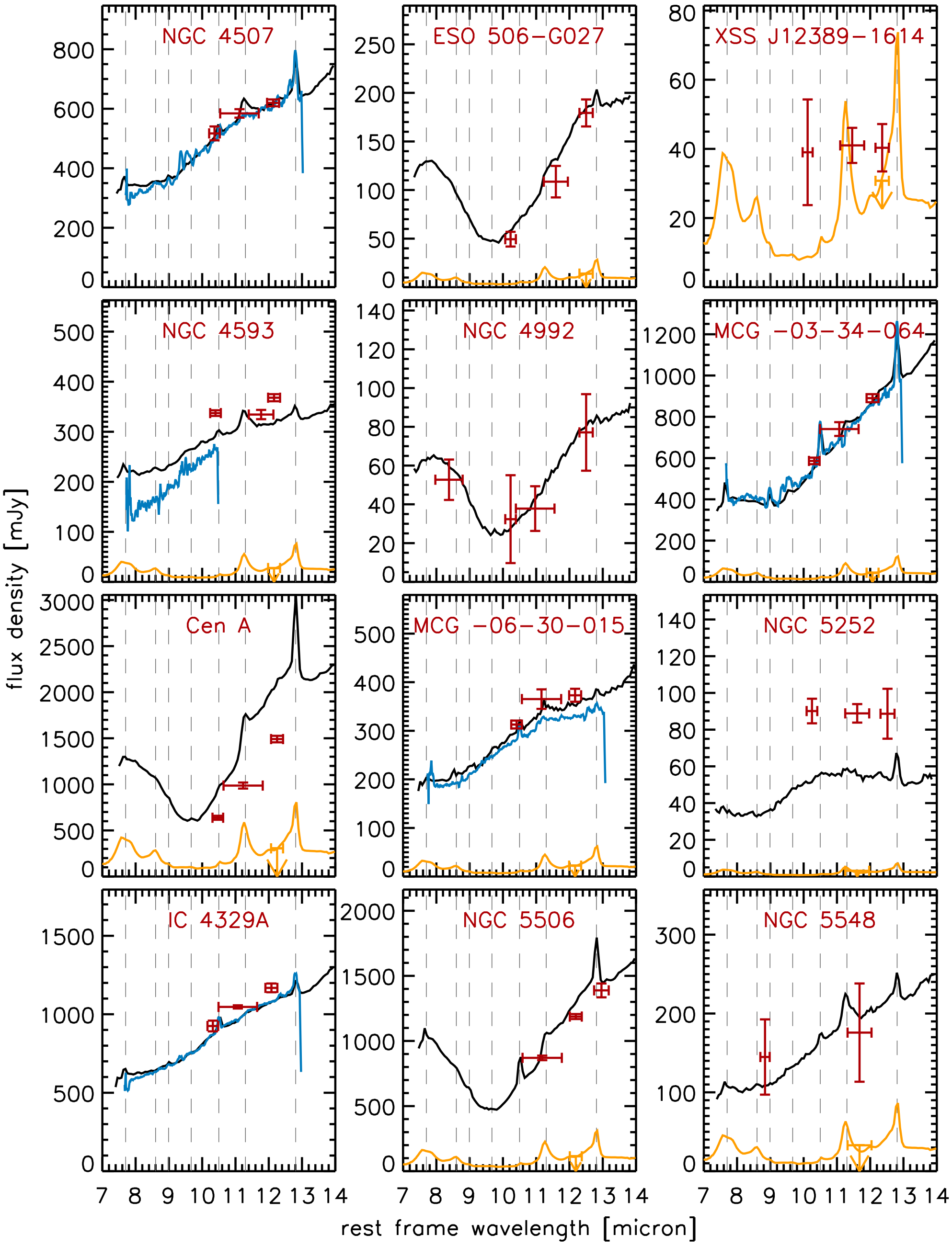

Figure B.2: continued.

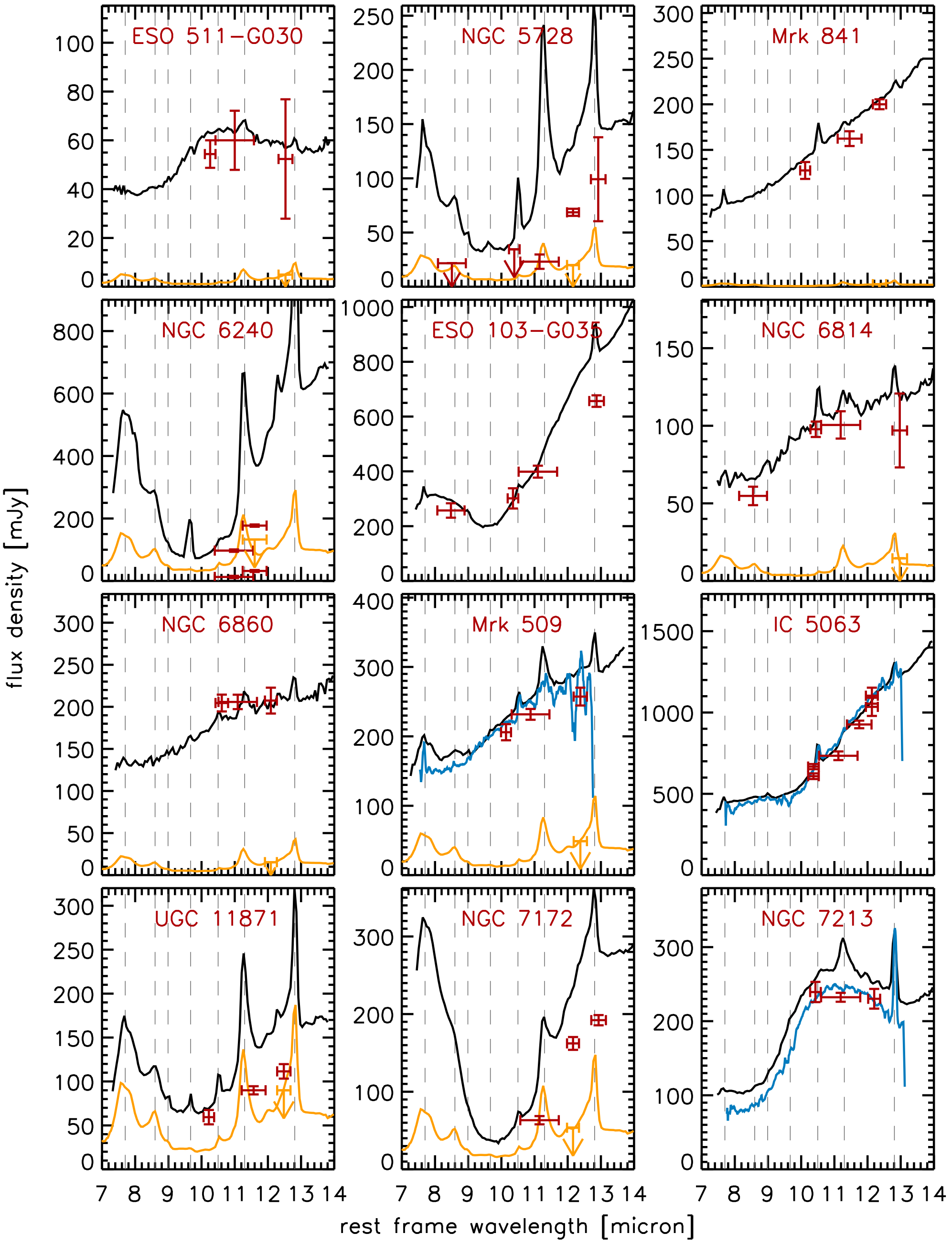

Figure B.2: continued.

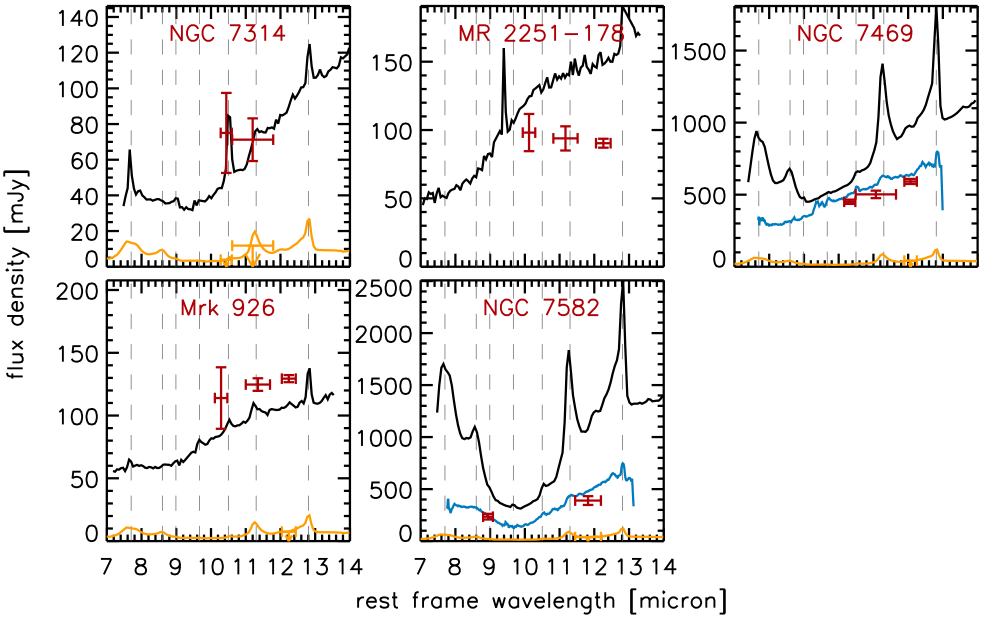

Figure B.2: continued.

Table B.3.: Comparison between HR photometry and *Spitzer*/IRS flux densities.

Object	$F_\nu^{\rm HR}(11\,\mu{\rm m})$ [mJy]	$F_\nu^{\rm IRS}(11\,\mu{\rm m})$ [mJy]	$R(11\,\mu{\rm m})$	$F_\nu^{\rm HR}({\rm cont})$ [mJy]	$F_\nu^{\rm IRS}({\rm cont})$ [mJy]	$R({\rm cont})$	$\log F({\rm PAH}11.3\mu{\rm m})$ [erg/s/cm^2]	$F_\nu^{\rm SF}(12\mu{\rm m})$ [mJy]	$c_<^{\rm SF}$ %
NGC 235A	53.7 ± 17.8	93.0	0.6	87.6 ± 8.4	125.2	0.7	-12.22	78.8	89
NGC 454	91.9 ± 8.7	53.3	1.7	150.9 ± 10.0	64.8	2.3	-12.84	15.8	10
Fairall 9	265.4 ± 4.6	280.5	0.9	301.5 ± 13.3	278.3	1.1	-12.98	12.0	3
NGC 526A	...	...	...	239.3 ± 9.8	207.1	1.2	-13.23	6.6	2
NGC 612	≤ 14.5	93.5	0.2	≤ 29.8	72.6	0.4	-12.20	...	...
ESO 297-G018	31.4 ± 13.8	53.4	0.6	23.5 ± 9.7	66.8	0.4	-12.77	25.6	100
NGC 788	95.2 ± 16.1	...	...	130.4 ± 4.7	...	...	-13.08	...	5
Mrk 1018	58.7 ± 16.7	...	...	66.1 ± 16.2	...	...	...	...	0
Mrk 590	86.8 ± 8.2	104.1	0.8	108.5 ± 15.1	119.1	0.9	-13.11	11.5	10
NGC 985	145.3 ± 27.8	...	...	181.9 ± 18.4	...	...	-12.97	...	5
ESO 416-G002	20.3 ± 4.9	...	...	24.6 ± 2.9	...	...	...	20.6	83
ESO 198-G024	32.1 ± 8.5	39.8	0.8	44.6 ± 5.9	39.7	1.1	-13.63	2.7	6
NGC 1142	21.0 ± 6.6	96.3	0.2	50.5 ± 7.4	105.0	0.5	-12.45	19.4	38
NGC 1365	422.5 ± 11.5	935.9	0.5	494.2 ± 77.6	933.3	0.5	-11.45	359.2	72
ESO 548-G081	115.5 ± 15.6	131.2	0.9	111.0 ± 10.4	121.0	0.9	-12.86	15.6	14
PGC 13946	≤ 8.7	22.4	0.4	≤ 8.7	12.1	0.7	-12.84	...	...
2MASX J03565655	28.2 ± 12.3	...	...	28.7 ± 9.5	...	...	...	21.0	72
3C 105	≤ 7.2	40.0	0.2	8.5 ± 6.7	49.4	0.2	...	...	0
1H 0419-577	62.5 ± 6.5	...	...	61.8 ± 6.5	...	...	...	44.4	71
3C 120	258.5 ± 12.3	258.8	1.0	266.4 ± 9.5	264.9	1.0	-12.89	17.5	6
MCG -01-13-025	42.3 ± 3.9	40.1	1.1	30.9 ± 6.6	37.1	0.8	-13.35	4.9	15
XSS J05054-2348	59.0 ± 5.4	61.0	1.0	65.1 ± 4.7	67.2	1.0	-13.15	...	0
Ark 120	254.8 ± 15.4	262.4	1.0	251.2 ± 16.0	236.0	1.1	-12.76	23.7	9
ESO 362-G018	131.7 ± 4.0	150.2	0.9	155.2 ± 11.0	150.7	1.0	-12.41	42.9	27
Pictor A	82.0 ± 7.6	70.6	1.2	83.2 ± 25.7	71.5	1.2	-13.89	...	0
NGC 2110	...	...	...	364.5 ± 7.2	355.7	1.0	-12.37	...	0
EXO 055620-3820	385.1 ± 20.0	363.7	1.1	465.2 ± 42.8	414.1	1.1	...	304.1	65
ESO 005-G004	21.0 ± 6.2	89.2	0.2	34.3 ± 15.7	90.9	0.4	-12.36	15.4	45
Mrk 3	443.9 ± 5.4	520.8	0.9	443.9 ± 5.4	520.8	0.9	...	...	0
ESO 121-G028	11.8 ± 4.5	11.2	1.1	14.8 ± 6.3	14.9	1.0	-14.00	...	0
2MASX J06403799	...	...	...	29.8 ± 5.7	...	...	...	...	0
2MASX J09180027	...	...	...	15.8 ± 7.9	...	...	...	...	0
MCG -01-24-012	94.6 ± 14.9	71.9	1.3	143.1 ± 24.0	98.9	1.4	-13.07	9.5	6

Table B.3.: continued.

Object	$F_\nu^{\mathrm{HR}}(11\,\mu\mathrm{m})$ [mJy]	$F_\nu^{\mathrm{IRS}}(11\,\mu\mathrm{m})$ [mJy]	$R(11\,\mu\mathrm{m})$	$F_\nu^{\mathrm{HR}}(\mathrm{cont})$ [mJy]	$F_\nu^{\mathrm{IRS}}(\mathrm{cont})$ [mJy]	$R(\mathrm{cont})$	$\log F(\mathrm{PAH}11.3\mu\mathrm{m})$ [erg/s/cm^2]	$F_\nu^{\mathrm{SF}}(12\mu\mathrm{m})$ [mJy]	$c_<^{\mathrm{SF}}$ %
NGC 2992	139.9 ± 13.0	254.2	0.6	164.7 ± 8.9	271.9	0.6	-11.93	118.4	71
MCG -05-23-016	…	…	…	632.7 ± 24.3	620.0	1.0	-12.66	21.9	3
NGC 3081	154.7 ± 50.9	238.2	0.6	180.2 ± 57.5	332.7	0.5	-12.58	44.7	24
NGC 3227	358.7 ± 41.5	420.5	0.9	311.7 ± 7.7	387.4	0.8	-12.47	32.4	10
NGC 3281	454.3 ± 8.2	384.1	1.2	640.7 ± 10.5	525.0	1.2	…	…	0
1RXS J112716	37.3 ± 18.3	…	…	40.6 ± 2.9	…	…	…	28.6	70
NGC 3783	…	…	…	708.6 ± 39.2	664.8	1.1	-12.90	…	0
2MASX J11454045	45.1 ± 10.7	67.7	0.7	51.6 ± 7.5	69.3	0.7	-13.59	3.5	6
CGCG 041-020	25.3 ± 8.1	61.4	0.4	34.9 ± 5.6	57.4	0.6	-12.64	19.2	54
NGC 4051	456.9 ± 5.4	480.5	1.0	456.9 ± 5.4	480.5	1.0	-12.06	117.1	25
NGC 4074	…	…	…	80.6 ± 6.2	89.9	0.9	-13.25	8.8	10
NGC 4138	17.1 ± 2.7	44.7	0.4	17.1 ± 2.7	44.7	0.4	-13.19	8.7	50
NGC 4151	1315.3 ± 200.0	1808.1	0.7	1294.4 ± 77.3	1857.1	0.7	-12.24	55.9	4
NGC 4388	200.8 ± 41.7	309.7	0.6	433.9 ± 79.9	597.7	0.7	-12.19	113.2	26
NGC 4395	…	…	…	5.7 ± 1.7	8.4	0.7	-13.67	3.4	60
NGC 4507	584.3 ± 14.3	584.8	1.0	619.7 ± 11.4	624.6	1.0	-12.33	…	0
ESO 506-G027	108.6 ± 16.2	126.9	0.9	179.3 ± 13.9	179.5	1.0	-13.04	14.0	7
XSS J12389-1614	41.0 ± 5.1	…	…	40.3 ± 6.8	…	…	…	30.8	76
NGC 4593	…	…	…	368.0 ± 7.1	320.6	1.1	-12.61	27.7	7
NGC 4992	37.8 ± 11.5	43.2	0.9	77.1 ± 19.8	78.8	1.0	-14.23	…	0
MCG -03-34-064	740.6 ± 33.3	705.1	1.1	890.3 ± 19.5	883.4	1.0	-12.40	44.2	4
Cen A	987.0 ± 32.6	1538.8	0.6	1491.5 ± 35.4	2120.9	0.7	-11.58	306.0	20
MCG -06-30-015	365.2 ± 20.1	339.9	1.1	373.1 ± 13.4	357.0	1.0	-12.70	22.5	6
NGC 5252	88.9 ± 5.0	57.0	1.6	88.9 ± 5.0	57.0	1.6	-13.63	3.1	3
IC 4329A	1046.7 ± 10.4	970.0	1.1	1168.1 ± 28.0	1086.0	1.1	-12.79	…	0
NGC 5506	870.1 ± 17.5	943.8	0.9	1187.7 ± 19.4	1312.2	0.9	-12.00	114.0	9
NGC 5548	175.8 ± 62.3	203.1	0.9	175.8 ± 62.3	203.1	0.9	-12.55	32.8	18
ESO 511-G030	60.0 ± 12.1	64.8	0.9	52.3 ± 24.5	57.2	0.9	-13.50	5.0	9
NGC 5728	23.2 ± 6.6	139.0	0.2	68.7 ± 3.3	133.6	0.5	-11.98	20.1	29
Mrk 841	162.3 ± 8.1	178.0	0.9	200.0 ± 5.4	202.3	1.0	-13.66	2.8	1
NGC 6240	97.1 ± 3.9	277.0	0.4	177.2 ± 3.8	476.2	0.4	-11.60	132.8	74
ESO 103-G035	398.9 ± 21.8	437.4	0.9	656.5 ± 21.1	888.3	0.7	…	…	0
NGC 6814	100.5 ± 8.8	113.6	0.9	96.9 ± 23.8	121.2	0.8	-13.00	14.6	15

Table B.3.: continued.

Object	$F_\nu^{\mathrm{HR}}(11\,\mu\mathrm{m})$ [mJy]	$F_\nu^{\mathrm{IRS}}(11\,\mu\mathrm{m})$ [mJy]	$R(11\,\mu\mathrm{m})$	$F_\nu^{\mathrm{HR}}(\mathrm{cont})$ [mJy]	$F_\nu^{\mathrm{IRS}}(\mathrm{cont})$ [mJy]	$R(\mathrm{cont})$	$\log F(\mathrm{PAH}11.3\mu\mathrm{m})$ [erg/s/cm^2]	$F_\nu^{\mathrm{SF}}(12\mu\mathrm{m})$ [mJy]	$c_<^{\mathrm{SF}}$ %
NGC 6860	205.8 ± 8.6	196.9	1.0	207.4 ± 15.3	203.6	1.0	-12.86	15.4	7
Mrk 509	231.7 ± 7.8	262.4	0.9	257.3 ± 12.8	292.8	0.9	-12.43	49.0	19
IC 5063	733.8 ± 26.6	823.1	0.9	1103.4 ± 49.1	1086.1	1.0	…	…	0
UGC 11871	89.9 ± 4.7	183.6	0.5	111.5 ± 8.2	176.7	0.6	-12.09	89.9	80
NGC 7172	63.2 ± 5.3	139.9	0.5	162.2 ± 8.3	237.7	0.7	-12.32	53.6	33
NGC 7213	232.2 ± 6.0	286.0	0.8	230.2 ± 13.3	254.2	0.9	-12.50	…	0
NGC 7314	71.2 ± 12.0	67.8	1.1	75.0 ± 22.4	55.7	1.3	-13.06	3.9	5
MR 2251-178	93.9 ± 8.9	139.1	0.7	90.4 ± 3.3	150.7	0.6	-13.70	…	0
NGC 7469	501.9 ± 25.9	950.7	0.5	591.7 ± 17.7	986.1	0.6	-12.41	42.5	7
Mrk 926	124.7 ± 5.0	103.6	1.2	129.4 ± 2.8	107.0	1.2	-13.18	7.6	5
NGC 7582	…	…	…	389.8 ± 42.3	1094.9	0.4	-12.40	38.7	9

– *Notes:* The given IRS fluxes are extracted from the post-BCD spectra convolved with the normalized HR filter transfer functions; the 11 μm fluxes contain not only the PAH feature at 11.3 μm but also the underlying continuum; $R(11\,\mu\mathrm{m})$ and $R(\mathrm{cont})$ give the flux ratios ($F_\nu^{\mathrm{HR}}/F_\nu^{\mathrm{IRS}}$) for the corresponding filters. $c_<^{\mathrm{SF}}$ signifies the maximum SF contribution (in percent) to the nuclear 12 μm continuum flux (at 0.4″scale).

Table B.4.: X-ray properties for the BAT AGN sample.

Object	W09 log $L_{2-10\,\mathrm{keV}}$ [erg/s]	Sat.	Other log $L_{2-10\,\mathrm{keV}}$ [erg/s]	Other sat.	Other ref.	Notes
NGC 235 A	43.11	XR	...	...	...	
Mrk 348	42.52	A	43.36 ± 0.30	X	2 , 31	buried AGN candidate
Mrk 352	42.65	X	...	...	...	*XMM* data only published in W09
NGC 454	42.26	XR	42.28 ± 0.60	X, S	28	changing look AGN
Fairall 9	43.91	A	43.84 ± 0.15	X, C	22	
NGC 526A	43.37	A	43.09 ± 0.10	B, R	22	
NGC 612	43.42	X	43.42 ± 0.30	S	11	*XMM* data only in W09
ESO 297-G018	43.14	S	43.55 ± 0.30	S, XR	18	buried AGN candidate
NGC 788	42.88	A	...	...	...	
Mrk 1018	43.60	XR	...	...	...	*XMM* data in Trippe et al. (2011), but no $L_{2-10\mathrm{keV}}$
Mrk 590	42.90	X	43.57 ± 0.25	X, C	22	
NGC 931	42.24	A	43.35 ± 0.30	X	46	
NGC 985	44.28	C	...	...	...	*XMM* data, but unpublished
ESO 416-G002	43.70	X	43.53 ± 0.30	X	17	
ESO 198-G024	43.64	X	43.69 ± 0.30	X	34	
NGC 1142	43.47	X	43.44 ± 0.30	S	51 , 31	buried AGN candidate
NGC 1365	42.21	XR	42.32 ± 0.30	S, C	37	changing covering fraction, very complex source
ESO 548-G081	42.78	X	...	...	...	*XMM* data only in W09
PGC 13946	43.15	XR	43.12 ± 0.30	S	10	
2MASX J03565655	43.90	XR	...	...	...	
3C 105	43.93	XR	43.11 ± 0.30	C	29	
1H 0419-577	44.31	A	44.37 ± 0.30	X	16	flux variation of factor ~ 2
3C 120	43.98	A	43.97 ± 0.30	X	48	*Chandra* images only of the jet?
MCG -01-13-025	43.01	X	42.69 ± 0.30	X	17	
XSS J05054-2348	43.63	XR	44.14 ± 0.30	S	10	
Ark 120	43.76	A	43.88 ± 0.30	X	48	
ESO 362-G018	42.36	X	42.36 ± 0.30	X	6	
Pictor A	43.44	A	...	...	...	*Chandra*/*XMM* data: no nuclear properties published
NGC 2110	42.51	A	42.69 ± 0.30	C, X, B	7 , 15	
EXO 055620-3820	43.76	A	...	...	...	no *XMM* luminosities published
ESO 005-G004	41.90	S	41.82 ± 0.30	S, XR	18	buried AGN candidate, see App. C.3
Mrk 3	42.96	A	43.32 ± 0.30	S	23	reflection dominated, broad Fe Kα, highly obscured

Table B.4.: continued.

Object	W09 log $L_{2-10\,\mathrm{keV}}$ [erg/s]	Sat.	Other log $L_{2-10\,\mathrm{keV}}$ [erg/s]	Other sat.	Other ref.	Notes
ESO 121-G028	43.34	XR	…	…	…	
2MASX J06403799	43.10	XR	…	…	…	
Mrk 6	42.94	XR	43.16 ± 0.30	X	24	
Mrk 79	43.62	X	43.28 ± 0.30	X	48	
2MASX J09180027	43.84	S	…	…	…	
MCG -01-24-012	43.09	XR	…	…	…	
NGC 2992	41.58	A	42.54 ± 1.00	X, S	6 , 44	strong variation, at least factor ~ 20
MCG -05-23-016	43.23	A	43.16 ± 0.30	X	2	
NGC 3081	42.55	A	42.69 ± 0.30	A	18	
NGC 3227	42.16	A	42.02 ± 0.33	X, C, XR	47 , 6 , 43	
NGC 3281	42.52	A	43.35 ± 0.15	B	18	
NGC 3516	42.69	A	42.96 ± 0.78	X	6 , 48 , 5	factor ~ 10 variability
1RXS J112716.6+	43.94	XR	…	…	…	
NGC 3783	43.19	A	43.24 ± 0.15	X	22	
2MASX J11454045	43.51	XR	…	…	…	
CGCG 041-020	43.31	X	…	…	…	*XMM* data only in W09
NGC 4051	41.58	A	41.32 ± 0.60	X	49	factor ~ 5 variability, see App. C.22
NGC 4074	42.31	XR	42.89 ± 0.30	X	31	buried AGN candidate
NGC 4138	41.27	X	41.30 ± 0.15	X	32 , 52	buried AGN candidate, see App. C.23
NGC 4151	42.55	A	42.80 ± 0.70	C	50	factor ~ 10 variability
NGC 4253	42.87	A	42.74 ± 0.30	X	38	
NGC 4388	41.92	A	42.35 ± 0.30	X, I	18	buried AGN candidate
NGC 4395	40.14	A	39.76 ± 0.56	A, C, X	52	emission $\lesssim 3\,\mathrm{keV}$ varies drastically, see App. C.26
NGC 4507	43.06	A	43.33 ± 0.15	A	22	
ESO 506-G027	43.26	X	43.54 ± 0.15	S	51 , 31	buried AGN candidate
XSS J12389-1614	43.52	XR	…	…	…	
NGC 4593	42.83	A	43.02 ± 0.20	X, C	22	
NGC 4992	43.05	X	43.25 ± 0.30	S	18	
MCG -03-34-064	42.91	A	43.59 ± 0.40	X	30	
Cen A	-	-	41.69 ± 0.15	X, C	13	see App. C.1
MCG -06-30-015	42.71	A	42.78 ± 0.40	S	22	
NGC 5252	42.90	A	43.11 ± 0.30	C	8	

Table B.4.: continued.

Object	W09 log $L_{2-10\,\mathrm{keV}}$ [erg/s]	Sat.	Other log $L_{2-10\,\mathrm{keV}}$ [erg/s]	Other sat.	Other ref.	Notes
IC 4329A	43.65	A	43.87 ± 0.30	B	7	
Mrk 279	43.67	A	43.71 ± 0.30	X, C	48 , 41	
NGC 5506	42.90	A	42.98 ± 0.30	X, C	26 , 4	
NGC 5548	43.56	A	43.42 ± 0.30	X, C	1 , 35	
ESO 511-G030	43.13	A	43.14 ± 0.30	X	45	
NGC 5728	41.84	C	42.88 ± 0.30	S	18	
Mrk 841	43.43	X	43.57 ± 0.30	X	33 , 5	
Mrk 290	43.20	A	43.35 ± 0.30	X, C	52	
NGC 6240	-	-	42.63 ± 0.76	X, C	25 , 21 , 6	*XMM* fluxes 1 dex higher, cannot be 2nd nucleus
3C 382	44.30	A	44.56 ± 0.30	C	19 , 40	
ESO 103-G035	42.75	A	43.41 ± 0.15	I	18	buried AGN candidate
3C 390.3	44.08	A	44.45 ± 0.30	X, C	14 , 39	
NGC 6814	40.70	A	42.01 ± 0.40	R, A	18	
NGC 6860	42.61	X	. . .	. . .	. . .	*XMM* data only in W09
Mrk 509	44.00	A	44.06 ± 0.15	X, C	22	
IC 5063	42.71	A	42.81 ± 0.20	A	22	
UGC 11871	42.90	XR	. . .	. . .	. . .	
NGC 7172	42.77	A	42.61 ± 0.40	X	22	buried AGN candidate
NGC 7213	42.21	A	42.10 ± 0.15	S	27	see App. C.34
NGC 7314	42.32	A	42.22 ± 0.15	X	22	
3C 452	-	C	43.96 ± 0.30	C	14 , 42	
MR 2251-178	44.32	A	44.38 ± 0.30	S	20 , 36	
NGC 7469	43.16	A	43.08 ± 0.10	X, C	22	
Mrk 926	44.13	A	44.11 ± 0.30	X	5	
NGC 7582	41.98	A	42.42 ± 0.30	B	7 , 6	

– *Notes:* W09 log $L_{2-10\,\mathrm{keV}}$: absorption-corrected X-ray luminosity from Winter et al. (2009a) and data of the following satellites: A: *ASCA*, B: *BeppoSAX*, C: *Chandra*, I: *INTEGRAL*, R: *RXTE*, S: *Suzaku*, X: *XMM-Newton*, XR: *XRT*; other log $L_{2-10\,\mathrm{keV}}$: absorption-corrected X-ray luminosity selected from the literature; references: 1: Andrade-Velázquez et al. (2010); 2: Awaki et al. (2006); 3: Ballantyne and Fabian (2005); 4: Bianchi et al. (2003); 5: Bianchi et al. (2004); 6: Brightman and Nandra (2011); 7: Dadina (2007); 8: Dadina et al. (2010); 9: Dewangan et al. (2008); 10: Eguchi et al. (2009); 11: Eguchi et al. (2011); 12: Emmanoulopoulos et al. (2011); 13: Evans et al. (2004); 14: Evans et al. (2006); 15: Evans et al. (2007); 16: Fabian et al. (2005); 17: Gallo et al. (2006); 18: Gandhi et al. (2009); 19: Gliozzi et al. (2007); 20: Gofford et al. (2011); 21: González-Martín et al. (2009b); 22: Horst et al. (2008); 23: Ikeda et al.

(2009); 24: Immler et al. (2003); 25: Komossa et al. (2003); 26: LaMassa et al. (2011); 27: Lobban et al. (2010); 28: Marchese et al. (2012); 29: Massaro et al. (2010); 30: Miniutti et al. (2007); 31: Noguchi et al. (2009); 32: Panessa et al. (2006); 33: Petrucci et al. (2007); 34: Porquet et al. (2004); 35: Pounds et al. (2003); 36: Ramírez et al. (2008); 37: Risaliti et al. (2009); 38: Risaliti et al. (2011); 39: Sambruna et al. (2009); 40: Sambruna et al. (2011); 41: Scott et al. (2004); 42: Shelton et al. (2011); 43: Shu et al. (2010c); 44: Shu et al. (2010b); 45: Tombesi et al. (2010); 46: Tripathi et al. (2011); 47: Tueller et al. (2008); 48: Vasudevan et al. (2009); 49: Vaughan et al. (2011); 50: Wang et al. (2010); 51: Winter et al. (2009b); 52: Zhang et al. (2009);

Table B.5.: Relevant nuclear properties for all BAT AGN used in this work.

Object	AGN type	$\log N_{\mathrm{H}}$ cm^{-2}	$\log L_{2-10\,\mathrm{keV}}$ [erg/s]	$\log L_{14-195\,\mathrm{keV}}$ [erg/s]	$\log \lambda L_{\lambda}(12\,\mu\mathrm{m})$ [erg/s]	$\log M_{\mathrm{BH}}$ [$M_{\odot}$]	Ref.
NGC 235 A	1.0	23.45	43.11 ± 0.30	43.59 ± 0.11	43.30 ± 0.04	8.23 ± 0.37	Hyp
Mrk 348	2.0	23.21	43.36 ± 0.30	43.75 ± 0.16	43.20 ± 0.15	7.63 ± 0.37	Hyp
Mrk 352	1.0	20.00	42.65 ± 0.30	43.22 ± 0.05	≤ 42.55	7.26 ± 0.50	W09
NGC 454	2.0	23.50	42.28 ± 0.60	42.81 ± 0.30	43.02 ± 0.03	6.23 ± 0.50	W09
Fairall 9	1.2	20.48	43.84 ± 0.15	44.38 ± 0.04	44.56 ± 0.02	8.41 ± 0.09	P04
NGC 526A	1.9	22.11	43.09 ± 0.10	43.62 ± 0.06	43.62 ± 0.02	8.23 ± 0.37	G05
NGC 612	2.0	24.05	43.42 ± 0.30	43.98 ± 0.22	≤ 43.11	8.47 ± 0.50	W09
ESO 297-G018	2.0	23.60	43.55 ± 0.30	43.97 ± 0.18	42.85 ± 0.15	9.68 ± 0.50	W09
NGC 788	2.0	22.28	42.88 ± 0.30	43.49 ± 0.20	43.03 ± 0.02	7.56 ± 0.37	Hyp
Mrk 1018	1.9	20.00	43.60 ± 0.30	44.13 ± 0.07	43.79 ± 0.10	8.45 ± 0.37	Hyp
Mrk 590	1.0	19.41	43.57 ± 0.25	43.70 ± 0.30	43.55 ± 0.06	7.68 ± 0.06	P04
NGC 931	1.0	21.30	43.35 ± 0.30	43.38 ± 0.04	43.41 ± 0.13	7.31 ± 0.36	Hyp
NGC 985	1.5	20.00	44.28 ± 0.30	44.13 ± 0.05	44.25 ± 0.04	8.94 ± 0.50	W09
ESO 416-G002	1.9	≤ 20.50	43.53 ± 0.30	44.41 ± 0.07	43.66 ± 0.05	9.02 ± 0.50	W09
ESO 198-G024	1.0	≤ 20.30	43.69 ± 0.30	44.34 ± 0.11	43.68 ± 0.05	8.36 ± 0.50	W09
NGC 1142	2.0	23.86	43.44 ± 0.30	44.23 ± 0.11	43.31 ± 0.06	9.36 ± 0.50	W09
NGC 1365	1.8	24.60	42.32 ± 0.30	42.59 ± 0.03	42.81 ± 0.06	7.27 ± 0.36	Hyp
ESO 548-G081	1.0	20.00	42.78 ± 0.30	43.27 ± 0.14	43.05 ± 0.04	8.94 ± 0.50	W09
PGC 13946	2.0	23.93	43.12 ± 0.30	43.94 ± 0.06	≤ 42.78	8.75 ± 0.50	W09
2MASX J03565655	1.9	22.53	43.90 ± 0.30	44.48 ± 0.30	43.95 ± 0.12	8.64 ± 0.50	W09
3C 105	2.0	22.93	43.11 ± 0.30	44.85 ± 0.06	43.59 ± 0.25	7.79 ± 0.50	W09
1H 0419-577	1.5	21.60	44.37 ± 0.30	44.73 ± 0.14	44.60 ± 0.04	9.00 ± 0.50	W09
3C 120	1.5	21.20	43.97 ± 0.30	44.43 ± 0.03	44.17 ± 0.02	7.74 ± 0.20	P04
MCG -01-13-025	1.2	≤ 19.59	42.69 ± 0.30	43.37 ± 0.30	42.60 ± 0.08	8.06 ± 0.50	W09
XSS J05054-2348	2.0	23.46	44.14 ± 0.30	44.27 ± 0.07	43.62 ± 0.03	7.53 ± 0.50	W09
Ark 120	1.0	20.00	43.88 ± 0.30	44.21 ± 0.13	44.14 ± 0.03	8.18 ± 0.05	P04
ESO 362-G018	1.5	23.19	42.36 ± 0.30	43.31 ± 0.09	43.10 ± 0.03	9.00 ± 0.50	W09
Pictor A	1.0	20.78	43.44 ± 0.30	44.00 ± 0.23	43.73 ± 0.12	7.60 ± 0.50	W09
NGC 2110	2.0	22.51	42.69 ± 0.30	43.66 ± 0.14	43.00 ± 0.01	8.73 ± 0.37	Hyp
EXO 055620-3820	1.2	22.41	43.76 ± 0.30	44.00 ± 0.12	44.45 ± 0.04	8.44 ± 0.50	W09
ESO 005-G004	2.0	24.04	41.82 ± 0.30	42.43 ± 0.05	41.72 ± 0.16	7.89 ± 0.50	W09
Mrk 3	2.0	≥ 24.00	43.32 ± 0.30	43.76 ± 0.19	43.64 ± 0.09	8.94 ± 0.37	Hyp
ESO 121-G028	2.0	23.21	43.34 ± 0.30	44.00 ± 0.30	43.11 ± 0.15	9.00 ± 0.50	W09

Table B.5.: continued.

Object	AGN type	$\log N_\mathrm{H}$ cm^{-2}	$\log L_{2-10\,\mathrm{keV}}$ [erg/s]	$\log L_{14-195\,\mathrm{keV}}$ [erg/s]	$\log \lambda L_\lambda(12\,\mu\mathrm{m})$ [erg/s]	$\log M_\mathrm{BH}$ $[M_\odot]$	Ref.
2MASX J06403799	2.0	23.21	43.10 ± 0.30	44.35 ± 0.30	43.76 ± 0.08	…	…
Mrk 6	1.5	23.00	43.16 ± 0.30	43.75 ± 0.06	≤ 43.73	8.24 ± 0.50	W09
Mrk 79	1.2	≤ 19.80	43.28 ± 0.30	43.72 ± 0.04	43.92 ± 0.13	7.72 ± 0.11	P04
2MASX J09180027	2.0	23.05	43.84 ± 0.30	45.29 ± 0.30	44.56 ± 0.18	8.57 ± 0.50	W09
MCG -01-24-012	2.0	23.06	43.09 ± 0.30	43.61 ± 0.05	43.51 ± 0.07	7.16 ± 0.50	W09
NGC 2992	1.9	21.60	42.54 ± 1.00	42.69 ± 0.14	42.61 ± 0.02	7.45 ± 0.36	Hyp
MCG -05-23-016	2.0	22.06	43.16 ± 0.30	43.59 ± 0.02	43.48 ± 0.02	8.03 ± 0.37	Hyp
NGC 3081	2.0	23.80	42.69 ± 0.30	43.24 ± 0.07	42.85 ± 0.13	7.38 ± 0.37	G05
NGC 3227	1.5	22.59	42.02 ± 0.33	42.85 ± 0.04	42.59 ± 0.01	6.88 ± 0.09	D10
NGC 3281	2.0	24.29	43.35 ± 0.15	43.41 ± 0.09	43.66 ± 0.01	7.39 ± 0.36	G05
NGC 3516	1.5	23.51	42.96 ± 0.78	43.36 ± 0.07	≤ 43.27	7.50 ± 0.05	D10
1RXS J112716.6+	1.8	21.40	43.94 ± 0.30	44.97 ± 0.20	44.44 ± 0.03	9.00 ± 0.50	W09
NGC 3783	1.5	20.94	43.24 ± 0.15	43.67 ± 0.08	43.57 ± 0.02	7.47 ± 0.05	P04
2MASX J11454045	1.5	20.00	43.51 ± 0.30	44.20 ± 0.21	43.49 ± 0.06	6.70 ± 0.50	W09
CGCG 041-020	2.0	23.03	43.31 ± 0.30	43.86 ± 0.08	43.40 ± 0.06	8.46 ± 0.50	W09
NGC 4051	1.2	≥ 23.27	41.32 ± 0.60	41.89 ± 0.03	42.32 ± 0.01	6.24 ± 0.11	D10
NGC 4074	2.0	23.28	42.89 ± 0.30	43.65 ± 0.22	43.35 ± 0.03	8.12 ± 0.50	W09
NGC 4138	1.9	≥ 23.59	41.30 ± 0.15	41.92 ± 0.24	41.00 ± 0.06	7.25 ± 0.37	H09
NGC 4151	1.5	22.57	42.80 ± 0.70	43.12 ± 0.22	42.86 ± 0.06	7.69 ± 0.50	W09
NGC 4253	1.5	≤ 21.00	42.74 ± 0.30	42.98 ± 0.05	43.52 ± 0.13	7.85 ± 0.50	W09
NGC 4388	2.0	23.43	42.35 ± 0.30	43.18 ± 0.14	42.54 ± 0.10	6.76 ± 0.36	Hyp
NGC 4395	1.8	23.58	39.76 ± 0.56	40.88 ± 0.08	39.52 ± 0.12	5.56 ± 0.12	P05
NGC 4507	2.0	23.46	43.33 ± 0.15	43.88 ± 0.07	43.71 ± 0.01	7.19 ± 0.36	C04
ESO 506-G027	2.0	24.00	43.54 ± 0.15	44.30 ± 0.02	43.79 ± 0.03	8.59 ± 0.50	W09
XSS J12389-1614	2.0	22.51	43.52 ± 0.30	44.30 ± 0.07	43.45 ± 0.07	8.88 ± 0.50	W09
NGC 4593	1.0	20.23	43.02 ± 0.20	43.32 ± 0.03	43.28 ± 0.01	6.99 ± 0.08	D06
NGC 4992	2.0	23.65	43.25 ± 0.30	43.95 ± 0.12	43.43 ± 0.10	8.56 ± 0.50	C04
MCG -03-34-064	1.8	23.59	43.59 ± 0.40	43.31 ± 0.17	44.15 ± 0.01	7.75 ± 0.37	P06
Cen A	2.0	22.95	41.69 ± 0.15	42.11 ± 0.09	41.70 ± 0.01	7.74 ± 0.07	C09
MCG -06-30-015	1.5	20.23	42.78 ± 0.40	43.08 ± 0.03	43.15 ± 0.02	6.38 ± 0.36	G05
NGC 5252	2.0	22.37	43.11 ± 0.30	43.99 ± 0.09	43.40 ± 0.06	8.21 ± 0.37	Hyp
IC 4329A	1.2	21.65	43.87 ± 0.30	44.30 ± 0.04	44.24 ± 0.01	7.00 ± 0.46	P04
Mrk 279	1.0	≤ 20.11	43.71 ± 0.30	44.02 ± 0.08	≤ 43.84	7.54 ± 0.10	P04

Table B.5.: continued.

Object	AGN type	log N_{H} cm^{-2}	log $L_{2-10\,\mathrm{keV}}$ [erg/s]	log $L_{14-195\,\mathrm{keV}}$ [erg/s]	log $\lambda L_{\lambda}(12\,\mu\mathrm{m})$ [erg/s]	log M_{BH} [$M_{\odot}$]	Ref.
NGC 5506	1.9	22.50	42.98 ± 0.30	43.41 ± 0.04	43.47 ± 0.01	7.61 ± 0.36	Hyp
NGC 5548	1.5	20.85	43.42 ± 0.30	43.73 ± 0.14	43.48 ± 0.13	7.65 ± 0.12	D10
ESO 511-G030	1.0	20.99	43.14 ± 0.30	43.73 ± 0.06	43.15 ± 0.17	8.66 ± 0.50	W09
NGC 5728	1.9	24.32	42.88 ± 0.30	43.35 ± 0.07	42.55 ± 0.02	7.88 ± 0.36	M95
Mrk 841	1.5	20.00	43.57 ± 0.30	43.94 ± 0.24	44.16 ± 0.01	8.15 ± 0.50	W09
Mrk 290	1.5	21.18	43.35 ± 0.30	43.68 ± 0.07	$\leq$ 43.68	7.68 ± 0.50	W09
NGC 6240	2.0	23.87	42.63 ± 0.76	43.97 ± 0.19	43.76 ± 0.01	9.32 ± 0.37	Hyp
3C 382	1.0	20.00	44.56 ± 0.30	44.79 ± 0.02	$\leq$ 44.27	9.22 ± 0.50	W09
ESO 103-G035	2.0	23.28	43.41 ± 0.15	43.61 ± 0.06	43.69 ± 0.02	7.13 ± 0.37	C04
3C 390.3	1.5	20.30	44.45 ± 0.30	44.89 ± 0.05	$\leq$ 44.23	8.46 ± 0.09	P04
NGC 6814	1.5	$\leq$ 20.51	42.01 ± 0.40	42.51 ± 0.10	41.97 ± 0.10	7.25 ± 0.36	W10
NGC 6860	1.5	22.66	42.61 ± 0.70	43.46 ± 0.12	43.36 ± 0.03	8.24 ± 0.50	W09
Mrk 509	1.2	19.48	44.06 ± 0.15	44.35 ± 0.03	44.17 ± 0.02	8.16 ± 0.03	P04
IC 5063	2.0	23.38	42.81 ± 0.20	43.32 ± 0.08	43.80 ± 0.02	7.82 ± 0.37	Hyp
UGC 11871	1.9	22.38	42.90 ± 0.30	43.69 ± 0.07	43.56 ± 0.03	8.34 ± 0.50	W09
NGC 7172	2.0	22.70	42.61 ± 0.40	43.35 ± 0.16	42.69 ± 0.02	7.31 ± 0.36	G05
NGC 7213	1.5	20.30	42.10 ± 0.15	42.49 ± 0.05	42.48 ± 0.02	7.42 ± 0.36	Hyp
NGC 7314	1.9	21.86	42.22 ± 0.15	42.40 ± 0.09	42.08 ± 0.05	5.53 ± 0.36	C04
3C 452	2.0	23.70	43.96 ± 0.30	44.75 ± 0.06	$\leq$ 43.94	...	...
MR 2251-178	1.5	21.52	44.38 ± 0.30	44.91 ± 0.07	44.29 ± 0.02	8.76 ± 0.50	W09
NGC 7469	1.5	20.69	43.08 ± 0.10	43.50 ± 0.10	43.84 ± 0.01	7.09 ± 0.05	P04
Mrk 926	1.5	20.00	44.11 ± 0.30	44.66 ± 0.27	44.15 ± 0.01	8.95 ± 0.50	W09
NGC 7582	2.0	21.79	42.42 ± 0.30	42.70 ± 0.07	42.80 ± 0.04	7.33 ± 0.36	Hyp

– *Notes:* Optical AGN classification adopted from Véron-Cetty and Véron (2010); $L_{2-10\mathrm{keV}}$ and N_{H} from the references given in Table B.4. $L_{14-195\mathrm{keV}}$ from Tueller et al. (2008) and Tueller et al. (2010). $\lambda L_{\lambda}(12\,\mu\mathrm{m})$ from the HR data presented in this work; References on M_{BH}: C04 Cid Fernandes et al. (2004); C09 Cappellari et al. (2009); D06 Denney et al. (2006); D10 Denney et al. (2010); G05 Garcia-Rissmann et al. (2005); Hyp Hyperleda database (Paturel et al. 2003); L06 Lewis and Eracleous (2006); M95 McElroy (1995); P04 Peterson et al. (2004); P05 Peterson et al. (2005); W09 Winter et al. (2009a); W10 Woo et al. (2010).

Table B.6.: Relevant host properties for all non-BAT, non-LLAGN AGN used in this work.

Object	Morphology	Incl. [°]	Redshift	D [Mpc]	r_0 [pc]	$\log \lambda L^{\mathrm{G}}_{\lambda}(12\,\mu\mathrm{m})$ [erg/s]
NGC 1068	Sb	24	0.0038	14	24	44.37 ± 0.001
ESO 209-G012	Sa	90	0.0396	179	304	44.29 ± 0.06
ESO 263-G013	SABb	43	0.0329	143	243	...
NGC 3393	SBa	31	0.0125	53	90	43.04 ± 0.10
IC 3639	SBbc	22	0.0111	46	78	43.66 ± 0.02
ESO 323-G032	S0-a	43	0.0159	68	115	43.17 ± 0.10
NGC 5135	Sab	25	0.0137	60	102	43.83 ± 0.02
NGC 5995	SABa	42	0.0251	108	183	44.13 ± 0.04
ESO 138-G001	E-S0	61	0.0092	38	64	43.32 ± 0.03
NGC 6300	SBb	53	0.0037	16	27	43.12 ± 0.01
ESO 141-G055	Sb	52	0.0382	156	265	44.25 ± 0.04
PG 2130+099	?	?	0.0620	274	465	44.62 ± 0.02
3C 445	?	36	0.0564	247	419	44.49 ± 0.06
NGC 7674	SBbc	27	0.0300	125	212	44.50 ± 0.02
NGC 7679	S0-a	59	0.0171	73	124	43.90 ± 0.03
ESO 323-G077	S0	58	0.0090	38	64	...
NGC 5643	Sc	30	0.0161	71	120	...

– *Notes:* All objects and their distances are from G09, except the last two, which are from Hönig et al. (2010). Description is similar to Table B.1.

Table B.7.: Relevant nuclear properties for all non-BAT, non-LLAGN AGN used in this work.

Object	AGN type	$\log N_{\mathrm{H}}$ cm^{-2}	$\log L_{2-10\,\mathrm{keV}}$ [erg/s]	$\log L_{14-195\,\mathrm{keV}}$ [erg/s]	$\log \lambda L_{\lambda}(12\,\mu\mathrm{m})$ [erg/s]	$\log M_{\mathrm{BH}}$ $[M_{\odot}]$	Ref.
NGC 1068	1h	≥ 25.00	43.40 ± 0.30	41.94 ± 0.06	43.80 ± 0.03	6.93 ± 0.36	L03
ESO 209-G012	1.5	19.00	43.65 ± 0.15	...	44.22 ± 0.06	...	...
ESO 263-G013	2	23.60	43.30 ± 0.40	43.81 ± 0.08	43.42 ± 0.02	...	...
NGC 3393	2	24.18	43.04 ± 0.30	...	42.90 ± 0.02	7.77 ± 0.36	Hyp
IC 3639	1h	≥ 25.00	43.62 ± 0.50	...	43.51 ± 0.02	6.40 ± 0.36	G05
ESO 323-G032	1.9	≤ 22.00	42.43 ± 0.40	...	42.96 ± 0.04	7.40 ± 0.37	C04
NGC 5135	2	24.18	43.00 ± 0.50	...	43.06 ± 0.05	6.96 ± 0.36	G05
NGC 5995	1.9	21.95	43.54 ± 0.15	...	44.11 ± 0.06	7.11 ± 0.40	W07
ESO 138-G001	2	≥ 24.30	43.00 ± 0.30	...	43.54 ± 0.02	6.43 ± 0.37	C04
NGC 6300	2	23.34	42.30 ± 0.30	42.50 ± 0.03	42.69 ± 0.02	6.34 ± 0.36	G05
ESO 141-G055	1	20.74	43.90 ± 0.15	44.19 ± 0.05	44.04 ± 0.11	7.91 ± 0.50	W07
PG 2130+099	1.5	19.48	43.65 ± 0.20	...	44.53 ± 0.07	7.91 ± 0.10	P04
3C 445	1.5	23.11	44.26 ± 0.15	44.50 ± 0.05	44.50 ± 0.06	8.15 ± 0.40	B03
NGC 7674	1h	24.18	44.56 ± 0.50	43.64 ± 0.30	44.31 ± 0.03	7.26 ± 0.36	Hyp
NGC 7679	1.9	20.34	42.52 ± 0.15	...	42.82 ± 0.15	5.99 ± 0.36	Hyp
ESO 323-G077	1.2	23.25	42.76 ± 0.30	43.39 ± 0.06	43.71 ± 0.01	...	...
NGC 5643	2	≥ 24.00	41.40 ± 0.30	...	42.51 ± 0.01	7.00 ± 0.50	B09

– *Notes:* $N_{\mathrm{H}}, L_{2-10\mathrm{keV}}$ and $\lambda L_{\lambda}(12\,\mu\mathrm{m})$ are from G09 for all objects, except for the last two, which are from Hönig et al. (2010). Description is similar to Table B.5 and additional references on M_{BH}: B03 Bettoni et al. (2003); B09 Beifiori et al. (2009); L03 Lodato and Bertin (2003); W07 Wang and Zhang (2007).

Appendix C.

Additional notes on individual objects

C.1. Cen A – NGC 5128

Cen A is one of the best studied AGN at all because of its proximity ($\sim 3.4\,\mathrm{Mpc}$) and extreme brightness in terms of flux. This object might presently undergo a major merger between a massive elliptical and a spiral galaxy, as indicated by its peculiar morphology. Furthermore, a massive bipolar jet larger than the whole galaxy is visible at radio wavelengths. Cen A has been included both in the LLAGN and BAT AGN sample, and the X-ray properties reported by Evans et al. (2004) are adopted. These are based on *Chandra* and *XMM-Newton* observations, and are consistent with previous measurements in the literature. Two components, one of an absorbed standard accretion disk and another from the base of the jet, are identified in the high-quality X-ray data. The high obscuration might possibly arise from a large-scale dust lane belonging to the spiral, HR MIR photometry was obtained by Horst et al. (2008) and Reunanen et al. (2010), both in good agreement. The latter authors note marginally extended, but weak, emission and a significant elongation at $18.7\,\mu\mathrm{m}$ in this object, which is attributed to synchrotron emission from the jet. On the other hand, MIR interferometric observations of Cen A show an unresolved ($< 1\,\mathrm{pc}$) central source that is attributed to jet emission, and some extended disk-like component, perpendicular to the jet axis. Hence the MIR emission of Cen A is presumably dominated by the jet, while the putative torus might be completely absent.

C.2. Circinus

Similar to Cen A, the Circinus galaxy harbors one of the nearest AGNs ($\sim 4\,\mathrm{Mpc}$) and thus enables very detailed studies of its highly obscured Sy 2.0 nucleus ($N_\mathrm{H} \sim 4 \cdot 10^{24}\,\mathrm{cm}^{-2}$). A broad H_α component has been found in polarized light, giving firm evidence that this object is intrinsically a type 1 AGN. Circinus has been observed in X-rays with *Chandra* and the corresponding 2-10 keV luminosity is published in Smith and Wilson (2001), which is used in this work. Their results agree with previous *BeppoSAX* measurements (Matt et al. 1999) and later *Suzaku* follow-ups (Yang et al. 2009). The X-ray spectrum is dominated by a hard power-law continuum and a strong Fe Kα emission line, characteristic for Compton-thick obscuration. The torus of Circinus seems to be orientated almost edge-on. The HR MIR photometry show a bright central source surrounded by an extended halo and some beamed emission (compare Fig. A.1 and Reunanen et al. 2010). MIR interferometric measurements could even resolve the clumpy torus-like structure in this object, which surrounds a hot compact disk component (Tristram et al. 2007).

C.3. ESO 005-G004 – SWIFT J0601.9-8636

ESO 005-G004 has only recently been discovered to harbor an AGN (Landi et al. 2007), which is presumably related to the high nuclear obscuration in this object. Note that this object is included both in the LLAGN and BAT AGN sample. Ueda et al. (2007) present a combined *Swift* and *Suzaku* data analysis and classify this object as a buried AGN candidate. G09 used their results as is done in this work as well.

C.4. IC 1459

Detailed X-ray modeling of *Chandra* observations of IC 1459 are presented in González-Martín et al. (2009b). Satyapal et al. (2004) give comparable model parameters for the same data set. For the X-ray luminosity the mean of both works was used. There is no [OIII] $\lambda 5007\,\text{Å}$ or [OIV] $\lambda 25.89\,\mu\text{m}$ luminosity measurement in the literature. The X-ray data suggest that the object is not Compton-thick. In addition, a compact radio core was detected by Slee et al. (1994), confirming the AGN nature of this object. Accordingly, the non-detection with VISIR may be explainable by the bad weather conditions during the observations of IC 1459.

C.5. M 49 – NGC 4472

M 49 was included in Horst et al. (2008) erroneously because the nuclear X-ray luminosity was ambiguous owing to many off-nuclear X-ray sources. Only an upper limit for the AGN ($L_{2-10\text{keV}} < 10^{39.32}$ erg/s) derived from *Chandra* observations is given in Panessa et al. (2006). On the other hand, in a very detailed analysis Maccarone et al. (2003) found a nuclear X-ray source with $L_{2-10\text{keV}} \sim 10^{39}$ erg/s in the same data. This agrees very well with the [OIII] emission line brightness stated in Diamond-Stanic et al. (2009) while the [OIV] data indicate a much higher luminosity ($L_{2-10\text{keV}} \sim 10^{41.4}$ erg/s). This seems to be the only indication of Compton-thickness, which is also not supported by the non-detection with VISIR. NGC 4472 might be a so-called “true” Seyfert 2 candidate – meaning that the broad emission lines are intrinsically absent rather than obscured by a torus (Nicastro et al. 2003). This was discussed in Akylas and Georgantopoulos (2009), but the *XMM-Newton* data presented there are heavily contaminated by off-nuclear emission and therefore are unreliable. Unfortunately, I can reach no conclusion about the existence of a torus in M 49.

C.6. M 51a – NGC 5194

The nuclear region of M 51a is very complex in soft X-rays ($< 2\,\mathrm{keV}$) with diffuse emission and several point sources, while it is rather compact in the hard band ($> 2\,\mathrm{keV}$; Cappi et al. 2006. Interestingly, this AGN has been assumed to be Compton-thick in Panessa et al. (2006) based on *Chandra* data and the existence of an extremely strong Fe Kα line ($L_{2-10\mathrm{kev}} = 10^{40.86}$ erg/s). On the other hand, Brightman and Nandra (2011) have found an unabsorbed fit for *XMM-Newton* yielding $L_{2-10\mathrm{kev}} = 10^{40.28}$ erg/s. To account for both possibilities the mean of both luminosities is used.

C.7. M 81 – NGC 3031

M 81 is one of the intrinsically weakest AGN but at the same time nearest AGN ($\sim 3.7\,\mathrm{Mpc}$). It exhibits both LINER and Sy 1.0 characteristics and extraordinary low obscuration ($N_\mathrm{H} \sim 5 \cdot 10^{2}0\,\mathrm{cm}^{-2}$; Page et al. 2003). Motivated by its similarity to Sgr A*, an extensive multiwavelength campaign has been performed on M 81 by Markoff et al. (2008) in order to compare and characterize SED and the short-term (daily) variability that occurs in this object (in addition to the yearly variations). They find striking similarities to the hard state of X-ray binaries. In addition, *XMM-Newton* observations of M 81 have been presented in Cappi et al. (2006) and Panessa et al. (2006), who state a $L_{2-10\mathrm{kev}} = 10^{39.59}$ erg/s. On the other hand, Ho et al. (2001) have given $L_{2-10\mathrm{kev}} = 10^{40.20}$ erg/s based on *Chandra* data. Here, I use the mean of all X-ray measurements and adopt an uncertainty of 0.3 dex to account for the significant variability in M 81.

C.8. M 87 – NGC 4486

I have used the mean of the X-ray luminosities of González-Martín et al. (2009b) and Satyapal et al. (2004) for M 87. Both were using the same *Chandra* data and state very comparable results. The flux visible in the *Spitzer* IRS spectrum matches the VISIR data well. Interestingly, Perlman et al. (2007) explained all observed MIR emission with synchrotron emission by the jet and conclude that there is probably no torus present in M 87. Very recent *Herschel*/PACS and SPIRE observations (Baes et al. 2010) showed the absence of significant thermal components in the MIR to far-infrared SED on large-scale ($> 10''$): a single power law can roughly fit the overall SED from MIR all way to the radio with a slope of ~ -0.7. But because of the comparably low spatial resolution no conclusion about the presence of a torus can be drawn from these data.

C.9. M 104 – NGC 4594

The X-ray properties of M 104 are taken from González-Martín et al. (2009b) and Ho et al. (2001) based on *Chandra* with marginally different results. This object was detected in the N-band by Grossan (2004) with the Keck LWS. The reported nuclear flux at 10.2 μm (11.1 mJy) is consistent with the upper limit I have derived and would place this object close to the correlation. The *Spitzer*/IRS spectrum is very noisy and the much higher flux implies heavy non-nuclear contamination at this lower spatial resolution. Similar to M 49, M 104 is a so-called "true" Sy 2 candidate as well and was investigated in detail in Shi et al. (2010). They found strong silicate emission, indicating that this object possesses a face-on dusty torus. The combined multiwavelength properties, including X-ray and optical/UV imply that M 104 indeed lacks broad emission lines, which contradicts the simple unification models.

C.10. M 106 – NGC 4258

For M 106, I use the X-ray properties presented in Panessa et al. (2006) based on *Chandra* data. Zhang et al. (2009) yields a 0.6 dex lower luminosity from analyzing the same data. However, the combined analysis of *XMM-Newton*, *Suzaku* and *Swift* observations yields results that are rather consistent with the higher luminosity but also show significant variability (~ 0.3 dex) on $\lesssim$ day timescales (Reynolds et al. 2009). The same authors emphasize a remarkable clean X-ray view of the central view and speculate the no dusty torus is present in this object. Instead, the observed $N_{\mathrm{H}} \approx 9 \cdot 10^{22}\mathrm{cm}^{-2}$ would arise from the warped accretion disk itself. On the other hand, M 106 shows a strong silicate feature in the MIR (Fig. 4.4) and lies also above the MIR–X-ray correlation close to the LINERs. It is in general very similar to M 81 as noted by, e.g., Reynolds et al. (2009), albeit accreting at higher rates. Also, the accretion structure in this object is heavily debated: Lasota et al. (1996) have proposed an ADAF model, while Yuan et al. (2002) argues that a jet is dominating the nuclear emission, and finally Panessa et al. (2006) and Fiore et al. (2001) favor a standard disk. The accretion rate and MIR–X-ray ratio of M 106 place it close to the putative transition in Fig. 7.6, and hence it might indeed be a LARAGN.

C.11. NGC 676

The only redshift-independent distance measurement for NGC 676 available in the literature is by Tully (1988) employing the Tully-Fisher relation, and this is used in this work. This object is included in the Palomar optical spectroscopic survey (Ho et al. 1995). But it was not detected in radio by Ho and Ulvestad (2001). The used X-ray data based on *XMM-Newton* is published in Panessa et al. (2006). They interpret this object as Compton-thick in accordance with Akylas and Georgantopoulos (2009) based on the same data. This is also supported by the relatively strong [OIII] emission (Panessa et al. 2006). Unfortunately, there are no *Spitzer* data available, and therefore no [OIV] measurement.

C.12. NGC 1052

The X-ray properties of NGC 1052 are described in González-Martín et al. (2009b) based on *Chandra* data. The derived X-ray luminosity is very similar to the one given in Satyapal et al. (2004) for the same observation after correction for the different distances. The mean of both was used in this work. Counting as a prototypical LINER, NGC 1052 is surprisingly bright and obscured in X-rays. While the [OIII] luminosity agrees with the X-ray luminosity (González-Martín et al. 2009a), no [OIV] emission line has been detected (Satyapal et al. 2004). Very recently Brightman and Nandra (2011) published high S/N *XMM-Newton* data of this object, stating a higher intrinsic $L_{2-10\mathrm{keV}} = 10^{41.5}$ erg/s, which would bring this object closer to the correlation.

C.13. NGC 1097

The X-ray luminosity of NGC 1097 is taken from Nemmen et al. (2006) using *Chandra* observations. It is interesting to note that the measured [OIV] brightness would imply a much higher X-ray luminosity ($L_{2-10\mathrm{keV}} \sim 10^{42.2}$ erg/s) according to the correlation found between both (Diamond-Stanic et al. 2009), while the [OIII] luminosity implies a lower value ($L_{2-10\mathrm{keV}} \sim 10^{40.0}$ erg/s) using the [OIII]:X-ray correlation (Panessa et al. 2006). At a larger scale ($\sim 10''$) the well-known starburst ring is evident in both filters but is only partly visible in the small VISIR field of view. The infrared properties of the nucleus have already been investigated in detail by Mason et al. (2007). They find the absence of PAH 3.3 μm emission at subarcsec scale, which seems to be typical for strong radiation fields. On the other hand, attempts to fit the infrared data with torus models failed, which led them to the conclusion that the torus is absent or weak. Instead, a nuclear star-forming region, co-existing with the LLAGN, is assumed to dominate the observed MIR emission. The likely PAH 11.3 μm emission in the VISIR data indicates that the nucleus is indeed dominated by emission coming from such a star-forming region. This also matches the finding of Storchi-Bergmann et al. (2005) of UV evidence for a nuclear star cluster inside the innermost 9 parsec of NGC 1097. But on the other hand, the MIR excess relative to the luminosity correlation is consistent with the co-existence of star-forming region and a torus inside the nucleus of NGC 1097. To distinguish these components better, additional MIR observations are needed.

C.14. NGC 1386

NGC 1386 is one of the objects, for which the different methods used to determine the distance show the largest discrepancies ($\sim$ 50 % variation). Because this object is very likely Compton-thick it is difficult to derive a reliable X-ray luminosity. I have followed the approach of Levenson et al. (2006) and estimated the luminosity by using the [OIII] line strength. The derived value is consistent with the Fe Kα emission line properties observed by Chandra that are analyzed in the same work. It also agrees with the [OIV] brightness stated in Diamond-Stanic et al. (2009) and LaMassa et al. (2010). Therefore, all available evidence favors a Compton-thick nature for this object. Note that the nucleus NGC 1386 shows biconical extended emission along the North-South axis in the MIR (Fig. A.1), as noted also by Reunanen et al. (2010). This extended emission is aligned with the NLR and thus presumably originates from hot optically thin dust in the NLR. To take this into account for the $F_\nu(12\,\mu\mathrm{m})$ measurement, a Gaussian with the FWHM fixed to the value from the STD has been scaled such that the distribution of the residual emission has become smooth. The resulting flux agrees well with Reunanen et al. (2010).

C.15. NGC 1404

The elliptical galaxy NGC 1404 is falling into the center of the Fornax cluster, which leads to large differences in the different distance measurement methods. It is classified as NELG in the optical. No evidence for AGN activity was found in the literature. Nevertheless, it is relatively bright in X-rays with a luminosity of $L_{2-10\mathrm{keV}} \sim 10^{41}$ erg/s reported by Kim et al. (2006) based on *Chandra* observations. Because this value was calculated for the whole galaxy including soft X-ray emission, it has to be regarded as an upper limit for any Compton-thin AGN in this object. Very recently, Grier et al. (2011) re-examined the *Chandra* data and found a clear detection of a nuclear point source with $L_{2-10\mathrm{keV}} \sim 10^{40}$ erg/s, which makes a LLAGN in this object likely.

C.16. NGC 1566

Similar to NGC 1386, NGC 1566 shows huge discrepancies in the different distance measurement methods. The only published X-ray data of this objects are from *ROSAT* (Liu and Bregman 2005), where the emphasis was on off-nuclear ultra-luminous X-ray sources. The nuclear point source was fitted only by a simple power-law. In the lack of any other available data, I have still used these values. This X-ray luminosity agrees well with the predicted values from the [OIII] and [OIV] emission line measurements stated in Diamond-Stanic et al. (2009).

C.17. NGC 1667

Bianchi et al. (2005) found an X-ray flux variation of a factor of 100 for NGC 1667 and interpreted the data in a way that the object is Compton-thick. Unfortunately, they give no intrinsic X-ray luminosity or flux derived from the used *XMM-Newton* data. Therefore I use the value of Panessa et al. (2006) based on *ASCA* observations. These authors also interpreted the data in favor of Compton-thickness. This is supported by the appearance of a strong Fe Kα line (Bassani et al. 1999). On the other hand, the same *ASCA* data were originally used by Pappa et al. (2001) for a Compton-thin fit, giving an X-ray luminosity that is two orders of magnitude lower for a similar observed flux. The stated [OIII] measurements in Panessa et al. (2006) support a Compton-thick nature. The [OIV] emission (Diamond-Stanic et al. 2009; LaMassa et al. 2010) also predicted an intrinsic X-ray luminosity similar to the one for the Compton-thick case. The VISIR observations support this scenario because NGC 1667 is much closer to the MIR-X-ray correlation than in the unabsorbed scenario.

C.18. NGC 3147

NGC 3147 is the best "true" Seyfert 2 candidate found so far (Bianchi et al. 2008). This is supported by the weak Fe K alpha line and an X-ray spectrum well-fitted by a model without absorption components. Bianchi et al. (2008) state $L_{2-10\mathrm{kev}} = 10^{41.23}$ erg/s based on *XMM-Newton* data while *Chandra* observations have been presented in Panessa et al. (2006) ($L_{2-10\mathrm{kev}} = 10^{41.62}$ erg/s). On the other hand, Brightman and Nandra (2008) have argued that a fit including absorption components gives as well a good fit to the *XMM-Newton* data, and state $L_{2-10\mathrm{kev}} = 10^{41.45}$ erg/s. I use the mean of all three luminosities.

C.19. NGC 3312

NGC 3312 was classified as a LINER by Carrillo et al. (1999). The X-ray data were taken from Hudaverdi et al. (2006), who describe *XMM-Newton* observations of this object. No other X-ray data or *Spitzer* or [OIII] observations are available.

C.20. NGC 3486

NGC 3486 is as well a "true" Seyfert 2 candidate. This object has not been detected with *Chandra* (Ho et al. 2001). *XMM-Newton* data is presented in, e.g., Panessa et al. (2006) fitting the data without absorption ($L_{2-10\mathrm{kev}} = 10^{39.39}$ erg/s). Similar results have been shown by Brightman and Nandra (2011) using also *XMM-Newton* and I use the mean of both. However, as for NGC 3147, Brightman and Nandra (2008) mention that a highly obscured model ($L_{2-10\mathrm{kev}} = 10^{41.50}$ erg/s) might give a better fit to the observed spectrum. This would be in contradiction with the MIR–X-ray relation. To account for the large uncertainty in the intrinsic X-ray luminosity of NGC 3486 we adopt an error of 0.6 dex. Note that the nucleus of NGC 3486 has been only weakly detected in *XMM-Newton* and is surrounded by diffuse X-ray emission (Cappi et al. 2006).

C.21. NGC 3982

For NGC 3982, I use the X-ray properties presented in Panessa et al. (2006) based on *ASCA* observations. They have fitted the X-ray data with a Compton-thick absorption model and find a much higher luminosity than Brightman and Nandra (2011) using *XMM-Newton* and LaMassa et al. (2011) using *Chandra*. Note that circum-nuclear diffuse X-ray emission that is visible in the *Chandra* image and included in the *XMM-Newton* and *ASCA* beams. However, the observed 2-10 keV flux given by Panessa et al. (2006) is lower than the one from LaMassa et al. (2011).

C.22. NGC 4051

NGC 4051 is included both in the LLAGN and the BAT AGN sample. It is highly variable in X-rays (e.g. Steenbrugge et al. 2009; Lobban et al. 2011). Therefore I adopt an uncertainty of 0.6 dex and use the X-ray luminosity given by Vaughan et al. (2011), which is the mean value for 2009 as observed with *XMM-Newton*.

C.23. NGC 4138

NGC 4138 is also included both in the LLAGN and the BAT AGN sample. The X-ray luminosity of NGC 4138 is similar in *Chandra* (Zhang et al. 2009) and *XMM-Newton* (Panessa et al. 2006). Cappi et al. (2006) reports marginal evidence for diffuse X-ray component which seems to not affect the measurements above. In addition, a weak point-like radio emission core verifies the AGN nature of this object (Ho and Ulvestad 2001). Furthermore, NGC 4138 is a buried AGN candidate (Noguchi et al. 2009).

C.24. NGC 4235

For NGC 4235, I have used the *XMM-Newton* data that was analyzed by Papadakis et al. (2008) and Bianchi et al. (2009) and yielded similar results. Panessa et al. (2006) derived a luminosity 0.6 dex higher but based on *ASCA* observations, which I treat with a lower priority because of their poorer spatial resolution. It is noteworthy that the properties of this type 1 LLAGN agree well with those of brighter objects, and it is therefore likely that NGC 4235 accretes in radiatively efficient mode as well (Papadakis et al. 2008).

C.25. NGC 4261 – 3C 270

González-Martín et al. (2009b) and Satyapal et al. (2005) arrived at very similar X-ray luminosities based on the same *Chandra* observation of NGC 4261. It is interesting to note that van der Wolk et al. (2010) reports a non-detection with VISIR in the SiC filter for this source. I have re-analyzed these observations and found a weak but clear detection. The measured flux matches the new observations presented here, and is six times higher than their reported upper limit (2 mJy). Additional evidence for MIR emission of hot dust in the nucleus of this galaxy has been found by Leipski et al. (2009). Therefore a dusty torus is likely present in NGC 4261, which agrees with the fact that the object aligns well with the MIR-X-ray correlation.

C.26. NGC 4395

NGC 4395 is also included both in the LLAGN and the BAT AGN sample. Dewangan et al. (2008) have presented an *XMM-Newton* data analysis of NGC 4395 yielding an X-ray luminosity of $L_{2-10\mathrm{kev}} = 10^{39.86}$ erg/s which is a factor 2 lower than the value given by Panessa et al. (2006) for the same data. On the other hand, Zhang et al. (2009) also state $L_{2-10\mathrm{kev}} = 10^{39.92}$ erg/s based on *Chandra* observations, while Ho et al. (2001) have given only $L_{2-10\mathrm{kev}} = 10^{38.97}$ erg/s. I use the mean of all these works.

C.27. NGC 4501

NGC 4501 is also a "true" Seyfert 2 candidate and it possesses an unresolved radio core (Ho and Ulvestad 2001). It has been observed by *XMM-Newton* yielding $L_{2-10\mathrm{kev}} = 10^{39.70}$ erg/s (Panessa et al. 2006) and *Chandra* yielding $L_{2-10\mathrm{kev}} = 10^{39.87}$ erg/s (Brightman and Nandra 2008). The *Chandra* data can be better fitted with an absorption column of $N_\mathrm{H} = 10^{23.3}\mathrm{cm}^{-2}$ contradicting the unobscured scenario, which has been favored by the weak detection in the *XMM-Newton* data (Cappi et al. 2006). Still, I use the mean of the values from both satellites.

C.28. NGC 4698

Cappi et al. (2006) and González-Martín et al. (2009b) give X-ray spectral fits for NGC 4698 with low absorption derived from *XMM-Newton* and *Chandra* data, which differ by 0.4 dex ($L_{2-10\mathrm{keV}} = 10^{39.39}$ erg/s and $10^{38.97}$ erg/s, respectively). But González-Martín et al. (2009a) interpreted NGC 4698 as Compton-thick using the same *Chandra* data. This conclusion was based on the [OIII] to X-ray flux ratio. Similarly high [OIII] fluxes were stated in Panessa et al. (2006) and Diamond-Stanic et al. (2009). In addition, a high X-ray obscuration is consistent with the [OIV] emission line brightness of the latter work. Therefore, the object is very likely Compton-thick, but with a large luminosity uncertainty. However, the MIR upper limit of NGC 4698 is consistent with both the Compton-thin or -thick scenario.

C.29. NGC 4941

Unfortunately, no *Chandra* or *XMM-Newton* data of NGC 4941 is available so far. Instead, I use the X-ray properties as determined from *BeppoSAX* data by Maiolino et al. (1998), $L_{2-10\mathrm{keV}} = 10^{41.43}$ erg/, similar to Horst et al. (2008). At the same time, Terashima et al. (2002) reports a slightly higher X-ray luminosity ($10^{41.67}$ erg/s) because they find CT obscuration based on *ASCA* observations. Therefore, an uncertainty of 0.3 dex is adopted.

C.30. NGC 5033

The *Chandra* data of NGC 5033 has been analyzed in Ho et al. (2001) ($L_{2-10\mathrm{kev}} = 10^{40.71}$ erg/s) while *XMM-Newton* data is presented in Panessa et al. (2006) ($L_{2-10\mathrm{kev}} = 10^{41.08}$ erg/s) and Papadakis et al. (2008) ($L_{2-10\mathrm{kev}} = 10^{41.26}$ erg/s). Once more, here the mean is used.

C.31. NGC 5273

NGC 5273 has a bright compact core in X-rays (Cappi et al. 2006) and radio (Ho and Ulvestad 2001). Panessa et al. (2006) and Papadakis et al. (2008) have analyzed the *XMM-Newton* data of NGC 5273 yielding very similar results ($L_{2-10\mathrm{kev}} = 10^{41.3}$ erg/s). However, also *Chandra* data has become available in the meantime and is presented in Liu (2011) but with a much lower luminosity ($L_{2-10\mathrm{kev}} = 10^{40.1}$ erg/s). Therefore, the *XMM-Newton* might be contaminated by non-AGN X-ray emission. Further investigation will be necessary to better constrain the intrinsic X-ray luminosity of NGC 5273. In the meantime I use the average of all measurements.

C.32. NGC 5363

Initial X-ray studies by González-Martín et al. (2009b) and Sansom et al. (2006) applied unobscured spectral fits to the available *XMM-Newton* observations and calculated a low X-ray luminosity ($L_{2-10\mathrm{keV}} = 10^{39.68}$ erg/s and $10^{40.30}$ erg/s) for NGC 5363. However, in the most recent analysis González-Martín et al. (2009a) give a much higher luminosity from the same data but with a Compton-thick model. This is supported by the [OIII] brightness and a relatively flat spectrum above 2 keV. Unfortunately, there is no *Spitzer*/IRS spectrum and no available [OIV] measurement. Consequently I adopt the Compton-thick fit.

C.33. NGC 5813

I have used the X-ray luminosity of González-Martín et al. (2009b) based on *Chandra* for NGC 5813. The X-ray image shows extremely diffuse soft emission. But no hard emission core is visible, which makes an AGN in this object highly unlikely. On the other hand, it could be a Compton-thick object as argued in González-Martín et al. (2009a). But the [OIII] luminosity given in the same work predicts a only slightly higher X-ray luminosity than in the Compton-thin fit. The AGN nature is supported by the detection of a compact radio core by Nagar et al. (2005). But even if the Compton-thick luminosity ($L_{2-10\mathrm{keV}} = 10^{40.55}$ erg/s) is adopted, the non-detection with VISIR is not surprising and the derived upper limit does not constrain the correlation.

C.34. NGC 7213

The X-ray measurements by *XMM-Newton* (e.g. Starling et al. 2005), *Chandra* (Shu et al. 2010c) and *Suzaku* (Lobban et al. 2010) available in the literature give very similar X-ray luminosities for NGC 7213. I have used the mean value. Because these come from different satellites and epochs, it seems unlikely that this object varies strongly in the X-rays. Therefore I adopted a smaller uncertainty for this object (0.1 dex).

C.35. NGC 7590

XMM-Newton data revealed that the X-ray emission of NGC 7590 is dominated by an off-nuclear source and extended soft emission from the host galaxy (Shu et al. 2010a). Both dominate the older *ASCA* observation by Bassani et al. (1999), which has a poorer spatial resolution. Unfortunately, there are no *Chandra* observations available yet for this object. I have used the estimated nuclear hard X-ray luminosity of Shu et al. (2010a). But note that based on the [OIII] to 2-10 keV flux ratio, the object is likely Compton-thick, which would imply a much higher intrinsic value. This contradicts the hypothesis that this object is a “true” Sy 2 candidate (compare also Shi et al. 2010). The upper MIR flux limit derived from the VISIR observation does not help to constrain its nature because even an intrinsic 2-10 keV luminosity higher by 2 orders of magnitude would be consistent with the correlation found. Similarly, the IRS spectrum is too noisy for a more detailed analysis and it remains unclear if the nucleus was detected at all.

C.36. NGC 7626

The *Chandra* observation of NGC 7626 has only been published by Humphrey and Buote (2006) for the whole galaxy in the 0.1-10 keV band. The [OIII] flux measured by Ho et al. (1997) predicts a much lower value ($L_{2-10\mathrm{keV}} = 10^{39.56}$ erg/s) and will be used in this study. Dudik et al. (2009) analyzed the forbidden emission lines visible in *Spitzer* data and concluded that this object might not be an AGN based on the non-detection of [NeV] and broad Hα emission. But the upper limit for the predicted X-ray luminosity ($L_{2-10\mathrm{keV}} < 10^{41.03}$ erg/s) from the upper-limit of the [OIV] non-detection is consistent with the [OIII] prediction. In addition, a point source was detected in radio (Nagar et al. 2005). Accordingly, the nuclear nature of NGC 7626 remains uncertain. The non-detection with VISIR favors a low X-ray luminosity but the upper-limit would be consistent with the MIR-X-ray correlation in any case.

C.37. NGC 7743

The properties of NGC 7743 are very similar to NGC 5363: it could either be highly absorbed or not absorbed at all: based on *XMM-Newton* González-Martín et al. (2009b) give an unobscured fit ($L_{2-10\mathrm{keV}} = 10^{39.5}$ erg/s), while Panessa et al. (2006), González-Martín et al. (2009a), and Akylas and Georgantopoulos (2009) interpreted the X-ray data as Compton-thick. The [OIII] data (e.g. González-Martín et al. 2009a; Panessa et al. 2006) favor Compton-thickness in agreement with [OIV] measurements stated in Diamond-Stanic et al. (2009). Although there is no broad Hα line detected (Terashima et al. 2000), a compact radio core is present (Ho and Ulvestad 2001). In summary, the true nature of this source remains unclear but it is likely Compton-thick. Therefore I use the X-ray luminosity given by González-Martín et al. (2009b). Note however that a Compton-thin nature would agree better with the MIR-X-ray correlation.

Appendix D.

List of acronyms

2MASS Two Micron All-Sky Survey

ADAF Advection Dominated Accretion Flow

AGN Active Galactic Nuclei

BAT Burst Alert Telescope (instrument on board of *Swift*)

BCD Basic Calibrated Data

BLR Broad-Line Region

CT Compton-Thick

FITS Flexible Image Transport System (common digital file format in astronomy)

FOV Field Of View

FWHM Full Width Half Maximum

HR High-angular Resolution

HST Hubble Space Telescope

IDL Interactive Data Language (name of a specific programing language)

INTEGRAL INTErnational Gamma-Ray Astrophysics Laboratory

IR InfraRed

IRAC InfraRed Array Camera (instrument on board of *Spitzer*)

IRAS InfraRed Astronomical Satellite

IRS InfraRed Spectrograph (instrument on board of *Spitzer*)

ISM InterStellar Medium

ISO Infrared Space Observatory

ISOCAM Infrared Space Observatory CAMera

KS Kolmogorov-Smirnov (test)

LARAGN Low-Accretion Rate Active Galactic Nuclei

LINER Low Ionization Nuclear Emission line Region

LLAGN Low-Luminosity Active Galactic Nuclei

MIR Mid-InfraRed

NED Nasa/ipac Extragalactic Database

BLR Narrow-Line Region

PAH Polycyclic Aromatic Hydrocarbon

PSF Point Spread Function

QSO Quasi-Stellar Object (a class of AGN)

RIAF Radiation Inefficient Accretion Flow

SED Spectral Energy Distribution

SF Star Formation

SMBH SuperMassive Black Hole

S/N Signal-to-Noise ratio

STD STandarD star (used for flux calibration)

UV Ultra Violet

UVOT UltraViolet/Optical Telescope (instrument on board of *Swift*)

VISIR Vlt Imager and Sprectrometer for the mid-InfraRed (instrument on the VLT)

VLT Very Large Telescope (observatory in Cerro Paranal, Chile)

WISE Wide-Field Infrared Survey Explorer

XRT X-Ray Telescope (instrument on board of *Swift*)

Appendix E.

List of symbols

Symbol	**Description**
a	Intercept coefficient of a linear regression fit
b	Slope coefficient of a linear regression fit
c	Speed of light: $c = 2.99793 \cdot 10^{10}\mathrm{cm/s}$
$c_{<}^{\mathrm{SF}}$	Maximum SF contribution at $12\,\mu$m in %
D_{best}	Distance with the most precise (redshift-independent) measurement in [Mpc]
D_{KS}	Maximum distance of the cumulative distribution functions in the KS test
D_{TF}	Distance with the Tully-Fisher method in [Mpc]
D_L	Luminosity distance from redshift in [Mpc]
E	Energy
$F_\nu(12\,\mu\mathrm{m})$	$12\,\mu$m flux density in [mJy]
$F_{14-195\mathrm{keV}}$	Observed 14-195 keV X-ray flux in [erg cm^{-2}s^{-1}]
$F_{2-10\mathrm{keV}}$	Absorption-corrected 2-10 keV X-ray flux in [erg/s/cm^2]
$F_\nu^{\mathrm{HR}}(11\,\mu\mathrm{m})$	$11\,\mu$m High-angular resolution flux density in [mJy]
$F_\nu^{\mathrm{IRS}}(11\,\mu\mathrm{m})$	$11\,\mu$m IRS synthetic flux density in [mJy]

Continues on next page

Symbol	**Description**
$F_\nu^{\mathrm{HR}}(12\,\mu\mathrm{m})$	$12\,\mu$m High-angular resolution flux density in [mJy]
$F_\nu^{\mathrm{IRS}}(12\,\mu\mathrm{m})$	$12\,\mu$m IRS synthetic flux density in [mJy]
$F(\mathrm{PAH}11.3\mu\mathrm{m})$	Flux of the PAH $11.3\,\mu$m emission line feature in [erg/s/cm^{-2}]
$F_\nu^{\mathrm{SF}}(12\mu\mathrm{m})$	Flux density of the scaled SF component at $12\,\mu$m in [mJy]
G	Gravitational constant: $G = 6.668 \cdot 10^{-8}\mathrm{cm}^3/\mathrm{g}/\mathrm{s}^2$
i	Inclination angle of a galaxy with respect to the observer in [°]
L_{bol}	Bolometric luminosity in [erg/s]
L_{Edd}	Eddington luminosity in [erg/s]
$L_{14-195\mathrm{keV}}$	Observed 14-195 keV X-ray luminosity in [erg/s]
$L_{2-10\mathrm{keV}}$	Absorption-corrected 2-10 keV X-ray luminosity in [erg/s]
$\dot{M}$	Mass accretion rate in [$M_\odot$/yr]
$M_\odot$	Mass of the sun: $1.9891 \cdot 10^{33}$g
M_{BH}	Black hole mass in [$M_\odot$]
m_{e}	Mass of an electron: $m_{\mathrm{e}} = 9.1093897 \times 10^{-28}$g
m_{p}	Mass of a proton: $m_{\mathrm{p}} = 1.6726231 \times 10^{-24}$g
N_{H}	Column density in [cm^{-2}]
p	Null-hypothesis probability
p_{KS}	Null-hypothesis probability in the KS test
r	Radius

Continues on next page

Symbol	Description
r_S	Schwarzschild radius: $r_\mathrm{S} = 2GM_\mathrm{BH}/c^2 \approx 3 \times 10^5 M_\mathrm{BH}/M_\odot\,\mathrm{cm}$
$R(\mathrm{PAH})$	$F_\nu^\mathrm{HR}(11\,\mu\mathrm{m})/F_\nu^\mathrm{IRS}(11\,\mu\mathrm{m})$
$R(\mathrm{cont})$	$F_\nu^\mathrm{HR}(12\,\mu\mathrm{m})/F_\nu^\mathrm{IRS}(12\,\mu\mathrm{m})$
r_0	Resolved scale at an object's distance in [pc]
r_sub	Dust sublimation radius in [pc]
R^M_X	Logarithmic luminosity ratio: $R^\mathrm{M}_\mathrm{X} = \log \lambda L_\lambda(12\,\mu\mathrm{m}) - \log L_{2-10\mathrm{keV}}$
R^M_HX	Logarithmic luminosity ratio: $R^\mathrm{M}_\mathrm{HX} = \log \lambda L_\lambda(12\,\mu\mathrm{m}) - \log L_{14-195\mathrm{keV}}$
R^X_HX	Logarithmic luminosity ratio: $R^\mathrm{X}_\mathrm{HX} = \log L_{2-10\mathrm{keV}} - \log L_{14-195\mathrm{keV}}$
s_wr	Intrinsic scale threshold for well-resolved AGN in r_sub
T	Temperature in [K]
T_sub	Dust sublimation temperature in [K]
v	Velocity
z	Redshift of an astrophysical object
α	Spectral index
γ	Lorentz factor: $\gamma = 1/\sqrt{1-(v/c)^2}$
η	Efficiency
η_Edd	Eddington ratio: $\eta_\mathrm{Edd} = L_\mathrm{bol}/L_\mathrm{Edd}$
θ_0	Angular resolution of a telescope at a given wavelength in $''$
λ_c	Central filter wavelength in [μm]

Continues on next page

Symbol	**Description**
$\lambda L_\lambda(12\,\mu\mathrm{m})$	Monochromatic 12 μm MIR luminosity in [erg/s]
$\lambda L_\lambda^{\mathrm{G}}(12\,\mu\mathrm{m})$	Total monochromatic 12 μm luminosity of the galaxy (host+AGN) [erg/s]
λ_{rest}	Restframe wavelength in [μm]
ν	Frequency in [Hz]
ρ	Spearman rank correlation coefficient
σ_{BG}	Standard deviation of the background
σ_{SB}	Stefan-Boltzmann constant: $\sigma_{\mathrm{SB}} = 5.67032 \cdot 10^{-5} \mathrm{erg/cm^2/K^4/s}$
σ_{int}	Intrinsic scatter (as determined by `linmix_err`)
σ_{T}	Thompson cross-section: $\sigma_{\mathrm{T}} = 6.65 \times 10^{-25} \mathrm{cm}^{-2}$
τ	Optical depth

Bibliography

Akylas, A., Georgantopoulos, I., 2009. *XMM-Newton observations of Seyfert galaxies from the Palomar spectroscopic survey: the X-ray absorption distribution*. A&A, 500, 999–1012. URL `http://adsabs.harvard.edu/abs/2009A%26A...500..999A`

Alonso-Herrero, A., Ramos Almeida, C., Mason, R., Asensio Ramos, A., et al., 2011. *Torus and Active Galactic Nucleus Properties of Nearby Seyfert Galaxies: Results from Fitting Infrared Spectral Energy Distributions and Spectroscopy*. ApJ, 736, 82. URL `http://adsabs.harvard.edu/abs/2011ApJ...736...82A`

Amanullah, R., Lidman, C., Rubin, D., Aldering, G., et al., 2010. *Spectra and Hubble Space Telescope Light Curves of Six Type Ia Supernovae at* $0.511 < z < 1.12$ *and the Union2 Compilation*. ApJ, 716, 712–738. URL `http://adsabs.harvard.edu/abs/2010ApJ...716..712A`

Andrade-Velázquez, M., Krongold, Y., Elvis, M., Nicastro, F., et al., 2010. *The Two-Phase, Two-Velocity Ionized Absorber in the Seyfert 1 Galaxy NGC 5548*. ApJ, 711, 888–906. URL `http://adsabs.harvard.edu/abs/2010ApJ...711..888A`

Antonucci, R., 1993. *Unified models for active galactic nuclei and quasars*. ARA&A, 31, 473–521. URL `http://adsabs.harvard.edu/abs/1993ARA%26A..31..473A`

Antonucci, R. R. J., Miller, J. S., 1985. *Spectropolarimetry and the nature of NGC 1068*. ApJ, 297, 621–632. URL `http://adsabs.harvard.edu/abs/1985ApJ...297..621A`

Asmus, D., Gandhi, P., Smette, A., Hönig, S. F., Duschl, W. J., 2011. *Mid-infrared properties of nearby low-luminosity AGN at high angular resolution*. A&A, 536, 36. URL `http://adsabs.harvard.edu/abs/2011A%26A...536A..36A`

Awaki, H., Murakami, H., Ogawa, Y., Leighly, K. M., 2006. *Variability Study of Seyfert 2 Galaxies with XMM-Newton*. ApJ, 645, 928–939. URL `http://cdsads.u-strasbg.fr/abs/2006ApJ...645..928A`

Baes, M., Clemens, M., Xilouris, E. M., Fritz, J., et al., 2010. *The Herschel Virgo Cluster Survey . VI. The far-infrared view of M 87*. A&A, 518, L53. URL `http://adsabs.harvard.edu/abs/2010A%26A...518L..53B`

Baganoff, F. K., Bautz, M. W., Brandt, W. N., Chartas, G., et al., 2001. *Rapid X-ray flaring from the direction of the supermassive black hole at the Galactic Centre*. Nature, 413, 45–48. URL `http://adsabs.harvard.edu/abs/2001Natur.413...45B`

Balbus, S. A., Hawley, J. F., 1991. *A powerful local shear instability in weakly magnetized disks. I - Linear analysis. II - Nonlinear evolution*. ApJ, 376, 214–233. URL `http://adsabs.harvard.edu/abs/1991ApJ...376..214B`

Baldwin, J. A., Phillips, M. M., Terlevich, R., 1981. *Classification parameters for the emission-line spectra of extragalactic objects*. PASP, 93, 5–19. URL `http://adsabs.harvard.edu/abs/1981PASP...93....5B`

Ballantyne, D. R., Fabian, A. C., 2005. *Evidence of an Untruncated Accretion Disk in the Broad-Line Radio Galaxy 4C 74.26*. The ApJL, 622, L97–L100. URL `http://cdsads.u-strasbg.fr/abs/2005ApJ...622L..97B`

Balmaverde, B., Capetti, A., 2006. *The host galaxy/AGN connection in nearby early-type galaxies. Is there a miniature radio-galaxy in every "core" galaxy?* A&A, 447, 97–112. URL `http://adsabs.harvard.edu/abs/2006A%26A...447...97B`

Barthel, P. D., 1989. *Is every quasar beamed?* ApJ, 336, 606–611. URL `http://adsabs.harvard.edu/abs/1989ApJ...336..606B`

Barthelmy, S. D., Barbier, L. M., Cummings, J. R., Fenimore, E. E., et al., 2005. *The Burst Alert Telescope (BAT) on the SWIFT Midex Mission*. Space Science Reviews, 120, 143–164. URL `http://adsabs.harvard.edu/abs/2005SSRv..120..143B`

Barvainis, R., 1987. *Hot dust and the near-infrared bump in the continuum spectra of quasars and active galactic nuclei*. ApJ, 320, 537–544. URL `http://adsabs.harvard.edu/abs/1987ApJ...320..537B`

Bassani, L., Dadina, M., Maiolino, R., Salvati, M., et al., 1999. *A Three-dimensional Diagnostic Diagram for Seyfert 2 Galaxies: Probing X-Ray Absorption and Compton Thickness*. ApJSS, 121, 473–482. URL `http://adsabs.harvard.edu/abs/1999ApJS..121..473B`

Beckert, T., Duschl, W. J., 2004. *The dynamical state of a thick cloudy torus around an AGN*. A&A, 426, 445–454. URL `http://adsabs.harvard.edu/abs/2004A%26A...426..445B`

Beckmann, V., Gehrels, N., Shrader, C. R., Soldi, S., 2006. *The First INTEGRAL AGN Catalog*. ApJ, 638, 642–652. URL `http://adsabs.harvard.edu/abs/2006ApJ...638..642B`

Begelman, M. C., Blandford, R. D., Rees, M. J., 1980. *Massive black hole binaries in active galactic nuclei*. Nature, 287, 307–309. URL `http://adsabs.harvard.edu/abs/1980Natur.287..307B`

Beifiori, A., Sarzi, M., Corsini, E. M., Dalla Bont, E., et al., 2009. *Upper Limits on the Masses of 105 Supermassive Black Holes from Hubble Space Telescope/Space Telescope Imaging Spectrograph Archival Data*. ApJ, 692, 856–868. URL `http://adsabs.harvard.edu/abs/2009ApJ...692..856B`

Belloni, T., *The Jet Paradigm*. vol. 794 (2010). URL `http://adsabs.harvard.edu/abs/2010LNP...794.....B`

Bettoni, D., Falomo, R., Fasano, G., Govoni, F., 2003. *The black hole mass of low redshift radiogalaxies*. A&A, 399, 869–878. URL `http://adsabs.harvard.edu/abs/2003A%26A...399..869B`

Bianchi, S., Balestra, I., Matt, G., Guainazzi, M., Perola, G. C., 2003. *The recent X-ray history of NGC 5506*. A&A, 402, 141–149. URL `http://adsabs.harvard.edu/abs/2003A%26A...402..141B`

Bianchi, S., Bonilla, N. F., Guainazzi, M., Matt, G., Ponti, G., 2009. *CAIXA: a catalogue of AGN in the XMM-Newton archive. II. Multiwavelength correlations*. A&A, 501, 915–924. URL `http://adsabs.harvard.edu/abs/2009A%26A...501..915B`

Bianchi, S., Corral, A., Panessa, F., Barcons, X., et al., 2008. *NGC 3147: a 'true' type 2 Seyfert galaxy without the broad-line region*. MNRAS, 385, 195–199. URL `http://adsabs.harvard.edu/abs/2008MNRAS.385..195B`

Bianchi, S., Guainazzi, M., Matt, G., Chiaberge, M., et al., 2005. *A search for changing-look AGN in the Grossan catalog*. A&A, 442, 185–194. URL `http://adsabs.harvard.edu/abs/2005A%26A...442..185B`

Bianchi, S., Matt, G., Balestra, I., Guainazzi, M., Perola, G. C., 2004. *X-ray reprocessing in Seyfert galaxies: Simultaneous XMM-Newton/BeppoSAX observations*. A&A, 422, 65–76. URL `http://cdsads.u-strasbg.fr/abs/2004A%26A...422...65B`

Blakeslee, J. P., Lucey, J. R., Barris, B. J., Hudson, M. J., Tonry, J. L., 2001. *A synthesis of data from fundamental plane and surface brightness fluctuation surveys*. MNRAS, 327, 1004–1020. URL `http://adsabs.harvard.edu/abs/2001MNRAS.327.1004B`

Brandl, B. R., Bernard-Salas, J., Spoon, H. W. W., Devost, D., et al., 2006. *The Mid-Infrared Properties of Starburst Galaxies from Spitzer-IRS Spectroscopy*. ApJ, 653, 1129–1144. URL `http://adsabs.harvard.edu/abs/2006ApJ...653.1129B`

Brightman, M., Nandra, K., 2008. *On the nature of unabsorbed Seyfert 2 galaxies*. MNRAS, 390, 1241–1249. URL `http://adsabs.harvard.edu/abs/2008MNRAS.390.1241B`

Brightman, M., Nandra, K., 2011. *An XMM-Newton spectral survey of 12 m selected galaxies - I. X-ray data*. MNRAS, 413, 1206–1235. URL `http://adsabs.harvard.edu/abs/2011MNRAS.413.1206B`

Broderick, J. W., Fender, R. P., 2011. *Is there really a dichotomy in active galactic nucleus jet power?* MNRAS, 417, 184–197. URL `http://adsabs.harvard.edu/abs/2011MNRAS.417..184B`

Burtscher, L., Jaffe, W., Raban, D., Meisenheimer, K., et al., 2009. *Dust Emission from a Parsec-Scale Structure in the Seyfert 1 Nucleus of NGC 4151*. The ApJL, 705, L53–L57. URL `http://adsabs.harvard.edu/abs/2009ApJ...705L..53B`

Calzetti, D., Kennicutt, R. C., Engelbracht, C. W., Leitherer, C., et al., 2007. *The Calibration of Mid-Infrared Star Formation Rate Indicators*. ApJ, 666, 870–895. URL `http://adsabs.harvard.edu/abs/2007ApJ...666..870C`

Cappellari, M., Neumayer, N., Reunanen, J., van der Werf, P. P., et al., 2009. *The mass of the black hole in Centaurus A from SINFONI AO-assisted integral-field observations of stellar kinematics*. MNRAS, 394, 660–674. URL `http://adsabs.harvard.edu/abs/2009MNRAS.394..660C`

Cappellari, M., Verolme, E. K., van der Marel, R. P., Kleijn, G. A. V., et al., 2002. *The Counterrotating Core and the Black Hole Mass of IC 1459*. ApJ, 578, 787–805. URL `http://adsabs.harvard.edu/abs/2002ApJ...578..787C`

Cappi, M., Panessa, F., Bassani, L., Dadina, M., et al., 2006. *X-ray spectral survey with XMM-Newton of a complete sample of nearby Seyfert galaxies*. A&A, 446, 459–470. URL `http://adsabs.harvard.edu/abs/2006A%26A...446..459C`

Carrillo, R., Masegosa, J., Dultzin-Hacyan, D., Ordoez, R., 1999. *A Multifrequency Catalog of LINERs*. Rev. Mex. Astron. Astrofis., 35, 187. URL `http://adsabs.harvard.edu/abs/1999RMxAA..35..187C`

Cid Fernandes, R., Gu, Q., Melnick, J., Terlevich, E., et al., 2004. *The star formation history of Seyfert 2 nuclei*. MNRAS, 355, 273–296. URL `http://adsabs.harvard.edu/abs/2004MNRAS.355..273C`

Cohen, M., Walker, R. G., Carter, B., Hammersley, P., et al., 1999. *Spectral Irradiance Calibration in the Infrared. X. A Self-Consistent Radiometric All-Sky Network of Absolutely Calibrated Stellar Spectra*. AJ, 117, 1864–1889. URL `http://adsabs.harvard.edu/abs/1999AJ....117.1864C`

Colina, L., Gonzalez Delgado, R., Mas-Hesse, J. M., Leitherer, C., 2002. *Detection of a Super-Star Cluster as the Ionizing Source in the Low-Luminosity Active Galactic Nucleus NGC 4303*. ApJ, 579, 545–553. URL `http://adsabs.harvard.edu/abs/2002ApJ...579..545C`

Cotton, W. D., Mason, B. S., Dicker, S. R., Korngut, P. M., et al., 2009. *90 GHz Observations of M87 and Hydra A*. ApJ, 701, 1872–1879. URL `http://adsabs.harvard.edu/abs/2009ApJ...701.1872C`

DADDI, E., ALEXANDER, D. M., DICKINSON, M., GILLI, R., ET AL., 2007. *Multiwavelength Study of Massive Galaxies at z˜2. II. Widespread Compton-thick Active Galactic Nuclei and the Concurrent Growth of Black Holes and Bulges*. ApJ, 670, 173–189. URL `http://adsabs.harvard.edu/abs/2007ApJ...670..173D`

DADINA, M., 2007. *BeppoSAX observations in the 2-100 keV band of the nearby Seyfert galaxies: an atlas of spectra*. A&A, 461, 1209–1252. URL `http://adsabs.harvard.edu/abs/2007A%26A...461.1209D`

DADINA, M., GUAINAZZI, M., CAPPI, M., BIANCHI, S., ET AL., 2010. *X-ray imaging of the ionisation cones in NGC 5252*. A&A, 516, 9. URL `http://adsabs.harvard.edu/abs/2010A%26A...516A...9D`

DENNEY, K. D., BENTZ, M. C., PETERSON, B. M., POGGE, R. W., ET AL., 2006. *The Mass of the Black Hole in the Seyfert 1 Galaxy NGC 4593 from Reverberation Mapping*. ApJ, 653, 152–158. URL `http://adsabs.harvard.edu/abs/2006ApJ...653..152D`

DENNEY, K. D., PETERSON, B. M., POGGE, R. W., ADAIR, A., ET AL., 2010. *Reverberation Mapping Measurements of Black Hole Masses in Six Local Seyfert Galaxies*. ApJ, 721, 715–737. URL `http://adsabs.harvard.edu/abs/2010ApJ...721..715D`

DEVEREUX, N., FORD, H., TSVETANOV, Z., JACOBY, G., 2003. *STIS Spectroscopy of the Central 10 Parsecs of M81: Evidence for a Massive Black Hole*. AJ, 125, 1226–1235. URL `http://adsabs.harvard.edu/abs/2003AJ....125.1226D`

DEWANGAN, G. C., MATHUR, S., GRIFFITHS, R. E., RAO, A. R., 2008. *X-Ray Emission from Active Galactic Nuclei with Intermediate-Mass Black Holes*. ApJ, 689, 762–774. URL `http://adsabs.harvard.edu/abs/2008ApJ...689..762D`

DIAMOND-STANIC, A., *The Relationship Between Black Hole Accretion Rate and Star Formation in Seyfert Galaxies*. p. 5 (2011). URL `http://adsabs.harvard.edu/abs/2011sacm.confE...5D`

DIAMOND-STANIC, A. M., RIEKE, G. H., 2010. *The Effect of Active Galactic Nuclei on the Mid-infrared Aromatic Features*. ApJ, 724, 140–153. URL `http://adsabs.harvard.edu/abs/2010ApJ...724..140D`

DIAMOND-STANIC, A. M., RIEKE, G. H., RIGBY, J. R., 2009. *Isotropic Luminosity Indicators in a Complete AGN Sample*. ApJ, 698, 623–631. URL `http://adsabs.harvard.edu/abs/2009ApJ...698..623D`

DONATO, D., SAMBRUNA, R. M., GLIOZZI, M., 2004. *Obscuration and Origin of Nuclear X-Ray Emission in FR I Radio Galaxies*. ApJ, 617, 915–929. URL `http://adsabs.harvard.edu/abs/2004ApJ...617..915D`

DRAINE, B. T., 2003. *Interstellar Dust Grains*. ARA&A, 41, 241–289. URL `http://adsabs.harvard.edu/abs/2003ARA%26A..41..241D`

DRAINE, B. T., LEE, H. M., 1984. *Optical properties of interstellar graphite and silicate grains*. ApJ, 285, 89–108. URL `http://adsabs.harvard.edu/abs/1984ApJ...285...89D`

DUDIK, R. P., SATYAPAL, S., GLIOZZI, M., SAMBRUNA, R. M., 2005. *A Chandra Snapshot Survey of Infrared-bright LINERs: A Possible Link Between Star Formation, Active Galactic Nucleus Fueling, and Mass Accretion*. ApJ, 620, 113–125. URL `http://adsabs.harvard.edu/abs/2005ApJ...620..113D`

DUDIK, R. P., SATYAPAL, S., MARCU, D., 2009. *A Spitzer Spectroscopic Survey of Low-Ionization Nuclear Emission-Line Regions: Characterization of the Central Source*. ApJ, 691, 1501–1524. URL `http://adsabs.harvard.edu/abs/2009ApJ...691.1501D`

DULLEMOND, C. P., VAN BEMMEL, I. M., 2005. *Clumpy tori around active galactic nuclei*. A&A, 436, 47–56. URL `http://adsabs.harvard.edu/abs/2005A%26A...436...47D`

Duschl, W. J., Strittmatter, P. A., 2011. *The cosmogony of supermassive black holes*. MNRAS, 413, 1495–1504. URL http://adsabs.harvard.edu/abs/2011MNRAS.413.1495D

Efstathiou, A., Rowan-Robinson, M., 1995. *Dusty discs in active galactic nuclei*. MNRAS, 273, 649–661. URL http://adsabs.harvard.edu/abs/1995MNRAS.273..649E

Eguchi, S., Ueda, Y., Awaki, H., Aird, J., et al., 2011. *Suzaku View of the Swift/BAT Active Galactic Nuclei. III. Application of Numerical Torus Models to Two Nearly Compton Thick Active Galactic Nuclei (NGC 612 and NGC 3081)*. ApJ, 729, 31. URL http://adsabs.harvard.edu/abs/2011ApJ...729...31E

Eguchi, S., Ueda, Y., Terashima, Y., Mushotzky, R., Tueller, J., 2009. *Suzaku View of the Swift/BAT Active Galactic Nuclei. I. Spectral Analysis of Six Active Galactic Nuclei and Evidence for Two Types of Obscured Population*. ApJ, 696, 1657–1667. URL http://adsabs.harvard.edu/abs/2009ApJ...696.1657E

Elitzur, M., Ho, L. C., 2009. *On the Disappearance of the Broad-Line Region in Low-Luminosity Active Galactic Nuclei*. ApJ, 701, L91–L94. URL http://adsabs.harvard.edu/abs/2009ApJ...701L..91E

Elitzur, M., Shlosman, I., 2006. *The AGN-obscuring Torus: The End of the “Doughnut” Paradigm?* ApJ, 648, L101–L104. URL http://adsabs.harvard.edu/abs/2006ApJ...648L.101E

Elvis, M., 2000. *A Structure for Quasars*. ApJ, 545, 63–76. URL http://adsabs.harvard.edu/abs/2000ApJ...545...63E

Elvis, M., Wilkes, B. J., McDowell, J. C., Green, R. F., et al., 1994. *Atlas of quasar energy distributions*. ApJSS, 95, 1–68. URL http://adsabs.harvard.edu/abs/1994ApJS...95....1E

Emmanoulopoulos, D., Papadakis, I. E., McHardy, I. M., Nicastro, F., et al., 2011. *An XMM-Newton view of the ‘bare’ nucleus of Fairall 9*. MNRAS, 415, 1895–1906. URL http://cdsads.u-strasbg.fr/abs/2011MNRAS.415.1895E

Eracleous, M., Hwang, J. A., Flohic, H. M. L. G., 2010. *Spectral Energy Distributions of Weak Active Galactic Nuclei Associated with Low-Ionization Nuclear Emission Regions*. ApJSS, 187, 135–148. URL http://adsabs.harvard.edu/abs/2010ApJS..187..135E

Evans, D. A., Kraft, R. P., Worrall, D. M., Hardcastle, M. J., et al., 2004. *Chandra and XMM-Newton Observations of the Nucleus of Centaurus A*. ApJ, 612, 786–796. URL http://adsabs.harvard.edu/abs/2004ApJ...612..786E

Evans, D. A., Lee, J. C., Turner, T. J., Weaver, K. A., Marshall, H. L., 2007. *Probing Unification with Chandra HETGS and XMM-Newton EPIC and RGS Spectroscopy of the Narrow Emission Line Galaxy NGC 2110*. ApJ, 671, 1345–1354. URL http://adsabs.harvard.edu/abs/2007ApJ...671.1345E

Evans, D. A., Worrall, D. M., Hardcastle, M. J., Kraft, R. P., Birkinshaw, M., 2006. *Chandra and XMM-Newton Observations of a Sample of Low-Redshift FR I and FR II Radio Galaxy Nuclei*. ApJ, 642, 96–112. URL http://adsabs.harvard.edu/abs/2006ApJ...642...96E

Fabian, A. C., Iwasawa, K., Reynolds, C. S., Young, A. J., 2000. *Broad Iron Lines in Active Galactic Nuclei*. PASP, 112, 1145–1161. URL http://adsabs.harvard.edu/abs/2000PASP..112.1145F

Fabian, A. C., Miniutti, G., Iwasawa, K., Ross, R. R., 2005. *X-ray reflection in the Seyfert galaxy 1H 0419-577 revealing strong relativistic effects in the vicinity of a Kerr black hole*. MNRAS, 361, 795–802. URL http://cdsads.u-strasbg.fr/abs/2005MNRAS.361..795F

Falcke, H., Markoff, S., 2000. *The jet model for Sgr A*: Radio and X-ray spectrum*. A&A, 362, 113–118. URL http://adsabs.harvard.edu/abs/2000A%26A...362..113F

Ferrarese, L., Ford, H. C., Jaffe, W., 1996. *Evidence for a Massive Black Hole in the Active Galaxy NGC 4261 from Hubble Space Telescope Images and Spectra*. ApJ, 470, 444. URL `http://adsabs.harvard.edu/abs/1996ApJ...470..444F`

Ferrarese, L., Merritt, D., 2000. *A Fundamental Relation between Supermassive Black Holes and Their Host Galaxies*. ApJ, 539, L9–L12. URL `http://adsabs.harvard.edu/abs/2000ApJ...539L...9F`

Ferrarese, L., Mould, J. R., Stetson, P. B., Tonry, J. L., et al., 2007. *The Discovery of Cepheids and a Distance to NGC 5128*. ApJ, 654, 186–218. URL `http://adsabs.harvard.edu/abs/2007ApJ...654..186F`

Fiore, F., Pellegrini, S., Matt, G., Antonelli, L. A., et al., 2001. *The BeppoSAX View of the X-Ray Active Nucleus of NGC 4258*. ApJ, 556, 150–157. URL `http://adsabs.harvard.edu/abs/2001ApJ...556..150F`

Frank, J., King, A., Raine, D. J., *Accretion Power in Astrophysics: Third Edition* (2002). URL `http://adsabs.harvard.edu/abs/2002apa..book.....F`

Galliano, E., Alloin, D., Pantin, E., Granato, G. L., et al., 2008. *Extremely massive young clusters in NGC 1365*. A&A, 492, 3–22. URL `http://adsabs.harvard.edu/abs/2008A%26A...492....3G`

Galliano, E., Alloin, D., Pantin, E., Lagage, P. O., Marco, O., 2005. *Mid-infrared imaging of active galaxies. Active nuclei and embedded star clusters*. A&A, 438, 803–820. URL `http://adsabs.harvard.edu/abs/2005A%26A...438..803G`

Gallimore, J. F., Yzaguirre, A., Jakoboski, J., Stevenosky, M. J., et al., 2010. *Infrared Spectral Energy Distributions of Seyfert Galaxies: Spitzer Space Telescope Observations of the 12 m Sample of Active Galaxies*. ApJSS, 187, 172–211. URL `http://adsabs.harvard.edu/abs/2010ApJS..187..172G`

Gallo, L. C., Lehmann, I., Pietsch, W., Boller, T., et al., 2006. *XMM-Newton observations of bright ROSAT selected active galactic nuclei with low intrinsic absorption*. MNRAS, 365, 688–698. URL `http://adsabs.harvard.edu/abs/2006MNRAS.365..688G`

Gandhi, P., 2005. *X-ray studies of active galactic nuclei*. Asian Journal of Physics, 13, 90–107. URL `http://adsabs.harvard.edu/abs/2005AsJPh..13...90G`

Gandhi, P., Fabian, A. C., 2003. *X-ray background synthesis: the infrared connection*. MNRAS, 339, 1095–1102. URL `http://adsabs.harvard.edu/abs/2003MNRAS.339.1095G`

Gandhi, P., Horst, H., Smette, A., Hönig, S., et al., 2009. *Resolving the mid-infrared cores of local Seyferts*. A&A, 502, 457–472. URL `http://adsabs.harvard.edu/abs/2009A%26A...502..457G`

Garcia-Rissmann, A., Vega, L. R., Asari, N. V., Cid Fernandes, R., et al., 2005. *An atlas of calcium triplet spectra of active galaxies*. MNRAS, 359, 765–780. URL `http://adsabs.harvard.edu/abs/2005MNRAS.359..765G`

Gebhardt, K., Adams, J., Richstone, D., Lauer, T. R., et al., 2011. *The Black Hole Mass in M87 from Gemini/NIFS Adaptive Optics Observations*. ApJ, 729, 119. URL `http://adsabs.harvard.edu/abs/2011ApJ...729..119G`

Gebhardt, K., Bender, R., Bower, G., Dressler, A., et al., 2000. *A Relationship between Nuclear Black Hole Mass and Galaxy Velocity Dispersion*. ApJ, 539, L13–L16. URL `http://adsabs.harvard.edu/abs/2000ApJ...539L..13G`

Gehrels, N., Chincarini, G., Giommi, P., Mason, K. O., et al., 2004. *The Swift Gamma-Ray Burst Mission*. ApJ, 611, 1005–1020. URL `http://adsabs.harvard.edu/abs/2004ApJ...611.1005G`

Genzel, R., Schödel, R., Ott, T., Eckart, A., et al., 2003. *Near-infrared flares from accreting gas around the supermassive black hole at the Galactic Centre*. Nature, 425, 934–937. URL http://adsabs.harvard.edu/abs/2003Natur.425..934G

Ghez, A. M., Duchłne, G., Matthews, K., Hornstein, S. D., et al., 2003. *The First Measurement of Spectral Lines in a Short-Period Star Bound to the Galaxy's Central Black Hole: A Paradox of Youth*. The ApJL, 586, L127–L131. URL http://adsabs.harvard.edu/abs/2003ApJ...586L.127G

Gillessen, S., Eisenhauer, F., Trippe, S., Alexander, T., et al., 2009. *Monitoring Stellar Orbits Around the Massive Black Hole in the Galactic Center*. ApJ, 692, 1075–1109. URL http://adsabs.harvard.edu/abs/2009ApJ...692.1075G

Gilli, R., Comastri, A., Hasinger, G., 2007. *The synthesis of the cosmic X-ray background in the Chandra and XMM-Newton era*. A&A, 463, 79–96. URL http://adsabs.harvard.edu/abs/2007A%26A...463...79G

Glasse, A. C., Atad-Ettedgui, E. I., Harris, J. W., *Michelle Midinfrared Spectrometer and Imager*. vol. 2871, pp. 1197–1203 (1997). URL http://adsabs.harvard.edu/abs/1997SPIE.2871.1197G

Gliozzi, M., Sambruna, R. M., Eracleous, M., Yaqoob, T., 2007. *The Nature of a Broad-Line Radio Galaxy: Simultaneous RXTE and Chandra HETG Observations of 3C 382*. ApJ, 664, 88–100. URL http://adsabs.harvard.edu/abs/2007ApJ...664...88G

Gofford, J., Reeves, J. N., Turner, T. J., Tombesi, F., et al., 2011. *A broad-band X-ray view of the warm absorber in radio-quiet quasar MR 2251-178*. MNRAS, 414, 3307–3321. URL http://adsabs.harvard.edu/abs/2011MNRAS.414.3307G

González-Martín, O., Masegosa, J., Márquez, I., Guainazzi, M., 2009a. *Fitting Liner Nuclei within the Active Galactic Nucleus Family: A Matter of Obscuration?* ApJ, 704, 1570–1585. URL http://adsabs.harvard.edu/abs/2009ApJ...704.1570G

González-Martín, O., Masegosa, J., Márquez, I., Guainazzi, M., Jiménez-Bailón, E., 2009b. *An X-ray view of 82 LINERs with Chandra and XMM-Newton data*. A&A, 506, 1107–1121. URL http://adsabs.harvard.edu/abs/2009A%26A...506.1107G

Gorjian, V., Werner, M. W., Jarrett, T. H., Cole, D. M., Ressler, M. E., 2004. *10 Micron Imaging of Seyfert Galaxies from the 12 Micron Sample*. ApJ, 605, 156–167. URL http://adsabs.harvard.edu/abs/2004ApJ...605..156G

Goulding, A. D., Alexander, D. M., 2009. *Towards a complete census of AGN in nearby Galaxies: a large population of optically unidentified AGN*. MNRAS, 398, 1165–1193. URL http://adsabs.harvard.edu/abs/2009MNRAS.398.1165G

Graham, A. W., Onken, C. A., Athanassoula, E., Combes, F., 2011. *An expanded Mbh- diagram, and a new calibration of active galactic nuclei masses*. MNRAS, 412, 2211–2228. URL http://adsabs.harvard.edu/abs/2011MNRAS.412.2211G

Greenhill, L. J., Jiang, D. R., Moran, J. M., Reid, M. J., et al., 1995. *Detection of a Subparsec Diameter Disk in the Nucleus of NGC 4258*. ApJ, 440, 619. URL http://adsabs.harvard.edu/abs/1995ApJ...440..619G

Grier, C. J., Mathur, S., Ghosh, H., Ferrarese, L., 2011. *Discovery of Nuclear X-ray Sources in Sings Galaxies*. ApJ, 731, 60. URL http://adsabs.harvard.edu/abs/2011ApJ...731...60G

Grossan, B., 2004. *High Resolution Mid-Infrared Observations of Low-Luminosity AGN with the Keck Telescope and LWS*. astro-ph/0405190. URL http://arxiv.org/abs/astro-ph/0405190

Groves, B., Dopita, M., Sutherland, R., 2006. *The infrared emission from the narrow line region*. A&A, 458, 405–416. URL http://adsabs.harvard.edu/abs/2006A%26A...458..405G

Haas, M., Siebenmorgen, R., Pantin, E., Horst, H., et al., 2007. *VISIR/VLT mid-infrared imaging of Seyfert nuclei: nuclear dust emission and the Seyfert-2 dichotomy*. A&A, 473, 369–376. URL http://adsabs.harvard.edu/abs/2007A%26A...473..369H

Haas, M., Siebenmorgen, R., Schulz, B., Krügel, E., Chini, R., 2005. *Spitzer IRS spectroscopy of 3CR radio galaxies and quasars: testing the unified schemes*. A&A, 442, L39–L43. URL http://adsabs.harvard.edu/abs/2005A%26A...442L..39H

Hadfield, L. J., Crowther, P. A., 2006. *How extreme are the Wolf-Rayet clusters in NGC3125?**. MNRAS, 368, 1822–1832. URL http://adsabs.harvard.edu/abs/2006MNRAS.368.1822H

Hardcastle, M. J., Evans, D. A., Croston, J. H., 2009. *The active nuclei of $z < 1.0$ 3CRR radio sources*. MNRAS, 396, 1929–1952. URL http://adsabs.harvard.edu/abs/2009MNRAS.396.1929H

Heckman, T. M., 1980. *An optical and radio survey of the nuclei of bright galaxies - Activity in normal galactic nuclei*. A&A, 87, 152–164. URL http://adsabs.harvard.edu/abs/1980A%26A....87..152H

Heckman, T. M., Lebofsky, M. J., Rieke, G. H., van Breugel, W., 1983. *An infrared and optical investigation of galactic nuclei with compact radio sources*. ApJ, 272, 400–410. URL http://adsabs.harvard.edu/abs/1983ApJ...272..400H

Hernán-Caballero, A., Hatziminaoglou, E., 2011. *An atlas of mid-infrared spectra of star-forming and active galaxies*. MNRAS, 414, 500–511. URL http://adsabs.harvard.edu/abs/2011MNRAS.414..500H

Herrnstein, J. R., Greenhill, L. J., Moran, J. M., Diamond, P. J., et al., 1998. *VLBA Continuum Observations of NGC 4258: Constraints on an Advection-dominated Accretion Flow*. The ApJL, 497, L69. URL http://adsabs.harvard.edu/abs/1998ApJ...497L..69H

Ho, L. C., 2008. *Nuclear Activity in Nearby Galaxies*. ARA&A, 46, 475–539. URL http://adsabs.harvard.edu/abs/2008ARA%26A..46..475H

Ho, L. C., Feigelson, E. D., Townsley, L. K., Sambruna, R. M., et al., 2001. *Detection of Nuclear X-Ray Sources in Nearby Galaxies with Chandra*. ApJ, 549, L51–L54. URL http://adsabs.harvard.edu/abs/2001ApJ...549L..51H

Ho, L. C., Filippenko, A. V., Sargent, W. L., 1995. *A search for 'dwarf' Seyfert nuclei. 2: an optical spectral atlas of the nuclei of nearby galaxies*. ApJSS, 98, 477–593. URL http://adsabs.harvard.edu/abs/1995ApJS...98..477H

Ho, L. C., Filippenko, A. V., Sargent, W. L. W., 1997. *A Search for "Dwarf" Seyfert Nuclei. III. Spectroscopic Parameters and Properties of the Host Galaxies*. ApJSS, 112, 315. URL http://adsabs.harvard.edu/abs/1997ApJS..112..315H

Ho, L. C., Greene, J. E., Filippenko, A. V., Sargent, W. L. W., 2009. *A Search for "Dwarf" Seyfert Nuclei. VII. A Catalog of Central Stellar Velocity Dispersions of Nearby Galaxies*. ApJSS, 183, 1–16. URL http://adsabs.harvard.edu/abs/2009ApJS..183....1H

Ho, L. C., Ulvestad, J. S., 2001. *Radio Continuum Survey of an Optically Selected Sample of Nearby Seyfert Galaxies*. ApJSS, 133, 77–118. URL http://adsabs.harvard.edu/abs/2001ApJS..133...77H

Hönig, S. F., Beckert, T., 2007. *Active galactic nuclei dust tori at low and high luminosities*. MNRAS, 380, 1172–1176. URL http://adsabs.harvard.edu/abs/2007MNRAS.380.1172H

HÖNIG, S. F., BECKERT, T., OHNAKA, K., WEIGELT, G., 2006. *Radiative transfer modeling of three-dimensional clumpy AGN tori and its application to NGC 1068.* A&A, 452, 459–471. URL `http://adsabs.harvard.edu/abs/2006A%26A...452..459H`

HÖNIG, S. F., KISHIMOTO, M., 2010. *The dusty heart of nearby active galaxies. II. From clumpy torus models to physical properties of dust around AGN.* A&A, 523, 27. URL `http://adsabs.harvard.edu/abs/2010A%26A...523A..27H`

HÖNIG, S. F., KISHIMOTO, M., GANDHI, P., SMETTE, A., ET AL., 2010. *The dusty heart of nearby active galaxies. I. High-spatial resolution mid-IR spectro-photometry of Seyfert galaxies.* A&A, 515, 23. URL `http://adsabs.harvard.edu/abs/2010A%26A...515A..23H`

HÖNIG, S. F., LEIPSKI, C., ANTONUCCI, R., HAAS, M., 2011. *Quantifying the Anisotropy in the Infrared Emission of Powerful Active Galactic Nuclei.* ApJ, 736, 26. URL `http://adsabs.harvard.edu/abs/2011ApJ...736...26H`

HORST, H., DUSCHL, W. J., GANDHI, P., SMETTE, A., 2009. *Mid-infrared imaging of 25 local AGN with VLT-VISIR.* A&A, 495, 137–146. URL `http://adsabs.harvard.edu/abs/2009A%26A...495..137H`

HORST, H., GANDHI, P., SMETTE, A., DUSCHL, W. J., 2008. *The mid IR - hard X-ray correlation in AGN and its implications for dusty torus models.* A&A, 479, 389–396. URL `http://adsabs.harvard.edu/abs/2008A%26A...479..389H`

HORST, H., SMETTE, A., GANDHI, P., DUSCHL, W. J., 2006. *The small dispersion of the mid IR - hard X-ray correlation in active galactic nuclei.* A&A, 457, L17–L20. URL `http://adsabs.harvard.edu/abs/2006A%26A...457L..17H`

HOUCK, J. R., ROELLIG, T. L., VAN CLEVE, J., FORREST, W. J., ET AL., 2004. *The Infrared Spectrograph (IRS) on the Spitzer Space Telescope.* ApJSS, 154, 18–24. URL `http://adsabs.harvard.edu/abs/2004ApJS..154...18H`

HUDAVERDI, M., KUNIEDA, H., TANAKA, T., HABA, Y., ET AL., 2006. *Overdensity of X-Ray Sources in the Field of Two Nearby Clusters of Galaxies: XMM-Newton View of A 194 and A 1060.* PASJ, 58, 931–943. URL `http://adsabs.harvard.edu/abs/2006PASJ...58..931H`

HUMPHREY, P. J., BUOTE, D. A., 2006. *A Chandra Survey of Early-Type Galaxies. I. Metal Enrichment in the Interstellar Medium.* ApJ, 639, 136–156. URL `http://adsabs.harvard.edu/abs/2006ApJ...639..136H`

IKEDA, S., AWAKI, H., TERASHIMA, Y., 2009. *Study on X-Ray Spectra of Obscured Active Galactic Nuclei Based on Monte Carlo SimulationAn Interpretation of Observed Wide-Band Spectra.* ApJ, 692, 608–617. URL `http://adsabs.harvard.edu/abs/2009ApJ...692..608I`

IMMLER, S., BRANDT, W. N., VIGNALI, C., BAUER, F. E., ET AL., 2003. *Probing the Complex and Variable X-Ray Absorption of Markarian 6 with XMM-Newton.* AJ, 126, 153–157. URL `http://cdsads.u-strasbg.fr/abs/2003AJ....126..153I`

ISOBE, T., FEIGELSON, E. D., AKRITAS, M. G., BABU, G. J., 1990. *Linear regression in astronomy.* ApJ, 364, 104–113. URL `http://adsabs.harvard.edu/abs/1990ApJ...364..104I`

JACOBY, G. H., BRANCH, D., CIARDULLO, R., DAVIES, R. L., ET AL., 1992. *A critical review of selected techniques for measuring extragalactic distances.* PASP, 104, 599–662. URL `http://adsabs.harvard.edu/abs/1992PASP..104..599J`

Jaffe, W., Meisenheimer, K., Röttgering, H. J. A., Leinert, C., et al., 2004. *The central dusty torus in the active nucleus of NGC 1068*. Nature, 429, 47–49. URL http://adsabs.harvard.edu/abs/2004Natur.429...47J

Jensen, J. B., Tonry, J. L., Barris, B. J., Thompson, R. I., et al., 2003. *Measuring Distances and Probing the Unresolved Stellar Populations of Galaxies Using Infrared Surface Brightness Fluctuations*. ApJ, 583, 712–726. URL http://adsabs.harvard.edu/abs/2003ApJ...583..712J

Jiménez-Bailón, E., Santos-Lleó, M., Mas-Hesse, J. M., Guainazzi, M., et al., 2003. *Nuclear Activity and Massive Star Formation in the Low-Luminosity Active Galactic Nucleus NGC 4303: Chandra X-Ray Observations*. ApJ, 593, 127–141. URL http://adsabs.harvard.edu/abs/2003ApJ...593..127J

Kato, S., Fukue, J., Mineshige, S., *Black-Hole Accretion Disks — Towards a New Paradigm —* (2008). URL http://adsabs.harvard.edu/abs/2008bhad.book.....K

Kelly, B. C., 2007. *Some Aspects of Measurement Error in Linear Regression of Astronomical Data*. ApJ, 665, 1489–1506. URL http://adsabs.harvard.edu/abs/2007ApJ...665.1489K

Kewley, L. J., Groves, B., Kauffmann, G., Heckman, T., 2006. *The host galaxies and classification of active galactic nuclei*. MNRAS, 372, 961–976. URL http://adsabs.harvard.edu/abs/2006MNRAS.372..961K

Kewley, L. J., Heisler, C. A., Dopita, M. A., Lumsden, S., 2001. *Optical Classification of Southern Warm Infrared Galaxies*. ApJSS, 132, 37–71. URL http://adsabs.harvard.edu/abs/2001ApJS..132...37K

Khachikian, E. Y., Weedman, D. W., 1974. *An atlas of Seyfert galaxies*. ApJ, 192, 581–589. URL http://adsabs.harvard.edu/abs/1974ApJ...192..581K

Kim, D., Barkhouse, W. A., Romero-Colmenero, E., Green, P. J., et al., 2006. *Chandra Multiwavelength Project: Normal Galaxies at Intermediate Redshift*. ApJ, 644, 829–842. URL http://adsabs.harvard.edu/abs/2006ApJ...644..829K

Kishimoto, M., Hönig, S. F., Beckert, T., Weigelt, G., 2007. *The innermost region of AGN tori: implications from the HST/NICMOS type 1 point sources and near-IR reverberation*. A&A, 476, 713–721. URL http://adsabs.harvard.edu/abs/2007A%26A...476..713K

Komossa, S., Burwitz, V., Hasinger, G., Predehl, P., et al., 2003. *Discovery of a Binary Active Galactic Nucleus in the Ultraluminous Infrared Galaxy NGC 6240 Using Chandra*. ApJ, 582, L15–L19. URL http://adsabs.harvard.edu/abs/2003ApJ...582L..15K

Krabbe, A., Böker, T., Maiolino, R., 2001. *N-Band Imaging of Seyfert Nuclei and the Mid-Infrared-X-Ray Correlation*. ApJ, 557, 626–636. URL http://adsabs.harvard.edu/abs/2001ApJ...557..626K

Krolik, J. H., *Active galactic nuclei : from the central black hole to the galactic environment* (1999). URL http://adsabs.harvard.edu/abs/1999agnc.book.....K

Krolik, J. H., Begelman, M. C., 1988. *Molecular tori in Seyfert galaxies - Feeding the monster and hiding it*. ApJ, 329, 702–711. URL http://adsabs.harvard.edu/abs/1988ApJ...329..702K

Lagage, P. O., Pel, J. W., Authier, M., Belorgey, J., et al., 2004. *Successful Commissioning of VISIR: The Mid-Infrared VLT Instrument*. The Messenger, 117, 12–16. URL http://adsabs.harvard.edu/abs/2004Msngr.117...12L

LaMassa, S. M., Heckman, T. M., Ptak, A., Martins, L., et al., 2010. *Indicators of Intrinsic Active Galactic Nucleus Luminosity: A Multi-wavelength Approach*. ApJ, 720, 786–810. URL http://adsabs.harvard.edu/abs/2010ApJ...720..786L

LaMassa, S. M., Heckman, T. M., Ptak, A., Martins, L., et al., 2011. *Uncovering Obscured Active Galactic Nuclei in Homogeneously Selected Samples of Seyfert 2 Galaxies*. ApJ, 729, 52. URL http://adsabs.harvard.edu/abs/2011ApJ...729...52L

Landi, R., Masetti, N., Morelli, L., Palazzi, E., et al., 2007. *The AGN Nature of 11 out of 12 Swift/RXTE Unidentified Sources through Optical and X-Ray Spectroscopy*. ApJ, 669, 109–125. URL http://adsabs.harvard.edu/abs/2007ApJ...669..109L

Lasota, J., Abramowicz, M. A., Chen, X., Krolik, J., et al., 1996. *Is the Accretion Flow in NGC 4258 Advection Dominated?* ApJ, 462, 142. URL http://adsabs.harvard.edu/abs/1996ApJ...462..142L

Lawrence, A., 1991. *The relative frequency of broad-lined and narrow-lined active galactic nuclei - Implications for unified schemes*. MNRAS, 252, 586–592. URL http://adsabs.harvard.edu/abs/1991MNRAS.252..586L

Leipski, C., Antonucci, R., Ogle, P., Whysong, D., 2009. *The Spitzer View of FR I Radio Galaxies: On the Origin of the Nuclear Mid-Infrared Continuum*. ApJ, 701, 891–914. URL http://adsabs.harvard.edu/abs/2009ApJ...701..891L

Levenson, N. A., Heckman, T. M., Krolik, J. H., Weaver, K. A., Życki, P. T., 2006. *Penetrating the Deep Cover of Compton-thick Active Galactic Nuclei*. ApJ, 648, 111–127. URL http://adsabs.harvard.edu/abs/2006ApJ...648..111L

Levenson, N. A., Radomski, J. T., Packham, C., Mason, R. E., et al., 2009. *Isotropic Mid-Infrared Emission from the Central 100 pc of Active Galaxies*. ApJ, 703, 390–398. URL http://adsabs.harvard.edu/abs/2009ApJ...703..390L

Lewis, K. T., Eracleous, M., 2006. *Black Hole Masses of Active Galaxies with Double-peaked Balmer Emission Lines*. ApJ, 642, 711–719. URL http://adsabs.harvard.edu/abs/2006ApJ...642..711L

Liu, J., 2011. *Chandra ACIS Survey of X-ray Point Sources in 383 Nearby Galaxies. I. The Source Catalog*. ApJSS, 192, 10. URL http://adsabs.harvard.edu/abs/2011ApJS..192...10L

Liu, J., Bregman, J. N., 2005. *Ultraluminous X-Ray Sources in Nearby Galaxies from ROSAT High Resolution Imager Observations I. Data Analysis*. ApJSS, 157, 59–125. URL http://adsabs.harvard.edu/abs/2005ApJS..157...59L

Lobban, A. P., Reeves, J. N., Miller, L., Turner, T. J., et al., 2011. *Contemporaneous Chandra HETG and Suzaku X-ray observations of NGC 4051*. MNRAS, 414, 1965–1986. URL http://adsabs.harvard.edu/abs/2011MNRAS.414.1965L

Lobban, A. P., Reeves, J. N., Porquet, D., Braito, V., et al., 2010. *Evidence for a Truncated Accretion Disc in the Low Luminosity Seyfert Galaxy, NGC 7213?* 1006.1318. URL http://arxiv.org/abs/1006.1318

Lodato, G., Bertin, G., 2003. *Non-Keplerian rotation in the nucleus of NGC 1068: Evidence for a massive accretion disk?* A&A, 398, 517–524. URL http://adsabs.harvard.edu/abs/2003A%26A...398..517L

Lutz, D., Maiolino, R., Spoon, H. W. W., Moorwood, A. F. M., 2004. *The relation between AGN hard X-ray emission and mid-infrared continuum from ISO spectra: Scatter and unification aspects*. A&A, 418, 465–473. URL http://adsabs.harvard.edu/abs/2004A%26A...418..465L

Lynden-Bell, D., 1969. *Galactic Nuclei as Collapsed Old Quasars*. Nature, 223, 690–694. URL http://adsabs.harvard.edu/abs/1969Natur.223..690L

Maccarone, T. J., Kundu, A., Zepf, S. E., 2003. *The Low-Mass X-Ray Binary-Globular Cluster Connection. II. NGC 4472 X-Ray Source Properties and Source Catalogs*. ApJ, 586, 814–825. URL http://adsabs.harvard.edu/abs/2003ApJ...586..814M

Madore, B. F., Freedman, W. L., Silbermann, N., Harding, P., et al., 1999. *The Hubble Space Telescope Key Project on the Extragalactic Distance Scale. XV. A Cepheid Distance to the Fornax Cluster and Its Implications*. ApJ, 515, 29–41. URL http://adsabs.harvard.edu/abs/1999ApJ...515...29M

Maiolino, R., Rieke, G. H., 1995. *Low-Luminosity and Obscured Seyfert Nuclei in Nearby Galaxies*. ApJ, 454, 95. URL http://adsabs.harvard.edu/abs/1995ApJ...454...95M

Maiolino, R., Salvati, M., Bassani, L., Dadina, M., et al., 1998. *Heavy obscuration in X-ray weak AGNs*. A&A, 338, 781–794. URL http://adsabs.harvard.edu/abs/1998A%26A...338..781M

Malizia, A., Landi, R., Bassani, L., Bird, A. J., et al., 2007. *Swift XRT Observation of 34 New INTEGRAL IBIS AGNs: Discovery of Compton-Thick and Other Peculiar Sources*. ApJ, 668, 81–86. URL http://adsabs.harvard.edu/abs/2007ApJ...668...81M

Maoz, D., 2007. *Low-luminosity active galactic nuclei: are they UV faint and radio loud?* MNRAS, 377, 1696–1710. URL http://adsabs.harvard.edu/abs/2007MNRAS.377.1696M

Marchese, E., Braito, V., Della Ceca, R., Caccianiga, A., Severgnini, P., 2012. *NGC454: unveiling a new "changing look" AGN*. arXiv:1201.2169. URL http://arxiv.org/abs/1201.2169

Markoff, S., Nowak, M., Young, A., Marshall, H. L., et al., 2008. *Results from an Extensive Simultaneous Broadband Campaign on the Underluminous Active Nucleus M81*: Further Evidence for Mass-scaling Accretion in Black Holes*. ApJ, 681, 905–924. URL http://adsabs.harvard.edu/abs/2008ApJ...681..905M

Markwardt, C. B., Tueller, J., Skinner, G. K., Gehrels, N., et al., 2005. *The Swift/BAT High-Latitude Survey: First Results*. The ApJL, 633, L77–L80. URL http://adsabs.harvard.edu/abs/2005ApJ...633L..77M

Mason, R. E., Geballe, T. R., Packham, C., Levenson, N. A., et al., 2006. *Spatially Resolved Mid-Infrared Spectroscopy of NGC 1068: The Nature and Distribution of the Nuclear Material*. ApJ, 640, 612–624. URL http://adsabs.harvard.edu/abs/2006ApJ...640..612M

Mason, R. E., Levenson, N. A., Packham, C., Elitzur, M., et al., 2007. *Dust and PAH Emission in the Star-forming Active Nucleus of NGC 1097*. ApJ, 659, 241–249. URL http://adsabs.harvard.edu/abs/2007ApJ...659..241M

Massaro, F., Harris, D. E., Tremblay, G. R., Axon, D., et al., 2010. *Chandra Observations of 3C Radio Sources with $z < 0.3$: Nuclei, Diffuse Emission, Jets, and Hotspots*. ApJ, 714, 589–604. URL http://adsabs.harvard.edu/abs/2010ApJ...714..589M

Matt, G., Guainazzi, M., Maiolino, R., Molendi, S., et al., 1999. *One more surprise from the Circinus Galaxy: BeppoSAX discovery of a transmission component in hard X-rays*. A&A, 341, L39–L42. URL http://adsabs.harvard.edu/abs/1999A%26A...341L..39M

McElroy, D. B., 1995. *A Catalog of Stellar Velocity Dispersions. II. 1994 Update*. ApJSS, 100, 105. URL http://adsabs.harvard.edu/abs/1995ApJS..100..105M

Mei, S., Blakeslee, J. P., Cté, P., Tonry, J. L., et al., 2007. *The ACS Virgo Cluster Survey. XIII. SBF Distance Catalog and the Three-dimensional Structure of the Virgo Cluster*. ApJ, 655, 144–162. URL http://adsabs.harvard.edu/abs/2007ApJ...655..144M

Meléndez, M., Kraemer, S. B., Armentrout, B. K., Deo, R. P., et al., 2008. *New Indicators for AGN Power: The Correlation between [O IV] 25.89 m and Hard X-Ray Luminosity for Nearby Seyfert Galaxies*. ApJ, 682, 94–103. URL `http://adsabs.harvard.edu/abs/2008ApJ...682...94M`

Milosavljević, M., Merritt, D., 2001. *Formation of Galactic Nuclei*. ApJ, 563, 34–62. URL `http://adsabs.harvard.edu/abs/2001ApJ...563...34M`

Miniutti, G., Ponti, G., Dadina, M., Cappi, M., Malaguti, G., 2007. *IRAS 13197-1627 has them all: Compton-thin absorption, photoionized gas, thermal plasmas and a broad Fe line*. MNRAS, 375, 227–239. URL `http://adsabs.harvard.edu/abs/2007MNRAS.375..227M`

Miyoshi, M., Moran, J., Herrnstein, J., Greenhill, L., et al., 1995. *Evidence for a black hole from high rotation velocities in a sub-parsec region of NGC4258*. Nature, 373, 127–129. URL `http://adsabs.harvard.edu/abs/1995Natur.373..127M`

Mor, R., Netzer, H., Elitzur, M., 2009. *Dusty Structure Around Type-I Active Galactic Nuclei: Clumpy Torus Narrow-line Region and Near-nucleus Hot Dust*. ApJ, 705, 298–313. URL `http://adsabs.harvard.edu/abs/2009ApJ...705..298M`

Morrison, R., McCammon, D., 1983. *Interstellar photoelectric absorption cross sections, 0.03-10 keV*. ApJ, 270, 119–122. URL `http://adsabs.harvard.edu/abs/1983ApJ...270..119M`

Mullaney, J. R., Alexander, D. M., Goulding, A. D., Hickox, R. C., 2011. *Defining the intrinsic AGN infrared spectral energy distribution and measuring its contribution to the infrared output of composite galaxies*. MNRAS, p. 474. URL `http://adsabs.harvard.edu/abs/2011MNRAS.tmp..474M`

Mundell, C. G., Wrobel, J. M., Pedlar, A., Gallimore, J. F., 2003. *The Nuclear Regions of the Seyfert Galaxy NGC 4151: Parsec-Scale H I Absorption and a Remarkable Radio Jet*. ApJ, 583, 192–204. URL `http://adsabs.harvard.edu/abs/2003ApJ...583..192M`

Murphy, K. D., Yaqoob, T., Terashima, Y., 2007. *Monitoring the Violent Activity from the Inner Accretion Disk of the Seyfert 1.9 Galaxy NGC 2992 with RXTE*. ApJ, 666, 96–108. URL `http://adsabs.harvard.edu/abs/2007ApJ...666...96M`

Nagar, N. M., Falcke, H., Wilson, A. S., 2005. *Radio sources in low-luminosity active galactic nuclei. IV. Radio luminosity function, importance of jet power, and radio properties of the complete Palomar sample*. A&A, 435, 521–543. URL `http://adsabs.harvard.edu/abs/2005A%26A...435..521N`

Nandra, K., Pounds, K. A., 1994. *GINGA Observations of the X-Ray Spectra of Seyfert Galaxies*. MNRAS, 268, 405. URL `http://adsabs.harvard.edu/abs/1994MNRAS.268..405N`

Narayan, R., 2005. *Black holes in astrophysics*. New Journal of Physics, 7, 199. URL `http://adsabs.harvard.edu/abs/2005NJPh....7..199N`

Narayan, R., Yi, I., 1994. *Advection-dominated accretion: A self-similar solution*. ApJ, 428, L13–L16. URL `http://adsabs.harvard.edu/abs/1994ApJ...428L..13N`

Nemmen, R., Storchi-Bergmann, T., Eracleous, M., 2011. *Spectral Energy Distribution Models for Low-luminosity Active Galactic Nuclei in LINERs*. arXiv:1112.4640. URL `http://arxiv.org/abs/1112.4640`

Nemmen, R. S., Storchi-Bergmann, T., Yuan, F., Eracleous, M., et al., 2006. *Radiatively Inefficient Accretion Flow in the Nucleus of NGC 1097*. ApJ, 643, 652–659. URL `http://adsabs.harvard.edu/abs/2006ApJ...643..652N`

Nenkova, M., Ivezić, v., Elitzur, M., 2002. *Dust Emission from Active Galactic Nuclei*. ApJ, 570, L9–L12. URL `http://adsabs.harvard.edu/abs/2002ApJ...570L...9N`

Nenkova, M., Sirocky, M. M., Ivezić, v., Elitzur, M., 2008a. *AGN Dusty Tori. I. Handling of Clumpy Media*. ApJ, 685, 147–159. URL `http://adsabs.harvard.edu/abs/2008ApJ...685..147N`

Nenkova, M., Sirocky, M. M., Nikutta, R., Ivezić, v., Elitzur, M., 2008b. *AGN Dusty Tori. II. Observational Implications of Clumpiness*. ApJ, 685, 160–180. URL `http://adsabs.harvard.edu/abs/2008ApJ...685..160N`

Neugebauer, G., Habing, H. J., van Duinen, R., Aumann, H. H., et al., 1984. *The Infrared Astronomical Satellite (IRAS) mission*. The ApJL, 278, L1–L6. URL `http://adsabs.harvard.edu/abs/1984ApJ...278L...1N`

Neugebauer, G., Matthews, K., 1999. *Variability of Quasars at 10 Microns*. AJ, 118, 35–45. URL `http://adsabs.harvard.edu/abs/1999AJ....118...35N`

Nicastro, F., Martocchia, A., Matt, G., 2003. *The Lack of Broad-Line Regions in Low Accretion Rate Active Galactic Nuclei as Evidence of Their Origin in the Accretion Disk*. ApJ, 589, L13–L16. URL `http://adsabs.harvard.edu/abs/2003ApJ...589L..13N`

Noguchi, K., Terashima, Y., Awaki, H., 2009. *A New Sample of Buried Active Galactic Nuclei Selected from the Second XMM-Newton Serendipitous Source Catalogue*. ApJ, 705, 454–467. URL `http://adsabs.harvard.edu/abs/2009ApJ...705..454N`

Osterbrock, D. E., 1977. *Spectrophotometry of Seyfert 1 galaxies*. ApJ, 215, 733–745. URL `http://adsabs.harvard.edu/abs/1977ApJ...215..733O`

Osterbrock, D. E., 1981. *Seyfert galaxies with weak broad H alpha emission lines*. ApJ, 249, 462–470. URL `http://adsabs.harvard.edu/abs/1981ApJ...249..462O`

Osterbrock, D. E., Martel, A., 1993. *Spectroscopic study of the CfA sample of Seyfert galaxies*. ApJ, 414, 552–562. URL `http://adsabs.harvard.edu/abs/1993ApJ...414..552O`

Page, M. J., Breeveld, A. A., Soria, R., Wu, K., et al., 2003. *X-ray emission line gas in the LINER galaxy M 81*. A&A, 400, 145–151. URL `http://adsabs.harvard.edu/abs/2003A%26A...400..145P`

Panessa, F., Bassani, L., Cappi, M., Dadina, M., et al., 2006. *On the X-ray, optical emission line and black hole mass properties of local Seyfert galaxies*. A&A, 455, 173–185. URL `http://adsabs.harvard.edu/abs/2006A%26A...455..173P`

Papadakis, I. E., Ioannou, Z., Brinkmann, W., Xilouris, E. M., 2008. *The X-ray variability and the near-IR to X-ray spectral energy distribution of four low luminosity Seyfert 1 galaxies*. A&A, 490, 995–1003. URL `http://adsabs.harvard.edu/abs/2008A%26A...490..995P`

Pappa, A., Georgantopoulos, I., Stewart, G. C., Zezas, A. L., 2001. *The X-ray spectra of optically selected Seyfert 2 galaxies: are there any Seyfert 2 galaxies with no absorption?* MNRAS, 326, 995–1006. URL `http://adsabs.harvard.edu/abs/2001MNRAS.326..995P`

Paturel, G., Petit, C., Prugniel, P., Theureau, G., et al., 2003. *HYPERLEDA. I. Identification and designation of galaxies*. A&A, 412, 45–55. URL `http://adsabs.harvard.edu/abs/2003A%26A...412...45P`

Perlman, E. S., Mason, R. E., Packham, C., Levenson, N. A., et al., 2007. *The Mid-Infrared Emission of M87*. ApJ, 663, 808–815. URL `http://adsabs.harvard.edu/abs/2007ApJ...663..808P`

Peterson, B. M., Bentz, M. C., Desroches, L., Filippenko, A. V., et al., 2005. *Multiwavelength Monitoring of the Dwarf Seyfert 1 Galaxy NGC 4395. I. A Reverberation-based Measurement of the Black Hole Mass*. ApJ, 632, 799–808. URL `http://adsabs.harvard.edu/abs/2005ApJ...632..799P`

Peterson, B. M., Ferrarese, L., Gilbert, K. M., Kaspi, S., et al., 2004. *Central Masses and Broad-Line Region Sizes of Active Galactic Nuclei. II. A Homogeneous Analysis of a Large Reverberation-Mapping Database*. ApJ, 613, 682–699. URL `http://adsabs.harvard.edu/abs/2004ApJ...613..682P`

Petrucci, P. O., Ponti, G., Matt, G., Longinotti, A. L., et al., 2007. *Unveiling the broad band X-ray continuum and iron line complex in Mrk 841*. A&A, 470, 889–902. URL `http://cdsads.u-strasbg.fr/abs/2007A%26A...470..889P`

Pier, E. A., Krolik, J. H., 1992. *Infrared spectra of obscuring dust tori around active galactic nuclei. I - Calculational method and basic trends*. ApJ, 401, 99–109. URL `http://adsabs.harvard.edu/abs/1992ApJ...401...99P`

Porquet, D., Kaastra, J. S., Page, K. L., O'Brien, P. T., et al., 2004. *XMM-Newton observation of the Seyfert 1 ESO 198-G24*. A&A, 413, 913–920. URL `http://cdsads.u-strasbg.fr/abs/2004A%26A...413..913P`

Pounds, K. A., Reeves, J. N., Page, K. L., Edelson, R., et al., 2003. *A simultaneous XMM-Newton and BeppoSAX observation of the archetypal broad line Seyfert 1 galaxy NGC 5548*. MNRAS, 341, 953–960. URL `http://cdsads.u-strasbg.fr/abs/2003MNRAS.341..953P`

Press, W. H., Teukolsky, S. A., Vetterling, W. T., Flannery, B. P., *Numerical recipes in FORTRAN. The art of scientific computing* (1992). URL `http://adsabs.harvard.edu/abs/1992nrfa.book.....P`

Pringle, J. E., 1996. *Self-induced warping of accretion discs*. MNRAS, 281, 357–361. URL `http://adsabs.harvard.edu/abs/1996MNRAS.281..357P`

Puget, J. L., Leger, A., 1989. *A new component of the interstellar matter - Small grains and large aromatic molecules*. ARA&A, 27, 161–198. URL `http://adsabs.harvard.edu/abs/1989ARA%26A..27..161P`

Raban, D., Jaffe, W., Röttgering, H., Meisenheimer, K., Tristram, K. R. W., 2009. *Resolving the obscuring torus in NGC 1068 with the power of infrared interferometry: revealing the inner funnel of dust*. MNRAS, 394, 1325–1337. URL `http://adsabs.harvard.edu/abs/2009MNRAS.394.1325R`

Ramírez, J. M., Komossa, S., Burwitz, V., Mathur, S., 2008. *Chandra LETGS Spectroscopy of the Quasar MR 2251-178 and Its Warm Absorber*. ApJ, 681, 965–981. URL `http://adsabs.harvard.edu/abs/2008ApJ...681..965R`

Ramos Almeida, C., Levenson, N. A., Rodríguez Espinosa, J. M., Alonso-Herrero, A., et al., 2009. *The Infrared Nuclear Emission of Seyfert Galaxies on Parsec Scales: Testing the Clumpy Torus Models*. ApJ, 702, 1127–1149. URL `http://adsabs.harvard.edu/abs/2009ApJ...702.1127R`

Ranalli, P., Comastri, A., Setti, G., 2003. *The 2-10 keV luminosity as a Star Formation Rate indicator*. A&A, 399, 39–50. URL `http://adsabs.harvard.edu/abs/2003A%26A...399...39R`

Reunanen, J., Prieto, M. A., Siebenmorgen, R., 2010. *VLT diffraction-limited imaging at 11 and 18m of the nearest active galactic nuclei*. MNRAS, 402, 879–894. URL `http://adsabs.harvard.edu/abs/2010MNRAS.402..879R`

Reynolds, C. S., Nowak, M. A., Markoff, S., Tueller, J., et al., 2009. *Probing the Accretion Disk and Central Engine Structure of NGC 4258 with Suzaku and XMM-Newton Observations*. ApJ, 691, 1159–1167. URL `http://adsabs.harvard.edu/abs/2009ApJ...691.1159R`

Rieke, G. H., 1978. *The infrared emission of Seyfert galaxies*. ApJ, 226, 550–558. URL `http://adsabs.harvard.edu/abs/1978ApJ...226..550R`

Risaliti, G., Braito, V., Laparola, V., Bianchi, S., et al., 2009. *A Strong Excess in the 20-100 keV Emission of NGC 1365*. The ApJL, 705, L1–L5. URL http://adsabs.harvard.edu/abs/2009ApJ...705L...1R

Risaliti, G., Elvis, M., Fabbiano, G., Baldi, A., Zezas, A., 2005. *Rapid Compton-thick/Compton-thin Transitions in the Seyfert 2 Galaxy NGC 1365*. ApJ, 623, L93–L96. URL http://adsabs.harvard.edu/abs/2005ApJ...623L..93R

Risaliti, G., Elvis, M., Fabbiano, G., Baldi, A., et al., 2007. *Occultation Measurement of the Size of the X-Ray-emitting Region in the Active Galactic Nucleus of NGC 1365*. ApJ, 659, L111–L114. URL http://adsabs.harvard.edu/abs/2007ApJ...659L.111R

Risaliti, G., Nardini, E., Salvati, M., Elvis, M., et al., 2011. *X-ray absorption by broad-line region clouds in Mrk 766*. MNRAS, 410, 1027–1035. URL http://cdsads.u-strasbg.fr/abs/2011MNRAS.410.1027R

Russell, D. G., 2002. *The H I Line Width/Linear Diameter Relationship as an Independent Test of the Hubble Constant*. ApJ, 565, 681–695. URL http://adsabs.harvard.edu/abs/2002ApJ...565..681R

Salpeter, E. E., 1964. *Accretion of Interstellar Matter by Massive Objects*. ApJ, 140, 796–800. URL http://adsabs.harvard.edu/abs/1964ApJ...140..796S

Sambruna, R. M., Reeves, J. N., Braito, V., Lewis, K. T., et al., 2009. *Structure of the Accretion Flow in Broad-Line Radio Galaxies: The Case of 3C 390.3*. ApJ, 700, 1473–1487. URL http://cdsads.u-strasbg.fr/abs/2009ApJ...700.1473S

Sambruna, R. M., Tombesi, F., Reeves, J. N., Braito, V., et al., 2011. *The Suzaku view of 3C 382*. ApJ, 734, 105. URL http://adsabs.harvard.edu/abs/2011ApJ...734..105S

Sanders, D. B., Mazzarella, J. M., Kim, D., Surace, J. A., Soifer, B. T., 2003. *The IRAS Revised Bright Galaxy Sample*. AJ, 126, 1607–1664. URL http://adsabs.harvard.edu/abs/2003AJ....126.1607S

Sansom, A. E., O'Sullivan, E., Forbes, D. A., Proctor, R. N., Davis, D. S., 2006. *X-ray observations of three young, early-type galaxies*. MNRAS, 370, 1541–1555. URL http://adsabs.harvard.edu/abs/2006MNRAS.370.1541S

Satyapal, S., Dudik, R. P., O'Halloran, B., Gliozzi, M., 2005. *The Link between Star Formation and Accretion in LINERs: A Comparison with Other Active Galactic Nucleus Subclasses*. ApJ, 633, 86–104. URL http://adsabs.harvard.edu/abs/2005ApJ...633...86S

Satyapal, S., Sambruna, R. M., Dudik, R. P., 2004. *A joint mid-infrared spectroscopic and X-ray imaging investigation of LINER galaxies*. A&A, 414, 825–838. URL http://adsabs.harvard.edu/abs/2004A%26A...414..825S

Schartmann, M., Meisenheimer, K., Camenzind, M., Wolf, S., Henning, T., 2005. *Towards a physical model of dust tori in Active Galactic Nuclei. Radiative transfer calculations for a hydrostatic torus model*. A&A, 437, 861–881. URL http://adsabs.harvard.edu/abs/2005A%26A...437..861S

Schartmann, M., Meisenheimer, K., Camenzind, M., Wolf, S., et al., 2008. *Three-dimensional radiative transfer models of clumpy tori in Seyfert galaxies*. A&A, 482, 67–80. URL http://adsabs.harvard.edu/abs/2008A%26A...482...67S

Schinnerer, E., Eckart, A., Tacconi, L. J., Genzel, R., Downes, D., 2000. *Bars and Warps Traced by the Molecular Gas in the Seyfert 2 Galaxy NGC 1068*. ApJ, 533, 850–868. URL http://adsabs.harvard.edu/abs/2000ApJ...533..850S

Schmidt, M., 1963. *3C 273 : A Star-Like Object with Large Red-Shift*. Nature, 197, 1040. URL http://adsabs.harvard.edu/abs/1963Natur.197.1040S

Schneider, P., *Extragalactic Astronomy and Cosmology* (2006). URL http://adsabs.harvard.edu/abs/2006eac..book.....S

Schödel, R., Ott, T., Genzel, R., Eckart, A., et al., 2003. *Stellar Dynamics in the Central Arcsecond of Our Galaxy*. ApJ, 596, 1015–1034. URL http://adsabs.harvard.edu/abs/2003ApJ...596.1015S

Schwope, A., Hasinger, G., Lehmann, I., Schwarz, R., et al., 2000. *The ROSAT Bright Survey: II. Catalogue of all high-galactic latitude RASS sources with PSPC countrate CR > 0.2 s-1*. Astron. Nachr., 321, 1–52. URL http://adsabs.harvard.edu/abs/2000AN....321....1S

Scott, J. E., Kriss, G. A., Lee, J. C., Arav, N., et al., 2004. *Intrinsic Absorption in the Spectrum of Markarian 279: Simultaneous Chandra, FUSE, and STIS Observations*. ApJSS, 152, 1–27. URL http://adsabs.harvard.edu/abs/2004ApJS..152....1S

Seyfert, C. K., 1943. *Nuclear Emission in Spiral Nebulae.* ApJ, 97, 28. URL http://adsabs.harvard.edu/abs/1943ApJ....97...28S

Shakura, N. I., Sunyaev, R. A., 1973. *Black holes in binary systems. Observational appearance.* A&A, 24, 337–355. URL http://adsabs.harvard.edu/abs/1973A%26A....24..337S

Shelton, D. L., Hardcastle, M. J., Croston, J. H., 2011. *The dynamics and environmental impact of 3C 452*. MNRAS, 418, 811–819. URL http://cdsads.u-strasbg.fr/abs/2011MNRAS.418..811S

Shi, Y., Rieke, G. H., Smith, P., Rigby, J., et al., 2010. *Unobscured Type 2 Active Galactic Nuclei*. ApJ, 714, 115–129. URL http://adsabs.harvard.edu/abs/2010ApJ...714..115S

Shu, X. W., Liu, T., Wang, J. X., 2010a. *XMM-Newton Observations of the Seyfert 2 Galaxy NGC 7590: The Nature of X-ray Absorption*. ApJ, 722, 96–101. URL http://adsabs.harvard.edu/abs/2010ApJ...722...96S

Shu, X. W., Yaqoob, T., Murphy, K. D., Braito, V., et al., 2010b. *NGC 2992 in an X-ray High State Observed by XMM-Newton: Response of the Relativistic Fe K Line to the Continuum*. ApJ, 713, 1256–1265. URL http://cdsads.u-strasbg.fr/abs/2010ApJ...713.1256S

Shu, X. W., Yaqoob, T., Wang, J. X., 2010c. *The Cores of the Fe K Lines in Active Galactic Nuclei: An Extended Chandra High Energy Grating Sample*. ApJSS, 187, 581–606. URL http://adsabs.harvard.edu/abs/2010ApJS..187..581S

Siebenmorgen, R., Freudling, W., Krügel, E., Haas, M., 2004. *ISOCAM survey and dust models of 3CR radio galaxies and quasars*. A&A, 421, 129–145. URL http://adsabs.harvard.edu/abs/2004A%26A...421..129S

Siebenmorgen, R., Haas, M., Pantin, E., Krügel, E., et al., 2008. *Nuclear activity in nearby galaxies. Mid-infrared imaging with the VLT*. A&A, 488, 83–90. URL http://adsabs.harvard.edu/abs/2008A%26A...488...83S

Sikora, M., Stawarz, Å., Lasota, J., 2007. *Radio Loudness of Active Galactic Nuclei: Observational Facts and Theoretical Implications*. ApJ, 658, 815–828. URL http://adsabs.harvard.edu/abs/2007ApJ...658..815S

Simpson, C., 2005. *The luminosity dependence of the type 1 active galactic nucleus fraction*. MNRAS, 360, 565–572. URL http://adsabs.harvard.edu/abs/2005MNRAS.360..565S

Slee, O. B., Sadler, E. M., Reynolds, J. E., Ekers, R. D., 1994. *Parsecscale Radio Cores in Early Type Galaxies*. MNRAS, 269, 928. URL http://adsabs.harvard.edu/abs/1994MNRAS.269..928S

SMETTE, A., VANZI, L., 2007. *Very Large Telescope Paranal Science Operations VISIR User Manual*

SMITH, D. A., WILSON, A. S., 2001. *A Chandra Observation of the Circinus Galaxy*. ApJ, 557, 180–192. URL `http://adsabs.harvard.edu/abs/2001ApJ...557..180S`

SMITH, J. D. T., DRAINE, B. T., DALE, D. A., MOUSTAKAS, J., ET AL., 2007. *The Mid-Infrared Spectrum of Star-forming Galaxies: Global Properties of Polycyclic Aromatic Hydrocarbon Emission*. ApJ, 656, 770–791. URL `http://adsabs.harvard.edu/abs/2007ApJ...656..770S`

SNIJDERS, L., VAN DER WERF, P. P., BRANDL, B. R., MENGEL, S., ET AL., 2006. *Subarcsecond Resolution Mid-Infrared Observations of Super Star Clusters in the Antennae (NGC 4038/4039)*. ApJ, 648, L25–L28. URL `http://adsabs.harvard.edu/abs/2006ApJ...648L..25S`

SPRINGOB, C. M., MASTERS, K. L., HAYNES, M. P., GIOVANELLI, R., MARINONI, C., 2007. *SFI++. II. A New I-Band Tully-Fisher Catalog, Derivation of Peculiar Velocities, and Data Set Properties*. ApJSS, 172, 599–614. URL `http://adsabs.harvard.edu/abs/2007ApJS..172..599S`

SPRINGOB, C. M., MASTERS, K. L., HAYNES, M. P., GIOVANELLI, R., MARINONI, C., 2009. *Erratum: "SFI++ II: A New I-Band Tully-Fisher Catalog, Derivation of Peculiar Velocities and Data Set Properties" (2007, ApJS, 172, 599)*. ApJSS, 182, 474–475. URL `http://adsabs.harvard.edu/abs/2009ApJS..182..474S`

STARLING, R. L. C., PAGE, M. J., BRANDUARDI-RAYMONT, G., BREEVELD, A. A., ET AL., 2005. *The X-ray spectrum of NGC 7213 and the Seyfert-LINER connection*. MNRAS, 356, 727–733. URL `http://adsabs.harvard.edu/abs/2005MNRAS.356..727S`

STEENBRUGGE, K. C., FENOVÍK, M., KAASTRA, J. S., COSTANTINI, E., VERBUNT, F., 2009. *High-resolution X-ray spectroscopy of the low and high states of the Seyfert 1 galaxy NGC 4051 with Chandra LETGS*. A&A, 496, 107–119. URL `http://adsabs.harvard.edu/abs/2009A%26A...496..107S`

STORCHI-BERGMANN, T., NEMMEN, R. S., SPINELLI, P. F., ERACLEOUS, M., ET AL., 2005. *Evidence of a Starburst within 9 Parsecs of the Active Nucleus of NGC 1097*. ApJ, 624, L13–L16. URL `http://adsabs.harvard.edu/abs/2005ApJ...624L..13S`

TERASHIMA, Y., HO, L. C., PTAK, A. F., 2000. *Hard X-Ray Emission and the Ionizing Source in LINERS*. ApJ, 539, 161–165. URL `http://adsabs.harvard.edu/abs/2000ApJ...539..161T`

TERASHIMA, Y., IYOMOTO, N., HO, L. C., PTAK, A. F., 2002. *X-Ray Properties of LINERs and Low-Luminosity Seyfert Galaxies Observed with ASCA. I. Observations and Results*. ApJSS, 139, 1–36. URL `http://adsabs.harvard.edu/abs/2002ApJS..139....1T`

THOMPSON, G. D., LEVENSON, N. A., UDDIN, S. A., SIROCKY, M. M., 2009. *Dust Emission from Unobscured Active Galactic Nuclei*. ApJ, 697, 182–193. URL `http://adsabs.harvard.edu/abs/2009ApJ...697..182T`

TOMBESI, F., CAPPI, M., REEVES, J. N., PALUMBO, G. G. C., ET AL., 2010. *Evidence for ultra-fast outflows in radio-quiet AGNs. I. Detection and statistical incidence of Fe K-shell absorption lines*. A&A, 521, 57. URL `http://cdsads.u-strasbg.fr/abs/2010A%26A...521A..57T`

TONRY, J. L., DRESSLER, A., BLAKESLEE, J. P., AJHAR, E. A., ET AL., 2001. *The SBF Survey of Galaxy Distances. IV. SBF Magnitudes, Colors, and Distances*. ApJ, 546, 681–693. URL `http://adsabs.harvard.edu/abs/2001ApJ...546..681T`

TRAN, H. D., MILLER, J. S., KAY, L. E., 1992. *Detection of obscured broad-line regions in four Seyfert 2 galaxies*. ApJ, 397, 452–456. URL `http://adsabs.harvard.edu/abs/1992ApJ...397..452T`

Tremaine, S., Gebhardt, K., Bender, R., Bower, G., et al., 2002. *The Slope of the Black Hole Mass versus Velocity Dispersion Correlation*. ApJ, 574, 740–753. URL `http://adsabs.harvard.edu/abs/2002ApJ...574..740T`

Tripathi, S., Misra, R., Dewangan, G., Rastogi, S., 2011. *Soft Time Lags in the X-Ray Emission of Mrk 1040*. The ApJL, 736, L37. URL `http://cdsads.u-strasbg.fr/abs/2011ApJ...736L..37T`

Trippe, M. L., Reynolds, C. S., Koss, M., Mushotzky, R. F., Winter, L. M., 2011. *XMM Follow-up Observations of Three Swift BAT-selected Active Galactic Nuclei*. ApJ, 736, 81. URL `http://adsabs.harvard.edu/abs/2011ApJ...736...81T`

Tristram, K. R. W., Meisenheimer, K., Jaffe, W., Schartmann, M., et al., 2007. *Resolving the complex structure of the dust torus in the active nucleus of the Circinus galaxy*. A&A, 474, 837–850. URL `http://adsabs.harvard.edu/abs/2007A%26A...474..837T`

Tristram, K. R. W., Raban, D., Meisenheimer, K., Jaffe, W., et al., 2009. *Parsec-scale dust distributions in Seyfert galaxies. Results of the MIDI AGN snapshot survey*. A&A, 502, 67–84. URL `http://adsabs.harvard.edu/abs/2009A%26A...502...67T`

Tristram, K. R. W., Schartmann, M., 2011. *On the size-luminosity relation of AGN dust tori in the mid-infrared*. A&A, 531, 99. URL `http://adsabs.harvard.edu/abs/2011A%26A...531A..99T`

Trouille, L., Barger, A. J., 2010. *The OPTX Project. IV. How Reliable is [O III] as a Measure of AGN Activity?* ApJ, 722, 212–221. URL `http://adsabs.harvard.edu/abs/2010ApJ...722..212T`

Tueller, J., Baumgartner, W. H., Markwardt, C. B., Skinner, G. K., et al., 2010. *The 22 Month Swift-BAT All-Sky Hard X-ray Survey*. ApJSS, 186, 378–405. URL `http://adsabs.harvard.edu/abs/2010ApJS..186..378T`

Tueller, J., Mushotzky, R. F., Barthelmy, S., Cannizzo, J. K., et al., 2008. *Swift BAT Survey of AGNs*. ApJ, 681, 113–127. URL `http://adsabs.harvard.edu/abs/2008ApJ...681..113T`

Tully, R. B., *Nearby galaxies catalog* (1988). URL `http://adsabs.harvard.edu/abs/1988ngc..book.....T`

Tully, R. B., Rizzi, L., Shaya, E. J., Courtois, H. M., et al., 2009. *The Extragalactic Distance Database*. AJ, 138, 323–331. URL `http://adsabs.harvard.edu/abs/2009AJ....138..323T`

Turner, T. J., Miller, L., 2009. *X-ray absorption and reflection in active galactic nuclei*. A&A Review, 17, 47–104. URL `http://adsabs.harvard.edu/abs/2009A%26ARv..17...47T`

Tzanavaris, P., Georgantopoulos, I., 2007. *Searching for hidden AGN in nearby star-forming galaxies with Chandra*. A&A, 468, 129–137. URL `http://adsabs.harvard.edu/abs/2007A%26A...468..129T`

Ueda, Y., Eguchi, S., Terashima, Y., Mushotzky, R., et al., 2007. *Suzaku Observations of Active Galactic Nuclei Detected in the Swift BAT Survey: Discovery of a "New Type" of Buried Supermassive Black Holes*. ApJ, 664, L79–L82. URL `http://adsabs.harvard.edu/abs/2007ApJ...664L..79U`

Urry, C. M., Padovani, P., 1995. *Unified Schemes for Radio-Loud Active Galactic Nuclei*. PASP, 107, 803. URL `http://adsabs.harvard.edu/abs/1995PASP..107..803U`

van der Wolk, G., Barthel, P. D., Peletier, R. F., Pel, J. W., 2010. *Dust tori in radio galaxies*. A&A, 511, 64. URL `http://adsabs.harvard.edu/abs/2010A%26A...511A..64V`

Vasudevan, R. V., Fabian, A. C., 2007. *Piecing together the X-ray background: bolometric corrections for active galactic nuclei*. MNRAS, 381, 1235–1251. URL http://adsabs.harvard.edu/abs/2007MNRAS.381.1235V

Vasudevan, R. V., Fabian, A. C., Gandhi, P., Winter, L. M., Mushotzky, R. F., 2010. *The power output of local obscured and unobscured AGN: crossing the absorption barrier with Swift/BAT and IRAS*. MNRAS, 402, 1081–1098. URL http://adsabs.harvard.edu/abs/2010MNRAS.402.1081V

Vasudevan, R. V., Mushotzky, R. F., Winter, L. M., Fabian, A. C., 2009. *Optical-to-X-ray emission in low-absorption AGN: results from the Swift-BAT 9-month catalogue*. MNRAS, 399, 1553–1575. URL http://adsabs.harvard.edu/abs/2009MNRAS.399.1553V

Vaughan, S., Uttley, P., Pounds, K. A., Nandra, K., Strohmayer, T. E., 2011. *The rapid X-ray variability of NGC 4051*. MNRAS, 413, 2489–2499. URL http://adsabs.harvard.edu/abs/2011MNRAS.413.2489V

Vedrenne, G., Atteia, J., *Gamma-Ray Bursts* (2009). URL http://adsabs.harvard.edu/abs/2009grb..book.....V

Véron-Cetty, M., Véron, P., 2010. *A catalogue of quasars and active nuclei: 13th edition*. A&A, 518, 10. URL http://adsabs.harvard.edu/abs/2010A%26A...518A..10V

Vignali, C., Brandt, W. N., Schneider, D. P., Kaspi, S., 2005. *X-Ray Lighthouses of the High-Redshift Universe. II. Further Snapshot Observations of the Most Luminous z>˜4 Quasars with Chandra*. AJ, 129, 2519–2530. URL http://adsabs.harvard.edu/abs/2005AJ....129.2519V

Vollmer, B., Beckert, T., Duschl, W. J., 2004. *From the Circumnuclear Disk in the Galactic Center to thick, obscuring tori of AGNs*. A&A, 413, 949–957. URL http://adsabs.harvard.edu/abs/2004A%26A...413..949V

Wang, J., Risaliti, G., Fabbiano, G., Elvis, M., et al., 2010. *Revisiting the Short-term X-ray Spectral Variability of NGC 4151 with Chandra*. ApJ, 714, 1497–1510. URL http://adsabs.harvard.edu/abs/2010ApJ...714.1497W

Wang, J., Zhang, E., 2007. *The Unified Model of Active Galactic Nuclei. II. Evolutionary Connection*. ApJ, 660, 1072–1092. URL http://adsabs.harvard.edu/abs/2007ApJ...660.1072W

Weaver, K. A., Meléndez, M., Mushotzky, R. F., Kraemer, S., et al., 2010. *Mid-infrared Properties of the Swift Burst Alert Telescope Active Galactic Nuclei Sample of the Local Universe. I. Emission-line Diagnostics*. ApJ, 716, 1151–1165. URL http://adsabs.harvard.edu/abs/2010ApJ...716.1151W

Werner, M. W., Roellig, T. L., Low, F. J., Rieke, G. H., et al., 2004. *The Spitzer Space Telescope Mission*. ApJSS, 154, 1–9. URL http://adsabs.harvard.edu/abs/2004ApJS..154....1W

Whysong, D., Antonucci, R., 2004. *Thermal Emission as a Test for Hidden Nuclei in Nearby Radio Galaxies*. ApJ, 602, 116–122. URL http://adsabs.harvard.edu/abs/2004ApJ...602..116W

Willick, J. A., Courteau, S., Faber, S. M., Burstein, D., et al., 1997. *Homogeneous Velocity-Distance Data for Peculiar Velocity Analysis. III. The Mark III Catalog of Galaxy Peculiar Velocities*. ApJSS, 109, 333. URL http://adsabs.harvard.edu/abs/1997ApJS..109..333W

Winter, L. M., Mushotzky, R. F., Reynolds, C. S., Tueller, J., 2009a. *X-Ray Spectral Properties of the BAT AGN Sample*. ApJ, 690, 1322–1349. URL http://adsabs.harvard.edu/abs/2009ApJ...690.1322W

Winter, L. M., Mushotzky, R. F., Terashima, Y., Ueda, Y., 2009b. *The Suzaku View of the Swift/BAT Active Galactic Nuclei. II. Time Variability and Spectra of Five "Hidden" Active Galactic Nuclei*. ApJ, 701, 1644–1664. URL http://adsabs.harvard.edu/abs/2009ApJ...701.1644W

Woo, J., Treu, T., Barth, A. J., Wright, S. A., et al., 2010. *The Lick AGN Monitoring Project: The M BH-* Relation for Reverberation-mapped Active Galaxies*. ApJ, 716, 269–280. URL `http://adsabs.harvard.edu/abs/2010ApJ...716..269W`

Wright, E. L., Eisenhardt, P. R. M., Mainzer, A. K., Ressler, M. E., et al., 2010. *The Wide-field Infrared Survey Explorer (WISE): Mission Description and Initial On-orbit Performance*. AJ, 140, 1868–1881. URL `http://adsabs.harvard.edu/abs/2010AJ....140.1868W`

Yang, Y., Wilson, A. S., Matt, G., Terashima, Y., Greenhill, L. J., 2009. *Suzaku Observations of the Circinus Galaxy*. ApJ, 691, 131–139. URL `http://adsabs.harvard.edu/abs/2009ApJ...691..131Y`

Yuan, F., *Advection-dominated Accretion: From Sgr A* to Other Low-luminosity AGNs*. vol. 373, p. 95 (2007). URL `http://adsabs.harvard.edu/abs/2007ASPC..373...95Y`

Yuan, F., Cui, W., 2005. *Radio-X-Ray Correlation and the "Quiescent State" of Black Hole Sources*. ApJ, 629, 408–413. URL `http://adsabs.harvard.edu/abs/2005ApJ...629..408Y`

Yuan, F., Markoff, S., Falcke, H., Biermann, P. L., 2002. *NGC 4258: A jet-dominated low-luminosity AGN?* A&A, 391, 139–148. URL `http://adsabs.harvard.edu/abs/2002A%26A...391..139Y`

Yuan, F., Yu, Z., Ho, L. C., 2009. *Revisiting the "Fundamental Plane" of Black Hole Activity at Extremely Low Luminosities*. ApJ, 703, 1034–1043. URL `http://adsabs.harvard.edu/abs/2009ApJ...703.1034Y`

Zhang, W. M., Soria, R., Zhang, S. N., Swartz, D. A., Liu, J. F., 2009. *A Census of X-ray Nuclear Activity in Nearby Galaxies*. ApJ, 699, 281–297. URL `http://adsabs.harvard.edu/abs/2009ApJ...699..281Z`

Acknowledgements

An erster Stelle möchte ich meinen Eltern, Hannelore und Uwe Asmus danken für die Liebe und Unterstützung, welche mir immer und überall beistehen und von unschätzbarer Bedeutung für mich sind.

In addition, a lot of people supported me and my work in various ways, and made it possible in the first place. In particular, I would like to thank (in no particular order)

- *Prof. Dr. Wolfgang J. Duschl* for supervision and enabling me to continue my enterprise into the wonderful world of astronomy.
- *Dr. Alain Smette* for his supervision, sharing his extensive knowledge while always having an open ear for my problems, and helping to solve them.
- *Dr. Poshak Gandhi* for his "co-"supervision, his extensive support – at any time – and the many motivating ideas on how to progress the research.
- *Dr. Sebastian F. Hönig* for a productive and supportive collaboration, which gave me the opportunity to participate in fascinating observations and learn so much as well.
- *Dr. Margaret Moerchen, Dr. Retha Pretorius* and *David Madlener* for reading – and helping to improve – large parts of the manuscript.
- *Prof. Dr. Michael West* for being a great "boss" during my time in Chile, and for allowing me to undertake so many journeys to nice places where I could experience astronomy at first hand.
- *Paulina Jiron* for her incredible job at making everything possible, while being so warm and friendly the whole time. In particular, I would like to thank her for the help with solving obstacles after the accident.
- *Brigitte Kuhr* and *Holger Boll* for their invaluable administrative and IT support that keeps the institute running, and their never-ending patience in dealing with astronomers.
- *All the administrative and IT staff at ESO Chile* for their important support in all the little bureaucratic and technical problems that occurred during my time in Chile. In particular, I thank Helpdesk linux support, for whom I created quite some work.
- *All the staff at Paranal* for giving visitors such an awesome time on the mountain and also doing a good job during service mode operations.
- *Florian Ober* for being such a nice and welcoming office mate and tolerating (or bearing) my crankiness, especially in the last months.
- *All my friends and colleagues at ESO and at the ITAP* for the nice atmosphere, the interesting, valuable (or funny) discussions during my time in Santiago and Kiel. In particular, I would like to thank the ESO fellows and students for those evenings (not only) at the OPEN.
- and *Dr. Amelia Bayo* not only for reading the manuscript, sharing her scientific knowledge and experience, or always motivating me, but also for everything – and much more than the, here available, space allows to write down.

I thank the European Southern Observatory for granting me the two-year studentship in Chile

This research is based on observations carried out in the ESO programme 083.B-0536, 084-B.0606 and 086.B-0349.

Furthermore, this research is based on observations carried out at Gemini-North during the programme GN-2010A-C-7, which was granted time through the Subaru–Gemini Time Exchange program (prog. ID S10A-094).

This research has made use of the NASA/IPAC Extragalactic Database (NED) which is operated by the Jet Propulsion Laboratory, California Institute of Technology, under contract with the National Aeronautics and Space Administration.

This research has also made use of the NASA/IPAC Infrared Science Archive, which is operated by the Jet Propulsion Laboratory, California Institute of Technology, under contract with the National Aeronautics and Space Administration.

I acknowledge the usage of the HyperLeda database (http://leda.univ-lyon1.fr).

Erklärung

Hiermit erkläre ich, dass

1. die Arbeit – abgesehen der Beratung durch meinen Betreuer – nach Inhalt und Form die eigene Arbeit ist;
2. die Arbeit keiner anderen Stelle im Rahmen eines Prüfungsverfahrens vorgelegen hat oder vorliegt;
3. Teile der Arbeit veröffentlicht worden sind in Asmus et al. (2011);
4. und die Arbeit unter Einhaltung der Regeln guter wissenschaftlicher Praxis der Deutschen Forschungsgemeinschaft entstanden ist.

Kiel, den ....

(Daniel Asmus)